



Universiteit
Leiden
The Netherlands

Probing protostars : the physical structure of the gas and dust during low-mass star formation

Kempen, T.A. van

Citation

Kempen, T. A. van. (2008, October 9). *Probing protostars : the physical structure of the gas and dust during low-mass star formation*. Retrieved from <https://hdl.handle.net/1887/13455>

Version: Corrected Publisher's Version

License: [Licence agreement concerning inclusion of doctoral thesis in the Institutional Repository of the University of Leiden](#)

Downloaded from: <https://hdl.handle.net/1887/13455>

Note: To cite this publication please use the final published version (if applicable).

Probing Protostars:

The physical structure of the gas and dust during
low-mass star formation

Probing Protostars: The physical structure of the gas and dust during low-mass star formation

Proefschrift

ter verkrijging van
de graad van Doctor aan de Universiteit Leiden,
op gezag van de Rector Magnificus prof. mr. P.F. van der Heijden,
volgens besluit van het College voor Promoties
te verdedigen op donderdag 9 Oktober 2008
klokke 16.15 uur

door

Tim Anton van Kempen

geboren te Utrecht
5 september 1980

Promotiecommissie

Promotor: Prof. dr. E. F. van Dishoeck

Co-promotor: Dr. M. R. Hogerheijde

Referent: Prof. dr. N. J. Evans II (University of Texas, Austin)

Overige leden: Dr. R. Güsten (Max Planck Institut für Radioastronomie, Bonn)

Prof. dr. V. Icke

Dr. J. K. Jørgensen (Universität Bonn, Bonn)

Prof. dr. K. H. Kuijken

Dr. P.P. van der Werf

voor Laura en mijn familie

Front Cover: The painting 'Starry Night over the Rhone' by Dutch painter Vincent van Gogh (Musée d'Orsay). Besides being a fantastic painting, it is in many ways representative of the science in thesis. The night-sky (with the wrongly positioned Ursa Major) depicts stars as large spheres, similar to how we perceive protostellar envelopes, over water, one of the key molecules in embedded YSOs, in which jet-like features from the town on the other side are reflected.

Table of contents

	Page
Chapter 1. Introduction	1
1.1 The framework of low mass star formation	4
1.1.1 Structure	4
1.1.2 Classification	5
1.2 Tools	7
1.2.1 Observations	7
1.2.2 Heterodyne array receivers	9
1.2.3 Molecular lines and astrochemistry	9
1.2.4 Radiative transfer modelling	10
1.3 This thesis	11
1.3.1 Envelope properties	11
1.3.2 Warm ($T > 50$ K) gas observations with the CHAMP ⁺ array	12
1.3.3 Water	12
1.3.4 Identifying truly embedded sources	13
1.3.5 Searching for gas-rich disks	13
1.4 Conclusions	14
1.5 Future	16
Chapter 2. The nature of the Class I population in Ophiuchus as revealed through gas and dust mapping	17
2.1 Introduction	18
2.2 Sample selection	23
2.3 Observations	27
2.3.1 Gas line maps	27
2.3.2 Gas single pixel spectra	27
2.3.3 Dust maps	27
2.3.4 SED and IRS spectra	34
2.4 Results	34
2.4.1 Gas maps	34
2.4.2 Dust maps	35
2.4.3 SED and IRS spectra	38
2.5 Analysis	46
2.5.1 Concentration	46
2.5.2 Environment	47
2.5.3 Gas column density	50
2.5.4 Dust	51
2.5.5 Effect of reddening on α_{IR}	52
2.5.6 SEDs: L_{Bol} and T_{Bol}	53

2.5.7	Ice and silicate absorption	54
2.6	Classification	55
2.6.1	Physical classification	55
2.6.2	Identifying embedded stage 1 sources with molecular emission	57
2.6.3	Late stage 1 sources	59
2.6.4	Confused sources	60
2.6.5	Comparison to other methods	60
2.7	Detailed description of all sources	62
2.8	Conclusions	66
Chapter 3. Warm molecular gas in the envelope and outflow of IRAS 12496–7650 (DK Cha)		69
3.1	Introduction	70
3.2	Observations	71
3.3	Results and analysis	71
3.3.1	Outflow emission	72
3.3.2	Envelope	73
3.4	Conclusions	75
Chapter 4. Dense and warm molecular gas in the envelopes and outflows of southern low-mass protostars		77
4.1	Introduction	78
4.2	Observations	84
4.3	Results	88
4.3.1	Single spectra at source position	88
4.3.2	Maps	89
4.4	Analysis	90
4.4.1	Envelope properties	90
4.4.2	Embedded or not?	95
4.4.3	Outflows	97
4.4.4	Individual sources	99
4.5	Conclusions	102
Chapter 5. Unraveling the structure of the molecular outflow and protostellar envelope of HH 46 using high-J CO observations		105
5.1	Introduction	106
5.2	Observations	107
5.3	Results	108
5.3.1	Single pixel spectra	108
5.3.2	Maps	109
5.4	Envelope and surrounding cloud	113
5.4.1	Envelope - dust	113
5.4.2	Envelope - gas	114
5.4.3	Surrounding cloud material	116
5.5	Outflow	116

5.5.1	Outflow temperature	116
5.5.2	Other outflow properties	120
5.6	Origin of the quiescent high- J CO line emission	122
5.6.1	Photon heating of cavity walls	122
5.6.2	Constraining the UV field	124
5.6.3	Importance of the outflow geometry	125
5.7	Conclusions	125
Chapter 6. The warm gas within young low-mass protostars: using CHAMP+ to observe extended high-J CO in envelopes and outflows 129		
6.1	Introduction	130
6.2	Sample and observations	132
6.2.1	Observations	132
6.2.2	Sample	135
6.2.3	Spectral energy distribution	135
6.3	Results	136
6.3.1	Maps	136
6.3.2	Outflow emission	136
6.3.3	Isotopologue observations at the central position	137
6.3.4	^{13}CO 6-5 and [C I] 2-1 maps	137
6.4	Envelope	137
6.4.1	Envelope models	137
6.4.2	CO emission within protostellar envelopes	139
6.5	Outflows	144
6.5.1	Shocks	144
6.5.2	Temperatures of the swept-up gas	145
6.6	Heating processes in the molecular outflow and protostellar envelope	152
6.6.1	Envelope and outflow of BHR 71	153
6.6.2	The 'fossil' outflow of L 1551 IRS 5	154
6.6.3	The PDR of RCrA IRS 7	154
6.6.4	Presence of [C I] 2-1	155
6.7	Conclusions	155
A.1	Chamaeleon II LABOCA map	157
Chapter 7. Modeling water emission from low-mass protostellar envelopes 159		
7.1	Introduction	160
7.2	Model	162
7.2.1	Physical structure of the envelope model	162
7.2.2	H_2O line modelling	164
7.3	Example : L 483	168
7.3.1	Physical structure	168
7.3.2	Results	169
7.3.3	Integrated emission	171
7.3.4	Line profiles	173
7.3.5	HIFI diagnostic lines	175

7.3.6	Comparison with ISO-LWS data	176
7.4	General parameter study	176
7.4.1	Luminosity	178
7.4.2	Density	178
7.4.3	Density profile index	179
7.4.4	H ₂ ¹⁸ O	179
7.4.5	Line profiles	180
7.4.6	Model limitations	181
7.5	Effects on H ₂ O excitation and line formation: dust and micro-turbulence	183
7.5.1	Dust	183
7.5.2	Micro-turbulence	185
7.6	Observational studies	186
7.6.1	ISO-LWS	187
7.6.2	SWAS	187
7.7	Summary and conclusions	188
Chapter 8. Searching for gas-rich disks around T Tauri stars in Lupus		197
8.1	Introduction	198
8.2	Observations	200
8.3	Results	201
8.4	Individual objects	204
8.5	Concluding remarks	209
Bibliography		213
Nederlandse samenvatting		227
Curriculum vitae		235
Nawoord		237

Chapter 1

Introduction

After the discovery of the fact that nuclear fusion of hydrogen into helium powers Sun-like low-mass stars ($M_{\text{star}} \sim 0.5\text{-}2 M_{\odot}$), astronomers realized that stars must have a limited lifetime. Although these lifetimes can be very long (a few billion years), a star 'dies' when the conditions for nuclear fusion are no longer met. Similar to a stellar 'death', it was concluded that stars must also have a 'birth'; a time when a star has not burned any of its hydrogen into helium. Since stars do not accrete new material during 99% of their life, they must accrete all of their mass in these very early stages of their life, a period now called star formation.

Within our Milky Way galaxy, and in all other known galaxies, stars form from the gas and dust within the Interstellar Medium (ISM), that resides within our galaxy. In the Milky Way, most of the ISM is warm (temperatures in excess of a few 100 Kelvin) and at a low density (a few atoms per cm^3). However, at places where the density of the ISM is higher (10^3 cm^{-3}), the gas and dust cool and large molecular cloud complexes are formed. Such complexes can span many parsecs in scale, with the hydrogen becoming molecular. Fig 1.1 shows one of the closest star-forming clouds to the Sun: the Ophiuchus molecular cloud as observed by the *Spitzer Space Telescope*. Deep within such complexes, low-mass stars, such as our Sun, form from the collapse of the densest regions that cannot support their own weight. Within the first Myr, a Young Stellar Object (YSO) is embedded within the large-scale parental cloud and an envelope of its own material, infalling onto the central star. This embedded or protostellar stage is also the era in which outflows are seen.

Our understanding of the evolution of a YSO between the initial collapse and the time that a full-grown stellar system emerges has been limited. A framework for low-mass star formation was only defined in the 1980's and early 1990's with use of observations at millimeter and submillimeter wavelengths, data obtained with infra-red space telescopes, such as *IRAS* and *ISO*, and the improvement of computer power, allowing theoretical models of, in particular, hydrodynamics and continuum and line radiative transfer to be developed to analyze these data. Many aspects of this framework have been subject to intensive research in the late 1990's and early 21st century, using ground-based submillimeter telescopes, such as *IRAM 30m*, *JCMT* and *CSO* as well as new infrared space telescopes such as *Spitzer*. A thorough review on the many aspects of star formation can be found in the proceedings of the "Protostars and Planets V" conference (Reipurth et al. 2007) or the Crete II summer school (Lada & Kylafis 1999).



Figure 1.1 — The Ophiuchus cloud as observed with the *Spitzer Space Telescope*. Ophiuchus is one of the closest star-forming regions to the Sun with a distance of 120 pc, containing numerous low-mass protostars. The Ophiuchus cloud and its protostars are discussed in detail in Chapter 2. This image is a composite of 3.6, 8 and 24 μm light, covering an area of about half a degree to half a degree. Image credit: Lori Allen, NASA/JPL-Caltech/Harvard-Smithsonian CfA.

Despite the significant progress of the recent decades, many details of this framework remain unknown. One of the greatest gaps in our understanding is on what time-scales YSOs and, more importantly, their components evolve. How does the protostellar envelope accrete onto the central star and disk system? What role do outflows play in the evolution of the protostellar envelopes, such as dispersion, heating and the creation of envelope cavities? Do disks form stable orbits in their early phases or are they nothing more than a temporary conduit for material accreting onto the star? What is the importance of the parental cloud structure and the characteristics of neighbouring YSOs on the evolution of the protostellar system?

Star formation research in the last decade has mostly focussed either on the larger scales or on specific individual objects. The first area of research concentrates on the structure of the parental molecular clouds, the influence of large-scale turbulence and magnetic fields, the statistical lifetimes of YSOs, covering both embedded and disk-dominated YSOs as well as the relation of YSOs with their environment. Studies on individual objects focus on the internal structure of YSOs: the characteristics of the protostellar envelope, disk and outflow, the chemical abundances, the influence of the

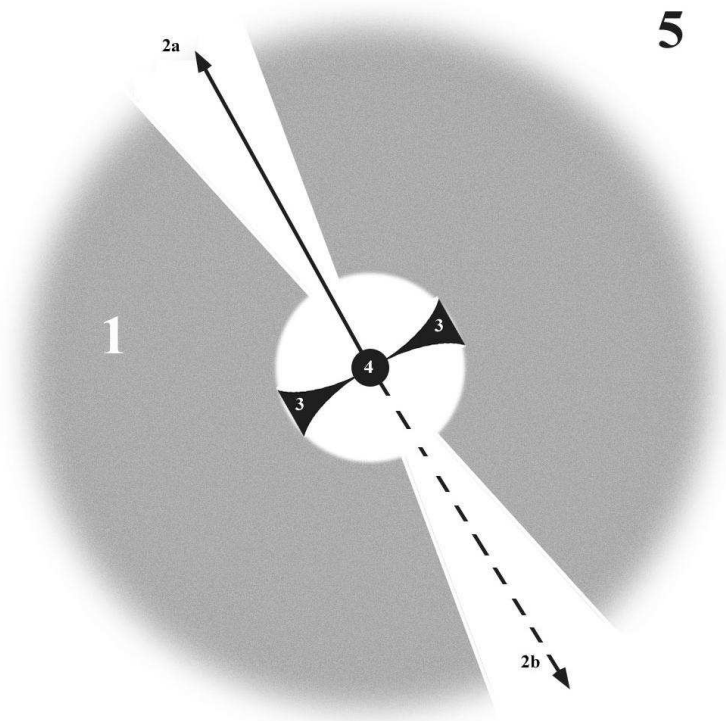


Figure 1.2 — Cartoon representation of the structure of a low-mass protostellar object, with the 5 components indicated. 1: The protostellar envelope (3,000-10,000 AU), 2: The bipolar outflow (up to 1 pc, a and b are the blue and red lobes), 3: The circumstellar disk (~ 500 AU), 4: The central star ($3 R_{\odot}$), 5: The surrounding cloud (a few pc).

immediate surroundings on these characteristics and the stellar properties. However, neither scale is able to accurately describe the entire evolution of YSOs from the initial collapse to a mature stellar system.

Answers to these important questions will rely heavily on the observations coming from two future facilities. The *Herschel Space Observatory*, scheduled to launch in early 2009, will be able to probe the far-IR (60-500 μm) at unprecedented spatial and spectral resolution. The *Atacama Large Millimeter/Submillimeter Array* (ALMA), located in Chajnantor in Chile, will be an interferometer of 54×12 -meter dishes and 12×7 -meter dishes operating at 80 to 900 GHz with spatial resolution down to 1 AU in the nearest star-forming regions. A single theory of low-mass star formation based on observations of these two facilities must include the evolution and characteristics of (the components of) YSOs from the earliest cloud stage to the final main sequence star, likely to include a full planetary system, as well as understand the influences on and from the parental cloud on all scales. This thesis will focus on the evolution of the protostellar envelope, the interaction with both outflow and immediate environment, as well as comparison with larger samples of embedded protostars at submillimeter and infra-red wavelengths.

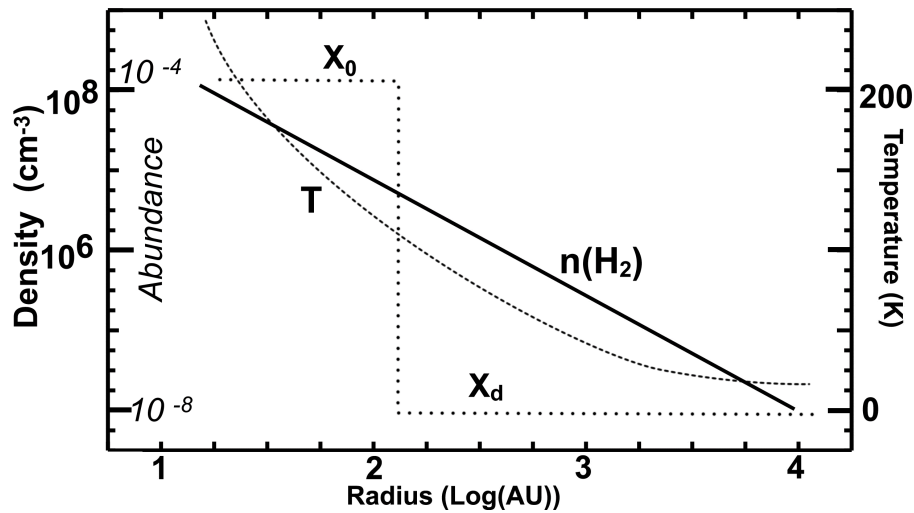


Figure 1.3 — Example of the physical structure of a model envelope ($L = 7L_{\odot}$, $M = 0.4M_{\odot}$) with the density (solid), temperature (dashed), and abundance (dotted) displayed versus radius. The density follows a powerlaw profile. The temperature increases more rapidly than a single powerlaw in the inner region because dust becomes optically thick. The abundance profile in this model envelope is a ‘jump’ abundance. The often-used ‘drop’ abundance has the same profile, but at large radii, the abundance rises again to X_0 due to the fact that freeze-out timescales become longer than the typical life-times of protostellar objects.

1.1 The framework of low mass star formation

1.1.1 Structure

Within the framework of low-mass star formation, a protostellar system consists of five components that are either present within the protostellar system or influence its evolution at certain stages of its evolution. Figure 1.2 shows the location of these components in a cartoon model (not to scale).

1. Protostellar envelope: The bulk of material that can still accrete onto the star resides in a protostellar envelope. The envelope is mostly spherical in nature and is infalling onto the central system. Fig. 1.3 shows the density and temperature structure within a protostellar envelope, which can be roughly characterized with a power-law for the density and temperature profile.
2. Bi-polar outflow: Observations show that most, if not all, protostars have bipolar molecular outflows. Such outflows are driven by high-velocity outflowing jets and wide-angle winds, originating close to the central star and are necessary to carry excess angular momentum away from the star to allow further accretion onto the star. Outflows have a big impact on the surrounding material, with prominent shocks heating and sweeping up the cold cloud material. Outflows have been observed at scales up to a parsec away from the central star.
3. Circumstellar disk: Due to the conservation of angular momentum, infalling matter falls towards a plane perpendicular to the rotation axis of the star. This circumstellar disk is the site of future planet formation. Although disks are difficult to observe during the embedded phases, gas-rich disks can be as large as 500-800 AU. Protostars accrete matter through their disks.

4. Central star: the central star is actively accreting matter. Although deuterium burning within the center of the star starts in the early embedded phases, accretion is responsible for the bulk of the emitted radiation in the early stages of star formation.
5. Surrounding cloud: The amount of material close to or near to a protostellar object, such as the presence of a neighbouring protostellar object or a dense cloud ridge, can distort protostellar envelopes. The amount of turbulence in the cloud can influence the infalling material. In addition, dense cloud material close to the star will allow the energy of bipolar outflows to be deposited much closer to the star. But the largest influence of the clouds is probably on the observational appearance of YSOs, as it reddens the IR emission from the star and produces its own emission.

All these components, with the exception of the parental cloud, evolve as the proto-star ages. The material in the envelope is accreted onto the central star and disk system or dispersed by the stellar wind and bipolar outflows. As accretion slowly comes to a halt, outflows become much less energetic but have already swept up a significant amount of surrounding material and show wider opening angles, whereas the central disks grow bigger and dust settles towards the mid-plane, seeding the initial condition of planet formation. A key component is the protostellar envelope, which contains most of the remaining mass not yet accreted onto the central star.

1.1.2 Classification

Traditionally, YSOs are classified using the spectral slope α_{IR} of their infrared (IR) emission between 2 and 24 μm (Lada 1987; Greene et al. 1994) or using their bolometric temperature (Myers & Ladd 1993). The classification initially identified four and later five classes, which were first thought to be sequential in evolution:

- Class 0, no α_{IR} , high $L_{\text{sub-mm}}/L_{\text{bol}}$
- Class I, $\alpha_{\text{IR}} > 0.3$, $T_{\text{bol}} < 650$ K
- Flat Spectrum, $-0.3 < \alpha_{\text{IR}} < 0.3$, $T_{\text{bol}} = 400\text{-}800$ K
- Class II, $-2 < \alpha_{\text{IR}} < -0.3$, $650 < T_{\text{bol}} < 2800$ K
- Class III, $\alpha_{\text{IR}} < -2$, $T_{\text{bol}} > 2800$ K

Although in general the sequential evolution has proven to be valid from the earliest Class 0 to the later Class III stages as derived from the evolution of the SED (e.g., Fig. 1.4), quite a few sources were found to be incorrectly classified, especially between late Class 0 to early Class II sources. The introduction of 'Flat-Spectrum' sources (Greene et al. 1994) already indicated that this observationally motivated classification cannot be directly incorporated as an evolutionary sequence. Deep near-IR continuum or spectroscopic observations, such as have been done for CRBR 2422.8-3423 and IRS 46 (Brandner et al. 2000; Lahuis et al. 2006) revealed that in some cases, excessive reddening from the cloud, neighbouring protostellar objects or perhaps the viewing angle onto circumstellar disks, can have a significant effect on the IR emission characteristics and thus on the classification. Other studies, such as Jayawardhana et al. (2001), put forward that the distinction between the Class 0 and I is related to the densities of

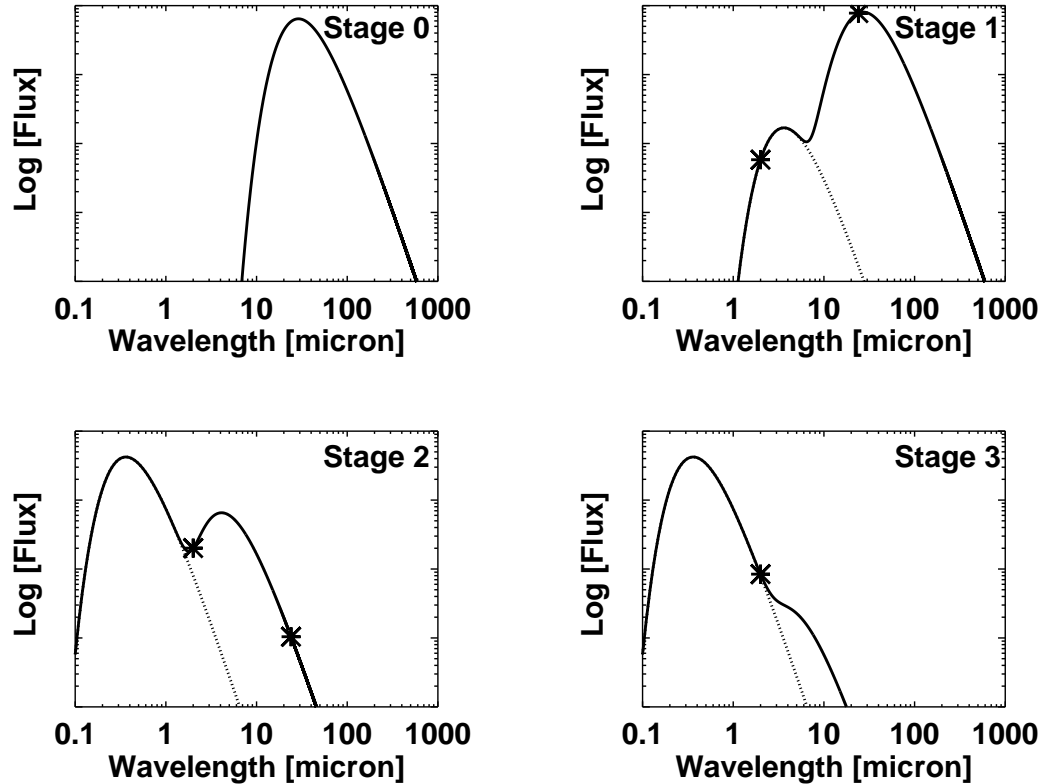


Figure 1.4 — Typical SEDs of the different stages in low-mass star formation. In Stage 1, 2 and 3, the 2 and 24 micron, used to determine α_{IR} are shown with stars.

the surrounding cloud and not from actual evolutionary age. Theoretical studies such as Whitney et al. (2003b) and Crapsi et al. (2008) indeed show that inclination of the circumstellar disk or protostellar envelope strongly affect the IR emission. The main conclusion is that the observationally driven traditional classification is not always a direct representation of the evolutionary stage of the YSO.

Recent modelling efforts (e.g., Whitney et al. 2003a; Robitaille et al. 2006; Crapsi et al. 2008) have therefore adopted a more physically driven classification method, based on the respective masses in each component, M_{star} , M_{env} and M_{disk} , with $M_{\text{circ}} = M_{\text{disk}} + M_{\text{env}}$.

- Stage 0 : a deeply embedded stage, in which the bulk of accretion takes place. $M_{\text{star}} \leq M_{\text{circ}}$.
- Stage 1 : a less embedded stage. The bulk of the material has accreted onto the central star $M_{\text{star}} > M_{\text{circ}}$, but the envelope still dominates the circumstellar material $M_{\text{env}} > M_{\text{disk}}$.
- Stage 2 : a gas-rich disk. The envelope has either accreted onto the central star or dispersed into the ISM. A circumstellar disk, containing gas, remains. Such stars are often identified as classical T Tauri stars.
- Stage 3 : a gas-poor disk. Due to planet formation and dispersal of most of the gas, only a tenuous disk, dominated by the dust, can be seen around the cen-

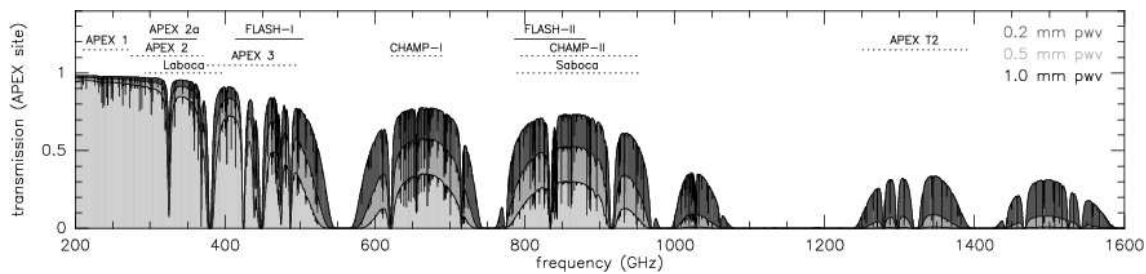


Figure 1.5 — Opacity of the atmosphere at submillimeter wavelengths from the Chajnantor site, Chile (Güsten et al. 2006). PWV is the amount of precipitable water vapor in the Earth atmosphere.

tral star that has almost reached the main sequence. The dust can be either the original interstellar dust or the ‘debris’ produced by collisions of planetesimals.

Fig. 1.4 shows the typical SEDs for the four different stages, originally used to define the classes, if geometry does not change the appearance. Early Stage 0 show a black-body associated with a low temperature. As the envelope diminishes, the central disk and star emit at infrared wavelengths. When the envelope has been dispersed, a Stage 2 source with a central star and disk remain, with a characteristic infra-red excess. In the last phases before the main sequence, this excess becomes lower as the disk loses its gas and dust to accretion, dispersion and the formation of planets.

Unique observable tracers of these four stages, especially the first two embedded stages, are difficult to determine. Single-dish continuum observations of the dust are able to trace the amount of material in the protostellar envelope, but are unable to constrain the central stellar and disk masses. Observations with (sub)millimeter interferometers can constrain M_{disk} compared to M_{env} and even M_* , and have been used to probe the physical structure of embedded YSOs down to scales of a few hundred AU (e.g. Looney et al. 2000). However, owing to long integration times, current generation interferometers are only able to cover small samples. One characteristic that has not been well constrained is the interaction between the outflow and the envelope. The manner in which the molecular outflow heats the envelope is not well understood. This also has influence on the classification and the physical and chemical structure of embedded sources.

1.2 Tools

1.2.1 Observations

Astronomical observations of low-mass star formation are limited to relatively long wavelengths due to a couple of reasons. First, the low temperatures encountered in cold molecular clouds cause the material to emit the bulk of their thermal radiation at (far-)infrared (IR) or even longer wavelengths. Second, the accretion of material onto a protostellar surface, as well as any nuclear fusion inside such a protostellar core, produces emission at Ultra-Violet (UV) and visible wavelengths and possibly Extreme UV and X-ray emission. The surrounding dust of the protostellar envelope and cloud absorbs almost all incoming radiation and efficiently reprocesses it into emission at far-IR and (sub)millimeter wavelengths. Although ground-based IR telescopes are able to

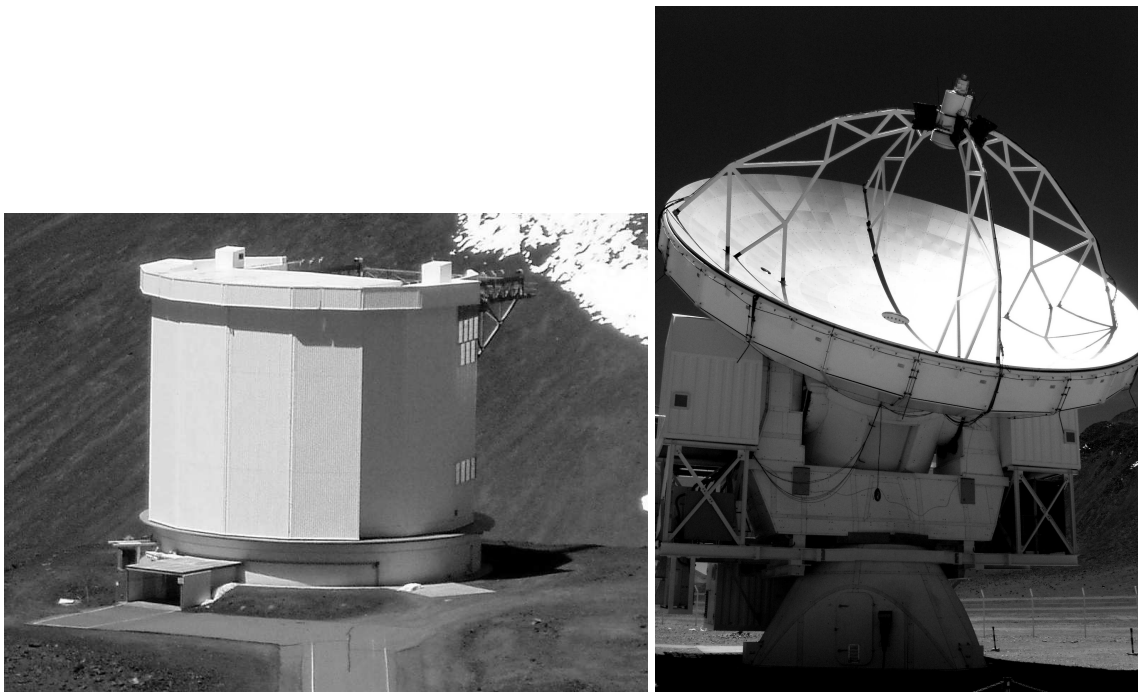


Figure 1.6 — The sub-mm telescopes *JCMT* (15 m dish) and *APEX* (12 m dish). The *JCMT* observes from the top of Mauna Kea, Hawaii, while *APEX* is located at the Chajantor plateau, Chile. (Images by Tim van Kempen).

detect the emission originating at the inner disk or inner envelope surfaces, the best-suited wavelength for observing continuum radiation of low-mass protostellar objects from the ground is the submillimeter. This wavelength range is not totally transparent as can be seen in Fig 1.5. The presence of Earth's atmosphere and the water in it divides the submillimeter regime, roughly defined as $< 1 \text{ mm}$ or $> 300 \text{ GHz}$, into observable windows. Therefore telescopes in this wavelength range, such as the *JCMT* or *APEX* (see Fig 1.6), are located at sites in the world with the driest conditions, such as Mauna Kea on Hawaii or Chajnantor in Chile. Fig 1.5 clearly identifies a few wavelength windows for which the atmosphere is almost completely transparent, as well as a few bands which need the best weather conditions. *APEX* is the first submillimeter telescope on the southern hemisphere, opening up these highest frequency windows for southern protostars.

Optically thin emission from the cold dust dominates the continuum emission at submillimeter wavelengths. Using bolometric arrays, such as SCUBA, LABOCA and MAMBO-II, the spatial distribution of the dust can be efficiently mapped. Both the large-scale cloud emission, as well as individual YSOs, ranging from pre-stellar cores to disks, can be detected (e.g. Motte et al. 1998; Shirley et al. 2000; Johnstone et al. 2001; Nutter et al. 2005). An additional advantage of observing at submillimeter wavelengths is the wealth of rotationally excited lines of common molecules present in the cold molecular clouds, protostellar envelopes and circumstellar disks. Within the more accessible atmospheric windows (100, 230 and 345 GHz), carbon monoxide (CO) emits its three lowest rotationally excited lines, perfectly suitable to probe cold material up

to 30-40 Kelvin. In these same windows, many lines of more complex molecules, such as CH_3OH , are also found.

1.2.2 Heterodyne array receivers

Emission of molecular species can only be fully understood when its spatial distribution is taken into account. Although spectral line maps have been routinely obtained since the 1970's, mapping with single-pixel heterodyne receivers at submillimeter have long been severely limited due to high system temperatures. Array receivers have been available at millimeter wavelengths for more than a decade (e.g. SEQUOIA at the FCRAO since the mid-1990's and HERA at IRAM 30m since 2002). In recent years, heterodyne array receivers have been built for the submillimeter bands. Two of the foremost instruments, which provide excellent coverage of the key atmospheric windows, are the *HARP-B* and *CHAMP*⁺ arrays, mounted on the JCMT and APEX, respectively. *HARP-B* is a 16 element heterodyne array receiver with a $2' \times 2'$ field of view covering the 345 GHz atmospheric band. In this band, CO emits in $J=3-2$ and HCO^+ in $J=4-3$ transition. In addition, many emission lines of methanol, formaldehyde and other species can be observed.

CHAMP⁺ is a 14-element heterodyne array receiver covering the high-frequency 690 and 800 GHz bands simultaneously (7 pixels per band). These bands are essential for observing the warm CO gas in the $J=6-5$, $7-6$ and $8-7$ transitions. *CHAMP*⁺ is a PI instrument (PI: R. Güsten) developed by Max Planck Institute für Radioastronomie and SRON Groningen.

Both instruments are the first of their kind in their frequency range. With the mapping speed increased by (almost) an order of magnitude, astronomers are for the first time able to sample a larger range of sources instead of limiting spectral line maps to only a few special cases.

1.2.3 Molecular lines and astrochemistry

Observations of molecular lines play a central role in the identification and characterisation of embedded YSOs and their evolution. Emission of rotationally excited molecules is uniquely tied to both the gas and dust conditions at the location of the molecule. Only molecular lines can probe the velocity structure of the gas and distinguish quiescent, infalling, rotating and outflowing gas. Combinations of emission lines from different molecules with different excitation conditions are able to trace a range of temperatures and densities. Since the most abundant molecule H_2 is symmetric and does not have strong rotational lines, tracer molecules are used to probe the gas. The molecule used most often is carbon monoxide (CO). CO is chemically very stable and its abundance is thought to be relatively constant with respect to H_2 . As CO is a linear rotor, rotational energy levels are spaced with increasing energy $\Delta E_{\text{rot}} \propto 2B_E(J_{\text{up}})$ where B_E is the rotational constant and J_{up} the upper rotational state of the transition. Thus, frequencies of the CO transitions are multiples of the 1-0 frequency of 115 GHz ($\lambda = 2.6$ mm), with any transition with J_{up} emitting at a frequency of $115 \times J_{\text{up}}$ GHz.

The lower lying levels have excitation temperatures ranging from 10 to 50 Kelvin and are thus excellent tracers of the cold ($T < 50$ Kelvin) gas. Only freeze-out of CO

onto the dust grains in the form of ice mantles influences the emission of such gas-phase rotational lines. The relatively low critical density of these transitions (a few times 10^4 cm^{-3} or less) also allows observations of relatively low density gas. Isotopologues of CO, such as ^{13}CO and C^{18}O provide optically thin alternatives.

For regions of high density material, other tracers are more suitable because CO has a small dipole moment. Molecules with rotational transitions with high critical densities, such as HCO^+ , are better suited to probe high density gas. The critical density of a transition scales as $\mu^2\nu^3$ with μ the dipole moment of the molecule and ν the frequency of the transition.

The inner regions of protostellar envelopes, the surfaces of circumstellar disks and the shocked gas of the bipolar outflows all contain warm gas ($T \sim 50 - 150$ Kelvin). Because cold gas is often in the line of sight of this warmer gas, low excitation lines of CO and HCO^+ are not able to probe this gas, unless it is at high density. The sole exception is the shocked, red- or blue-shifted gas within the bipolar outflows, traceable in the line wings of low- J CO lines (Bachiller & Tafalla 1999). An often proposed tracer of the warm gas is the water molecule, as water is frozen out onto the grains in large amounts up to temperatures of 100 K. However, the rotational transitions of water can only be observed from the ground in very rare cases (Cernicharo et al. 1990, 1996). Space-based observations in the far-IR, such as done with *ISO-LWS*, are able to probe rotational water lines over a large range of transitions (e.g., Nisini et al. 2002), but have so far lacked the spectral and spatial resolution to be used as physical probes. More complex molecules, such as methanol (CH_3OH), have transitions with high excitation temperatures, but their chemistry complicates their use as a physical probe. Such rotational lines do provide a unique insight into the chemistry of low-mass protostellar objects. CO is therefore one of the few reliable probes of warmer gas with its high-lying rotational lines. The disadvantage is that such lines emit at high frequencies (450 GHz - 1 THz), a range in submillimeter that is difficult to observe. Only a handful of studies have tried to use these transitions as physical probes of components of protostellar objects (Schuster et al. 1993; Hogerheijde et al. 1998). However, with the recent commissioning of the APEX telescopes, such frequencies now become more and more accessible.

1.2.4 Radiative transfer modelling

For both line and continuum emission, solving the radiative transfer equation allows for a much more detailed description of the protostellar structure, as well as the gas and dust characteristics throughout the envelope, than can be provided by observational maps alone. The radiative transfer of both line and continuum can be described by the following equation

$$I_\nu = I_\nu(0)e^{-\tau_\nu} + \int S_\nu(x)e^{-\int \tau_\nu(x) dx} dx \quad (1.1)$$

with the received intensity, I_ν , a sum of the intensity originating in the main radiation source $I_\nu(0)$, extinguished along a line of sight with optical depth τ_ν , and the intensities $\int S_\nu$ originating along the path x at frequency ν . Continuum radiation is often

integrated over a wide range of ν (broadband), while line radiation is sampled with channel widths of a certain frequency. Current generation heterodyne receivers have spectral resolutions of a few tens of kHz to a few MHz. Radiative transfer within protostellar systems is complex, as the density and temperature vary strongly along the path x . Both τ_ν and S_ν depend sensitively on such variations. Well-tested continuum radiative transfer codes have been publicly available since the mid-90's, such as *DUSTY* (Ivezić & Elitzur 1997). Advanced 1D and 2D molecular line radiative transfer codes such as *RADEX* (van der Tak et al. 2007) and *RATRAN* (Hogerheijde & van der Tak 2000) have in the last decade also become accessible to the general public as the main tool to correctly analyze the observed emission. See e.g., van Zadelhoff et al. (2002) or van Dishoeck (2003), for a more thorough discussion about combining dust and molecular line radiative transfer codes.

1.3 This thesis

In this thesis, we will focus on probing the physical structure of the gas and dust of embedded low-mass protostars, and address the following questions:

- What are the properties of the envelopes of Stage 1 low-mass protostellar objects, especially in their inner regions?
- How much warm gas is present in the inner regions of protostellar envelopes and from which location does it originate?
- What is the influence of the outflow and outflow cavities on the protostellar envelope and how are the inner envelope and outflow cavity walls heated?
- What is the role of water in low-mass embedded protostellar objects and can observations with Herschel add to our understanding of the inner envelope regions?
- What observational differences can be discerned between truly embedded sources and sources mistakenly classified as embedded due to their orientation, geometry or immediate surroundings?
- How do embedded YSOs lose their protostellar envelope and evolve toward a T Tauri star, where a gas-rich disk dominates the circumstellar material?

To answer these questions, we combine the tools discussed above. Observations of cold dust in the submillimeter continuum, observations of CO lines ranging from probes of the cold (CO $J=2-1$ and $3-2$), warm (CO $J=6-5$ and $7-6$), low density ($C^{18}O$ $3-2$) and high density (HCO^+ $4-3$) gas, as well as 1D radiative transfer modelling of both gas and dust are used to probe the warmer regions of protostellar objects, both in the envelope and molecular outflow.

1.3.1 Envelope properties

Throughout this thesis, the structure of the protostellar envelope plays a key role. In Chapter 2, we probe a large range of embedded Class I protostars in Ophiuchus with the $850 \mu\text{m}$ continuum, HCO^+ and $C^{18}O$. These data provide information about the presence of the dense gas (as predicted by the envelope models), column density of the envelope and environment. In Chapter 4, we present the molecular line observations of

a sample of southern sources which have received little attention so far, including both low and higher excitation CO transitions at the source position. Warm gas is found in the protostellar envelopes. The emission of high- J CO lines is further discussed in Chapters 3, 5 and 6, for example in IRAS 12496-7650 for which the fluxes of even higher- J CO lines seen in the ISO-LWS beam cannot be produced by a warm inner envelope.

1.3.2 Warm ($T > 50$ K) gas observations with the CHAMP⁺ array

The warm gas in the envelope and the extent and influence of the outflow at scales of $1'$ are traced, with the CHAMP⁺ instrument, the first heterodyne array receiver able to map at the shorter submillimeter wavelengths. Chapter 4 present the first results of more southern sources with the FLASH instrument as a precursor to CHAMP⁺. Chapters 5 and 6 show the results with this new instrument on samples of well-studied protostars. Not only warm outflowing gas, but also surprisingly strong narrow high- J CO emission is found on scales of almost $1'$ ($>40,000$ AU). A key question is how this warm gas is distributed and heated. Therefore, in addition to CO transitions, we also observe the [C I] 2–1 line to probe the amount of atomic carbon present in the envelopes. C is produced by photodissociation of CO and thus traces the strength and color of the radiation field in the outflow cavities and inner envelope. Chapters 5 and 6 both include a discussion of the heating of gas at the envelope and outflow cavities through UV photons, first discussed by Spaans et al. (1995). These photons are created in the accretion disk boundary layer and in outflow shocks and impinge on the outflow cavities. Chapter 5 shows that in the outflow of HH 46, at least three shocks produce an UV radiation field equivalent to at least 100 times the average interstellar field, which heats the gas to a few hundred K, but does not dissociate CO into C.

1.3.3 Water

With the upcoming launch of the *Herschel Space Observatory*, astronomers will for the first time have access to an instrument (HIFI, built by SRON Groningen (de Graauw et al. 2005)), that is well-suited for observations of rotationally excited water lines with a spectral resolution able to resolve these lines and a spatial resolution comparable to that of the *JCMT* and *APEX* at lower frequencies. Fig. 1.7 shows the energy levels of lines that will be observed with *HIFI* and *PACS*. Water cannot be observed from the ground, except under exceptional weather conditions. Water is expected to be an excellent tracer of the warm gas as it freezes out onto the grains at 100 K. It also stands at the basis of many chemical networks of more complex molecules. However, to use the water emission lines as a physical and chemical probe, the radiative transfer of water within the envelope must be understood. Chapter 7 presents a large grid of models, for which the radiative transfer was calculated to investigate the role and observability of rotationally excited water lines in low-mass embedded YSOs. These models reveal that water emission is sensitively dependent on the local conditions, such as temperature, density and abundance, throughout the envelope.

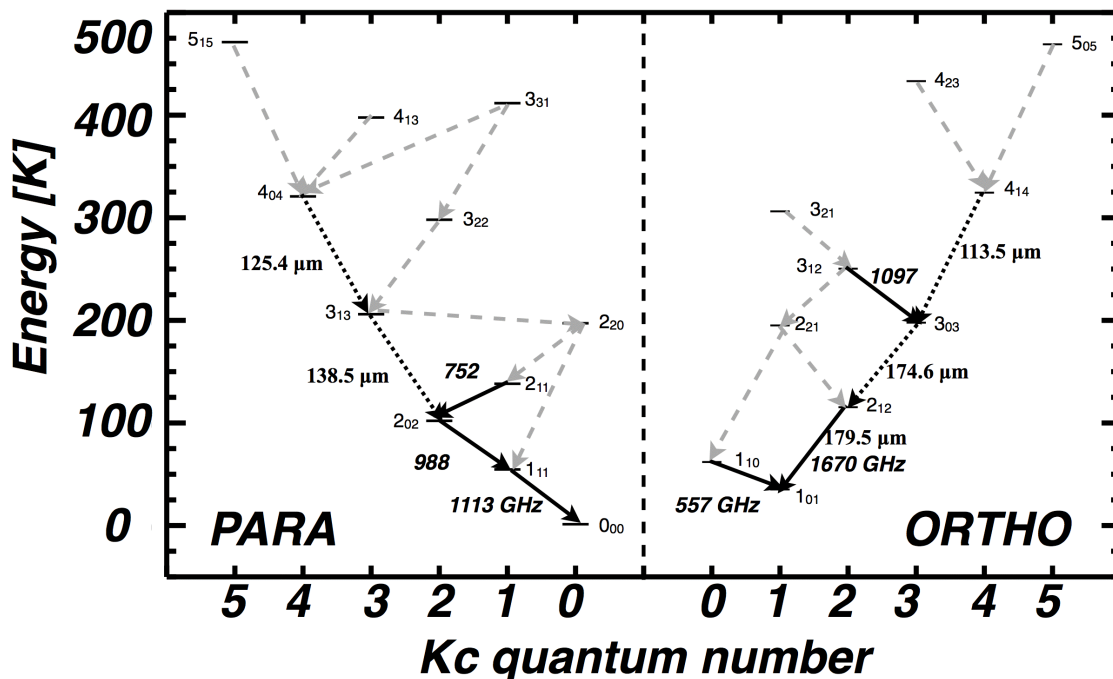


Figure 1.7 — The energy level diagram of water. Solid lines are the main water transitions to be observed with the *HIFI* instrument, dotted lines with the *PACS* instrument and dashed grey lines are all other main water transitions.

1.3.4 Identifying truly embedded sources

In Chapter 2 we survey all sources in the L 1688 region of the Ophiuchus molecular clouds, and use the molecular line emission of C^{18}O and HCO^+ , combined with the dust emission at $850 \mu\text{m}$ to identify all embedded sources from a large sample of sources classified as Class I using their spectral slopes. The aim is to divide them into Stage 1 and Stage 2 sources. It is found that single-dish HARP-B array observations of these molecules are able to correctly identify embedded sources and distinguish edge-on disks and severely reddened sources from the truly embedded sample. In Chapter 4, we use observations of the same molecular lines obtained with new single pixel receivers commissioned at the APEX telescope, of a sample of embedded southern sources using the more traditional method of mapping point by point. Although no observations were obtained of the dust, these data were successfully used to identify a few sources with no associated HCO^+ emission, which are likely to be not embedded.

1.3.5 Searching for gas-rich disks

When the envelope is completely accreted or dispersed, a pre-main sequence star with a circumstellar disk remains. Young Stage 2 disks are gas-rich and this gas can be revealed in single dish observations as a double peaked line characteristic of Keplerian rotation. Chapter 8 presents a single-dish JCMT study done on a sample of Class II T Tauri stars in Lupus. Observations taken at the source as well as slightly off-source indicate that, in contrast with many Class II sources in Taurus, the emission seen in

the single-dish is dominated by the surrounding cloud. For only a single source, IM Lup, clear evidence of a gas-rich disk was found, which will be an excellent target for future ALMA observations. For most other sources, gas associated with the cold cloud overwhelms any emission from the source, so that interferometers are needed to observe the gas in such disks directly.

1.4 Conclusions

The data and models presented in this thesis provide a detailed description of many components of the low-mass star formation framework. With new probes of the dense and warm gas new insights have been obtained of the structure of the inner part of the protostellar envelope and molecular outflow. This includes many southern YSOs which have not been studied in detail before. The combination of high frequency observations and radiative transfer modelling has proven to be essential in determining the physical conditions. The main conclusions of this thesis can be summed up with the following points:

1. The outer and inner region of the protostellar envelope, molecular outflow and surrounding cloud material can be efficiently probed by $2' \times 2'$ spectral line maps of low- J and high- J CO transitions, CO isotopologues such as $C^{18}O$, HCO^+ and water. With the arrival of array receivers such as HARP-B and CHAMP⁺, which allow for much faster mapping speeds than previously available with single pixel detectors, astronomers can for the first time take the full advantage of spectral maps of large samples, even for relatively weak lines ($T_{MB} < 1K$). The data in this thesis show that even the emission of high- J CO lines is extended on arcmin scale.
2. The dense inner regions ($\geq 10^6 \text{ cm}^{-3}$) of low-mass protostellar envelopes are a unique characteristic of embedded YSOs. HCO^+ 4–3 is an excellent tracer of this dense gas and thus of Stage 1 protostars in general. The concentration of the HCO^+ 4–3 emission is found to be a useful parameter to quantify this.
3. A sample of 45 sources in Ophiuchus, including all previously known Class I sources, several flat-spectrum sources and a few known disks, was reclassified into Stage 1, Stage 2 or confused sources with our new method using HCO^+ and $C^{18}O$ molecular emission. Of these, only 17 sources are definitely embedded YSOs. Four of these embedded YSOs have little ($0.1\text{--}0.2 M_{\odot}$) envelope material remaining and are likely at the interesting transitional stage from embedded YSO to T Tauri star.
4. Strong narrow quiescent ^{12}CO 6–5 and 7–6 emission is seen in a sample of eight protostars, both on source and up to $1'$ offset (Chapters 5 and 6). In two cases, the emission at the central position cannot be produced solely by passive heating of the envelope. One of these cases is HH 46, for which extensive new submillimeter line data from CO 2–1 up to 7–6 and LABOCA continuum emission have been obtained. Limits on $C^{18}O$ 6–5 are crucial to reach this conclusion. The extra warm gas is likely produced by UV irradiation of the envelope and outflow cavity walls, with the UV photons created in the accretion disk boundary layer.
5. The narrow high- J CO emission observed at much larger distances from the

- source along the outflow (a few 1,000 AU or more, Chapter 5 and 6) is likely also produced by UV photon heating of the cavity walls. Here UV photons can also be created by internal jet shocks within the cavity and by the bowshock where the jet interacts with the ambient cloud. All larger scale outflows, such as N 1333 IRAS 2, HH 46, L 1551 IRS 5 and BHR 71, clearly show this extended warm quiescent component, where the cavity walls are heated to several hundred K.
6. Molecular outflows play an integral role in the evolution of embedded YSOs. In Chapters 3–6, both low- J (3–2 and 4–3) and high- J (6–5 and 7–6) CO lines are used to trace the molecular outflows of a large sample of protostellar objects. Their physical and observational characteristics can differ wildly. Some sources, such as IRAS 12496-7650 (Chapters 3, 4 and 6) have cold molecular outflows ($T=30$ –50 K), viewed almost perfectly face-on. Other flows, such as HH 46 are much warmer ($T > 100$ K), are viewed at a different angle and thus cover a much bigger area on the sky (Chapters 5 and 6). Other outflow parameters, determined through the spectral line mapping, show that the surrounding cloud influences the physical properties of outflows. If less material is present forces with which the outflow is ejected can be up to two order of magnitude lower than expected (Chapters 4 and 5). The derived temperatures of 50–150 K agree well with predictions from a jet-driven bow shock outflow model. Shock heated gas emitting in the high- J CO is only seen for Class 0 flows and in relatively low quantities for the flows of the more massive Class I sources L 1551 IRS 5 and HH 46. For the other Class I sources, photon heating clearly dominates.
 7. The cloud environment of YSOs can significantly influence their observational appearance (Chapters 2, 4 and 8). In crowded regions, such as found in Ophiuchus, cloud material or neighbouring protostellar objects can confuse the classification of both embedded YSOs and disk-dominated T Tauri stars. Cloud material near T Tauri disks can overwhelm the emission from the gas within the circumstellar disk itself. The $C^{18}O$ line profiles over a $2' \times 2'$ region provide detailed information about the cloud structure. In L 1688 of Ophiuchus at least three layers are clearly identified from the line profiles of $C^{18}O$ 3–2 in some areas of the cloud.
 8. Water lines can be categorized as: (i) optically thick lines sensitive to the cold outer part of the envelopes; (ii) highly excited ($E_u > 200$ –250 K) optically thin lines sensitive to the warm inner region; and (iii) lines which vary from optically thick to thin depending on the abundances (Chapter 7). Dust influences the emission of water significantly by becoming optically thick at the higher frequencies. A good physical model of a source, including the correct treatment of dust, is a prerequisite for inferring the water abundance structure and possible jumps at the evaporation temperature from observations. The inner warm ($T > 100$ K) envelope can be probed by highly excited lines, while a combination of excited and spectrally resolved ground state lines probes the outer envelope. Observations of $H_2^{18}O$ lines, although weak, provide even stronger constraints on abundances.
 9. Emission from T Tauri stars with disks in Lupus is often overwhelmed by the cloud contribution in single-pixel molecular line observations (Chapter 8). Nevertheless, an interesting gas-rich disk (IM Lup) was identified using small CO 3–2

spectral maps, which is an excellent target for follow-up interferometric studies.

1.5 Future

In future years, the field of star formation will experience another major boost. Within a year, *Herschel*, covering the wavelength range from 60 to 600 μm with both continuum and heterodyne instruments, will have been launched by ESA. It carries three instruments: PACS, a far-IR low-resolution spectrometer and imager at 60-200 μm ; SPIRE, a submillimeter imaging bolometer array at 250, 350 and 500 μm ; and HIFI, a heterodyne spectrometer well-suited for water observations. The 3.5m dish provides spatial resolution comparable to ground-based facilities at longer wavelengths. Several large programs, such as *WISH* (Water In Star-forming region with *Herschel*), are scheduled to observe the far-IR continuum emission as well as a large range of molecular lines, in particular water and high- J CO transitions.

In addition, *ALMA*, the largest (sub)millimeter interferometer in the world with up to 54x12-m and 12x7-m dishes with baselines up to 15 km, will have experienced first light by 2010 and early science projects will start in 2011. The location of *ALMA* at Chajnantor, Chile, next to *APEX*, will also allow for observations at the highest possible frequencies, key to probing and imaging the warm gas through high- J CO transitions at subarcsecond scale.

On longer time-scales, the construction of the *James Webb Space Telescope* and giant optical and IR telescopes such as *E-ELT* will allow for unprecedented resolution and sensitivity at mid-IR wavelengths. However, without detailed understanding of the individual components of a protostellar objects, ranging from the cold neighbouring cloud material to the warm center of the protostellar envelope, observations from such facilities will be difficult to interpret. The data presented in this thesis will hopefully guide many future observations of protostars.

Chapter 2

The nature of the Class I population in Ophiuchus as revealed through gas and dust mapping

Abstract The Ophiuchus clouds, in particular L 1688, are an excellent region to study the embedded phases of star formation, due to the relatively large number of protostars. However, the standard method of finding and characterizing embedded young stellar objects (YSOs) through just their infrared spectral slope does not yield a reliable sample. This may affect the age determinations, often derived from the statistics on the total number of embedded YSOs and pre-main sequence stars within a cloud. Spectral maps of the HCO^+ $J=4-3$ and C^{18}O $J=3-2$ lines using the HARP-B array on the James Clerk Maxwell Telescope and SCUBA 850 μm dust maps are obtained of all sources in the L 1688 region with infrared spectral slopes consistent with, or close to, that of embedded YSOs. Selected 350 μm maps were obtained with the Caltech Submillimeter Observatory. The properties, extent and variation of dense gas, column density and dust up to $1'$ ($\sim 7,500$ AU) are probed at $15''$ resolution. Using the spatial variation of the gas and dust, together with the intensity of the HCO^+ $J=4-3$ line, we are able to accurately identify the truly embedded YSOs and determine their properties. The protostellar envelopes range from 0.05 to $0.5 M_{\odot}$ in mass. The concentration of HCO^+ emission (~ 0.5 to 0.9) is generally higher than that of the dust concentration. Combined with absolute intensities, HCO^+ proves to be a better tracer of protostellar envelopes than dust, which can contain disk and cloud contributions. Our total sample of 45 sources, including all previously classified Class I sources, several flat-spectrum sources and some known disks, was re-classified using the molecular emission. Of these, only 17 sources are definitely embedded YSOs. Four of these embedded YSOs have little ($0.1-0.2 M_{\odot}$) envelope material remaining and are likely at the interesting transitional stage from embedded YSO to T Tauri star. About half of the flat-spectrum sources are found to be embedded YSOs and about half are disks. The presented classification method is successful in separating embedded YSOs from edge-on disks and confused sources. The total embedded population of the L 1688 cloud is found almost exclusively in Oph-A, Oph-B2 and the Ophiuchus ridge. The detailed characterization presented will be necessary to interpret deep interferometric ALMA and future Herschel observations.

T.A. van Kempen, E.F. van Dishoeck, D.M. Salter, M.R. Hogerheijde, J.K. Jørgensen,
A.C.A. Boogert, *submitted to A&A*

2.1 Introduction

Low-mass young stellar objects (YSOs) have traditionally been classified using their observed infrared (IR) spectral slope, α_{IR} , from 2 to $\sim 20 \mu\text{m}$ (Lada & Wilking 1984; Adams et al. 1987) or their bolometric temperature, T_{bol} (Myers & Ladd 1993). Together with the subsequent discovery of the Class 0 stage (André et al. 1993) this led Greene et al. (1994) to identify 5 classes of YSOs:

- Class 0, no α_{2-14} , high $L_{\text{sub-mm}}/L_{\text{bol}}$
- Class I, $\alpha_{2-14} > 0.3$, $T_{\text{bol}} < 650 \text{ K}$
- Flat Spectrum, $-0.3 < \alpha_{2-14} < 0.3$, $T_{\text{bol}} \sim 400\text{-}800 \text{ K}$
- Class II, $-2 < \alpha_{2-14} < -0.3$, $650 < T_{\text{bol}} < 2800 \text{ K}$
- Class III, $\alpha_{2-14} < -2$, $T_{\text{bol}} > 2800 \text{ K}$

Each class is thought to represent a different category, and probably evolutionary stage, of YSOs. Class 0 sources are the earliest, deeply embedded YSO stage; Class I sources are thought to be more evolved embedded YSOs, Class II the T Tauri stars with gas-rich circumstellar disks and Class III the pre-main sequence stars surrounded by tenuous or debris disks. Deep mid-IR photometry introduced the ‘flat-spectrum’ (FS) sources (e.g. Greene et al. 1994), with IR spectral slope close to 0 and which may represent a stage intermediate between Class I and II. An accurate classification and physical characterization of YSOs is important for constraining the time scales of each of the phases and for determining the processes through which an object transitions from one phase to the next. In this study, we focus on the embedded YSO population and their transition to the T Tauri phase.

The ρ Ophiuchus molecular clouds, part of the Gould Belt, are some of the nearest star-forming regions and contain many Class I and II sources. Consisting of two main clouds, L 1688 and L 1689, the star formation history and protostellar population of these regions have been studied extensively. Although the distance to Ophiuchus has long been debated (Knude & Høg 1998), recent work constrains it to $120 \pm 4 \text{ pc}$ for L 1688 (Loinard et al. 2008). The large-scale structure of the Ophiuchus clouds at millimeter wavelengths was first mapped by Loren (1989) using the ^{13}CO molecular line emission with $2.4'$ resolution. It was found that much of the cloud is in filamentary structures, but also that a diffuse foreground layer is present in Ophiuchus, resulting in a higher average extinction toward YSOs than in other clouds such as Taurus (Dickman & Herbst 1990). Subsequent continuum observations at millimeter (mm) wavelengths mapped most of the large-scale structure present in detail, distinguishing the Oph-A through Oph-F regions within L 1688 (Mezger et al. 1992; Motte et al. 1998; Johnstone et al. 2000; Stanke et al. 2006; Young et al. 2006).

The YSO population was first identified by Elias (1978); Wilking & Lada (1983); Wilking et al. (1989); Comeron et al. (1993) and Greene et al. (1994) using IR observations. With the arrival of (sub-)mm telescopes, VLA 1623 in L 1688 was identified as the first deeply embedded YSO (Wootten 1989; Loren et al. 1990; André et al. 1993). In more recent years, a large population of Class I and Class II sources has been found based on their IR spectral slopes, using space-based observatories such as the *Infrared Space Observatory* (ISO) (e.g. Liseau et al. 1999; Bontemps et al. 2001) and ground-based IR (e.g. Barsony et al. 1997, 2005). Most embedded sources in L 1688 are clustered around the

filaments of the Oph-A, Oph-B2, Oph-E and Oph-F regions, while the Oph-C region only shows a single embedded source and Oph-D does not have any embedded YSO (Motte et al. 1998). In Oph-E and Oph-F most sources are lined up along a relatively small filament of material: for the purpose of this chapter, we will adopt the name ‘Ophiuchus ridge’ for this region.

With the launch of the *Spitzer Space Telescope*, the Ophiuchus cloud was included in the guaranteed time (GTO) and the ‘cores to disks’ (c2d) Legacy program (Evans et al. 2003). Padgett et al. (2008) report on the results at 24, 70 and 160 μm using the MIPS instrument, revealing the emission from the large-scale structure at mid and far-IR wavelengths. Jørgensen et al. (2008) compared the results from the c2d program with the COMPLETE 850 μm SCUBA sub-millimeter dust mapping from Johnstone et al. (2000) and Ridge et al. (2006) to determine the association of YSOs with dense cores.

The stellar ages of the Class II and III sources in Ophiuchus were found to be 0.1–1 Myr based on stellar spectroscopy compared with evolutionary tracks, indicating a relatively young age for the total cloud (Greene & Meyer 1995; Luhman & Rieke 1999). The Star-Formation Efficiency (SFE) was recently calculated with *Spitzer* and SCUBA photometry to be of the order of 13% within the cores and 4% in the cloud as found by Evans et al. (in prep) and (Jørgensen et al. 2008), lower than previous determinations (Wilking & Lada 1983).

The relative timescales of the different phases are determined by the number of objects in each class of YSOs (e.g. Evans et al. in prep). Recent high resolution ground-based (near)-IR imaging show that some of the Class I sources in Ophiuchus are physically different from an embedded YSO, confusing these timescales determinations. For example, the Class I source CRBR 2422.8-3423 was found to be an extincted edge-on disk from near-IR imaging (Brandner et al. 2000; Pontoppidan et al. 2005). The source OphE MM3, classified as a starless core by Motte et al. (1998), was also shown to be an edge-on disk in the same study (Brandner et al. 2000). The source IRS 46 has no associated protostellar envelope and was re-classified based on *Spitzer* and sub-mm data as a disk (Lahuis et al. 2006). Much of the reddening seen in the IR originates from the nearby envelope associated with IRS 44.

Foreground material can also heavily influence the identification and subsequent analysis of embedded sources (e.g., Luhman & Rieke 1999). An excellent example is provided by the Class I source Elias 29 in L 1688, which has two foreground layers in addition to the ridge of material in which the YSO is embedded (Boogert et al. 2002). Only a combination of molecular line emission at sub-millimeter and IR spectroscopy could constrain the protostellar envelope as well as the immediate environment around it (Boogert et al. 2000, 2002). Indeed, IR spectroscopy can be used as a complementary diagnostic and spectra of many of the YSOs in Ophiuchus have been taken, using ISO, *Spitzer* or ground-based telescopes (e.g. Alexander et al. 2003; Pontoppidan et al. 2003; Boogert et al. 2008). Ice absorption features such as the 3 μm H₂O and 15.2 μm CO₂ bands are usually associated with embedded sources whereas silicate emission at 10 and 20 μm is characteristic of Class II sources, but foreground absorption and edge-on disks can confuse this classification (Boogert et al. 2002; Pontoppidan et al. 2005).

In recent years, several detailed modelling efforts have been carried out to study the relations between the observed spectral energy distribution (SED) and the physical structure of embedded YSOs (e.g. Jørgensen et al. 2002; Whitney et al. 2003b; Schöier et al. 2004; Young et al. 2004; Robitaille et al. 2006, 2007; Crapsi et al. 2008). Whitney et al. (2003b) show that it is possible for embedded YSOs with a face-on projection to be classified as Class II. Due to their orientation, these sources are viewed straight down the outflow cone, directly onto the central star and disk system. Crapsi et al. (2008) show that a significant fraction of the Class I sources may be edge-on flaring disks, that have already lost their protostellar envelope. The spectral slope is much steeper than expected due to their structure.

A prime characteristic and component of embedded YSOs is the presence of dense centrally condensed envelopes. While dust maps at sub-millimeter wavelengths have become very popular to trace the early stages of star formation (e.g. Motte et al. 1998; Shirley et al. 2000; Johnstone et al. 2000; Stanke et al. 2006), the continuum emission at these wavelengths is dominated by the cold outer envelope and cloud material, with disks starting to contribute as the envelope disperses (e.g. Hogerheijde et al. 1997; Looney et al. 2000; Young et al. 2003). Single-dish dust continuum data by themselves are not able to distinguish between dense cores and envelope or foreground material, nor quantify any disk contributions. However, the dense gas ($\sim 10^6 \text{ cm}^{-3}$) located in the inner regions of protostellar envelopes is uniquely probed by molecular lines with high critical densities at sub-millimeter wavelengths. Observations of deeply embedded Class 0 YSOs have indeed revealed strong sub-millimeter lines of various molecules (e.g. Blake et al. 1994, 1995; Schöier et al. 2002; Jørgensen 2004; Maret et al. 2004, 2005), but only a few studies have been carried out on more evolved Class I embedded YSOs (e.g. Hogerheijde et al. 1997).

A good high density tracer is the HCO^+ molecule, for which the $J=4-3$ line both has a high critical density of $>10^6 \text{ cm}^{-3}$ and is accessible from the ground. Dense gas is also found in the circumstellar disk on scales of a few tens to hundreds AU, but such regions are generally diluted by an order of magnitude in single-dish observations.

In contrast, molecular lines with much lower critical densities, such as the low excitation C^{18}O transitions, contain much higher contributions from low density material. This makes these lines well-suited as column density tracers for large-scale cloud material and the cold outer regions of the protostellar envelope (e.g. Jørgensen et al. 2002). Both the HCO^+ and C^{18}O data have velocity resolutions of 0.1 km s^{-1} or better, thus allowing foreground clouds to be identified.

Most sub-millimeter line data so far have been single pixel spectra toward the YSO with at best a few positions around specific YSOs. The recently commissioned HARP-B instrument is a 16-pixel receiver, operating in the 320 to 370 GHz atmospheric window allowing rapid mapping of small ($2'$) regions (Smith et al. 2003). HARP-B is mounted on the James Clerk Maxwell Telescope (JCMT)¹.

We present here HARP-B maps of all Class I sources in the L 1688 region in C^{18}O 3–2 and HCO^+ 4–3. The combination of these two molecular lines allows us to differ-

¹The James Clerk Maxwell Telescope is operated by The Joint Astronomy Centre on behalf of the Science and Technology Facilities Council of the United Kingdom, the Netherlands Organisation for Scientific Research, and the National Research Council of Canada.

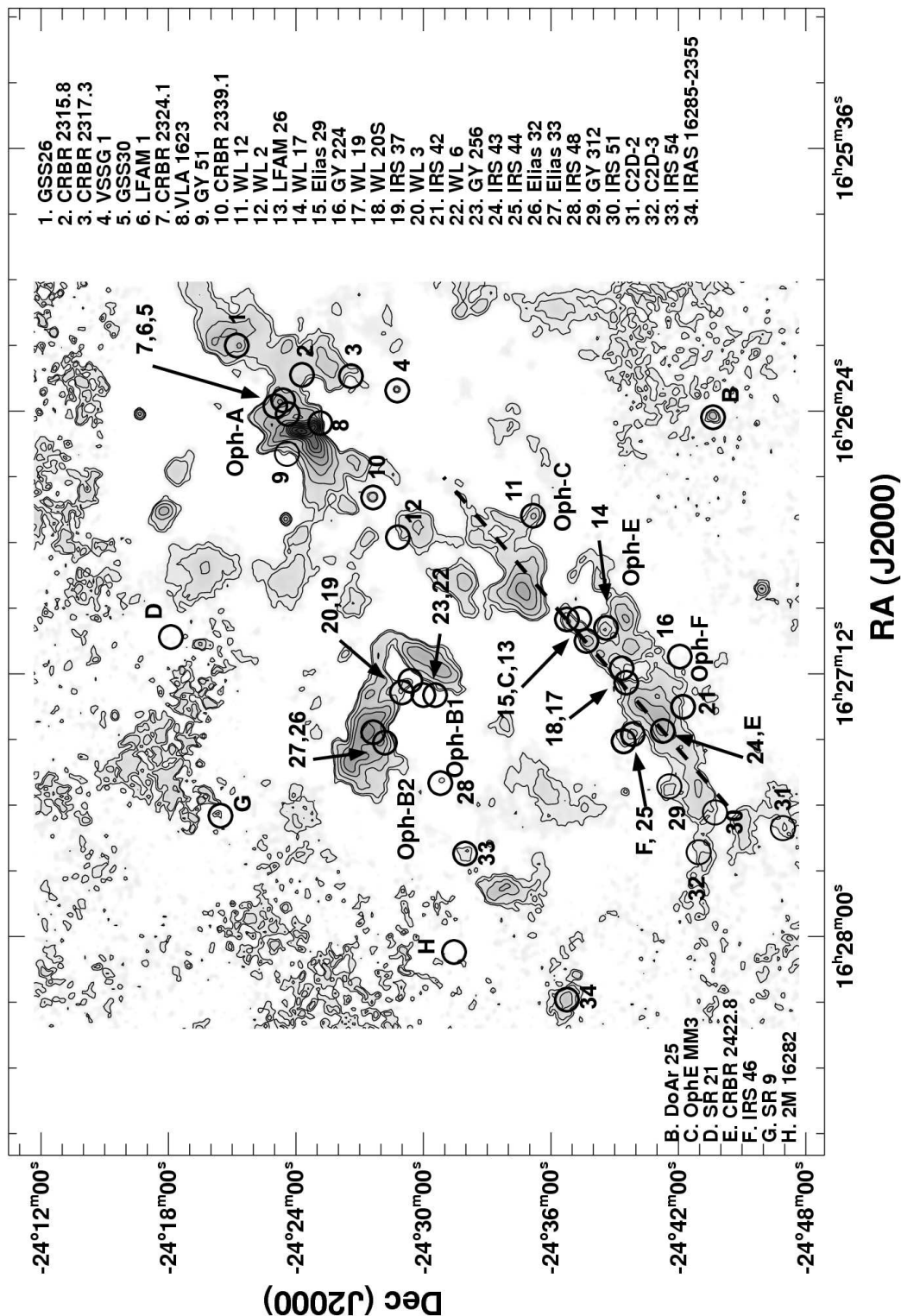


Figure 2.1 — The L 1688 core in Ophiuchus. In grey-scale and contours the 850 μm SCUBA map as published by Johnstone et al. (2000) and Di Francesco et al. (2008) is shown. The locations of all the sources as observed in this study are shown, except for C2D-162527.6, Haro 1-4, C2D-162748.2 and IRS 63. C2D-16274.1 is marked as C2D-2 and C2D-162748.2 as C2D-3. The dashed line indicates the Oph ridge.

entiate between protostellar envelopes, dense cores and foreground cloud material, as well as edge-on disks. The goal of this chapter is to characterize the envelopes of the embedded source population of L 1688, as well as present a new method for identifying truly embedded sources and separate them from (obscured) edge-on disks using the dense gas present in embedded YSOs. In § 2.2, a sample of Class I sources in the L 1688 core is selected. In § 2.3, we discuss the details of the heterodyne observations carried out at the JCMT and the Atacama Pathfinder EXperiment (APEX)², as well as the supplementary observations obtained at continuum wavelengths. § 2.4 presents the maps and spectra and in § 2.5 we analyze the properties of the gas and dust of the sources in the sample. The environment around the YSOs, column density, envelope gas and concentration of the HCO⁺ are discussed. In § 2.6, we present a new method for identifying embedded YSOs from (edge-on) disks and apply this method to the sample. This classification is then compared to traditional methods as well as other recently proposed methods. The main conclusions of the chapter are given in § 2.7.

Table 2.1 — Sample of embedded sources in L 1688, with additional known disks included.

Source	Other names	Coordinates (J2000)		Ref. ^a	$\alpha_{2-24\mu\text{m}}$ ^b
		RA	Dec		
C2D-162527.6	SSTc2d J162527.6-243648	16:25:27.6	-24:36:48.4	2	0.36
GSS 26		16:26:10.4	-24:20:58	1	-0.46
CRBR 2315.8-1700		16:26:17.2	-24:23:45.1	2	0.69
CRBR 2317.3-1925.3	SKS 1-10	16:26:18.8	-24:26:13	1	-0.56
VSSG 1	Elias 20	16:26:18.9	-24:28:22	1	-0.73
GSS 30	Elias 21/GSS 30-IRS1	16:26:21.4	-24:23:04.1	2	1.46
LFAM 1	GSS 30-IRS3	16:26:21.7	-24 22 51.4	2	0.73
CRBR 2324.1-1619		16:26:25.5	-24:23:01.6	2	0.87
VLA 1623	VLA 1623.4-2418	16:26:26.4	-24:24:30.3	2	no
GY 51	VSSG 27	16:26:30.5	-24:22:59	1	0.05
CRBR 2339.1-2032	GY 91	16:26:40.5	-24:27:14.3	2	0.45
WL 12	GY 111	16:26:44.0	-24:34:48	1	2.49
WL 2	GY 128	16:26:48.6	-24:28:39	1	0.02
LFAM 26	CRBR 2403.7/GY 197	16:27:05.3	-24:36:29.8	2	1.27
WL 17	GY 205	16:27:07.0	-24:38:16.0	1	0.61
Elias 29	WL15/GY 214	16:27:09.6	-24:37:21.0	1	0.36
GY 224		16:27:11.4	-24:40:46	1	-0.05
WL 19	GY 227	16:27:11.9	-24:38:31.0	1	-0.43
WL 20S	GY 240	16:27:15.9	-24:38:46	1	2.75
IRS 37	GY 244	16:27:17.6	-24:28:58	1	0.25
WL 3	GY 249	16:27:19.3	-24:28:45	1	-0.03
IRS 42	GY 252	16:27:21.6	-24:41:42	1	-0.03
WL 6	GY 254	16:27:21.8	-24:29:55	1	0.72

Continued on Next Page. . .

²This publication is based on data acquired with the Atacama Pathfinder Experiment (APEX). APEX is a collaboration between the Max-Planck-Institut für Radioastronomie, the European Southern Observatory, and the Onsala Space Observatory.

Table 2.1 – Continued

Source	Other names	Coordinates (J2000)		Ref. ^a	$\alpha_{2-24\mu\text{m}}$ ^b
		RA	Dec		
GY 256		16:27:22.0	-24:29:39.9	2	-0.24
IRS 43	GY 265	16:27:27.1	-24:40:51	1	1.17
IRS 44	GY 269	16:27:28.3	-24:39:33.0	1	2.29
Elias 32	IRS 45/VSSG 18	16:27:28.6	-24:27:19.8	2	-0.03
Elias 33	IRS 47/VSSG 17	16:27:30.1	-24:27:43	1	-0.12
IRS 48	GY 304	16:27:37.2	-24:30:34	1	0.88
GY 312		16:27:38.9	-24:40:20.5	2	0.64
IRS 51	GY3 15	16:27:40.0	-24:43:13	1	-0.15
C2D-162741.6	SSTc2d J162741.6-244645	16:27:41.6	-24:46:44.6	2	0.32
C2D-162748.2	SSTc2d J162748.2-244225	16:27:48.2	-24:42:35.6	2	1.98
IRS 54	GY 378	16:27:51.7	-24:31:46.0	1	0.03
IRAS 16285-2355		16:28:21.6	-24:36:23.7	2	1.23
C2D-162857.9	SSTc2d J162857.9-244055	16:28:57.9	-24:40:54.9	2	0.67
IRS 63		16:31:35.7	-24:01:29.5	2	0.14
Known Disks					
Haro 1-4	DoAr 16	16:25:10.5	-23:19:14.5	2	-0.89
DoAR 25	GY 17	16:26:24.0	-24:43:09.0	1	-1.12
OphE MM3		16:27:05.9	-24:37:08.2	2	-0.33
SR 21	Elias 30	16:27:10.2	-24:19:16.0	1	-0.79
CRBR 2422.8-3423.8	CRBR 85	16:27:24.8	-24:41:03.0	1	1.01
IRS 46	GY 274	16:27:29.7	-24:39:16.0	1	0.18
SR 9	IRS 52/Elias 34	16:27:40.5	-24:22:07.0	1	-1.07
2MASS 16282		16:28:13.7	-24:31:39.0	2	-1.55

^a References for positions : 1:Bontemps et al. (2001), 2: c2d delivery document

^b From c2d delivery document, based on the *Spitzer* c2d survey and 2MASS fluxes.

2.2 Sample selection

Of the known (embedded) YSO population within L 1688, 45 objects were selected for our sample using several criteria. First, we require all sources be located within the 850 μm dust continuum map made by the COMPLETE project of L 1688 using SCUBA on the JCMT (Johnstone et al. 2000). Second, sources must be included in the area covered by the c2d program using IRAC and MIPS on *Spitzer* (Evans et al. 2003; Padgett et al. 2008). All sources classified as Class I in either André & Montmerle (1994), Barsony et al. (1997), Bontemps et al. (2001) or the c2d delivery document (Evans et al. 2007)³ are included with luminosities $> 0.04 L_{\odot}$. Although these 41 objects have been classified as Class I in one or more of these papers, only 6 of these have been classified consistently as Class I in all studies. Most other sources are classified as either Class II or Flat spectrum sources at least once. All such sources are included in the analysis

³<http://ssc.spitzer.caltech.edu/>

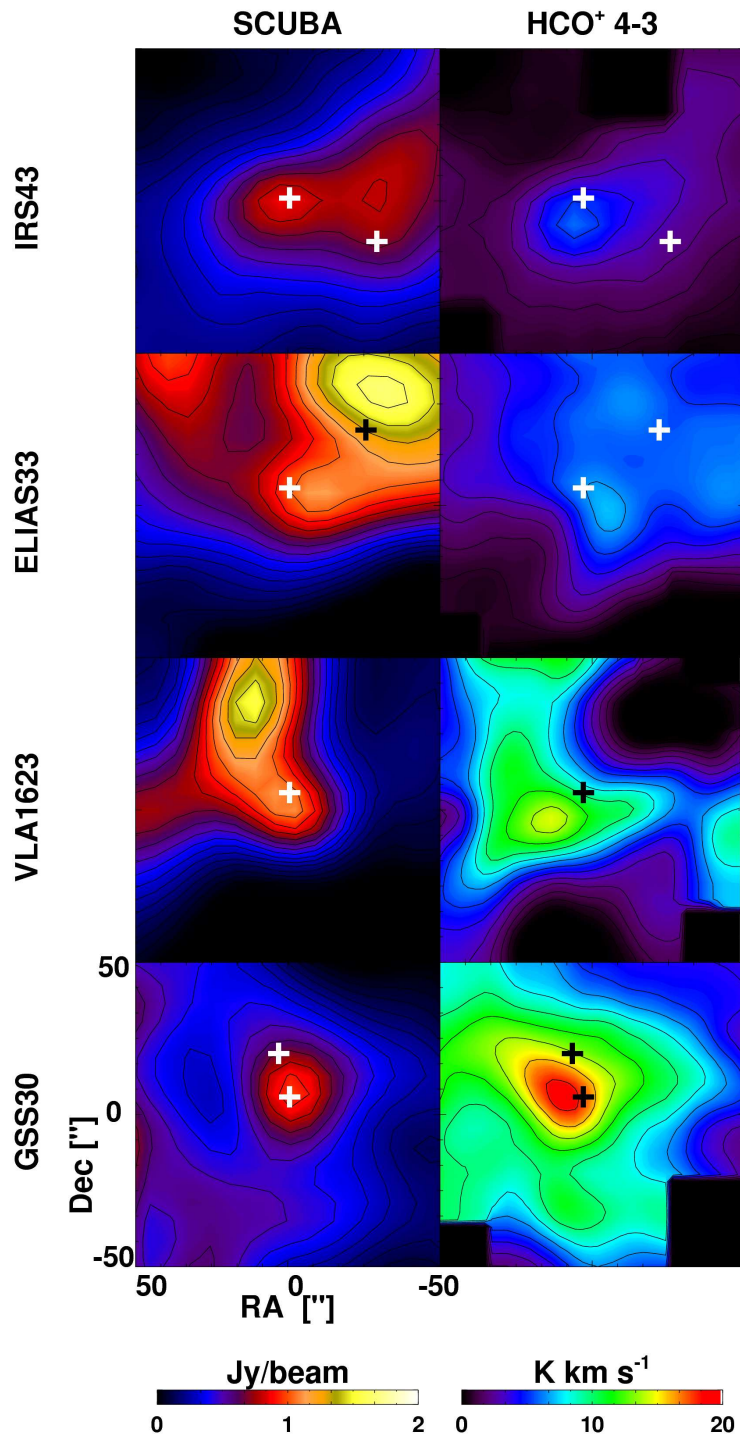


Figure 2.2 — SCUBA 850 μm continuum (*left*) and HCO⁺ 4-3 (*right*) integrated intensity maps plotted from bottom to top for GSS 30 IRS1, VLA 1623, Elias 33 and IRS 43. The IR source positions are marked in the SCUBA maps with white crosses. Note that the absolute scale of these maps is a factor 4 higher than those in Fig. 3 and 4. The 850 μm continuum flux for VLA 1623 has been scaled down by a factor 4. In the map of GSS 30, LFAM 1 is located north of the GSS 30 IRS1 position. Elias 32 is located at the north-west side of the Elias 33 map. CRBR 2422.8-3423 is located to the south-west of IRS 43. All four main targets show strong HCO⁺ and SCUBA peaking within 5'' of the IR position at (0,0), characteristic of truly embedded sources.

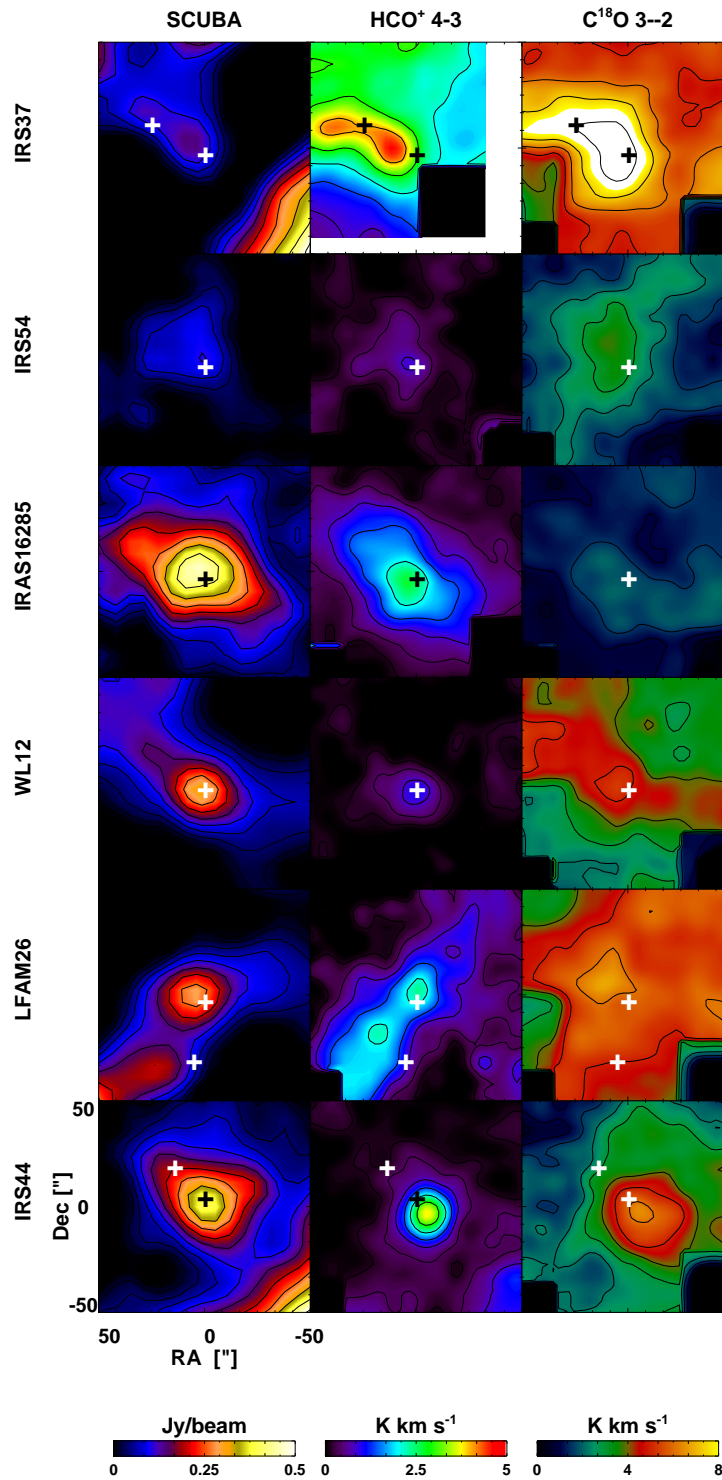


Figure 2.3 — SCUBA 850 μm continuum (left), HCO^+ 4–3 (middle) and C^{18}O 3–2 (right) integrated intensity maps plotted for (from bottom to top) IRS 44, LFA26, WL 12, IRAS 16285, IRS 54 and IRS 37. The locations of the IR sources are indicated in the SCUBA maps with white crosses. In the IRS 44 map, IRS 44 is indicated with a black cross, and IRS 46 with a white one. In the LFA26 field, OphE MM3 is located south of LFA26. In the IRS 37 field, WL 3 is located west of IRS 37. The sources at (0,0) in this figure show weaker HCO^+ images than in Fig. 2.2, but are still peaking on the IR positions in both SCUBA and HCO^+ , and are thus embedded YSOs according to our classification.

of this chapter, but conversely, our sample does not include all Flat spectrum or Class II sources listed in the c2d survey. Known edge-on disks such as 2MASS 16282, IRS 46, OphE MM3 and CRBR 2422.2-3423, are among these 41 sources and are included within the sample to illustrate the results of our method for such sources. The sample should not contain any reddened background main-sequence stars which are readily identified in the c2d analysis. However, other background sources, such as AGB stars or background infrared galaxies, may be present.

Four sources with $\alpha_{2-24\mu\text{m}} > 0.0$ were found only in the recent *Spitzer* observations. These are SSTc2d J162527.6-243648, SSTc2d J162741.6-244645, SSTc2d J162748.2-244225 and SSTc2d J162857.9-24405. The names C2D-162527.6, C2D-162741.6, C2D-162748.2 and C2D-162857.9 are adopted. VLA 1623-2418 is included as an embedded Class 0, but it is generally absent from the above studies. In addition, IRS 63 was included, although it is not part of the L 1688 core. Recent interferometric results suggest that this source is an embedded YSO with little envelope material left, and, as such, presents an interesting test case for the proposed method of identifying truly embedded sources (Lommen et al. 2008). Four disk sources within or near to the L 1688 region, Haro 1-4, DoAr 25, SR 9 and SR 21, were included to serve as a sample of known disk sources.

The final source sample, which covers all potential Class I sources, can be found in Table 2.1. The positions as found in Bontemps et al. (2001) were used where available. If the source was not included in Bontemps et al. (2001), or if confusion exists due to nearby IR sources, the position as found in the c2d delivery document (Evans et al. 2007) was adopted. For sources in common, most positions agree within $3''$. Fig. 2.1 shows the distribution of the sample as plotted on the SCUBA $850\ \mu\text{m}$ map of L 1688 (Johnstone et al. 2000; Ridge et al. 2006; Di Francesco et al. 2008).

The table includes the spectral index $\alpha_{2-24\mu\text{m}}$ given in the c2d delivery document (Evans et al. 2007), calculated from the 2MASS, IRAC and MIPS ($24\ \mu\text{m}$ only) fluxes. No α_{IR} could be determined from *Spitzer* data for VLA 1623 (too faint) and Elias 29 (saturated). The SED of Elias 29, as seen by ISO, shows a sharply rising spectrum between 1.5 and $5\ \mu\text{m}$, and a flat spectrum long-wards of $5\ \mu\text{m}$, resulting in an $\alpha_{2-24\mu\text{m}}$ of 0.36 (e.g. Boogert et al. 2000).

2.3 Observations

2.3.1 Gas line maps

The majority of the sample was observed in HCO⁺ 4–3 (356.7341 GHz) and C¹⁸O 3–2 (329.3305 GHz) using the recently commissioned 16-pixel heterodyne array receiver HARP-B on the James Clerk Maxwell Telescope (JCMT). The high spectral resolution mode of 0.05 km s⁻¹ available with the ACSIS back-end was used to disentangle foreground material as well as any contributions from outflowing material. Spectra were subsequently binned to 0.15 km s⁻¹.

HARP-B observations of 30 sources in 21 fields were carried out during July and August 2007 in C¹⁸O 3–2 and HCO⁺ 4–3 under weather conditions with an atmospheric optical depth, $\tau_{225\text{GHz}}$ ranging from 0.035 to 0.08 (precipitable water vapor of 0.7 to 1.6 mm). The fields were observed down to a rms noise of 0.1 K in a 0.5 km s⁻¹ bin. The HARP-B pixels have typical single side-band system temperatures of 300–350 K. The 16 receivers are arranged in a 4×4 pattern, separated by 30". This gives a total foot print of 2' with a spatial resolution of 15", the beam of the JCMT at 345 GHz. The 2' × 2' fields were mapped using the specifically designed jiggle mode HARP4⁴. A position switch of typically 30' was used, with larger throws if needed. The Class 0 source IRAS 16293-2422 was used as a line calibrator and pointing source. Calibration errors are expected to dominate the flux uncertainties, and are estimated at 20%. Pointing was checked every two hours and was generally found to be within 2–3". The map was re-sampled with a pixel size of 5", which is significantly larger than the pointing error. The main-beam efficiency was taken to be 0.67. Data were reduced using the STARLINK package GAIA and the CLASS reduction package.

2.3.2 Gas single pixel spectra

Supplementary data of HCO⁺ 4–3 were taken at the APEX telescope during July 2007, using the APEX-2a receiver. All sources were observed for which no HARP-B data were taken, except GSS 26 and GY 51. The APEX observations were done in excellent weather conditions with $\tau_{225\text{GHz}}$ ranging from 0.01 to 0.04 (PWV 0.2 to 0.8 mm). Single spectra were taken with a spectral resolution of 0.4 km s⁻¹ down to an rms of 0.3 K. Calibration errors are estimated to be ~ 20%. The APEX 12-m dish is slightly smaller than the JCMT 15-m dish, producing a beam of 18" instead of 15". Pointing errors are <4". Beam efficiency is 0.70.

For the sources GSS 30, VLA 1623, WL 20S, IRS 42, IRS 43, Elias 32 and Elias 33, C¹⁸O 3–2 spectra were obtained from the CADC archive⁵. These spectra were taken with the RxB receiver during September 2005.

2.3.3 Dust maps

The 850 μm continuum data of the Ophiuchus region, obtained within the scope of the COMPLETE project using the SCUBA instrument on the JCMT, were used to characterize the dust in the environments around all sources of the sample (Johnstone et al.

⁴See JCMT website <http://www.jcmt.jach.hawaii.edu/>

⁵See <http://www.cadc-ccda.hia-ihp.nrc-cnrc.gc.ca/jcmt/>

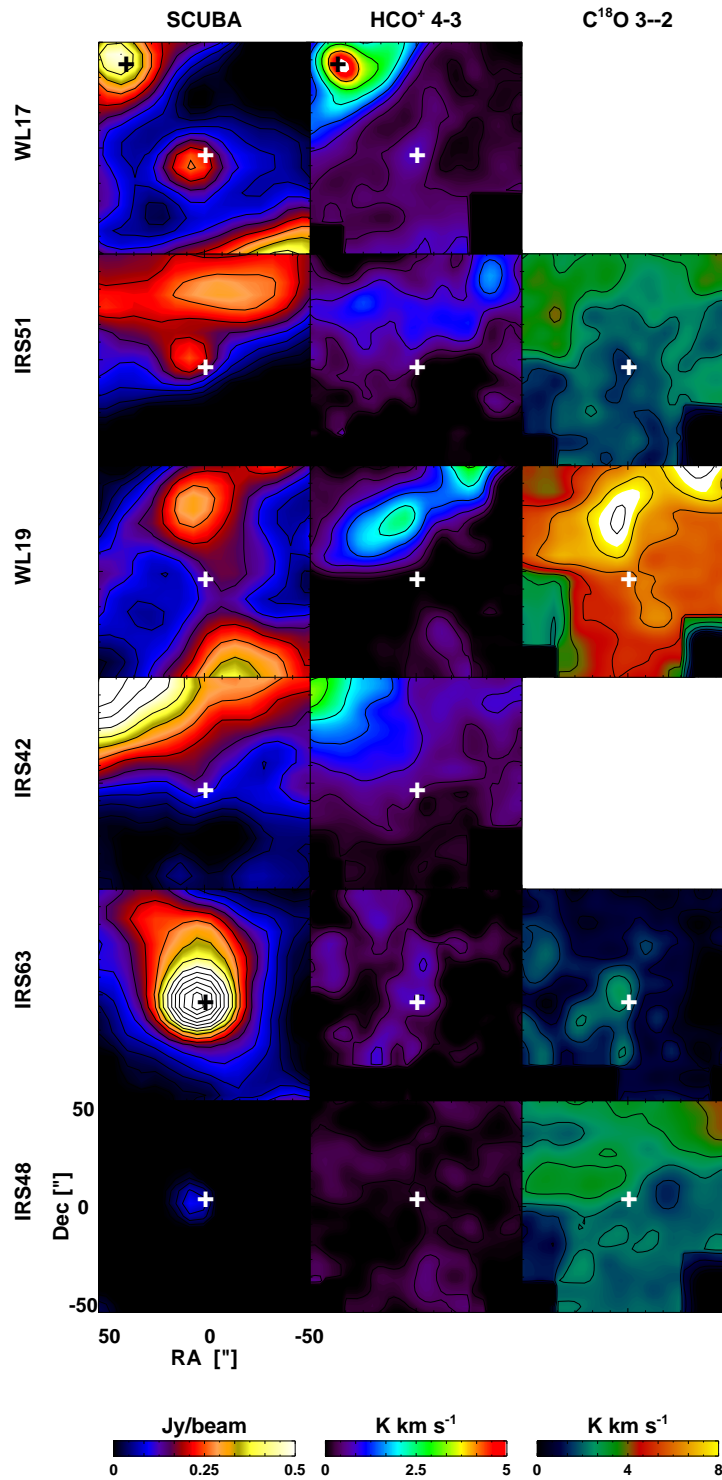


Figure 2.4 — SCUBA 850 μm continuum (*left*), HCO^+ 4–3 (*middle*) and C^{18}O 3–2 (*right*) plotted for (from *bottom* to *top*) IRS 48, IRS 63, IRS 42, WL 19, IRS 51 and WL17. The locations of the IR sources are indicated in the SCUBA maps with white crosses. The embedded source Elias 29 is shown with a black cross in the field of WL 17. The peak 850 μm flux density for IRS 63 is 1.1 Jy beam^{-1} ; it was not scaled to accentuate the extended dust emission. The sources at (0,0) in this image are mostly unresolved in SCUBA and show little or no HCO^+ emission related to the source. They are either transitional or confused sources or (edge-on) disks in our new classification, with the exception of IRS 63, which is classified as embedded (transitional).

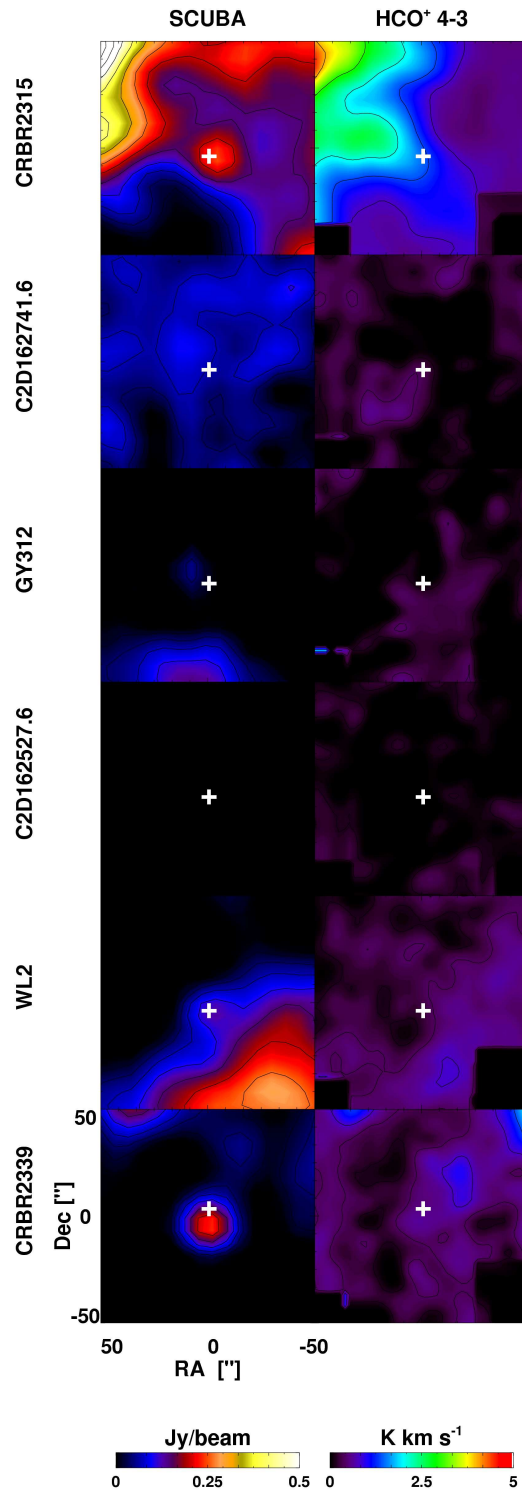


Figure 2.5 — SCUBA 850 μm continuum (*left*) and HCO⁺ 4-3 (*right*) plotted for (from *bottom* to *top*) CRBR 2339.1, WL 2, C2D 162527.6, GY 312, C2D 162741.6 and CRBR 2315.8. The locations of the sources are indicated in the SCUBA maps with white crosses. These sources have either unresolved or little or no emission in the SCUBA 850 μm and HCO⁺ 4-3 maps at (0,0), making them disk sources in our classification.

2000; Ridge et al. 2006; Di Francesco et al. 2008). The most recent map, version 3, was used to extract the information (see Fig. 2.1). This version includes a correction for the chopped out-emission. Integrated fluxes within regions with radii ranging from 25'' to 40'' were extracted from the map (see Table 2.4). The exact radii were selected by calculating the FWHM to the peak flux of each source. Comparison with the map and published fluxes by Johnstone et al. (2000) within similar radii found by a clumpfind routine showed that fluxes agreed within 5%, significantly better than the calibration error of 20% for SCUBA. The sensitivity of the SCUBA map is such that sources down to 90 mJy (3σ) can be detected.

In addition, 11 sources were observed using the SHARC-II 350 μm continuum instrument at the Caltech Submillimeter Observatory (CSO)⁶ during April 2003 (Dowell et al. 2003). The array has 12×32 pixels, spanning 4.85'' per pixel, which results in a footprint of $1' \times 2.6'$ and a beam size of 9''. The sources observed with the CSO were GSS 30, WL 12, Elias 29, VLA 1623, OphE MM3, WL 20S, WL 6, IRS 43, VSSG 17, IRS 51, 2MASS 16282. The data were reduced with the CRUSH package and calibrated using observations of Mars and Saturn. If no planets were available during the specific night, IRAS 16293-2422 was used to calibrate the data. The calibration errors are estimated to be on the order of 30–40% and assumed to dominate the error in the flux estimate over other instrumental errors or S/N considerations. The sensitivity of the SHARC-II maps is such that sources down to 400 mJy (3σ) can be detected. For a typical dust flux law $\propto \nu^{3.5}$, this implies that the SHARC-II data are a factor of 4 more sensitive to low-mass sources than the SCUBA data.

Table 2.2 — Results from HARP-B (HCO^+ 4–3 and C^{18}O 3–2), APEX-2a (HCO^+ 4–3) and RxB (C^{18}O 3–2) observations at the source position.

Source	HCO^+ 4-3 ^a		C^{18}O 3-2		Notes
	$\int T_{\text{MB}} dV$ [K km s ⁻¹]	T_{MB} [K]	$\int T_{\text{MB}} dV$ [K km s ⁻¹]	T_{MB} [K]	
C2D-162527.6	-	<0.09	-	-	Fig. 2.5
GSS 26	-	-	-	-	Fig. 2.9
CRBR 2315.8-1700	6.3	5.2*	-	-	Fig.2.5
CRBR 2317.3-1925	1.5 ^b	2.0 ^b	-	-	Fig. 2.9
VSSG 1	-	<0.4	-	-	Fig. 2.9
GSS 30	16.7	9.1	10.7 ^c	6.3 ^c	Fig.2.2 and 2.10
LFAM 1	18.4	10.8	-	-	Fig.2.2 and 2.10 (GSS 30)
CRBR 2324.1-1619	-	-	14.5	12.2	Fig.2.2 and 2.10 (VLA1623)
VLA 1623	16.2	9.0	10.4	17.9 ^d	Fig.2.2 and 2.10
GY51	-	-	-	-	Fig. 2.9
CRBR 2339.1-2032	0.55	0.45*	-	-	Fig.2.5
WL 12	0.87	1.4	4.8	3.9	Fig.2.3 and 2.10
WL 2	0.3	0.18*	-	-	Fig.2.5
LFAM 26	1.95	1.8	6.4	3.3	Fig.2.3
WL 17	0.6	0.45	-	-	Fig.2.4

Continued on Next Page...

⁶<http://www.submm.caltech.edu/cso/>

Table 2.2 – Continued

Source	HCO ⁺ 4-3 ^a		C ¹⁸ O 3-2		Notes
	$\int T_{\text{MB}} dV$ [K km s ⁻¹]	T_{MB} [K]	$\int T_{\text{MB}} dV$ [K km s ⁻¹]	T_{MB} [K]	
Elias 29	4.5 ^b	2 ^b	10.4 ^e	4.3 ^e	Fig.2.4, WL17 map and Fig. 2.9 and 2.10
GY 224	-	<0.27 ^b	-	-	Fig. 2.9
WL19	-	< 0.1	6.3	4.5	Fig.2.4
WL 20S	-	<0.26 ^b	5.0 ^c	2.3 ^c	Fig. 2.10
IRS 37	3.7	2.5	9.55	5.7	Fig.2.3
WL 3	3.7	2.2	8.8	6.3	Fig.2.3 (IRS 37)
IRS 42	0.45	0.7*	4.0	1.2*	Fig.2.4
WL 6	0.92	0.6	5.25	4.5*	Fig. 2.9 and 2.10
GY 256	0.75	0.45*	5.4	4.5*	Fig. 2.9 and 2.10 (WL6)
IRS 43	4.5 ^d	1.6 ^d	6.5 ^c	3.2 ^c	Fig. 2.2,2.9 and 2.10
IRS 44	3.4 ^d	0.5 ^d	5.8	2.8	Fig.2.3
Elias 32	5.6	4.3	3.1 ^c	4.5 ^c	Fig.2.2 and 2.10 (Elias 33)
Elias 33	6.3	5.7	6.0 ^c	3.0 ^c	Fig.2.2 and 2.10
IRS 48	-	<0.09	2.6	2.3	Fig.2.4
GY 312	-	<0.1	-	-	Fig.2.5
IRS 51	0.75	0.75	2.0	2.8*	Fig.2.4 and 2.10
C2D-162741.6	-	< 0.1	-	-	Fig.2.5
C2D-162748.1	-	< 0.34 ^b	-	-	Fig. 2.9
IRS 54	0.53	0.45	3.4	3.3	Fig.2.3
IRAS 16285-2355	2.1	3.0	2.3	3.0	Fig.2.3
C2D-162857.9	-	< 0.34 ^b	-	-	Fig. 2.9
IRS 63	0.75	1.2	1.7	3.3	Fig.2.4
Disks					
Haro 1-4	-	<0.29 ^b	-	-	Fig. 2.9
DoAR 25	-	<0.28 ^b	-	-	Fig. 2.9
OphE MM3	1.7	1.6*	5.5	3.0*	Fig.2.3 (LFAM 26)
SR 21	-	<0.28 ^b	-	-	Fig. 2.9
CRBR 2422.8-3423	1.9	1.4*	-	-	Fig. 2.2 (IRS 43) and Fig.2.4 (IRS 42)
IRS 46	-	<0.09	2.9	2.1	Fig.2.3 (IRS 44)
SR 9	-	<0.24 ^b	-	-	Fig. 2.9
2Mass 16282	-	<0.35 ^b	-	-	Fig. 2.9 and 2.10

^a Intensities marked with a * do not peak at source position.

^b APEX-2a receiver. Upper limits (2σ) in 0.4 km s⁻¹ bin.

^c JCMT RxB data.

^d Outflowing gas detected (width ~ 20 km s⁻¹)

^e C¹⁸O data taken from Boogert et al. (2002), obtained with the CSO.

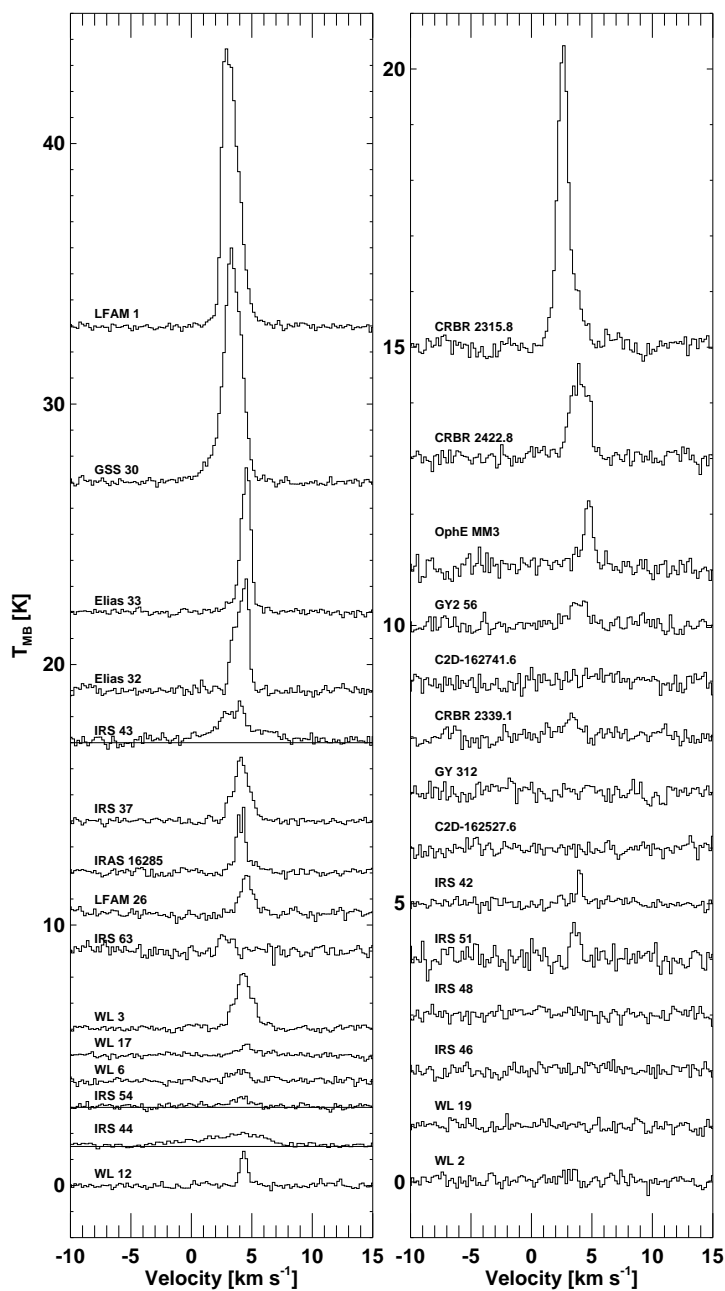


Figure 2.6 — HCO⁺ 4–3 spectra extracted from the HARP-B maps in a 15'' around the IR positions. Sources classified as embedded in §2.6.2 are shown in the left column. In the right column, the sources classified as confused or disks are plotted.

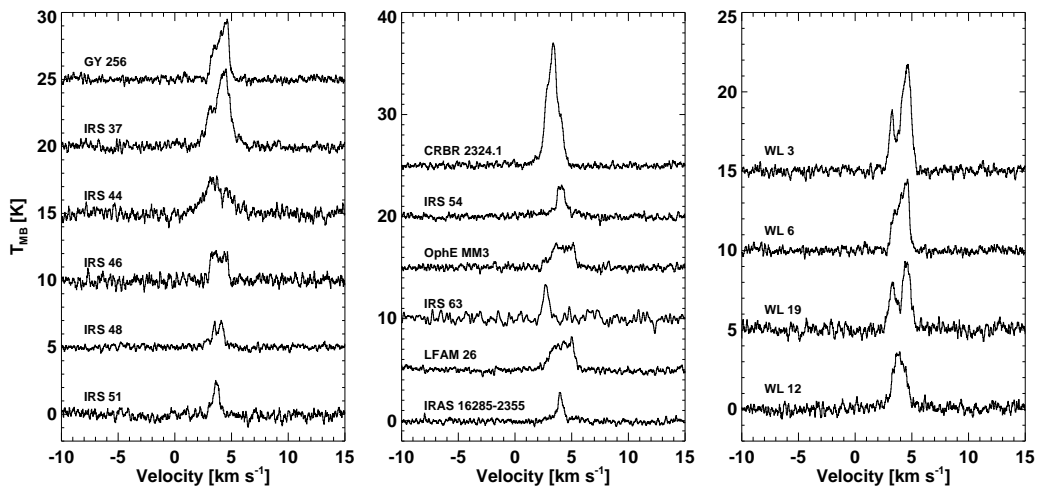


Figure 2.7 — C^{18}O 3–2 spectra extracted from the HARP-B maps at the source positions. Spectra are arranged in random order to illustrate the independence of C^{18}O to the environment instead of the protostellar envelope.

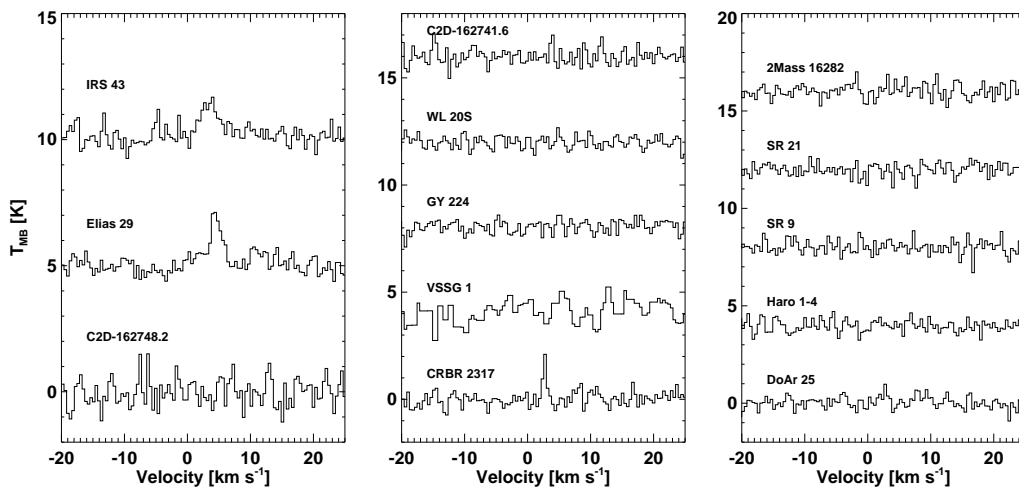


Figure 2.8 — HCO^+ 4–3 spectra at the source positions obtained at APEX. Elias 29 and IRS 43, with clear detections, are the only sources found to be embedded in § 2.6.2. The detection seen for CRBR 2317 is attributed to the cloud material and is classified as a disk.

2.3.4 SED and IRS spectra

The L 1688 core has been targeted by a large number of continuum surveys, covering wavelengths from 2 to 1300 μm . 2MASS (1.25, 1.66 and 2.2 μm) and Spitzer-IRAC (3.6, 4.5, 5.8 and 8 μm) and Spitzer-MIPS (24 μm) fluxes were obtained from the c2d delivery document (Evans et al. 2007). Recently, Padgett et al. (2008) presented Spitzer-MIPS 70 and 160 μm fluxes. The MIPS 160 μm data were not used in our analysis since a large part of the map was confused by either striping or saturation. For the MIPS 70 μm data, we chose to go back to the original data and retrieve the 70 μm fluxes source-by-source in a typical 10'' radius using PSF photometry without the extended contribution subtracted. This avoids potential errors in the flux estimates from automatic extraction in crowded or confused regions such as the Ophiuchus core. In addition to the SCUBA (850 μm) and/or SHARC-II (350 μm) fluxes, a limited number of sources was also observed using SHARC-II and/or SCUBA at 450 μm in a recent survey of disks in the L 1688 core, with fluxes given in the central 15'' beam (Andrews & Williams 2007). Where available, archival data at millimeter wavelengths were used from SEST and IRAM 30m, as reported in Andrews & Williams (2007) and originally obtained by André & Montmerle (1994); Jensen et al. (1996); Nuernberger et al. (1998); Motte et al. (1998) and Stanke et al. (2006).

A number of sources in our sample have also been observed with various observing programs using the IRS instrument on *Spitzer* at 5-40 μm (PID= 2, 172 and 179). These spectra are included in this study to confirm the continuum fluxes in the wavelength range of IRS, and to investigate the presence of ice absorption and silicate absorption or emission.

2.4 Results

2.4.1 Gas maps

Fig. 2.2 to 2.5 present the 21 observed HARP-B fields for HCO^+ 4–3 and C^{18}O 3–2, together with the SCUBA 850 μm continuum map. Note that the sources in Fig. 2.2 are much brighter and have different intensity scales. The integrated intensity and peak temperatures for all sources are listed in Table 2.2, columns 2 to 5. Column 7 states in which figure(s) the sources are mapped or in which figure(s) its spectra are plotted. Fig. 2.6 (HCO^+) and 2.7 (C^{18}O) show spectra extracted from the maps at the positions of the sources. About 70% of the sample was observed in C^{18}O 3–2. The sources for which APEX-2a HCO^+ spectra were taken can be found in Fig. 2.8.

Using the molecular line emission maps, the sample can be divided roughly into three groups. In the first (see Fig. 2.2 and 2.3), HCO^+ peaks at or close to the source positions, with peak intensities up to a few K. For these sources, GSS 30 IRS1, LFAM 1, VLA 1623, WL 12, LFAM 26, IRS 37, WL 3, WL 17, Elias 33, Elias 32, IRS 44, IRAS 16285 and IRS 54, HCO^+ seems to be extended on scales of a few 10''. C^{18}O is always present in these maps, and also extended on scales of a few 10'' to 1'.

Note that the HCO^+ maps in some case show minor offsets w.r.t. the IR positions. For offsets < 8'' this can be attributed to either the pointing accuracy of the JCMT or the differences between IR positions from Bontemps et al. (2001) and c2d. For a few

sources, in particular VLA 1623, IRS 44, larger offsets up to $12''$ were found. These can be accounted for by two effects. First, self-absorption of HCO^+ . Second, these sources show strong outflow emission, which peaks off-source and significantly influences the spectrally integrated maps

A second group (Fig. 2.4 and 2.5) lacks detections in HCO^+ , down to a limit 0.1 K. The sources, C2D-162527.6, WL 19, IRS 46, IRS 48, GY 312 and C2D-162741.6 belong to this group. The third group (Fig. 2.4 and 2.5) of sources contains CRBR 2315.8-1700, CRBR 2339.1-2032, WL 2, OphE MM3, IRS 51 and IRS 42. These show HCO^+ detections at the source position. The HCO^+ is extended, but there is no sign of a peak at the source positions. For IRS 63 and WL 6, detections of HCO^+ are marginal at $\sim 3\sigma$.

The HCO^+ 4–3 integrated intensities $\int T_{\text{MB}}dV$ in protostellar envelopes range from as high as 18.4 K km s^{-1} for LFAM 1 to 0.75 K km s^{-1} for IRS 63. In § 2.5.3 the HCO^+ 4–3 integrated intensities are compared with the column densities derived from the C^{18}O 3–2. This shows that most embedded sources with strong HCO^+ emission are located in regions with high column densities. The sole exception is IRAS 16285-2355, which is not located in a region with high column density (see Fig. 1 and 2.3). However, it is possible to find sources with little or no HCO^+ 4–3 emission, such as WL 19, in regions with similarly high column density.

2.4.2 Dust maps

For sources for which molecular emission was taken with the HARP-B array, the spatial extent of the dust is shown in the left column in Fig. 2.2-2.5. The sources for which no HARP-B maps were obtained can be found in Fig. 2.9. The SHARC-II maps are shown in Fig. 2.10. In these maps, the white contours show the 850 SCUBA emission. The integrated fluxes in a $25''$ beam are given in Tables 2.3 and 2.4.

Table 2.3 — Source fluxes at $350 \mu\text{m}$ in a $25''$ beam observed with SHARC-II at the CSO.

Source	Flux (Jy)	Concentration ^a
GSS 30	2.5	0.58
WL12	6.7	0.59
Elias 29	4.3	0.72
VLA1623	40	0.8
WL20S	0.82	0.64
WL6	<0.4	U
IRS 43	2.1	0.62
Elias 33	4.4	0.55
IRS 51	1.4	0.64
2MASS 16282	<0.2	U

^a See §2.5.1; U=not determined since only flux upper limits obtained.

Both the SHARC-II and SCUBA images clearly show that the dust is extended on scales of at least a few arcminutes at many positions in Ophiuchus. The smaller beam

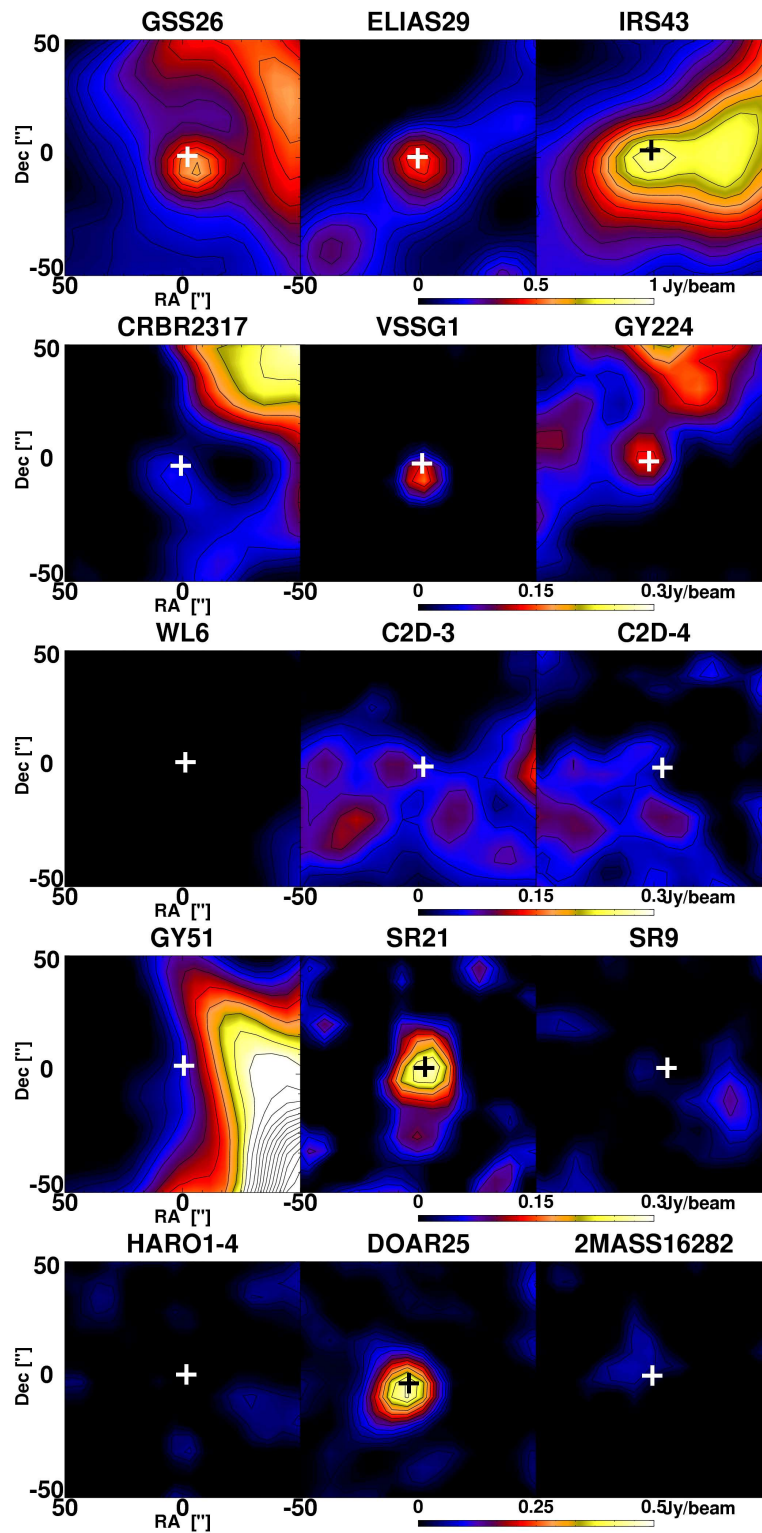


Figure 2.9 — Dust maps at $850 \mu\text{m}$ extracted from the JCMT-SCUBA COMPLETE map of GSS 26, Elias 29 and IRS 43; CRBR 2317.3-1925, VSSG 1 and GY 224; WL 6, C2D-162748.2 (C2D-3) and C2D-162857.9 (C2D-4); GY 51, SR 21 and SR 9; Haro 1-4, DoAr 25 and 2MASS 16282. Note that the emission toward GY 51 is scaled down by a factor of 4.

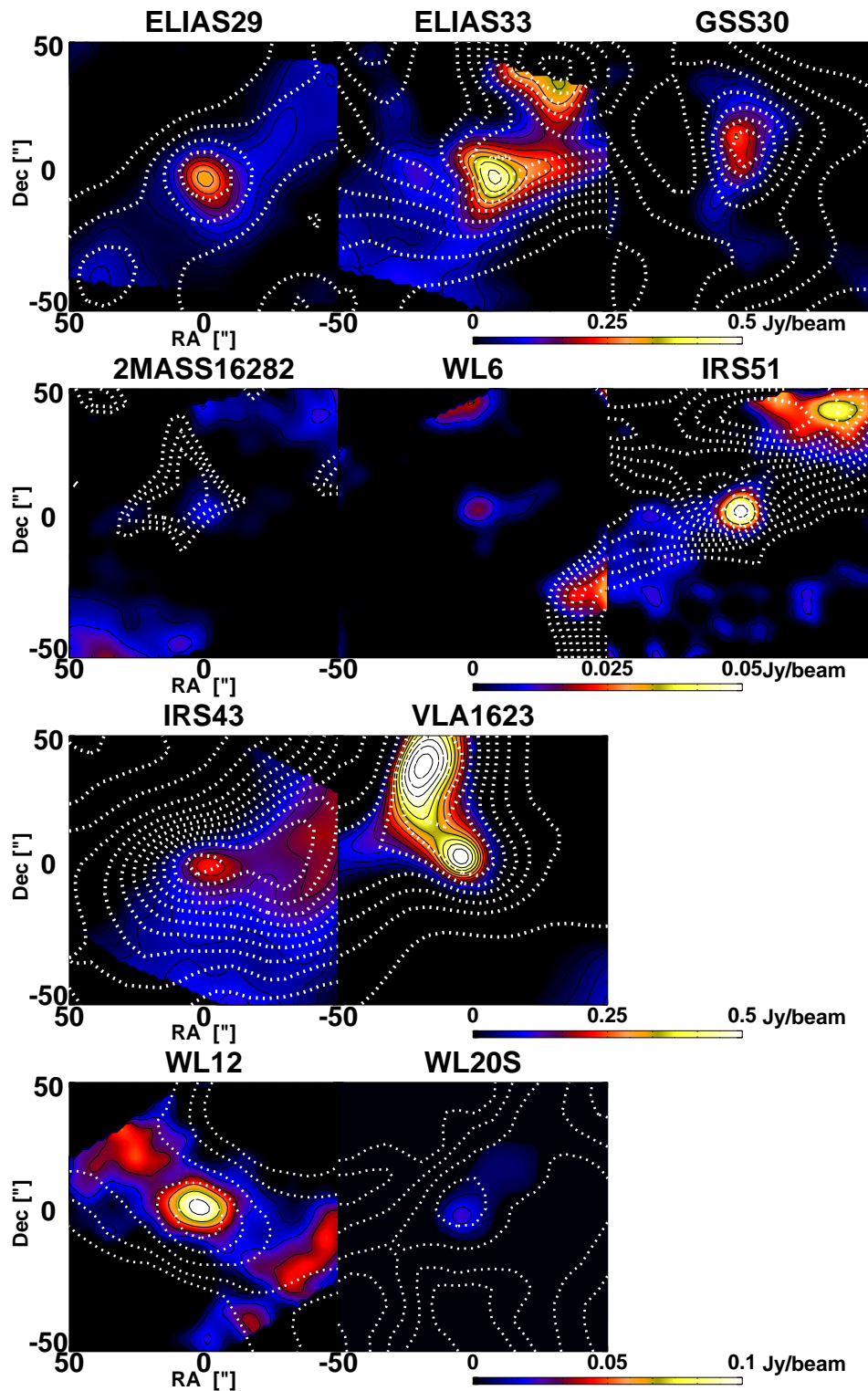


Figure 2.10 — Dust maps at $350 \mu\text{m}$ observed with the SHARC-II instrument at the CSO. In white, the contours for the JCMT-SCUBA $850 \mu\text{m}$ data are over-plotted, normalized for the maximum emission in the map in contours of 10%, 30%, 50% and 70 %. The shape of the contour levels at $850 \mu\text{m}$ agrees well with those found at $350 \mu\text{m}$.

and higher frequency of the SHARC-II observations is able to both resolve smaller envelopes (e.g., Elias 33) or confirm that other sources (e.g., WL 20S) are not resolved at $350 \mu\text{m}$ down to $9''$. The extended emission originates from cold dust in the parental cloud, as mapped by Motte et al. (1998); Johnstone et al. (2000) and Stanke et al. (2006). This cloud material can exist close to or in the line of sight of many of the Class I sources, but is not necessarily associated with a protostellar envelope, as is often assumed. A good example is the source WL 19 (Fig. 2.4), where dust emission is found close to the position of the source, but does not peak at the position of WL 19. This emission comes from a prestellar core within the Ophiuchus ridge and not a protostellar envelope.

Based on the spatial extent of the dust, the sample can be divided into four groups. First there are sources with spatially extended dust emission profiles, peaking at the source position. Examples are GSS 30 IRS1, Elias 29 and IRS 43. A second group shows extended dust emission, but with no central peak at the position of the source. A good example is GY 51 (see Fig. 2.9), located close to the Oph-A core. Some Class I sources only show unresolved dust emission at the source position, such as IRS 51 (see Fig. 2.10). A final group shows no emission at 350 or $850 \mu\text{m}$ down to our sensitivity limits. Good examples is Haro 1-4.

Cloud material can contribute significantly or even dominate the emission on the scales probed by SCUBA and SHARC-II. Two fluxes at $850 \mu\text{m}$ are therefore given in Table 2.4. The first flux is within the $15''$ beam obtained from Andrews & Williams (2007). If no value was given by them, it was extracted from the COMPLETE map for the central beam. Our extracted fluxes agree to within 15% for sources also listed in Andrews & Williams (2007), even though we include estimates to reconstruct the chopped-out extended emission. The second flux is extracted from the COMPLETE map for larger apertures encompassing the envelopes, up to a $25''$ ($\sim 3,000$ AU) radius, the typical envelope extent where the temperature and density drop to that of the surrounding cloud. The first number should thus be considered a lower limit on the total envelope and disk emission, while the second is an equivalent upper limit. For disk sources, all emission originating from the source is located within $15''$ ($< 1,800$ AU).

2.4.3 SED and IRS spectra

Tables 2.4 and 2.5 summarizes all the Spitzer and (sub-)millimeter fluxes. The $2 \mu\text{m}$ to 1.3 mm flux densities for all 45 sources are plotted in Fig. 2.11. In addition, low-resolution IRS spectra are over-plotted between $\sim 5\text{-}30 \mu\text{m}$, where available. These IRS spectra are also presented in Fig. 2.12.

Table 2.4 — Source fluxes including IRAC 1-4, MIPS 1-2

Source	$3.6\mu\text{m}^a$ IRAC I	$4.5\mu\text{m}^a$ IRAC II	$5.8\mu\text{m}^a$ IRAC III	$8.0\mu\text{m}^a$ IRAC IV	$24\mu\text{m}^a$ MIPS I	$70\mu\text{m}$ MIPS II $\sim 10''$
	mJy	mJy	mJy	mJy	mJy	mJy
C2D-162527.6	1.15e1	1.77e1	3.00e1	6.03e1	8.51e1	-

Continued on Next Page...

Table 2.4 – Continued

Source	$3.6\mu\text{m}^a$ IRAC I	$4.5\mu\text{m}^a$ IRAC II	$5.8\mu\text{m}^a$ IRAC III	$8.0\mu\text{m}^a$ IRAC IV	$24\mu\text{m}^a$ MIPS I	$70\mu\text{m}$ MIPS II $\sim 10''$
	mJy	mJy	mJy	mJy	mJy	mJy
GSS 26	2.86e2K	3.86e2K	5.09e2	6.17e2	7.98e2	-
CRBR 2315.8-1700	4.53e1	8.77e1	1.61e2	2.37e2	5.16e2	-
CRBR 2317.3-1925	1.05e1	1.15e1	1.39e1	2.05e1	1.46e1	-
VSSG 1	7.57e2	1.01e3	9.67e2	9.96e2	9.48e2	-
GSS 30	1.06e3	2.27e3	4.1e3	5.4e3	-	7.83e4
LFAM 1	1.28e1	1.82e1*	3.78e1	1.59e1*	2.41e2*	6.31e4
CRBR 2324.1-1619	9.37e0	1.59e1	2.17e1	2.95e1	4.47e2	-
VLA 1623	-	1.57e-1*	2.45e-1*	-	4.04e1	-
GY51	2.86e2	3.71e2	4.38e2	4.66e2	6.39e2*	-
CRBR 2339.1-2032	3.04e1	4.48e1	6.05e1	8.28e1	3.93e2	-
WL 12	2.39e2	7.44e2	1.61e3	2.24e3	-	7.0e3
WL 2	7.92e1	1.11e2	1.28e2	1.48e2	4.46e2	-
LFAM 26	6.11e0	1.07e1	1.66e1	2.96e1	4.59e2	-
WL 17	2.4e2	4.16e2	5.53e2	6.95e2	2.79e3	6.8e3
Elias 29	-	-	1.28e4	-	-	<4.7e4
GY 224	2.03e2	3.05e2K	3.58e2	3.67e2	9.07e2	-
WL19	2.15e2	3.54e2K	4.06e2	3.28e2	2.23e2	-
WL 20S	6.53e-1* ^b	2.97e1	3.74e1*	2.43e2	1.46e2*	1.4e4
IRS 37	1.27e2	2.06e2	2.86e2	2.68e2	7.8e2	1.4e4
WL 3	9.86e1	1.63e2	2.08e2	2.04e2	3.25e2	<2.4e4
IRS 42	1.06e3	1.63e3	2.1e3	2.98e3	3.45e3	3.0e3
WL 6	4.67e2K	9.25e2	1.44e3	1.73e3	4.36e3	3.5e3
GY 256	1.09e1	1.19e1	1.38e0*	8.58e-1*	2.86e1*	3.5e3
IRS 43	6.29e2	1.24e3	1.79e3	2.19e3	-	2.4e4
IRS 44	7.31e2	1.83e3	2.94e3	2.32e3	-	2.5e4
Elias 32	1.87e2	2.72e2	3.82e2	4.81e2	7.12e2	1.1e4
Elias 33	7.4e2	1.19e3	1.58e3	2.04e3	1.72e3	<1.0e4
IRS 48	1.41e3	1.6e3	4.06e3	6.0e3	-	1.7e4
GY 312	1.58e1	2.67e1	3.82e1	5.32e1	4.61e2	7.1e2
IRS 51	7.52e2	9.16e2	1.00e3	1.07e3	2.73e3	2.4e3
C2D-162741.6	8.31e0	1.39e1	2.04e1	2.86e1	6.89e1	5.3e2
C2D-162748.2	1.21e0	2.21e0	3.64e0	1.41e1	1.84e2	-
IRS 54	5.25e2K	7.12e2	9.31e2	1.01e3	3.56e3	5.0e3
IRAS 16285	5.89e-1	2.55e0	4.49e0K	3.13e0	9.01e1	1.7e3
C2D-162857.9	9.73e0	1.7e1	2.57e1	3.83e1	1.61e2	-
IRS 63	5.89e2	9.57e2	1.25e3	1.45e3	3.23e3	8.3e3
Disks						
Haro 1-4	5.19e2	-	3.73e2	-	8.39e2	5.6e2
DoAR 25	3.67e2	2.92e2	2.99e2	2.58e2	3.99e2	1.4e3
OphE MM3	1.42e0	1.79e0	1.88e0*	2.22e0	1.41e0*	-
SR 21	1.3e3	1.17e3	1.28e3	1.66e3	-	1.3e3

Continued on Next Page...

Table 2.4 – Continued

Source	3.6 μm^a IRAC I	4.5 μm^a IRAC II	5.8 μm^a IRAC III	8.0 μm^a IRAC IV	24 μm^a MIPS I	70 μm MIPS II $\sim 10''$
	mJy	mJy	mJy	mJy	mJy	mJy
CRBR 2422.8-3423	5.4e1	1.31e2	1.91e2	1.98e2	1.34e3	9.8e3
IRS 46	1.72e2K	2.71e2	4.02e2	4.11e2	6.39e2*	-
SR 9	7.84e2	5.75e2	4.65e2	4.84e2	1.04e3	-
2Mass 16282	2.32e0	2.00e0	1.39e0	8.15e-1	1.58e0	-

^a IRAC and MIPS-24 Fluxes marked with '*' are band-filled sources with a S/N < 5 or sources with S/N < 5. Such limits are caused either by saturation or a very low emission. A 'K' added to the flux indicates that the obtained flux was flagged as 'Complex', with multiple detection within 2-3''

^b two sources within 4'' with a total flux of 2e2 mJy.

Table 2.5 — Source fluxes including SHARC-II, SCUBA and 1.3 mm

Source	350 μm SHARC 9-25'' ^b	450 μm SCUBA 10'' ^b	850 μm SCUBA 15''	850 μm SCUBA 25''	1300 μm 15''
	mJy	mJy	mJy	mJy	mJy
C2D-162527.6			<3e1	<3e1	
GSS 26		6.5e2	3.0e2 ^b	1.6e3	1.e2
CRBR 2315.8-1700			2.1e2	7.5e2	8.5e1
CRBR 2317.3-1925			1.5e2 ^b	1.7e2	
VSSG 1		< 6.7e2	2.4e2 ^b	3.0e2	5e1
GSS 30	2.5e3 ^a	1.4e3	2.2e2 ^b	3.2e2	9e1
LFAM 1		2.7e3	5.7e2 ^b	2.6e3	1.1e3
CRBR 2324.1-1619			8.4e2	6.1e3	
VLA 1623	4e5 ^c	3.9e5 ^c	5.0e3	1.7e4	1.2e3
GY51			3.3e2	1.7e3	2e1
CRBR 2339.1-2032			8e1	3e2	3e2
WL 12	6.7e3 ^a	7.5e2	2.2e2 ^b	7.1e2	1.2e2
WL 2			4e1	1.4e2	3e1
LFAM 26			2.2e2	6.9e2	1e2
WL 17		<8.7e2	1e2 ^b	6.1e2	7.5e1
Elias 29	4.3e3 ^a	2.0e3	4.1e2 ^b	9.4e2	9.5e1
GY 224			1.3e2	3.7e2	5e1
WL19			2.0e2	8.3e2	3e1
WL 20S	8.2e2 ^a	4.0e2	1.8e2 ^b	6.0e2	4.7e1
IRS 37		< 5.9e2	9.3e1 ^b	3.0e2	< 1e1
WL 3		< 5.8e2	1.2e2 ^b	4.4e2	< 6e1
IRS 42	1.5e3 ^a		1.7e2	7.3e2	< 6e1
WL 6		1.4e2	<3e1	<3e1	< 2e1

Continued on Next Page...

Table 2.5 – Continued

Source	350 μm SHARC 9-25'' ^b mJy	450 μm SCUBA 10'' ^b mJy	850 μm SCUBA 15'' mJy	850 μm SCUBA 25'' mJy	1300 μm ^d 15'' mJy
GY 256			<3e1	<3e1	
IRS 43	2.1e3 ^b	1.8e3	2.5e2 ^b	2.7e3	8e1
IRS 44			3.6e2	1.2e3	6e1
Elias 32			1.7e3	6.4e3	< 5e1
Elias 33	4.4e3 ^a		1.2e3	4.4e3	< 2e1
IRS 48		< 1.6e3	1.8e2 ^b	1.9e2	6e1
GY 312			<3e1	<3e1	
IRS 51	1.4e3 ^a	< 6.8e2	2.2e2	7.8e2	1.1e2
C2D-162741.6			1e2	3.5e2	
C2D-162748.2			5e1	6e1	
IRS 54			1e2	3.2e2	3e1
IRAS 16285			5e2	1.6e3	
C2D-162857.9			5e1	8.5e2	
IRS 63	6.7e3 ^b	4.7e3	1.0e3 ^b	2.4e3	3.7e2
Disks					
Haro 1-4			-	-	
DoAR 25			4.6e2 ^b	5.2e2	2.8e2
OphE MM3	1.6e3 ^a	5.4e2	1.6e2	3.6e2	
SR 21	2.8e3 ^b	1.9e3	4.0e2 ^b	4.7e2	9.5e1
CRBR 2422.8-3423			1.3e3	3.2e3	1.5e2
IRS 46	1.4e3 ^a		1.8e2	5.1e2	4.5e1
SR 9			<25 ^b	2.9e1	1.5e1
2Mass 16282	9e1 ^b	8e1	5.8e1	2.7e2	

^a This chapter.^b 350/450 μm flux taken from Andrews & Williams (2007). Fluxes obtained with SHARC-II are given either in a 9'' beam (Andrews & Williams 2007) or in a 25'' radius (This work).^c Data taken from André et al. (1993).^d Data from Andrews & Williams (2007).

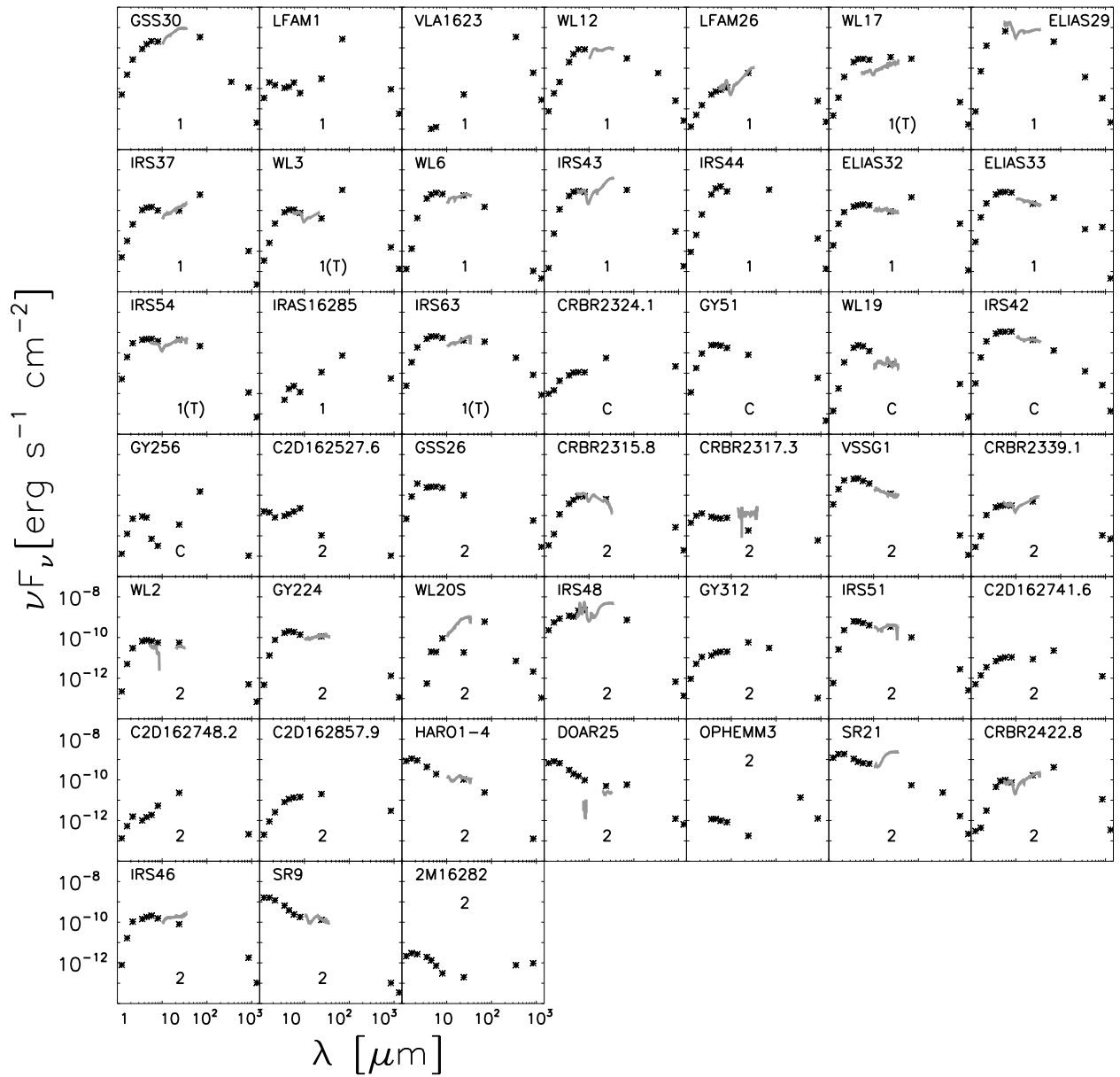


Figure 2.11 — The spectral energy distributions of all sources, supplemented by spectra taken with IRS. Our classification can be found near the center and bottom of each SED. 1 = Embedded Stage 1, 1(T) = Transitional from embedded to pre-main sequence, C = confused and 2 = (edge-on) disk.

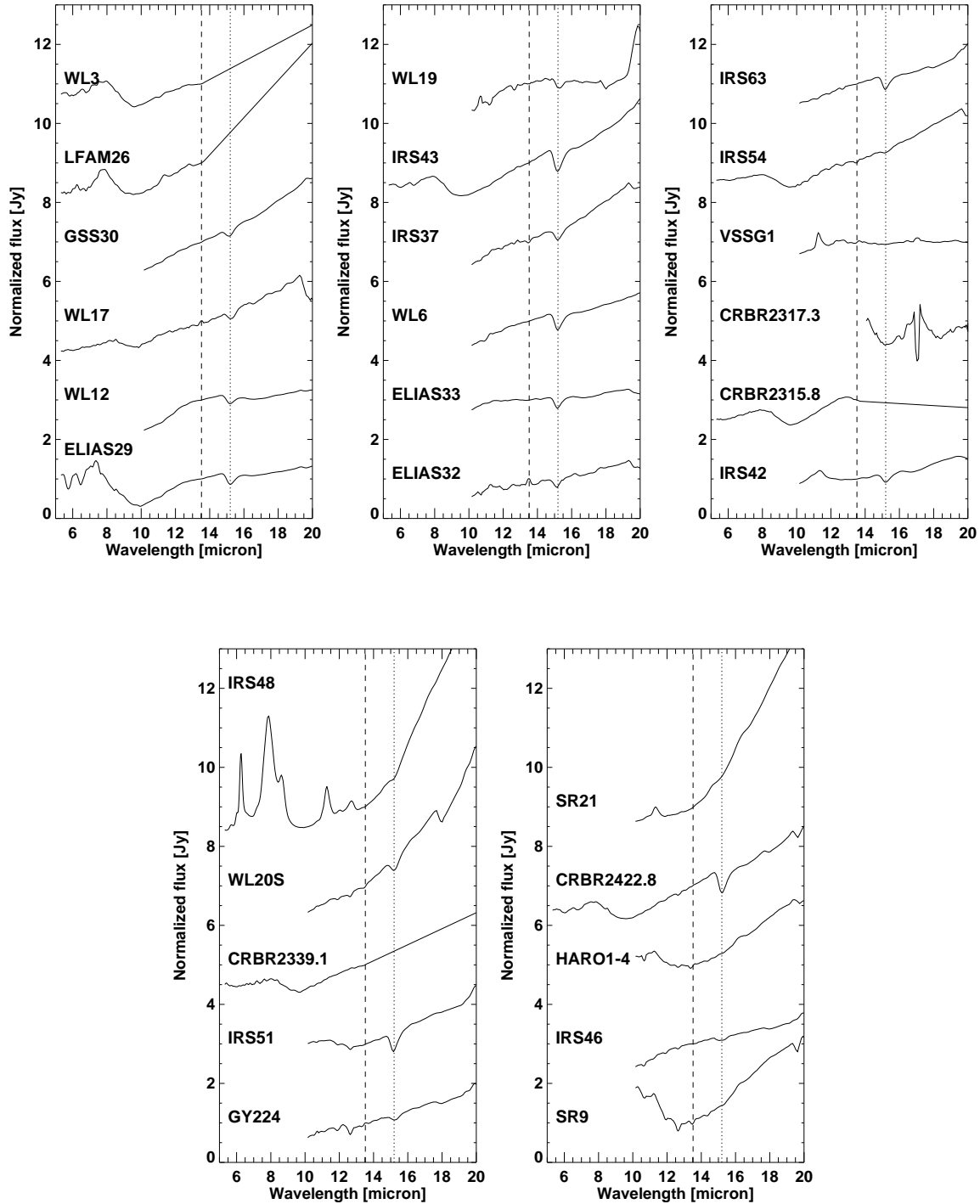


Figure 2.12 — The individual IRS spectra (where available). Each spectra is plotted from 5 to 20 μm . All spectra are normalised to their own emission at 13.5 micron, indicated with a vertical dashed line. The vertical dotted line is the position of the water band.

Table 2.6 — Source properties derived from the gas and dust. The table has been rearranged compared with Table 2.1 to reflect the classification in §2.6.2

Source	α_{IR}	$N_{\text{H}_2}^a$ (10^{22} cm $^{-2}$)	$\Delta\alpha^b$	Mass c ($10^{-2} M_{\odot}$)	L_{bol} ($10^{-1} L_{\odot}$)	T_{bol} (K)	C_{850}^d	$C_{\text{HCO}^+}^d$
Embedded sources								
GSS 30 e	1.46	23.3/19.4*	2.6	20.5	33	123	0.58 f	0.69
LFAM 1 e	0.73	50*	2.6	17.1	8.3	86	0.58 f	0.69
VLA 1623	no	441*	-	111	2.7	12	0.8 f	0.72
WL 12	2.49	10.5/15.2*	3.1	4.6	34	155	0.29 f	0.81
LFAM 26	1.27	14.0/18.5*	4.4	4.5	0.44	238	0.34 f	0.69
WL 17	0.61	8.4*	1.0	4.0	6.7	323	0.22 f	0.71
Elias 29	0.37 h	22.7/33.6*	1.5	6.2	25	424	0.48 f	- g
IRS 37 e	0.25	20.8	1.0	1.2	3.8	243	0.58	0.72
WL 3 e	-0.03	19.2/9.7*	2.3	2.9	4.6	192	0.25	0.67
WL 6	0.72	11.4	-	<0.4	8.5	394	U	0.77
IRS 43	1.17	14.2/20.7*	2.3	17.1	10	134	0.57 f	0.79
IRS 44	2.29	12.6/30.2D*	2.9	8.0	11	140	0.37 f	0.80
Elias 32	-0.03	6.8/140*	3.7	41.9	5	321	0.34 f	0.70
Elias 33	-0.12	13.1/96*	3.1	28.2	12	460	0.5 f	0.64
IRS 54	0.03	7.4	1.2	3.1	7.8	486	0.8	0.80
IRAS 16285-2355	1.23	5.0/41.9D*	3.1	10.3	0.57	77	0.39 f	0.80
IRS 63	0.14	3.7/84.0D*	-	16.4	13	363	0.72 f	0.60
Confused sources								
CRBR 2324.1-1619	0.87	31.6/70.5*	5.2	39.3	0.44	283	U	U
GY51	0.05	27.7*	4.5	11.1	2.3	706	U	U
WL19	-0.43	13.7/16.8*	4.9	5.5	1.5	730	0.15	0.53
IRS 42	-0.03	8.7/14.2*	1.3	4.7	14	540	0.44	0.60
GY 256	-0.24	11.8	-	<0.2	1.1	104	U	0.70
Disks								
C2D-162527.6	0.36	-	-	<0.4	0.16	1051	U	U
GSS 26	-0.46	24.3D*	1.8	10.2	3.2	877	0.65 f	U
CRBR 2315.8-1700	0.69	17.6*	1.0	5.1	0.93	456	0.32 f	0.74
CRBR 2317.3-1925	-0.56	12.6*	0.3	1.1	0.11	1105	0.85	S
VSSG 1	-0.73	20.1*	-	2.0	5.8	930	0.74	SU
CRBR 2339.1-2032	0.45	6.7*	-	2.0	0.55	426	0.53 f	0.58
WL 2	0.02	-	-	1.0	0.88	573	0.3	0.58
GY 224	-0.05	10.9*	1.0	2.4	2.1	614	0.63	SU
WL 20S	2.75	10.9/15.3D*	1.0	3.9	4.5	85	0.57	SU
IRS 48	0.88	5.7/15.2D*	2.1	1.2	81	238	0.70	U
GY 312	0.64	-	-	<0.2	0.73	285	U	0.3
IRS 51	-0.15	4.4/18.4D*	2.3	5.0	8	548	0.27 f	0.59
C2D-162741.6	0.32	-	-	2.3	0.28	279	U	U
C2D-162748.2	1.98	-	-	0.4	0.17	241	U	SU
C2D-162857.9	0.67	-	-	5.6	0.22	402	U	SU
Haro 1-4	-0.89	-	-	0.45	5.6	762	U	SU

Continued on Next Page...

Table 2.6 – Continued

Source	α_{IR}	$N_{\text{H}_2}^a$ (10^{22} cm^{-2})	$\Delta\alpha^b$	Mass ^c ($10^{-2} M_{\odot}$)	L_{bol} ($10^{-1} L_{\odot}$)	T_{bol} (K)	C_{850}^d	$C_{\text{HCO}^+}^d$
DoAR 25	-1.12	38.6*	-	3.4	4.7	1422	0.90	SU
OphE MM3	-0.33	12.0/13.4*	3.4	2.3	0.17	45	U	0.68
SR 21	-0.79	33.6*	-	3.1	1.8	1070	0.89	SU
CRBR 2422.8-3423	1.01	106.6*	2.3	20.5	4.4	157	U	- ^g
IRS 46	0.18	6.3/15.1*	2.8	3.3	1.9	684	U	SU
SR 9	-1.07	-	-	<0.4	8.7	1588	U	SU
2MASS 16282	-1.55	-	-	1.7	0.84	66	U	SU

^a Column densities marked with * are calculated from the SCUBA dust maps. Embedded sources where a large disk contribution is likely are indicated with a D. Note that no column densities could be calculated from the dust below $1 \times 10^{23} \text{ cm}^{-2}$.

^b $\Delta\alpha$ is an *upper limit* to change in 2-24 μm spectral slope due to the reddening by foreground clouds at this source. This is derived by considering the mean column density at 45'' off the source position.

^c Upper limit derived from the 850 μm data using the relation from Shirley et al. (2000), with the assumption that all 850 μm emission originates within a protostellar envelope.

^d U=Undetected or Unobserved, S=single position spectrum available only.

^e Circumbinary envelope.

^f From Jørgensen et al. (2008)

^g Although both Elias 29 and CRBR 2422.8-3423 were observed, these sources are located near the edge of a field and do not have sufficient coverage to obtain a concentration parameter for the HCO^+ .

^h Derived using the ISO-SWS spectrum from Boogert et al. (2000).

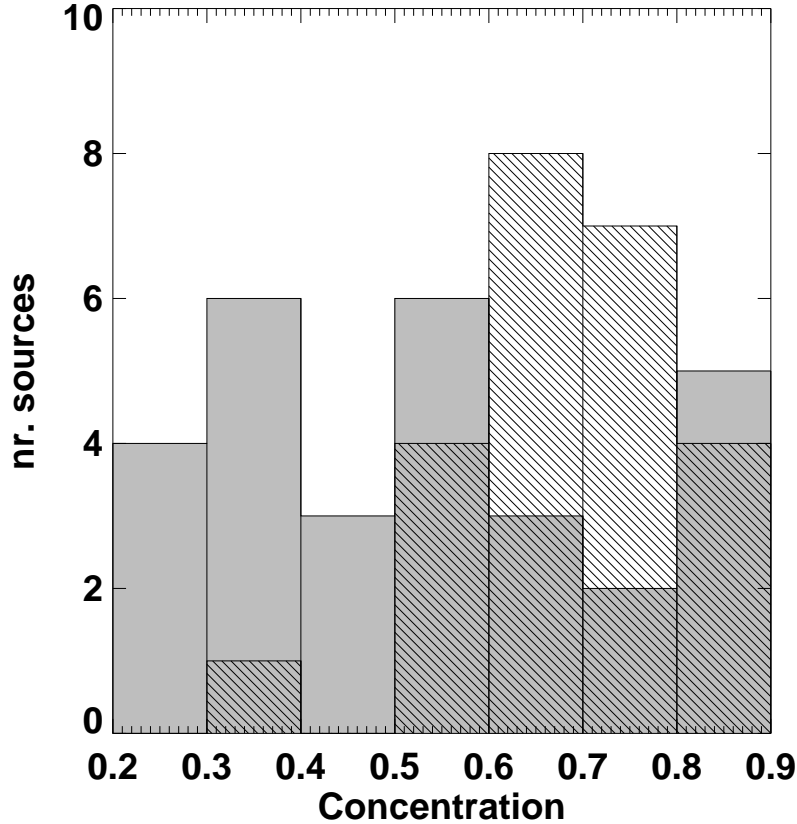


Figure 2.13 — The distribution of concentration of SCUBA (gray) and HCO⁺ 4–3 (striped). Only sources with spatially resolved profiles have been taken into account. Note that the total number of sources is greater for SCUBA than for HCO⁺.

2.5 Analysis

2.5.1 Concentration

One method to distinguish embedded YSOs from edge-on disks, starless cores or background sources such as AGB stars and galaxies, is to use a measure of how centrally concentrated the emission is. This method has been used previously in the analysis of SCUBA data (Johnstone et al. 2001; Walawender et al. 2005; Jørgensen et al. 2007) by defining a concentration parameter:

$$C = 1 - \frac{1.13B^2 S_{850}}{\pi R_{\text{obs}}^2 F_0} \quad (2.1)$$

where B is the beam-size, S_{850} is the total flux at 850 μm within the envelope, R_{obs}^2 is the observed radius of the envelope and F_0 is the peak flux of the envelope. The observed radii were selected by calculating the FWHM to the peak flux of each source. The level of concentration potentially provides an indication of the evolutionary stage. Highly concentrated cores ($C > 0.75$) have a very high probability to contain protostars, while

cores with low concentration ($C < 0.4$) are often starless, as indicated by the absence of near-IR emission. The observed radii in the 850 μm maps was defined by Kirk et al. (2006) as $R = (A/\pi)^{1/2}$, with A the area of the core to the lowest contour of their *clumpfind* routine.

The concentration of the 850 μm of a large part of our sample was previously calculated in Jørgensen et al. (2008) and those values are adopted here. The SHARC-II maps also allow a concentration at 350 μm to be made, as seen in Table 2.3. These concentrations are found to be within 10% to those found for the 850 μm data, with the exception of WL12 which is more than a factor 2 higher in the SHARC-II 350 μm data.

A similar concentration parameter can also be calculated for the distribution of HCO^+ , using integrated intensities between $V_{\text{LSR}} - 5$ to $+5 \text{ km s}^{-1}$:

$$C_{\text{HCO}^+} = 1 - \frac{1.13B^2 S_{\text{HCO}^+}}{\pi R_{\text{obs}}^2 T_{\text{MB}}}, \quad (2.2)$$

with S_{HCO^+} the spatially and spectrally integrated intensity $\int T_{\text{MB}} dV$ of HCO^+ over the entire envelope with radius R_{obs} , and T_{MB} the peak intensity in the central beam. Since no *clumpfind* routine was used to characterize the spectral maps, the observed radii of the HCO^+ concentration were set equal to the FWHM of each spectrally integrated core map. Although different methods to define radii result in different values, tests showed that the corresponding changes in concentration factor are less than 5 %.

Tables 2.3 and 2.6 list the concentrations of both the 850 μm data SCUBA maps and the HCO^+ HARP-B maps, where available. Although the number of sources with a concentration parameter determined by SCUBA maps is greater than those for HCO^+ , it is clear that HCO^+ is more concentrated than the continuum. Fig. 2.13 shows the distribution of the concentration parameters for spatially resolved sources.

2.5.2 Environment

In contrast with deeply embedded Class 0 YSOs, the environment around the embedded Class I YSOs has a large influence on the analysis of the generally weaker source data. Fig. 7 in Boogert et al. (2002) illustrates how complex the environment can become. Elias 29, an embedded YSO, is located in a dense ridge of material, but in front of that ridge, two foreground layers were identified using the emission from a dozen different molecules. Continuum emission and ice absorption originate in all these layers. For most of our sources, however, the situation appears to be less complex. Fig. 2.6 and 2.7 show that the HCO^+ 4–3 profiles are mostly single peaked. However, C^{18}O 3–2 often shows a more complex profile with multiple peaks.

LFAM 26, located at the top of the Ophiuchus ridge only a few arcmin north-east of Elias 29, is an especially complex case. Fig. 2.14 shows the spectral map in $17''$ spatial bins for HCO^+ 4–3 and C^{18}O 3–2 maps. It is clearly seen that besides the integrated emission (Fig. 2.3), the line profiles of HCO^+ and C^{18}O both vary over the entire map. The HCO^+ spectra show mostly single gaussians. At the position of LFAM 26, the HCO^+ profile has a small outflow signature on the blue side of the spectrum. The C^{18}O emission requires at least four distinct components (Fig. 2.15) at 2.7, 3.5, 4.4 and 5.0 km s^{-1} . The three components at 2.7, 3.5 and 5.0 km s^{-1} are the same as found in

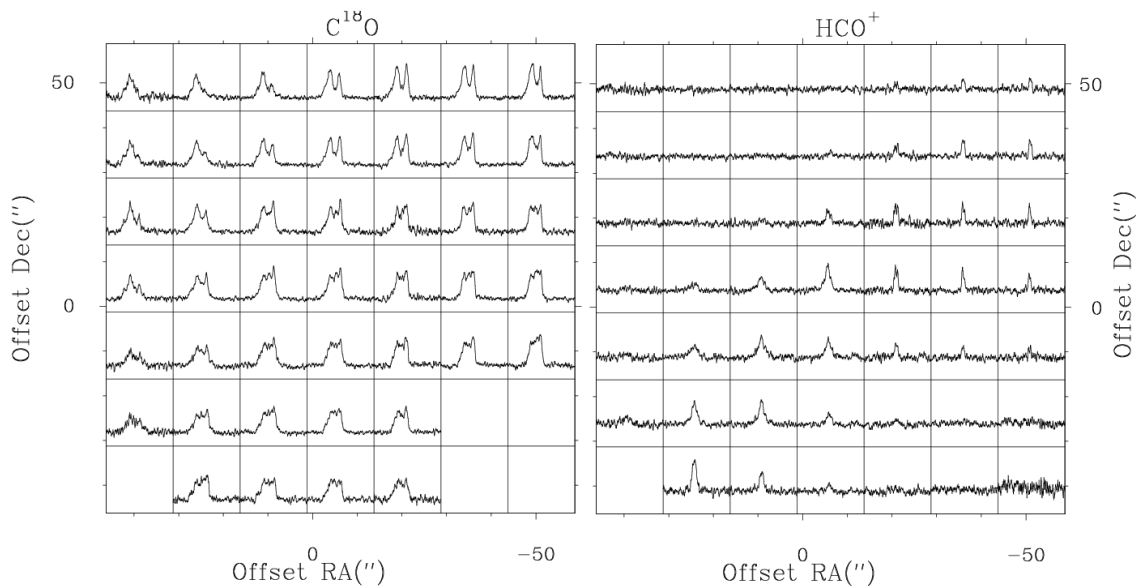


Figure 2.14 — The spectra of C^{18}O 3–2 and HCO^+ 4–3 of the LFAM 26 field. The intensity scale is -1 to 6 K in T_{MB} for C^{18}O and -1 to 3 K for HCO^+ . OphE-MM3 is located at $\Delta\text{RA} = +5''$ and $\Delta\text{Dec} = -40''$ in this field and has no associated HCO^+ emission, except from the extended cloud.

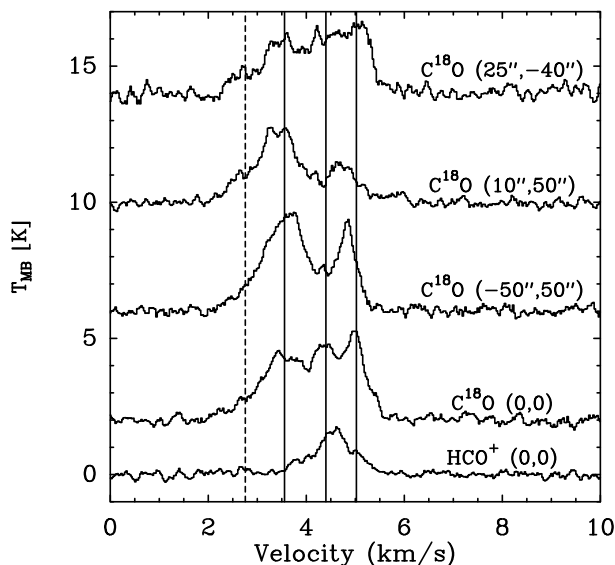


Figure 2.15 — Individual spectra at offset positions from LFAM 26 for HCO^+ (0'', 0'') and C^{18}O (0, 0), (-50, 50), (10, 50) and (25, -40). The three main components at 3.5, 4.4 and 5.0 km s^{-1} are shown with solid lines. The component at 2.7 km s^{-1} identified by Boogert et al. (2002) is shown with a dashed line and is generally weaker or absent. The main component of the HCO^+ emission is located between the components at 4.2 and 4.9 km s^{-1} and peaks at 4.6 km s^{-1} .

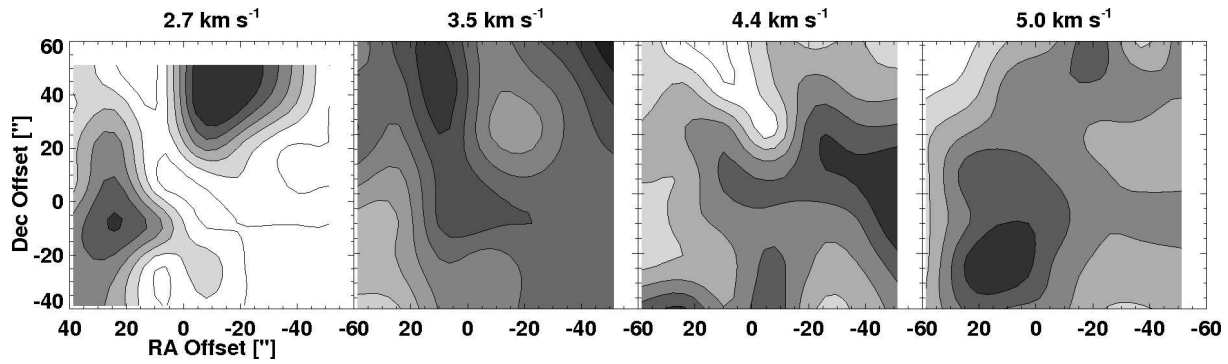


Figure 2.16 — The spatial distribution of the integrated Gaussians fitted to the $C^{18}O$ 3–2 spectra for each of the four layers seen in the field of LFAM 26.

Table 2.7 — The number and properties of the (foreground) layers for the fields of LFAM 26, IRS 44 and WL 19 in the Ophiuchus ridge and IRS 37 and IRS 48, located near Oph-B cores. The spectra can be found in Fig. 2.7.

Field	Position	Nr. ^a	V_{LSR} (km s^{-1})	$C^{18}O \int T_{MB} dV$ (K km s^{-1})	ΔV (km s^{-1})
LFAM 26	0,0	3	3.5, 4.4, 5.0	1.8, 0.9, 1.1	0.8, 0.7, 0.8
	-20,+35	4	2.7, 3.5, 4.4, 5.0	0.6, 1.5, 0.8, 1.1	0.9, 0.7, 0.7, 0.7
	+35, -22	3	3.5, 4.4, 5.0	1.3, 0.4, 0.5	1.2, 0.7, 0.5
IRS 44	0,0 ^b	3	2.6, 3.5, 4.5	0.5, 2.3, 2.3	1.9, 1.1, 0.8
	+20,+20 (IRS 46)	2	3.5, 4.3	1.9, 1.3	0.6, 0.5
	-50,20	2	3.3, 4.0	1.1, 2.5	0.4, 1.1
IRS 48	0,0	3	2.8, 3.5, 4.1	0.6, 1.7, 2.6	0.6, 0.4, 0.5
	-36,+36	3	2.9, 3.5, 4.1	0.8, 2.1, 4.3	0.4, 0.4, 0.5
	+38, 6	3	2.8, 3.5, 4.1	0.4, 1.1, 3.5	0.3, 0.5, 0.5
WL 19	0,0	2	3.3, 4.6	2.7, 4.7	0.8, 0.8
	-6, 36	2	3.4, 4.6	2.8, 5.6	1.1, 0.8
	-20,-38	2	3.2, 4.2	1.9, 3.0	0.7, 1.0
	-50, 50	4	2.6, 3.5, 4.3, 5.1	1.4, 3.3, 3.5, 3.2	0.5, 0.6, 0.7, 0.7
IRS 37	0,0	2	3.0, 4.4	2.3, 5.6	0.7, 1.1
	+23, +7 (WL3)	2	3.2, 4.4	2.7, 5.4	0.8, 1.0
	-36, 21	3	3.0, 3.6, 4.2	2.4, 0.8, 2.8	0.9, 0.2, 0.8

^a Number of components.

^b Outflow detected at 0,0 in HCO^+ 4–3 which is probably the component seen at 2.6 km s^{-1}

Boogert et al. (2002) at the position of Elias 29. Most lines observed in Boogert et al. (2002) peak short-wards of 5.0 km s^{-1} component, which could be indicative of the 4.4 km s^{-1} component. However, the difference between these two components is very pronounced in the spectra in Fig. 2.14 and 2.15 at the position of LFAM 26 so that we treat them as separate. HCO^+ is aligned with the 4.4 km s^{-1} component.

Using the molecular excitation program RADEX (van der Tak et al. 2007), one can calculate the expected average contribution from cloud material to the HCO^+ 4–3 emission. Using a HCO^+ abundance of 10^{-8} with respect to H_2 , a density of 10^4 cm^{-3} , a cloud temperature of 15 K, a width of 1 km s^{-1} and a H_2 column density of 10^{22} cm^{-2} ($A_V \approx 10$), a contribution of $\sim 0.1 \text{ K km s}^{-1}$ is found. Only at higher column ($\sim 10^{23} \text{ cm}^{-2}$) or volume densities ($\sim 1 \times 10^5 \text{ cm}^{-3}$) are contributions found from the cloud on the order of 1 K km s^{-1} , comparable to the observed 4.4 km s^{-1} emission at off-positions such as (-50,50). This is in agreement with the numbers given in Table 1 of Evans (1999). Thus, LFAM 26 is embedded in a high-density ridge.

Table 2.7 shows the results of gaussian fitting at other positions where multiple peaks in the C^{18}O 3–2 profiles were found. In the WL 19 field, south of the Elias 29 position, the same four components are again detected, although the 5.0 km s^{-1} layer is only seen north of WL 19. In the IRS 44 field along the same ridge to the south-west, the three layers at 2.6, 3.5 and 4.5 km s^{-1} are found.

Three layers are found in the Oph-B2 core, which contains the IRS 48 and IRS 37 sources. The first layer is at 2.8 km s^{-1} , the second at 3.5 km s^{-1} and the third at 4.2 km s^{-1} . Outside these two regions, spectra of C^{18}O can be fitted with a single gaussian, almost always at $\sim 3.6 \text{ km s}^{-1}$. The spatial variation in this layer seems to be minor compared with the other components and it is thus the most likely candidate for the foreground component with an extinction of $A_V \sim 5.5 \text{ mag}$, as suggested by Dickman & Herbst (1990). IRS 63, located far from the L 1688 core is at 2.8 km s^{-1} , the same velocity as one of the layers in both Oph-B2 and Ophiuchus ridge region.

2.5.3 Gas column density

The total column density, N_{H_2} , toward each source was calculated from the integrated intensity of the C^{18}O 3–2 line, $\int T_{\text{MB}} dV$, using the following formula :

$$N(\text{H}_2) = X \times 0.75 \times 10^{14} \frac{e^{(16.6/T)} \int T_{\text{MB}} dV}{1 - e^{(-33.2/T)}} \quad (2.3)$$

with X , the abundance of H_2 with respect to C^{18}O , assumed to be 5.6×10^6 (Wilson & Rood 1994) and T , the temperature of the cloud material, assumed to be 30 K. The temperature is chosen to be higher than that of the surrounding cloud material, $\sim 15 \text{ K}$, and reflects the warmer gas associated with the YSO where CO is not frozen out. This formula assumes the molecular excitation to be in LTE and isothermal. The C^{18}O 3–2 line is assumed to be completely optically thin. The resulting column densities can be found in Table 2.6, column 3. They range from $3.7 \times 10^{22} \text{ cm}^{-2}$ for IRS 63 and the Oph F core to $31.6 \times 10^{22} \text{ cm}^{-2}$ in the Oph A core. These correspond to visual extinctions A_V of 40-400 mag, assuming $N_{\text{H}}/A_V = 1.8 \times 10^{21} \text{ cm}^{-2} \text{ mag}^{-1}$ (Rachford et al. 2002) and $N_{\text{H}} \approx 2N(\text{H}_2)$ (all hydrogen in molecular form). This range of column densities

is similar to that found by Motte et al. (1998) and Stanke et al. (2006) using 1.3 mm continuum imaging, as well as the column densities found from the 850 μm dust, see §2.5.4.

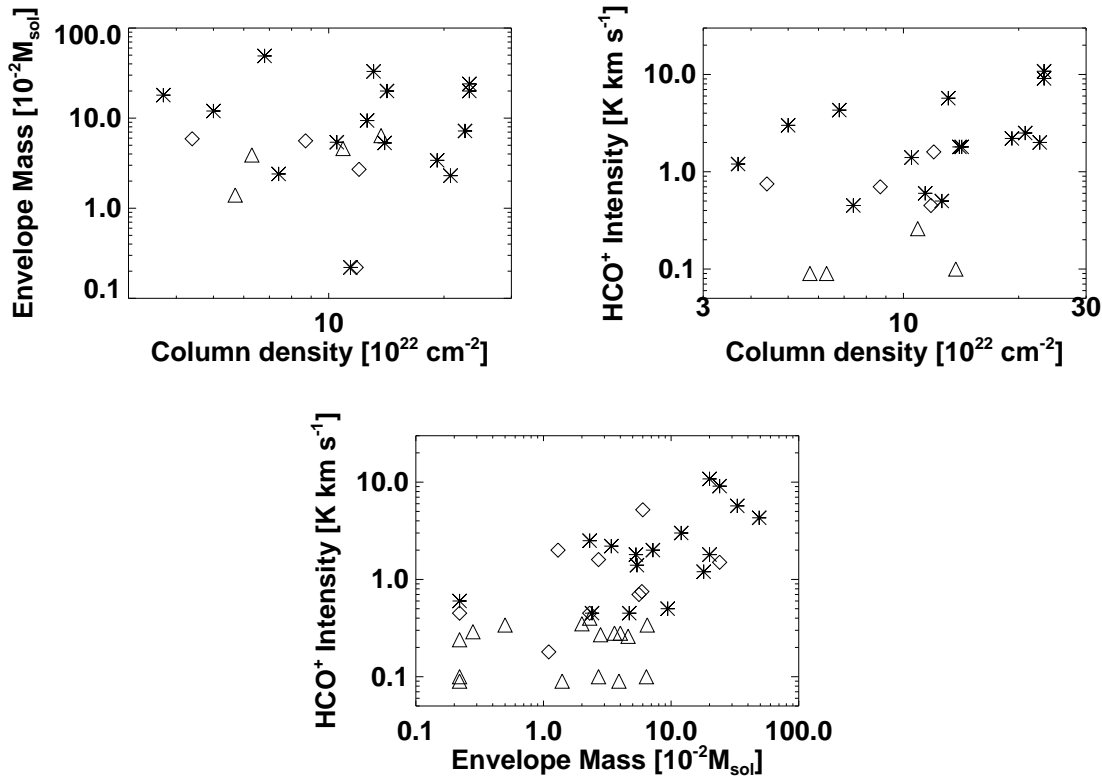


Figure 2.17 — *Upper left* : the gas column density (in 10^{22} cm^{-2}) derived from C^{18}O 3–2 vs. the envelope mass (in $10^{-2} M_{\odot}$), derived from the SCUBA maps. *Upper right* : the column density vs. the integrated intensity of HCO^{+} 4–3 in K km s^{-1} . *Lower row* : the integrated intensity of HCO^{+} 4–3 vs. the envelope mass. In all figures, sources with a centrally condensed HCO^{+} emission are shown with stars, sources with an upper limit on HCO^{+} 4–3 with triangles, and sources with HCO^{+} emission not peaking on the source with diamonds.

2.5.4 Dust

Table 2.6 includes the properties that can be derived from the continuum emission. The dust column density was calculated with the following equation.

$$N(\text{H}_2) = \frac{S_{850}}{\Omega \mu m_{\text{H}} \kappa_{850} B_{850}(T_d)} \quad (2.4)$$

where S_{850} is the flux in the central beam, Ω is the main beam solid angle of $15''$, $\mu = 2.33$ the mean molecular weight, m_{H} the mass of atomic hydrogen, κ_{850} the dust opacity per gram of gas and dust at 850 μm and $B_{850}(T)$ the Planck function at 850 μm for a temperature T , assumed to be 30 K. A $\kappa_{850} = 0.01 \text{ cm}^2 \text{ gr}^{-1}$ is adopted from Ossenkopf & Henning (1994) for dust with thin ice mantles (Table 1, column 4).

Two assumptions affect the comparison between the column densities derived from $C^{18}O$ and those from dust continuum. $C^{18}O$ can be frozen out onto the dust grains below ~ 30 K at sufficiently high densities, so that $C^{18}O$ column densities are expected to be lower than those obtained from dust data. Second, all dust emission is assumed to originate in envelope or cloud material, whereas for several sources the disk contributes significantly to the continuum. These combined effects likely explain the lack of correlation seen in Fig. 2.17 (left).

If one assumes that all emission detected at $850 \mu\text{m}$ is associated with an isothermal envelope, a source mass can be determined following Equation 4 from Shirley et al. (2000):

$$M_D = \frac{S_{850} D^2}{B_\nu(T_d) \kappa_\nu} = 3.69 \times 10^{-6} M_\odot \quad (2.5)$$

$$\times S_{850}(\text{Jy}) D^2(\text{pc}) \times (e^{16.9/T_d} - 1)$$

Since the 3σ sensitivity of the COMPLETE map is 80 mJy within a $15''$ beam, the lower limit to the detectable mass is $0.04 M_\odot$. Such a low mass implies either a source that has nearly shed its envelope and is close to the pre-main sequence phase or an intrinsically very low luminosity object (Dunham et al. 2008).

Fig. 2.17 shows the relation between the different column densities, envelope masses and the presence of dense gas as traced by HCO^+ . These figures clearly show that at higher envelope masses, the amount of dense gas and the total envelope mass correlate. The third figure illustrates that nearly all sources with centrally concentrated HCO^+ emission have larger envelope masses. Above an envelope mass of $0.1 M_\odot$, only a single source that is classified as confused in § 2.6 (indicated with diamonds) is seen with $HCO^+ > 2 \text{ K km/s}$. This is CRBR 2422.8-3423, which is located in the line of sight with the envelope of IRS 43. The high mass found for CRBR 2422.8-3423 can be fully attributed to this envelope.

2.5.5 Effect of reddening on α_{IR}

Foreground material reddens the YSO and steepens the spectral slope $\alpha_{2-24\mu\text{m}}$. An estimate can be made of the foreground column density based on our $C^{18}O$ maps, by assuming that the average column or A_V at $45''$ offset from the source position in all directions originates entirely from this cloud. Although it is not known *a priori* whether this material is foreground, back-ground, or a different YSO, we assume here that it is all foreground (see also § 2.5.2) which provides an *upper limit* to the reddening. Not that the column densities at these positions were calculated with a temperature of 15 K , a temperature associated with the surrounding cloud, instead of 30 K , a temperature associated with protostellar envelopes. For typical dust opacities and the $A_V=5.5 \text{ mag}$ layer as suggested by Dickman & Herbst (1990), $\alpha_{2-24\mu\text{m}}$ is only increased by 0.18 (see also Crapsi et al. (2008)). However, for higher A_V of $\sim 40 \text{ mag}$, as commonly found in the Ophiuchus ridge, this correction can be as high as 1.1 , enough to change the classification of a Class II T Tauri star with disk to an embedded Class I source. Table 2.6 includes the (maximum) change in $\alpha_{2-24\mu\text{m}}$ due to foreground reddening for each source derived by this method. Chapman et al. (2008) probe the A_K in the northern

part of Ophiuchus, including the northern part of the Oph-A area, where A_V values of 40 mag. and higher are found. In the Oph-A, Oph-B2 and Ridge regions, A_V of this magnitude were found from $C^{18}O$ column densities, reinforcing the conclusion that a strong extinction affects these regions on scales of only a few arcminutes, a resolution often not reached by extinction studies (Cambr esy 1999). Although these numbers have large uncertainties, they do illustrate the point that this potential extreme foreground reddening can lead to incorrect classifications for a significant number of sources in Ophiuchus.

An alternative is to use the velocity resolved $C^{18}O$ spectrum at the source position but subtract the layer that includes the source. For example, LFAM 26 ($\Delta\alpha_{IR}=4.4$), resides in a dense ridge (see § 2.5.2). Subtracting the gaussian profile of this layer at ~ 4.4 km s⁻¹ gives an integrated intensity of 2.9 K km s⁻¹, which corresponds to a column density of 10.7×10^{22} cm⁻², an A_V of ~ 60 mag and $\Delta\alpha_{IR} = 3.2$. If one assumes that the layers are arranged in distance in order of increasing V_{LSR} , only the front layer at 3.5 km s⁻¹ will redden and a column density of 6.6×10^{22} cm⁻², an A_V of ~ 40 and $\Delta\alpha_{IR}=1.9$ are found. Thus, $\Delta\alpha_{IR}$ is likely to be in between the maximum value listed in Table 4 and $\Delta\alpha_{IR}/2$, although exceptional cases, such as OphE-MM3, an edge-on disk in front of the cloud, do exist.

2.5.6 SEDs: L_{Bol} and T_{Bol}

The IR and submillimeter fluxes have also been used to calculate the bolometric luminosity, L_{bol} , and temperature, T_{bol} , of each source. These numbers were calculated using the prismoidal or the midpoint methods, with the inclusion of the 2MASS, IRAC, MIPS-24, MIPS-70, SHARC-II, SCUBA and 1.3 mm fluxes. Only fluxes with a $S/N > 5$ were included. For a more thorough discussion on the usage of these two methods, see Dunham et al. (in prep.) and Enoch et al. (2008).

Table 2.8 compares the values found for T_{bol} and L_{bol} in our work with those of Enoch et al. (2008) for several sources. The differences stem from the fact that Enoch et al. (2008) use CSO-Bolocam 1.1 millimeter data in a 30'' beam, together with 2MASS, IRAC, and MIPS (24, 70 and 160 μ m) fluxes. No SHARC-II or SCUBA fluxes were included, nor were sources with no detection at 1.1 mm. As can be seen from the results for Elias 29 and GSS 30 IRS1, the inclusion of Bolocam and MIPS-160 produces a higher L_{bol} of up to a factor of 6. In addition, T_{bol} is consistently lower for the brighter sources. This can be largely attributed to the contributions from the surrounding cloud, which add significantly to the MIPS-160 and Bolocam fluxes. Although cloud emission is present in the IRAM-30m 1.3 mm and SCUBA-850 μ m observations used in our studies, the higher resolution of 15'' limits such contributions. The exclusion of MIPS-160 in our work causes the L_{bol} to be underestimated and the T_{bol} to be overestimated, due to the lack of a point at far-IR wavelengths near the peak of the SED. Isolated, unresolved sources such as IRS 42 show little to no differences between the two studies, confirming the influence of the environment. Future high resolution ($< 10''$) observations with the PACS instrument on Herschel covering the 60 to 600 μ m window will be able to fully constrain the far-IR emission and SED.

Table 2.8 — Comparison between L_{bol} and T_{bol} as calculated in Enoch et al. (2008) (indicated with Enoch) and this work (indicated with van K.).

Source	L_{bol}	L_{bol}	T_{bol}	T_{bol}
	Enoch (L_{\odot})	van K. (L_{\odot})	Enoch (K)	van K (K)
LFAM 26	0.15	0.044	106	238
GSS 30	18.3	3.3	133	123
CRBR 2422.8	0.33	0.44	185	157
IRS 44	7.2	1.1	193	140
IRS 43	3.8	1.0	211	134
Elias 29	17.9	2.5	257	424
WL 17	0.6	0.67	310	323
CRBR 2339.1	0.33	0.055	191	426
WL 2	0.12	0.09	428	573
IRS 42	1.2	1.4	595	540

2.5.7 Ice and silicate absorption

In the online appendix, the IRS spectra for 28 of the sources in our sample are plotted. 17 sources show ice absorption bands at $15.2 \mu\text{m}$ due to CO_2 ice (see Table 2.9), and 11 do not (WL 3, LFAM 26, VSSG 1, CRBR 2317.3, CRBR 2315.8, IRS 48, CRBR 2339.1, SR 21, Haro 1-4, IRS 46 and SR 9). A few of the known edge-on disks, such as CRBR 2422.8-3423.2, show ice absorptions.

Crapsi et al. (2008) modelled the spectral features at $3 \mu\text{m}$ (H_2O ice), $10 \mu\text{m}$ (silicate) and $15.2 \mu\text{m}$ (CO_2 ice) for a large grid of models, including embedded sources and T Tauri disks, both seen at a wide variety of angles. The ice absorptions at 3 and $15.2 \mu\text{m}$ were found to be more prevalent for embedded sources. However, edge-on disks can also show such absorptions in almost equal strength. The relation of the $3 \mu\text{m}$ ice absorptions with the envelope mass of both embedded and disk sources is given in Fig. 4 of Crapsi et al. (2008) and a similar relation was found for the $15.2 \mu\text{m}$ band. Cold foreground clouds can also contribute significantly.

Using the determination of the column densities from the C^{18}O and SCUBA maps in § 2.5.3 and 2.5.4, Eq. 3 and 4, the ice absorption can be compared to the amount of reddening as indicated by $\Delta\alpha_{\text{IR}}$. Although ice absorptions are more commonly found in sources with a higher reddening, it is concluded that the YSOs must be characterized on a source by source basis to locate the origin of the ices. The disk source CRBR 2422.8 has deep ice absorptions (Pontoppidan et al. 2005), most likely originating the large column of foreground material ($\Delta\alpha = 0.9$). However, LFAM 26, which has an even higher reddening ($\Delta\alpha = 1.7$), shows no sign of ice absorption. Of course, it is possible LFAM 26 is located in front of the cloud and as such the presence or absence of ice absorption could serve as a useful diagnostic of the geometry of the YSO-cloud system. The silicate feature around $10 \mu\text{m}$ is detected for fewer sources than the 15.2CO_2 ice absorption. Although LFAM 26, WL17, Elias 29, IRS 42, WL 3, IRS 54, CRBR 2315.8-1700, CRBR 2339.1-2032 and CRBR 2422.8-3423 all have silicate absorption, many other sources were not observed at the wavelengths of the silicate feature.

2.6 Classification

2.6.1 Physical classification

A new classification based on physical parameters has gradually been introduced (Whitney et al. 2003b,a; Robitaille et al. 2006) but is not yet as commonly in use as the traditional Class system. This new classification identifies the evolutionary stage using the physical characteristics as opposed to the observed characteristics. The different evolutionary stages are determined from the ratios between M_{disk} , M_{envelope} and M_{star} . The total circumstellar mass, M_{circum} , is defined as $M_{\text{disk}} + M_{\text{envelope}}$. The evolutionary stages of this classification are:

- Stage 0, deeply embedded sources with $M_{\text{disk}}/M_{\text{envelope}} \ll 1$ and $M_{\text{circum}}/M_{\text{star}} \sim 1$
- Stage 1, embedded sources with $0.1 < M_{\text{disk}}/M_{\text{envelope}} < 2$ and $M_{\text{circum}} < M_{\text{star}}$
- Stage 2, classical T Tauri stars with gas-rich disks ($M_{\text{envelope}} = 0$ and $M_{\text{disk}}/M_{\text{star}} \ll 1$)
- Stage 3, Pre-main sequence stars with tenuous disks.

Stage 0 sources are equivalent to Class 0 sources and can be identified by their submm characteristics as originally put forward by André et al. (1993). Stage 2 and Stage 3 sources, corresponding to the classical T Tauri stars with disks and pre-main sequence stars with (gas-poor) tenuous disks, are identified using the IR excess combined with optical/near-IR spectroscopic properties. The amount of IR excess and the wavelength where this excess starts are often used to distinguish Stage 2 and 3 sources.

The Stage 1 sources are most problematic to uniquely identify based on observational characteristics. Both Whitney et al. (2003a) and Crapsi et al. (2008) show that the traditional identification methods of using the IR spectral slope α_{IR} and T_{bol} are insufficient to distinguish the edge-on disks from embedded sources, as well as missing evolved, face-on embedded YSOs that are (mis)classified as Class II. One of the main parameters to unambiguously identify Stage 1 sources is the $M_{\text{disk}}/M_{\text{envelope}}$ ratio as determined from millimeter continuum observations in a large and small ($\sim 2''$) beam (Crapsi et al. 2008). However, the interferometric observations needed to unambiguously constrain the disk masses are still time-consuming for large samples of sources.

Table 2.9 — The classification of the source sample.

Source	Code ^a	Stage
Embedded sources		
GSS 30	$S_{HC8} E_{H8} P_{H8} I$	1
LFAM 1	$S_{H8} N_C E_{H8} P_H O_8$	1
VLA 1623	$S_{HC8} E_{H8} P_{H8}$	0
WL 12	$S_{HC8} E_{HC8} P_{HC8} I$	1
LFAM 26	$S_{HC8} E_{HC8} P_{H8} O_C$	1
WL 17	$S_{H8} N_C P_{H8} I$	1(T)
Elias 29	$S_{HC8} E_{H8} P_{H8} I$	1
IRS 37	$S_{HC} W_8 E_{HC8} P_{HC8} I$	1
WL 3	$S_{HC} W_8 E_{HC8} P_H$	1
WL 6	$S_{HC} N_8 I$	1(T)
IRS 43	$S_{HC8} E_{H8} P_{H8} I$	1
IRS 44	$S_{HC8} E_{HC8} P_{HC8}$	1
Elias 32	$S_{HC8} E_{H8} P_{H8} I$	1
Elias 33	$S_{HC8} E_{H8} P_8 I$	1
IRS 54	$S_{HC} W_8 E_{HC8} P_{HC8} I$	1(T)
IRAS 16285-2355	$S_{H8} W_C E_{HC8} P_{HC8}$	1
IRS 63	$S_{H8} W_C E_{HC8} P_{HC8} I$	1(T)
Confused Sources		
CRBR 2324.1-1619	$S_{HC8} E_{HC8} O_{HC8}$	C
GY51	$S_8 N_{HC} E_8 O_8$	C
WL19	$S_{C8} N_H E_{HC8} O_{HC8} I$	C
IRS 42	$S_{HC8} E_{H8} O_{H8} I$	C
GY 256	$S_{HC} N_8$	C
Disks		
SSTc2d J162527.6-243648	N_{HC8}	2
GSS 26	$S_8 N_{HC} P_8$	2
CRBR 2315.8-1700	$S_{H8} N_C E_H P_8 O_H$	2
CRBR 2317.3-1925	$S_H W_8 N_C$	2
VSSG 1	$W_8 N_{HC} P_8$	2
CRBR 2339.1-2032	$S_H W_8 N_C P_8$	2
WL 2	$W_{H8} N_C E_{H8} O_{H8}$	2
GY 224	$W_8 N_{HC} P_8 I$	2
WL 20S	$S_{C8} N_H P_8 I$	2
IRS 48	$W_{C8} N_H E_C P_8$	2
GY 312	N_{HC8}	2
IRS 51	$S_{H8} W_C E_{HC8} P_8 O_{HC} I$	2
SSTc2d J162741.6-244645	$W_8 N_{HC}$	2
SSTc2d J162748.2-244225	N_{HC8}	2
SSTc2d J162857.9-244055	$S_8 N_{HC}$	2
Haro 1-4	N_{HC8}	2
DoAR 25	$S_8 N_{HC} P_8$	2
OphE MM3	$S_{HC} W_8 E_{HC8} O_{H8}$	2

Continued on Next Page...

Table 2.9 – Continued

Source	Code ^a	Stage
SR 21	W ₈ N _{HC} P ₈	2
CRBR 2422.8-3423	S _{H8} N _C E ₈ O ₈ I	2
IRS 46	S ₈ W _C N _H E _{HC8} O _{HC8}	2
SR 9	N _{HC8}	2
2Mass 16282	W ₈ N _{HC}	2

^aThe coding in column 2 is as follows: S, W and N determine if a line or continuum is Strong, Weak or Not detected/observed. E, P and O determine if a source is Extended, Peaking or Offset peaking. The subscripts H, C and 8 refer to the HCO⁺, C¹⁸O and 850 μ m. I is detected CO₂ ice absorption. Column 3 lists the classification. 1 is a Stage 1 embedded YSO, 2 is a disk and C is Confused.

2.6.2 Identifying embedded stage 1 sources with molecular emission

To uniquely identify embedded sources and distinguish them from edge-on disks, prestellar cores and possible background AGB stars and galaxies without having to resort to interferometers, we propose to use the single-dish molecular emission. Embedded sources will be bright and centrally peaked in HCO⁺ 4–3 and C¹⁸O 3–2. The HCO⁺ line maps will detect all but the most tenuous envelopes. The concentration parameter shows that HCO⁺ 4–3 is much more accurate in identifying protostellar envelopes than continuum dust emission. The HCO⁺ maps also spatially resolve larger envelopes (e.g., the VLA 1623 and GSS 30 envelopes). The nearby environment, including foreground layers, is in turn characterized by the C¹⁸O 3–2 (see § 2.4 and 2.5).

To distinguish embedded sources from isolated edge-on disks, a good limit on the HCO⁺ 4–3 emission is $T_{\text{MB}} > 0.4$ K. Thi et al. (2004) observed four well-studied gas-rich disk sources in a large range of molecular transitions, including HCO⁺ 4–3, and found $T_{\text{MB}} \sim 0.1$ K, four times below our adopted limit. Although disks around embedded sources could be somewhat larger and more massive, it is assumed that the contribution from even the largest embedded disks does not exceed our adopted limit. Indeed, for two embedded sources for which interferometric HCO⁺ data exist (IRS 63 and Elias 29, Lommen et al. (2008)), the HCO⁺ contribution of the disk does not exceed this limit (see § 2.6.3). The following definitions were therefore used to classify the sample:

- Stage 1
 - Extended HCO⁺ emission, peaking on source, with $C_{\text{HCO}^+} > 0.7$ and $\int T_{\text{MB}} dV > 0.4$ K km s⁻¹ and/or
 - an HCO⁺ profile that is not extended, but $\int T_{\text{MB}} dV > 0.4$ K km s⁻¹, with SCUBA both extended and $C_{850} > 0.7$.

- Ice absorptions are usually prominent.
- Stage 2
 - Absence of HCO⁺, SCUBA and C¹⁸O down to the rms limits at the IR position *or*
 - no variation of HCO⁺, SCUBA and C¹⁸O on scales of 30'' ($C < 0.4$) *or*
 - no C¹⁸O 3–2 or SCUBA is seen at scales larger than the central beam of 15'' with HCO⁺ 4–3 not extended and $< 0.4 \text{ K km s}^{-1}$ *or*
 - $\alpha_{\text{IR}} < -0.5$.
- Confused
 - HCO⁺, SCUBA or C¹⁸O peaking more than 20'' away from the IR position

In the rare case that an embedded source is viewed face-on (into the outflow cone, see Whitney et al. (2003b)), the above restrictions will identify such a source as stage 1, having $\alpha_{\text{IR}} < -0.3$, but with extended HCO⁺ emission, peaking on source ($\int T_{\text{MB}} dV > 0.4 \text{ K km s}^{-1}$).

Table 2.9 shows the results for this classification. In Appendix C the sources and their classifications are discussed on a source by source basis. Sixteen Class I sources were identified as embedded Stage 1 sources with envelopes varying in mass and size. The sources GSS 30 IRS 1 and LFAM 1 appear to be embedded within an approximately spherical envelope encompassing both sources. The sources IRS 37 and WL 3 are embedded in a highly non-spherical envelope covering both sources. In addition to these 16 sources, VLA 1623 is classified as embedded, but considered a Stage 0 source due to its high sub-mm flux relative to the total luminosity. From comparison with Jørgensen et al. (2008) (see § 2.6.5), we can conclude that all embedded sources were found down to a mass limit (envelope+disk) of $0.04 M_{\odot}$. Deep searches for even lower luminosity sources have found only two likely candidate sources within our field (Dunham et al. 2008). Deep (interferometric) sub-mm observations are needed to identify if such sources are truly embedded.

Five sources were found to be confused (C in Table 2.9). The exact nature of these sources (obscured, disk or other) cannot be determined without interferometric observations. However, molecular emission rules out a protostellar envelope. Observations of C¹⁸O show that cloud material is located in the line of sight towards these sources. They will be further discussed in § 2.6.4.

Twenty-three sources were found to be Stage 2 sources (2 in in Table 2.9). Of this sample, sources with $\alpha_{\text{IR}} > 0$ and with no correction from extinction (see Table 4) are likely to be edge-on or close to edge-on disks. Sources that do have a potential correction to α_{IR} , such as CRBR 2422.8 or IRS 48, do not have to be edge-on. All sources that were initially known to be disk sources are identified as Stage 2 sources using this method. If one considers that disk sources with $\alpha_{\text{IR}} > -0.3$, when corrected for the maximum $\Delta\alpha_{\text{IR}}$, are edge-on, only 7 out of 23 Stage 2 sources of our sample are expected

to be edge-on. The total amount of Class II sources found in Ophiuchus by c2d is 176, and although this includes L 1689, the bulk of these disks exist close to or are part of the L 1688 region (Evans et al. in prep). Thus, our number of edge-on disks appears to be only a small fraction of the total disk sample.

No face-on embedded sources were found that have $\alpha_{\text{IR}} < -0.3$ but a HCO^+ spectrum that is both peaking on source and stronger than 0.4 K km s^{-1} . This very low fraction is not surprising, since such sources have strong restrictions on the line of sight.

Using the results from Spitzer (c2d delivery document (Evans et al. 2007), Jørgensen et al. (2006), Allen et al. in prep, Evans et al. in prep) a comparison can be made between the classification using α_{IR} and the new method. It is found that $\sim 50\%$ (11 out of 22) of the sources classified as Class I are Stage 2 disks and not embedded. Note that this includes the known disks OphE MM3 and CRBR 2422.8. However, of the Flat spectrum sources, $\sim 50\%$ (6 out of 13) appear to be embedded, while the other half is either confused or classified as a Stage 2 disk. In the end, the sample of embedded sources found by c2d changes from 22 out of 45 to 17 out of 45.

Table 2.10 — Comparison between the classification of YSOs using α_{IR} by Evans et al. in prep and our method using molecular emission.

	Class I	Flat Spectrum	Class II	Total
Stage 1	11	6	0	17
Confused ^a	1	3	1	5
Stage 2	10	4	9	23
Total	22	13	10	45

^aNote that although it is possible for Flat Spectrum sources to be embedded, confused sources are ruled out to be embedded.

2.6.3 Late stage 1 sources

Of the sixteen embedded Stage 1 sources, four sources (WL 6, WL 17, IRS 54 and IRS 63) were found to have only marginal envelopes left, with C^{18}O and $850 \mu\text{m}$ emission suggesting that at most a few $\times 0.01 M_{\odot}$ remains in the envelope. Lommen et al. (2008) observed IRS 63 using the Sub-Millimeter Array (SMA) and found that 50 % of the continuum emission originates within a disk no bigger than 200 AU in size with a mass of $0.055 M_{\odot}$ and the remainder in a remnant envelope with a mass of $0.058 M_{\odot}$. HCO^+ 3–2 was also detected with the SMA, originating mostly in the disk. When convolved with the JCMT beam, the observed brightness is 0.28 K km s^{-1} . The HCO^+ 4–3 single-dish intensity as observed with HARP-B is 0.75 K km s^{-1} , 3 times as bright. For typical disk conditions, HCO^+ 4–3 is expected to be equal or weaker compared to the 3–2, so that at least half of the 4–3 emission within the JCMT beam likely originates in the protostellar envelope.

In all four sources, little to no extended C^{18}O is seen. The distributions and strengths in the HCO^+ and C^{18}O lines of the other three sources are similar to that of IRS 63, but the SCUBA image of IRS 63 is a factor of 4 brighter. For IRS 54, the envelope is spatially resolved in HCO^+ , C^{18}O and SCUBA.

Although rare, it is concluded that these sources are Stage 1 sources in transition to a Stage 2 source (marked with 1(T) in Table 2.9). They have accreted or dispersed almost their entire envelope. Continuum emission in the sub-mm is likely to contain a large contribution from the protostellar disk.

2.6.4 Confused sources

For the five confused sources, CRBR 2324.1-1619, GY 51, WL 19, IRS 42 and GY 256, the exact nature cannot be determined using HCO^+ , except that such sources are ruled out as embedded YSOs. None of them have the characteristic peak of HCO^+ that most Stage 1 embedded YSOs have. However, at least two out of the three tracers, HCO^+ , C^{18}O and SCUBA, are detected so a few possibilities remain. The first is an (edge-on) disk, in *front* of cloud material. This would be similar to the case of OphE-MM3, which was confirmed to be an edge-on disk in front of a dense core (Brandner et al. 2000). Without the near-IR imaging, OphE-MM3 would have been classified as confused. A second possibility is that they are background sources. The most likely options are then a T Tauri star with disk *behind* the cloud (possibly edge-on), or an AGB star. Background main sequence stars are identified within the c2d delivery document (Evans et al. 2007) and are thus highly unlikely to be included in our sample. Chances of background AGB stars or galaxies being aligned with the cloud are small, but according to Jørgensen et al. (2008), a single background source can be expected. A final possibility is that the sources are very late Stage 1 embedded YSOs, very close to the Stage 2 phase. An upper limit of only $0.02 M_{\odot}$ is found for their envelope mass.

2.6.5 Comparison to other methods

Fig. 2.18 shows the effectiveness of the classification of sources using the method above, as compared to methods using α_{IR} and T_{bol} . A key parameter is the strength of the HCO^+ integrated intensity. The following limits were adopted between embedded and disk sources: $\alpha_{\text{IR}} > 0$, $T_{\text{bol}} < 650 \text{ K}$ and $\text{HCO}^+ > 0.4 \text{ K km s}^{-1}$.

The advantages of the method using molecular emission are immediately apparent. Although the classical methods of using T_{bol} and α_{IR} are able to identify embedded sources, both methods also incorrectly identify a number of Stage 2 disks as embedded, especially for $L_{\text{bol}} < 1 L_{\odot}$. These are the edge-on disks. If one uses the limits of the integrated intensity for HCO^+ , isolated disk sources are easily identified. With the additional restriction of having a peak within the HCO^+ map, confused sources or sources in front of the cloud can be readily identified.

The use of ice absorption, as studied by Crapsi et al. (2008), is limited by similar constraints. Most embedded sources, with the exception of LFAM 26 and WL 3, show CO_2 ice absorption at $15.2 \mu\text{m}$. However, 4 disk sources IRS 51, WL 19, WL 20S and CRBR 2422.8-3423 also show strong ice absorptions. These ice absorptions are caused both by the foreground layers as discussed in § 2.5.2 as well as the material in the disk itself, if viewed edge-on (as is the case for CRBR 2422.8). Thus, the presence of ice absorption cannot be used to unambiguously identify embedded sources from other sources. Even if the origin of the ice absorption can be attributed to a protostellar envelope, its strength does not seem to be an indication of evolution, e.g. IRS 63, a

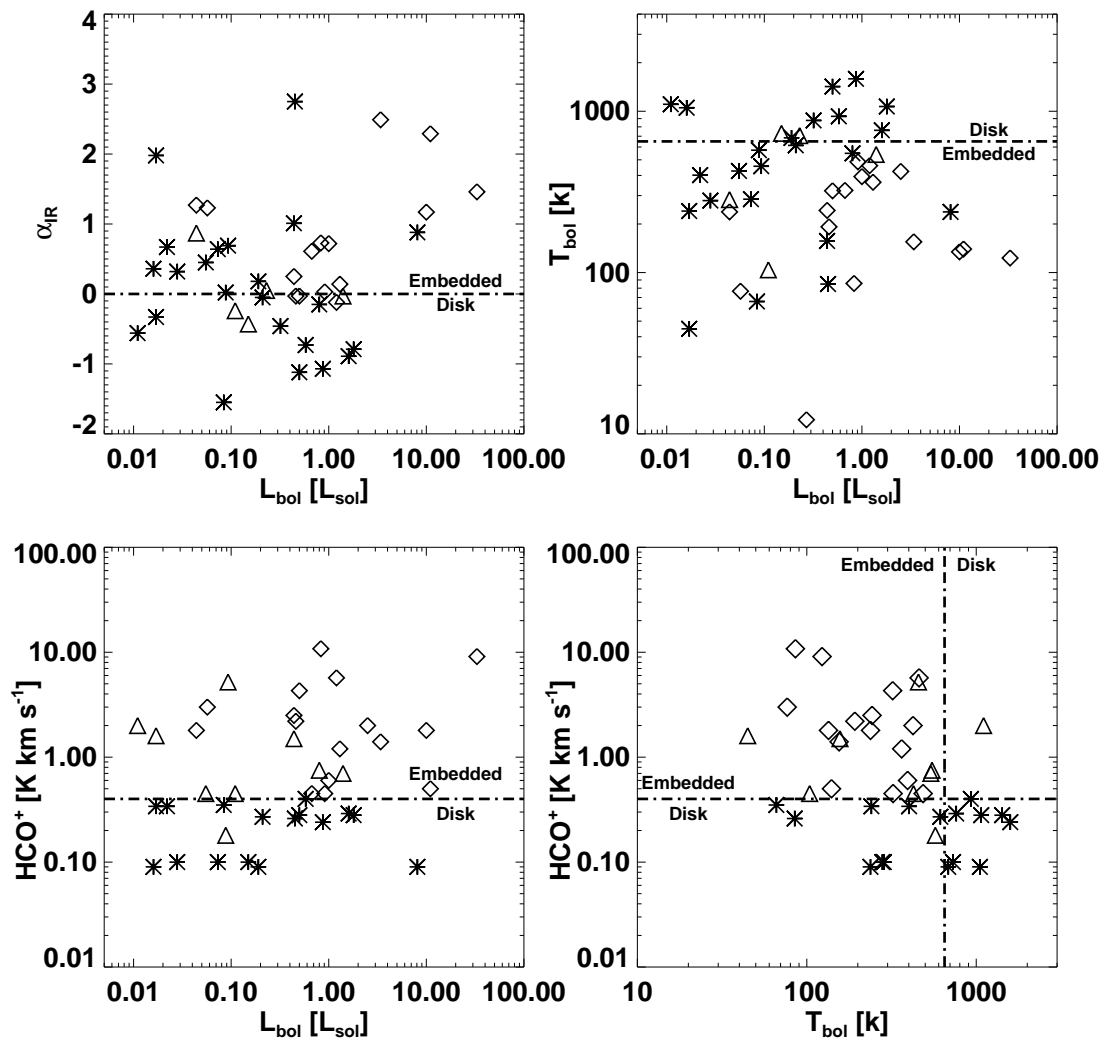


Figure 2.18 — Classification of sources using the spectral slope (*upper left*), bolometric temperature (*upper right*), HCO^+ intensity (*lower left*) and HCO^+ intensity combined with the bolometric temperature (*lower right*). In the upper two plots, embedded sources are shown with a diamond, disks are shown with a star, and confused sources with a triangle. In the lower two plots, diamonds are again embedded sources, stars represent sources with an upper limit on the HCO^+ and triangles are sources with no HCO^+ peak associated with the source. Note that the confused sources and disk sources are both represented with triangles and stars. The traditional limits used for classification, $\alpha_{\text{IR}} > 0$ and $T_{\text{bol}} < 650$ K as well as our criterion, $\text{HCO}^+ > 0.4$ K km s^{-1} , are shown with dashed lines.

small envelope, has a deeper ice absorption than the large envelope of GSS 30.

Jørgensen et al. (2008) published a list of ‘candidate’ embedded YSOs based on two criteria. First the colors of sources using the IRAC and MIPS results ($[3.6] - [4.5]$ and $[8] - [24]$). Second, the proximity of MIPS sources to SCUBA cores. For these cores, the concentration is an important parameter. Although most candidate embedded objects are identified by both criteria, several sources are included in their list based on only a single one. Comparison between their list (Table 1 in Jørgensen et al. (2008) limited to L 1688, further referenced as JJ1) and the list in this chapter yields the following results:

- Four embedded YSOs with SCUBA fluxes below the cut-off adopted by JJ1 ($< 0.15 \text{ Jy beam}^{-1}$, the very low envelope masses) are absent from the JJ1 list. Two of these sources (WL6 and IRS 54) are classified by us as late Stage 1 sources with little to no envelope left. The other two embedded YSOs not included in JJ1 are IRS 37 and WL 3.
- Four sources are included in the JJ1 list that have been classified as Stage 2 disks by our method. These are GSS 26, CRBR 2315.8, CRBR 2339.1-2032 and IRS 51. All four sources have associated SCUBA cores and MIPS detections. See the appendix for the classification reasoning of each of these sources.

2.7 Detailed description of all sources

GSS 30 and LFAM 1. These sources are both Stage 1 sources with a separation of $15''$, but share a common circumbinary envelope on scales up to $40''$. Strong HCO^+ is seen, peaking in between both IR positions. Although outflowing gas was detected, the bulk of the emission is believed to be quiescent.

VLA 1623. HCO^+ is found to be extended on scales of $30''$, larger than that found for most sources. The lack of any emission at IR-wavelengths confirms this to be a Stage 0 source.

WL 12. This source is a good example of a small embedded Stage 1 YSO. It is embedded in a small ridge of material, extending from a north-east to west direction, as can be clearly seen in both dust and C^{18}O mapping. This ridge contributes only little to the HCO^+ emission, which is concentrated at the source position. It is spatially resolved and peaks to 1.4 K. This is much too bright to be associated with a disk.

LFAM 26. This Stage 1 is located at the tip of the Ophiuchus ridge that extends from LFAM 26 down to IRS 51. See § 2.5.2 for a discussion on the environment of LFAM 26. The onset of this ridge is clearly seen, extending to the south-east direction, with much less material present in the north-west direction. Both HCO^+ and $850 \mu\text{m}$ peak at the source position and are bright. Even if the emission originating in the cloud is subtracted from the HCO^+ emission at the source position, it is too bright to be associated with a disk. This classification is confirmed by the very high α_{IR} of 1.27.

WL 17. This is a Stage 1 source, but evolving towards a Stage 2, which we classified ‘late’ Stage 1. The emission of HCO^+ is too bright to be associated with a disk. Since little to no extended emission is seen at scales of $40''$, the source is probably unobscured by cloud material.

Elias 29. This is a well-studied Stage 1 source (Boogert et al. 2002; Lommen et al. 2008). The analysis of HCO^+ and continuum, both from SCUBA and SHARC-II, confirm this

source to be embedded.

IRS 37 and WL 3. The Stage 1 sources IRS 37 and WL 3, separated by 20'' share a common envelope, with both C¹⁸O and HCO⁺ peaking on both source positions. This envelope is highly non-spherical. The proximity of the two sources is probably responsible for this. Most of the mass is located near IRS 37, although the amount of HCO⁺ emission and concentration of the cores are equal.

WL 6 and GY 256. The weak HCO⁺ seen for these two sources with a separation of 12'' is brighter than that assumed to originate within a disk. In the dust maps, no emission is seen. WL 6 is probably a more evolved Stage 1 source with little envelope mass left. It is possible that GY 256 is a second component in a binary due to the rising spectra between 2 and 24 μm. However, since the flux from GY 256 at 6 and 8 μm is less than at 4.5, it is more likely that GY 256 is a Stage 2 source. GY 256 is classified as confused.

IRS 43. This is a Stage 1 source, with a well-defined envelope that is bright in HCO⁺ and C¹⁸O. Both the SCUBA and HCO⁺ maps show a slightly elongated envelope with a possible second component about 30'' to the east. This component is relatively much weaker in HCO⁺ than in the dust. However, no IR source is detected at that position. At the position of IRS 43, dense outflowing gas is prominently detected in HCO⁺ 4–3.

IRS 44 and IRS 46. The Stage 2 source IRS 46 was studied by Lahuis et al. (2006) in detail using IRS spectroscopy. Supplementary data from the JCMT confirmed that this source was a disk, reddened by a nearby envelope. The outflowing gas around the Stage 1 source IRS 44 is responsible for the reddening of IRS 46, as seen in Fig. 2.3.

Elias 32 and 33. The Oph-B2 region dominates the environment around these two Stage 1 sources. At the position of Elias 33, HCO⁺ and 850 μm continuum clearly peaks. Elias 32 is located in the middle of the Oph-B2 region. A more pronounced SCUBA and a less pronounced HCO⁺ peak are seen within 10'' of Elias 32 and α_{IR} is in both cases near 0.0.

IRS 54. Extended emission was found for SCUBA, HCO⁺ and C¹⁸O. In all three cases, the emission is weak. IRS 54 is located outside of the main clouds. Classified as a late Stage 1, this source has accreted most of its envelope mass.

IRAS 16285-2355. This is the only non-late stage 1 source that is located outside of the Ophiuchus ridge, Oph-B2 or Oph-A region. All emission in HCO⁺, C¹⁸O and 850 μm continuum is associated with the source in a spherical envelope.

IRS 63. This stage 1 source consists of a large disk with little envelope material. The observed HCO⁺ intensity of 1.2 K km s⁻¹ confirms that not all envelope material has accreted onto the disk, as suggested by Lommen et al. (2008).

CRBR 2324.1-1619. Due to the location of this source, within 2' of both VLA 1623 and LFAM 1/GSS 30, and located in between these bright sources, large amounts of material associated with the Oph A core are present, greatly confusing this source. However, the HCO⁺, C¹⁸O or SCUBA emission do not peak at the source position. The spectrum is sharply rising with $\alpha_{\text{IR}}=0.87$. However, this is mainly due to the very high flux seen at 24 μm.

GY 51. This source was not observed in HCO⁺. The SCUBA map shows no peak at the position, but bright extended emission in the direction of the Oph-A core. The source is classified as confused, but due to the α_{IR} of 0.05, this source is likely a background disk, heavily extinguished by the Oph-A cloud material.

WL 19. In the continuum and molecular emission maps, a large amount of material is found, centered $20''$ north of WL 19. This material, probably associated with a pre-stellar core, is responsible for obscuring WL 19. Since the $\alpha_{\text{IR}} = -0.43$ this source is not embedded.

IRS 42. Most of the emission from IRS 42, in both $850 \mu\text{m}$ and HCO^+ originates within the Ophiuchus ridge, near the core of IRS 43 and the location of CRBR 2422.8-3423.2. This source is classified as confused. However, with a $\alpha_{\text{IR}} = -0.03$ it is more likely that this source is a disk, probably edge-on. The less likely possibility is that this source is a back-ground source.

SSTc2d J162527.6-243648. This source, located far from the main L 1688 regions, is a disk. There is no detected SCUBA or HCO^+ emission. The rising IR spectrum of 0.36, combined with the bolometric temperature of 1051 K, is a strong indication that this source is an edge-on Stage 2 source.

GSS 26. Extended SCUBA emission is seen near the source but is likely mostly associated with nearby cloud material. If this cloud emission is subtracted, a small unresolved core remains. The falling α_{IR} of -0.46 is the main reason that this source was classified as Stage 2.

CRBR 2315.8-1700. Strong HCO^+ emission and a strongly rising spectrum ($\alpha_{\text{IR}} = 0.69$) are seen for this source. The HCO^+ map however suggests that this source is reddened by the large amount of material present in Oph A. An unresolved source is seen in the $850 \mu\text{m}$ data, but that core is not apparent in the HCO^+ map. No variation was found in the HCO^+ 4-3 at a level of 0.2 K km s^{-1} . Thus, this source is likely an disk, in line of sight of the cloud material.

CRBR 2317.3-1925. CRBR 2317.3-1925 was observed with APEX-2a in HCO^+ and was found to be reasonably strong with a peak temperature of 1.5 K. However, the source does not have a rising spectrum and the SCUBA core seen at the source position is very weak. In addition, the SCUBA emission is extended to the south-east. This source is classified as Stage 2.

VSSG 1. Similar to CRBR 2317.3-1925, VSSG 1 does not have a rising spectrum. Unlike, CRBR 2317.3-1925, however, no HCO^+ was found with APEX-2a. $850 \mu\text{m}$ emission is detected, but unresolved. The very high T_{bol} , caused by sharply falling spectra longward of $24 \mu\text{m}$, confirms this source to be a Stage 2 source, most likely edge-on.

CRBR 2339.1-2032. This Stage 2 source has unresolved emission at $850 \mu\text{m}$. Although HCO^+ was detected, the contribution is weak, only just above our cut-off for Stage 1, and does not seem associated with the source but with a patch of cloud material about $30''$ to the north-east of CRBR 2339.1-2032.

WL 2. No HCO^+ is detected associated with the source. In the dust, a small enhancement is seen at the source position, but it is not brighter than $0.15 \text{ Jy beam}^{-1}$. All HCO^+ seen in the JCMT map is associated with a small core located between Oph-A and Oph-C. Combined with $\alpha_{\text{IR}} = 0.02$ and $T_{\text{bol}} = 573 \text{ K}$, the source is classified as a disk, probably edge-on as well as extinguished by the cloud material.

GY 224. This source, located south of the Oph ridge, shows no rising spectrum and no HCO^+ . Since no $850 \mu\text{m}$ emission was found down to the noise limits of the COMPLETE map, this source is concluded to be a Stage 2.

WL 20S. The emission seen in the SCUBA map does not peak at the position of WL 20S.

In the SHARC-II map, a very weak ($0.05 \text{ Jy beam}^{-1}$) and unresolved peak is detected. In addition, no HCO^+ was detected down to the limit adopted for disks. Its location on the Ophiuchus ridge confuses the environment of this source. The very high $\alpha_{\text{IR}} = 2.7$ suggests that this source must be an edge-on disk, even if located behind the Ophiuchus ridge.

IRS 48. The disk source IRS 48 is isolated, away from the main cores in Ophiuchus. A weak, unresolved peak is seen in the SCUBA. The absence of any C^{18}O and HCO^+ confirms the classification to be Stage 2.

GY 312. GY 312 is not detected in the dust or gas mapping. In addition, no contribution from large-scale material is seen. Its clearly rising IR spectrum identifies this source as an edge-on Stage 2 source.

IRS 51. IRS 51 is located at the south end of the Ophiuchus ridge. The ridge is clearly seen in SCUBA as well as in C^{18}O and HCO^+ maps around IRS 51. Although a clear peak is seen at IRS 51 in the dust map, no peak was seen in the molecular line mapping at the position of IRS 51. It is concluded that IRS 51 is a Stage 2 source with strong disk emission, reddened by the Ophiuchus ridge.

SSTc2d J162741.6-244645. This stage 2 source, located south of the Ophiuchus ridge, was not detected in either HCO^+ or SCUBA. The rising spectrum suggests that this source must be edge-on since no cloud material is nearby to redden the source.

SSTc2d J162748.2-244225. For this source, located east of the southern tip of the Ophiuchus ridge, no SCUBA or HCO^+ emission was found. The very high α_{IR} of 1.98 suggests that this source must be an edge-on disk.

SSTc2d J162857.9-244055. This source is located between the L 1688 and L 1689 regions. The combination of a steeply rising spectrum and an absence of HCO^+ and $850 \mu\text{m}$ continuum indicates that this source is a edge-on Stage 2 source.

Haro 1-4. Located north of the main Ophiuchus clouds, this source has no HCO^+ or $850 \mu\text{m}$ associated with it and clearly is a disk.

DoAr 25. Although a bright peak is seen in the $850 \mu\text{m}$ map, the α_{IR} of -1.12 clearly confirms this to be a disk source.

OphE MM3. This source, located within the Ophiuchus ridge, was first discovered in the mm-regime by Motte et al. (1998). Both the $850 \mu\text{m}$ continuum and HCO^+ show little material associated with an envelope at this source. Near-IR observations (Brandner et al. 2000) confirm it to be an edge-on disk.

SR 21. This source has a very high bolometric temperature of 1070 K. Although a clear signal is seen in the $850 \mu\text{m}$ data, no emission is seen in HCO^+ . It has been confirmed as a cold disk with a large inner hole by Brown et al. (2007).

CRBR 2422.8-3423. CRBR 2422.8-3423 is located along the Ophiuchus ridge. From near-IR imaging (Brandner et al. 2000) CRBR 2422.8-3423 is an edge-on disk, located in line of sight of the IRS 43 envelope. Even at far-IR wavelengths, emission from the Ophiuchus ridge dominates. HCO^+ mapping confirms this.

SR 9. This source is not detected at $850 \mu\text{m}$. Combined with $\alpha_{\text{IR}} < -1$, it is concluded that SR 9 is a Stage 2 source.

2MASS 16282. Although 2MASS 16282 has a low bolometric temperature of 66 K, the $\alpha_{\text{IR}} < -1$ identifies this source as a disk.

2.8 Conclusions

A sample of young stellar objects in L 1688 was analyzed using gas mapping obtained with the new HARP-B heterodyne array receiver in the HCO^+ 4–3 and C^{18}O 3–2 lines. Complementary dust maps were obtained from the COMPLETE project, as observed by JCMT-SCUBA, and with SHARC-II on the CSO. The original sample consisted of 45 sources, mostly classified as embedded YSOs or flat-spectrum sources using their spectral slope α_{IR} in previous work. Of this sample a few sources were recently discovered to be edge-on disks. As a control sample, 4 known disk sources in L 1688 were included. The observations were supplemented by single-pixel observations from APEX, Spitzer-IRS spectroscopy and continuum photometry ranging from 1 μm to 1.3 mm, using a variety of space-based and ground-based observatories.

The main conclusions are:

- The concentration of the dense gas, as traced by the HCO^+ 4–3 line mapping, provides a unique tool to characterize the dense gas in the inner regions of protostellar envelopes. Material in the cold outer envelopes, (edge-on) disks, prestellar cores or cloud material does not emit strongly in HCO^+ 4–3.
- Most envelopes in L 1688 have low masses, ranging from 0.05 to 0.5 M_{\odot} . The main accretion phase onto the star has already taken place. The only exception is the Stage 0 source VLA 1623 which contains nearly 1 M_{\odot} .
- A new classification tool based on molecular emission to uniquely identify embedded sources is proposed. Of the total sample, 17 sources were found to be embedded, 5 sources were confused and 23 sources were identified as (edge-on) disks. Due to the foreground layers found through the C^{18}O , it is concluded that a significant fraction of the sources previously classified as Class I or Flat Spectrum are disks and have been strongly reddened. Combined with the analysis in Jørgensen et al. (2008) all embedded sources in L 1688 were included and characterized down to a mass limit of 0.04 M_{\odot} (envelope+disk).
- Four embedded YSOs are found that are in transition from the Stage 1 embedded phase to the Stage 2 T Tauri phase. These sources, IRS 63, IRS 54, WL 6 and WL 17, have little envelope left ($M_{\text{env}} \approx 0.05 M_{\odot}$).
- Five sources are so confused by cloud material that identifying them as T Tauri disks or background sources is not possible with our data. The (lack of) variation and concentration of the molecular emission rules them out as embedded YSOs, however.
- All sources previously identified as disks using traditional methods such as T_{bol} and α_{IR} are indeed recovered as disks as are all edge-on disk sources, identified by near-IR mapping (e.g. IRS 46, CRBR 2422.8-3423 and OphE-MM3).
- Spectral line mapping of C^{18}O reveals that foreground layers are predominantly present in the Ophiuchus ridge and the Oph-B core. Outside these regions, foreground layers are absent. These foreground layers are responsible for heavy reddening with typical $A_V > 20$, confusing classification schemes based on IR colors.

The YSOs in the Ophiuchus clouds show a wide variety of characteristics, ranging from the rare Stage 0 deeply embedded source VLA 1623 and Stage 1 embedded YSOs such as Elias 29, IRS 43 and WL 12 to the embedded YSOs with wimpy en-

velopes in transition to the T Tauri stage like IRS 63. The results above imply that the molecular emission maps uniquely characterize the envelopes associated with embedded YSOs, while simultaneously identifying disks erroneously classified as embedded YSOs. Such characterization is needed before statistical studies can be used to estimate time scales and star formation efficiencies within L 1688.

One characteristic that has yet to be determined is the ratio of the disk to envelope mass. Interferometric studies with advanced facilities such as the SMA, CARMA or the PdB interferometer will allow the disks to be characterized and, through comparison with continuum single dish studies, the envelope (e.g. Jørgensen et al. 2005a; Lommen et al. 2008). Such detailed information will be necessary as a starting point for the interpretation of future observations with Herschel and ALMA of the embedded YSOs in Ophiuchus and other clouds. A central role is envisioned for molecular line data.

Acknowledgements

TvK and astrochemistry at Leiden Observatory are supported by a Spinoza prize and by NWO grant 614.041.004. Remo Tilanus and Jan Wouterloot are thanked for the extensive support on the observing and reduction of HARP-B data and Arno Kockx for carrying out a large part of the HARP-B observations. The support from the APEX and MPIfR staff on the APEX2a data is greatly appreciated. The assistance on the usage of the COMPLETE data from Doug Johnstone and Helen Kirk is recognized. The authors are grateful to the c2d team, especially Mike Dunham (general), Luisa Rebull (MIPS) and Fred Lahuis (IRS), for their help on the Spitzer data and useful discussion.

Chapter 3

Warm molecular gas in the envelope and outflow of IRAS 12496–7650 (DK Cha)

Abstract To obtain insight into the physical structure of the warm gas in the inner envelope of protostars and the interaction with the outflow. Sub-millimeter observations of ^{12}CO , ^{13}CO and/or C^{18}O in $J=3-2$, $J=4-3$ and $J=7-6$ were obtained with the APEX Telescope towards IRAS 12496-7650, an intermediate mass young stellar object. The data are compared to ISO-LWS observations of CO $J=14-13$ up to $J=19-18$ lines to test the different proposed origins of the CO lines. The outflow is prominently detected in the 3–2 and 4–3 lines, but not seen at similar velocities in the 7–6 line, constraining the temperature in the high-velocity ($> 5 \text{ km s}^{-1}$ from line center) gas to less than 50 K, much lower than inferred from the analysis of the ISO-LWS data. In addition, no isothermal gas model can reproduce the emission in both the 7–6 and the higher- J ISO-LWS lines. The 7–6 line probably originates in the inner ($< 250 \text{ AU}$) region of the envelope at $\sim 150 \text{ K}$. Detailed radiative transfer calculations suggest that the ISO-LWS lines are excited by a different mechanism, possibly related to the larger-scale outflow. All possible mechanisms on scales smaller than $8''$ are excluded. High-resolution continuum as well as high- J ^{12}CO and isotopic line mapping are needed to better constrain the structure of the warm gas in the inner envelope and the interaction with the outflow.

T. A. van Kempen, M. R. Hogerheijde, E. F. van Dishoeck, R. Güsten and P. Schilke, 2006, *A&A*, 454, L75

3.1 Introduction

The early stages of star formation are dominated by circumstellar envelopes and bipolar outflows. Both astrophysical phenomena have been observed over a wide range of proto-stellar masses, including low- and very high-mass young stellar objects (YSOs) (Bachiller & Tafalla 1999; Evans 1999). Outflows are an essential ingredient in the formation of stars as it is theorized that large amounts of angular momentum are transported outwards, necessary for effective accretion of the mass stored in the circumstellar envelope onto the central star and circumstellar disk. Resolved circumstellar envelopes have been observed and modelled around both low-mass (e.g., Shirley et al. 2000; Jørgensen et al. 2002) and high-mass protostars (e.g., van der Tak et al. 2000; Mueller et al. 2002). The region where the central part of the envelope and the outflow interact is generally not resolved in single-dish observations, but is a crucial link in understanding star formation. High-frequency single-dish observations could probe these regions effectively. This chapter presents the first observations of CO 4–3 and 7–6 toward a southern YSO, IRAS 12496-7650 (DK Cha), using the *Atacama Pathfinder EXperiment* (APEX)¹.

CO and its isotopologues ^{13}CO , C^{18}O and C^{17}O are often used to characterize the envelopes in these early stages (e.g. Jørgensen et al. 2002). The low excitation $J=3-2$, $2-1$ and $1-0$ lines of the CO isotopologues primarily trace the very cold material in the outer envelope. Highly excited lines of CO in the far-infrared, such as $J=14-13$ to $J=17-16$, probe the warm gas and have been detected with the *Long Wavelength Spectrometer* (LWS) on board the *Infrared Space Observatory* (ISO) toward YSOs (e.g., Giannini et al. 1999; Maret et al. 2002). Two interpretations have been put forward to explain this emission: warm (~ 200 K) gas in the innermost envelope (e.g., Ceccarelli et al. 1999; Maret et al. 2002) or hot (~ 750 K) gas in an outflow (e.g., Giannini et al. 2001; Nisini et al. 2002). Because the ISO-LWS data lack both spatial ($90''$ beam) and spectral ($\lambda/\Delta\lambda \approx 100$) resolution, the origin of this high- J emission could not be firmly identified.

Much higher spatial and spectral resolution is available for intermediate- J CO lines such as $J=6-5$ up to $J=8-7$. These lines are well suited to probe gas of 100–200 K expected in the inner envelopes of protostars and distinguish between these two models. Due to technological challenges and the high opacity of the atmosphere, they are not commonly observed. Hogerheijde et al. (1998, 1999) found surprisingly bright lines of ^{12}CO 4–3 and 6–5 and ^{13}CO 6–5 for a number of low-mass YSOs using the *Caltech Submillimeter Observatory* (CSO) in beams of 10–15'', which they interpreted with both outflows (^{12}CO) and (photon-)heated envelopes (^{13}CO) (Spaans et al. 1995). Since submillimeter continuum observations were still lacking at the time, the data were never interpreted in the context of envelope models.

APEX opens up the possibility to routinely obtain intermediate- J CO lines at high sensitivity in the Southern sky. We present initial APEX data for IRAS 12496-7650. This Class I source is part of the Chamaeleon II star-forming region (~ 250 pc) and is its

¹This chapter is based on data acquired with the *Atacama Pathfinder EXperiment*, which is a collaboration between the Max-Planck-Institut für Radioastronomie, the European Southern Observatory, and the Onsala Space Observatory

most luminous and massive member, $L_{\text{bol}}=50 L_{\odot}$. It has been classified as a Herbig Ae star with a circumstellar envelope and is associated with a weak bipolar outflow (Knee 1992). Continuum studies at infrared and millimeter wavelengths by Henning et al. (1998) give a H_2 column density of $1.0 \times 10^{23} \text{ cm}^{-2}$ and a gas mass of $0.16 M_{\odot}$ from a 1.3 mm flux of 0.5 Jy within a beam of $23''$. Spectroscopically, this source was detected by Giannini et al. (1999) with ISO-LWS in CO lines between 14–13 up to 19–18. No other molecular lines, such as H_2O or OH, could be identified, but the origin of this hot CO could not be determined. Using the detected lines and a LVG model, two possible sets of physical conditions were proposed: $T = 200$ or 750 K with a H_2 gas density of 4×10^6 or $5 \times 10^5 \text{ cm}^{-3}$, both within a region with a 300 AU radius.

3.2 Observations

The observations were performed in July 2005 during the science verification of the APEX telescope in Chajnantor, Chile, using the APEX-2a receiver for the ^{12}CO 3–2 (345.795 GHz) line and the FLASH receiver for the higher excited ^{12}CO lines: 4–3 (461.041 GHz) and 7–6 (806.651 GHz), observed simultaneously. Additional observations were taken of ^{13}CO and C^{18}O , both in 3–2. The APEX telescope, with its 12 m dish, has beam sizes of $18''$ at 345 GHz, $13.5''$ at 460 GHz and $8''$ at 806 GHz. Preliminary beam efficiencies, obtained by the APEX team from observations of planets, are 0.7 (345 GHz), 0.65 (460 GHz) and 0.47 (806 GHz) (Güsten et al., this volume). The Fast Fourier Transform Spectrometer (FFTS) was used as a back-end with a bandwidth of 500 MHz and a velocity resolution of 0.05 (345 GHz) to 0.09 (806 GHz) km s^{-1} . Integration times ranged from 5 minutes per line for ^{12}CO 3–2 to 10 minutes for the FLASH instrument. Typical system temperatures on the sky were ~ 1000 K at 460 and ~ 4000 K at 810 GHz. Beam switching was used with a switch of $180''$. Calibration uncertainties are estimated to be 30%. The coordinates of IRAS 12496-7650 were taken from the Spitzer IRAC image and are RA (J2000)

Spectra taken at different nights differed by 0.5 km s^{-1} in velocity, making the actual LSR velocity hard to determine. All spectra were carefully aligned fitting Gaussians (see Fig. 1), with the C^{18}O 3–2 line at $V_{\text{LSR}}=3.2 \text{ km s}^{-1}$ taken to be the source velocity.

3.3 Results and analysis

The resulting spectra are presented in Fig. 1, and line parameters in Table 1. The CO 4–3, 3–2 and ^{13}CO 3–2 lines suffer from absorption, probably caused by a combination of cold fore-ground cloud material, self-absorption from the outer cold envelope and emission of these lines in the off position. Because no absorption is seen in the CO 7–6 or C^{18}O 3–2 line profiles, the off-position likely consists of cold, low density gas, similar to any fore-ground material. To estimate the intrinsic source spectrum, Gaussian profiles were fitted to the lines using only the red side of the profile. Results can be seen in column 4 of Table 1. The dividing line between outflow and envelope at $<0 \text{ km s}^{-1}$ is based on the C^{18}O and ^{13}CO lines, which show only low-velocity emission.

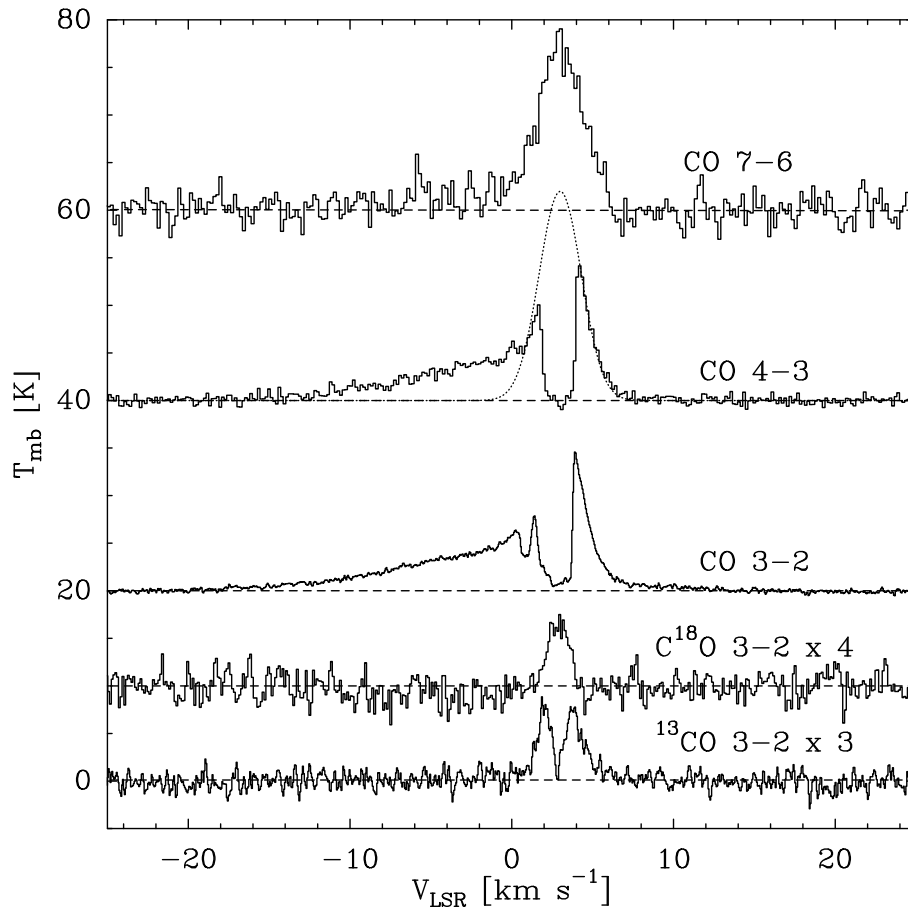


Figure 3.1 — CO observations of IRAS 12496-7650. Spectra have been shifted by +10,+20, +40 and +60 K for $C^{18}O$ 3-2, ^{13}CO 3-2, CO 4-3 and CO 7-6 respectively. $C^{18}O$ 3-2, ^{13}CO 3-2 have been multiplied with a factor of 3 and 4 respectively. The grey line in the 4-3 spectrum is the Gaussian fit to the central component corrected for absorption.

Table 3.1 — Observed line strengths

Line	$\int T_{MB} V^a$ (K km s $^{-1}$)	Gaussfit (K km s $^{-1}$)	Peak (K)	$\int T_{MB} dV^b$ (K km s $^{-1}$)
$C^{18}O$ 3-2	9.2	9.2	1.9	-
^{13}CO 3-2	6.7	12.5	3	-
^{12}CO 3-2	92.8	132	25	52.6
4-3	90.0	144	23	48.6
7-6	43.7	40.2	19.2	9.8 ^c

^a Total Emission. Integrated between -25 to 20 km s $^{-1}$

^b Outflow emission. Integrated between -25 to 0 km s $^{-1}$

^c Upper limit as some envelope material may be included

3.3.1 Outflow emission

The CO 3-2 and 4-3 spectra in Fig. 1 have an obvious outflow signature. Remarkably, the CO 7-6 line only shows a very weak sign of outflow material. Either the outflow is

Table 3.2 — Envelope model parameters

Model parameters			
General		Gas	
L_{bol}	$50 L_{\odot}$	$n_{1000\text{AU}}$	$7 \times 10^6 \text{ cm}^{-3}$
α	1.2	$X(^{12}\text{CO})$	10^{-4} for $T > 30 \text{ K}$
T_{in}	250 K		or $R > 9,000 \text{ AU}$
R_{in}	39 AU	$X(^{12}\text{CO})$	10^{-8} for $T < 30 \text{ K}$
R_{out}	$\sim 40,000 \text{ AU}$		and $R < 9,000 \text{ AU}$

not emitting in this transition or its spatial extent is larger than that of the 7–6 beam ($8''$) and smaller than that of the 4–3 beam ($15''$). Assuming the (undetected) red wing to have a similar velocity extent, the outflow spans a total FWHM of $\sim 25 \text{ km s}^{-1}$ around the central velocity of $\sim 3 \text{ km s}^{-1}$ in the LSR coordinate frame. It is excluded that the gas is highly optically thick, since no ^{13}CO 3–2 wing emission is detected at a level of 0.2 K, compared to levels of $\sim 3 \text{ K}$ seen in ^{12}CO 3–2. This limits the optical depth to ~ 2 .

The ^{12}CO line intensity ratios can be used to constrain the outflow parameters. The line ratio as a function of velocity is constant for 4–3/3–2 in a region up to -15 km s^{-1} from the line center and for 7–6/3–2 in a region up to -8 km s^{-1} . At higher velocities, noise becomes dominant. The ratios of 1.2 for 4–3/3–2 and ~ 0.25 for 7–6/3–2 constrain the temperature to $\sim 50 \text{ K}$ if the gas is thermalized. If the gas is subthermally excited ($n < n_{\text{cr}} = 5 \times 10^4 \text{ cm}^{-3}$), higher temperatures are possible up to 200 K for $n \sim 10^4 \text{ cm}^{-3}$. The observed line ratio excludes $n < 10^4 \text{ cm}^{-3}$ for any temperature (following plots by Jansen et al. 1994). An important conclusion is that either the temperature and/or density of the outflowing gas in CO 3–2 and 4–3 are much lower than those needed to explain the CO 14–13 to 19–18 lines (Giannini et al. 1999). Combined with the lack of a prominent wing in CO 7–6, this indicates that the high-velocity gas seen with APEX in ^{12}CO 4–3 and 3–2 is unlikely to be the same as the warm gas detected by ISO-LWS.

3.3.2 Envelope

The C^{18}O intensity can be used to estimate a column density of the material in the envelope. The inferred C^{18}O column density is $\sim 5 \times 10^{15} \text{ cm}^{-2}$, corresponding to a H_2 column density of $3 \times 10^{22} \text{ cm}^{-2}$ in the $18''$ beam, assuming LTE, a constant CO/ H_2 ratio of 10^{-4} and a CO/ C^{18}O isotopologue ratio of 600. This column density is a factor 3 lower than that of Henning et al. (1998), possibly due to dust properties or freeze-out.

The CO 7–6 line does not show a clear outflow signature between $V_{\text{LSR}} = -20$ to 0 km s^{-1} and over 80% of its intensity originates at velocities nominally associated with the envelope. Thus, it is natural to investigate whether such a bright high-excitation line can originate in the inner regions of the envelope. Considering that the $J=7$ energy level of CO lies at $T \sim 155 \text{ K}$ and assuming $T_{\text{kin}} = 155 \text{ K}$, an optical depth > 3 , LTE and spherical symmetry, the emitting region would have a radius of about 325 AU.

To investigate whether the hot gas traced through the high- J CO lines, observed with ISO-LWS, can explain the 7–6 emission, we perform a statistical equilibrium calculation using the RADEX code with updated rate coefficients from Flower (2001)

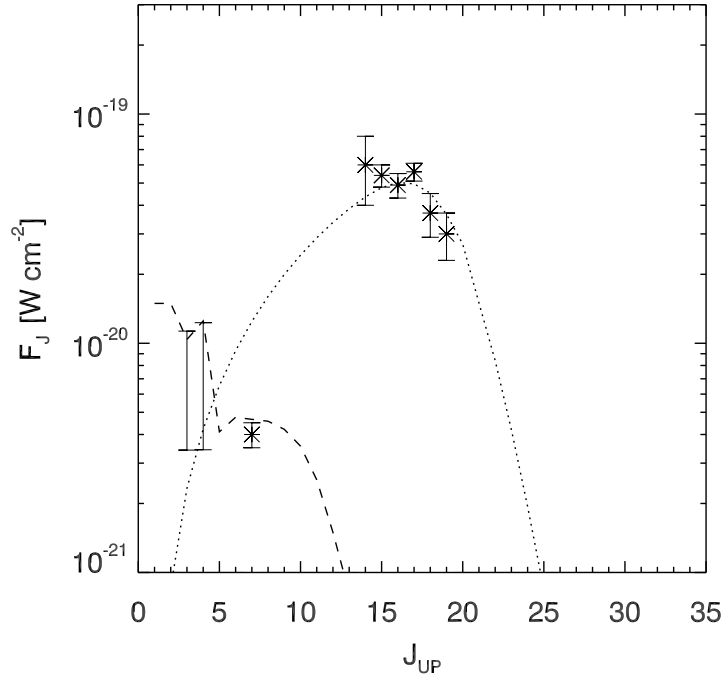


Figure 3.2 — Observed fluxes in various CO lines (points) and the best model fit ($T_{\text{kin}} = 200$ K, $n(\text{H}_2) = 4 \times 10^6 \text{ cm}^{-3}$) of the ISO-LWS data following Giannini et al. (1999) using RADEX (dotted line). Our best fit model using a full radiative transfer model for the envelope with parameters in Table 2 is indicated with a dashed line. Note that the 3–2 and 4–3 lines are indicated by upper and lower limits only. Lower limit is defined by observed emission between 0 and 10 km s⁻¹. Upper limit is defined using the correction discussed (see Table 1).

(Schöier et al. 2005). This analysis is similar to that of Giannini et al. (1999) where a warm (~ 200 K) or hot (~ 750 K) region with a radius of ~ 300 AU is needed to reproduce the observed ISO-LWS fluxes. It is assumed that the 3–2 and 4–3 emission traces the cold outer envelope only (see below). A line width of 3.5 km s⁻¹ was chosen in the formulation of the escape probability, corresponding to that observed for the 7–6 line. The ortho/para ratio of the collision partner, H₂, was taken to be thermalized at the gas temperature. Figure 2 shows the observed APEX and ISO-LWS fluxes together with such a model for $T = 200$ K and $n = 4 \times 10^6 \text{ cm}^{-3}$ within a region with a radius of 300 AU. It is clear that this fit gives a flux in the 7–6 line that is a factor of at least 4 too high compared with the observed value. No single temperature-density fit could be found that reproduces both the 7–6 and the ISO-LWS lines, including the hottest model proposed by Giannini et al. (1999) of 750 K. Such a model would still overestimate the 7–6 emission by a factor of 3. This shows that the central region of the envelope is not filled with large quantities of hot gas, otherwise the observed emission in 7–6 would be higher. Even assuming that the origin of the 7–6 line is limited to a central hot region, only 25 % of the ISO-LWS flux would originate in the inner 8'', while all other emission would be located within the 90'' ISO beam, but outside the 8'' beam of APEX.

If such hot gas cannot explain the intensity of the 7–6 line, can the inner warm region of the envelope around the 50 L_⊙ YSO reproduce this emission? And how much

can this warm gas contribute to the high- J CO lines? To investigate these questions we calculate the temperature structure in a spherical envelope using the radiative transfer code DUSTY (Ivezić & Elitzur 1997), with relevant parameters as seen in Table 2, based upon previous dust observations (Henning et al. 1998). The modeling strategy by Jørgensen et al. (2002) and Schöier et al. (2002) for other Class I sources is followed and then adapted for the higher luminosity. A drop abundance profile was adopted in which the CO abundance is normal at 10^{-4} in the outermost part of the envelope ($n < 10^5 \text{ cm}^{-3}$) and in the inner part ($T > 30 \text{ K}$), but is orders of magnitude lower in the intermediate cold zone (Jørgensen 2004). A power-law envelope with a slope $\alpha=1.2$ was found to best explain the high 3–2 and 4–3 fluxes relative to the 7–6 flux. These calculations resulted in a temperature profile which is significantly colder than the mean temperature used in the RADEX analysis. At 350 AU, temperatures have already dropped as low as 75 K. The region with temperatures above 200 K has a radius of 40 AU, severely limiting the existence of a hotter inner region capable of producing strong ISO-LWS fluxes. The radiative transfer code RATRAN (Hogerheijde & van der Tak 2000) has subsequently been used to model all CO rotational lines between $J_{\text{up}}=1$ and 35.

The best fit model is included in Fig. 2 with all CO fluxes with $J_{\text{up}} > 7$ calculated for a $8''$ beam. Fluxes for lines with $J_{\text{up}} \leq 7$ or lower are convolved with the appropriate APEX beam. It is clear that such an envelope model can account for the 7–6, 4–3 and 3–2 emission, but cannot do the same for the observed ISO-LWS fluxes. The observed C^{18}O 3–2 is reproduced within 30%. We conclude that the material traced in the $90''$ ISO-LWS beam must be distributed over scales $>8''$. This main conclusion is not changed by a more complex source structure, including a possible clumpy distribution of the gas and dust on scales smaller than $8''$ (Giannini et al. 1999).

3.4 Conclusions

IRAS 12496-7650, a Herbig Ae star, is accompanied by both a large envelope as traced by the C^{18}O $J=3-2$, CO 3–2, 4–3 and CO $J=7-6$ lines and an outflow seen in CO $J=3-2$ and $J=4-3$ wings, reaching speeds up to $\pm 25 \text{ km s}^{-1}$. The ratios of the outflow wing emission constrain the gas in the outflow to a kinetic temperature of $\sim 50 \text{ K}$, or a density of $\sim \text{few} \times 10^4 \text{ cm}^{-3}$, depending on whether the outflow gas is thermalized or not. A spherically symmetric envelope model is able to reproduce the observed 7–6 line emission using a full radiative transfer code. This envelope model extends inwards towards radii of 30 AU and temperatures of 250 K. The ISO-LWS lines do not seem to originate in these physical components and only one possible scenario remains. The emission is produced on scales larger than $8''$, but within $90''$. The low-excitation lines of CO are dominated by the cold outer envelope.

Future observations such as can be performed at APEX are essential to further probe the inner warm regions of YSOs like IRAS 12496–7650. Both continuum mapping at different sub-mm wavelengths as well as spectral mapping in high- J CO lines (including isotopologues) with instruments like FLASH and CHAMP+ will be able to further distinguish envelope and outflow emission, as well as the energetics of their interaction.

Acknowledgements

The authors are grateful to the APEX staff for carrying out the observations. Antonio Crapsi and Jes Jørgensen are thanked for useful discussions. TvK and astrochemistry at Leiden Observatory are supported by a Spinoza prize and grant 614.041.004 from the Netherlands Organization of Scientific Research (NWO).

Chapter 4

Dense and warm molecular gas in the envelopes and outflows of southern low-mass protostars

Abstract Observations of molecular gas lie at the basis of our understanding of the physical structure, density and temperature of protostellar envelopes and molecular outflows. The recent commissioning of the *Atacama Pathfinder Experiment* (APEX) greatly increases the possibility to study southern ($\text{Dec} < -35^\circ$) protostars.

We aim to characterize the properties such as temperature and density of the protostellar envelope, molecular outflow and surrounding cloud, through observations of molecular gas within a sample of 17 embedded YSOs. All sources are located in the southern hemisphere, and have been specifically chosen for their likely inclusion in future ALMA and Herschel surveys, and include the most luminous Class I objects in Corona Australis and Chamaeleon.

Observations of CO, HCO^+ and their isotopologues, both single spectra and small maps (up to $80'' \times 80''$), were taken with the FLASH and 2a instruments mounted on APEX to trace the gas around the sample. HCO^+ mapping probes the presence of dense centrally condensed gas, a unique tracer of protostellar envelopes. The rare isotopologues C^{18}O and H^{13}CO^+ are also included to determine the optical depth, column density, and source velocity. The combination of multiple CO transition, such as 3–2 and 4–3, allows for an in-depth study of the outflow properties. Strong molecular outflows are found around five sources, with outflow forces an order of magnitude higher than for the northern sources. Using the degree of concentration of the warm and dense gas tracers, several sources are found not to be embedded, due to lack of HCO^+ 4–3 and CO 4–3 emission. The extended cloud material in RCrA can obscure small ($\sim 0.3 M_\odot$) envelopes. The C^{18}O 3–2 lines show that for none of the sources, foreground layers are present.

This study provides an excellent starting point for future ALMA and Herschel surveys by characterizing the envelope masses, evolutionary status, and outflow characteristics of southern embedded YSOs.

T.A. van Kempen, E.F. van Dishoeck, M.R. Hogerheijde, R. Güsten, in prep

4.1 Introduction

During the early stages of low-mass star formation, Young Stellar Objects (YSOs) are embedded in cold dark envelopes of gas and dust, which absorb the radiation from the central star (Lada 1987; André et al. 1993). This extinction is strong enough that low-mass embedded YSOs, or protostars, only emit weakly at infrared wavelengths (e.g., Jørgensen et al. 2005a; Gutermuth et al. 2008). Only at later evolutionary phases, in which the envelope has been accreted and/or dispersed, does emission in the optical and infrared (IR) dominate the Spectral Energy Distribution (SED) (e.g. Hartmann et al. 2005). Protostars emit the bulk of their radiation at far-IR and sub-millimeter wavelengths, both as continuum radiation, produced by the cold ($T < 30$ K) dust, and through molecular line emission from the gas-phase species present throughout the protostellar envelope. Although the bulk of the mass has accreted during the earliest embedded phases, more evolved protostellar envelopes still contain a reservoir of gas and dust that can accrete onto the central star and disk system and thus contain the initial conditions of the material for disk and planet formation. An important influence on the evolution of the circumstellar material is the molecular outflow.

Protostellar envelopes and molecular outflows can be directly observed through either the thermal emission of dust at (sub-)millimeter wavelengths (e.g. Shirley et al. 2000; Johnstone et al. 2001; Nutter et al. 2005) or through the line emission of molecules tracing the cold gas in the protostellar envelopes (Hogerheijde et al. 1998; Jørgensen et al. 2002; Maret et al. 2004) or molecular outflows (Snell et al. 1990; Cabrit & Bertout 1992; Bachiller & Tafalla 1999). Observations of dust using current generation bolometer arrays are able to map large areas and image the surroundings of protostars (e.g., Motte et al. 1998; Shirley et al. 2000; Stanke et al. 2006; Nutter et al. 2008). However, unless a radiative transfer model is used (e.g., Shirley et al. 2002; Jørgensen et al. 2002; Young et al. 2003) or additional information from shorter wavelengths is included (e.g., Hatchell et al. 2007b), the internal structure of the protostellar envelope and its interaction with the surrounding material remains hard to describe. Analysis of gas observations in the form of single spectra provide additional strong constraints to the protostellar envelope (Schöier et al. 2002; Maret et al. 2004; Jørgensen et al. 2005a; Evans et al. 2005) and outflowing gas (e.g., Cabrit & Bertout 1992; Bontemps et al. 1996; Hogerheijde et al. 1998; Hatchell et al. 1999; Parise et al. 2006; Hatchell et al. 2007a). An important factor in the analysis of protostars is the surrounding cloud or neighbouring embedded sources, in more extreme cases even causing incorrect identifications of disks or background sources as embedded sources (e.g., Boogert et al. 2002; Lahuis et al. 2006, Chapter 2). The use of a spectral line map over a small ($\sim 2' \times 2'$) region around the protostar is an elegant solution to disentangle the contributions of the surrounding cloud material to molecular emission lines (Boogert et al. 2002, Chapter 2). However, the choice of molecular lines with which all the components of an embedded YSO and its surrounding material can be probed, is limited. The intricate gas-phase and surface chemistry of more complex molecules such as CH_3OH complicates its use as a tracer of the physical structure. The different local densities, temperatures and thus different chemistries of the inner and outer envelope region, molecular outflow and the surrounding cloud limits the observations to only a few molecules with simple chemical

structures, which also should not be frozen out onto the grains at low temperatures ($T \sim 30$ K). The column density of the surrounding cloud and envelope is best probed by low excitation optically thin transitions of molecules with a low dipole moment, such as found for the isotopologues of CO, e.g., $C^{18}O$ 2–1 or 3–2 (Chapter 2). For molecular outflows the line wings of various ^{12}CO transitions have been efficiently used as tracers of their properties (Cabrit & Bertout 1992; Bontemps et al. 1996; Hogerheijde et al. 1998; Bachiller & Tafalla 1999; Hatchell et al. 1999, 2007a). The denser regions of the protostellar envelope needs to be probed with emission lines with a high critical density, such as HCO^+ 4–3. The spatial distribution of this line has also proven to be an excellent tracer for ‘false’ embedded sources (Chapter 2). The warm gas ($T > 50$ K), which can be present in both the molecular outflow and the inner region of the protostellar envelope, can only be traced by high- J CO transition, which have $E_{up} > 50$ K for J_{up} (Hogerheijde et al. 1998).

Due to a lack of submillimeter telescopes at high dry sites in the southern hemisphere, data on southern YSOs are still limited. Southern clouds, such as Chamaeleon, Corona Australis, Vela or Lupus, are much less studied than their counterparts in the northern sky, such as Ophiuchus, Taurus and Perseus, where such observations have been readily available for over a decade (e.g., Hogerheijde et al. 1997; Motte et al. 1998; Hogerheijde et al. 1998; Johnstone et al. 2000; Jørgensen et al. 2002; Nutter et al. 2005, 2008).

With the development the *Atacama Large Millimeter/Submillimeter Array* (ALMA) in Chajnantor, Chile, surveys of sources in southern star-forming clouds will be undertaken at high resolution ($\leq 1''$) at a wide range of frequencies, and are expected to reveal much about the inner structure of protostars and their circumstellar disks. However, such observations rely heavily on complementary single-dish observations for interpretation. Apart from providing the necessary information about the structure on larger scales, single-dish studies of low-mass star formation in the southern sky will also put the results obtained from studies that have focussed on the northern clouds in perspective. Two regions have proven especially interesting. The Chamaeleon I cloud ($D=130$ pc, Dec = -77°), first observed with *IRAS* and the *Infrared Space Observatory* (ISO) and included in the guaranteed time and ‘Cores to disks’ (c2d) Legacy programs on *Spitzer* (Persi et al. 2000; Evans et al. 2003; Damjanov et al. 2007; Luhman et al. 2008) was found to contain some embedded sources, especially around the Cederblad region (Persi et al. 2000; Lehtinen et al. 2001; Hiramatsu et al. 2007). Corona Australis is a nearby star-forming region ($D=170$ pc, see Knude & Høg (1998); Dec = -36°), well-known for the central Coronet cluster near the R CrA star (Loren 1979; Taylor & Storey 1984; Wilking et al. 1986; Brown 1987). Large-scale $C^{18}O$ 1–0 maps show that it contains about $50 M_\odot$ of gas and dust (Harju et al. 1993). Many surveys have been undertaken in the IR (e.g., Wilking et al. 1986, 1997; Olofsson et al. 1999; Nisini et al. 2005), but only a few studies mapped this region at submillimeter wavelengths (Chini et al. 2003; Nutter et al. 2005). Although Corona Australis has only a few protostars with rising infrared SEDs, the cloud does contains the most massive protostars in the neighbourhood of the Sun ($D < 200$ pc) with luminosities of up to $20 L_\odot$.

The newly commissioned Atacama Pathfinder EXperiment (APEX)¹ telescope (Güsten et al. 2006), provides access to the atmospheric windows in the submm wavelength regime ranging from 200 to 900 μm with a wide variety of receivers under excellent weather conditions. Located at the Chajnantor Plateau in Northern Chile, it allows observations of the entire southern sky.

Table 4.1 — Overview of the observations.

Line		Instrument	Cloud ^a	Note
¹² CO	3–2	2a	Cha, CrA, Iso.	
	map	2a	Various	80'' × 80''
	4–3	FLASH-I	Cha, Iso	
	map	FLASH-I	Cha, Iso	40'' × 40''
	7–6	FLASH-II	Cha, Iso	
	map	FLASH-II	Cha, Iso	40'' × 40''
C ¹⁸ O	3–2	2a	Cha, CrA, Iso.	
HCO ⁺	4–3	2a	Cha, CrA, Iso.	
	map	2a	Various	80'' × 80''
H ¹³ CO ⁺	4–3	2a	Cha, CrA, Iso.	

^a Cha = Chamaeleon, CrA = Corona Australis and Iso. = Isolated sample

¹This publication is based on data acquired with the Atacama Pathfinder Experiment (APEX) with programs E-77.C-0217, E-77.C-4010 and E-78.C-0576. APEX is a collaboration between the Max-Planck-Institut für Radioastronomie, the European Southern Observatory, and the Onsala Space Observatory.

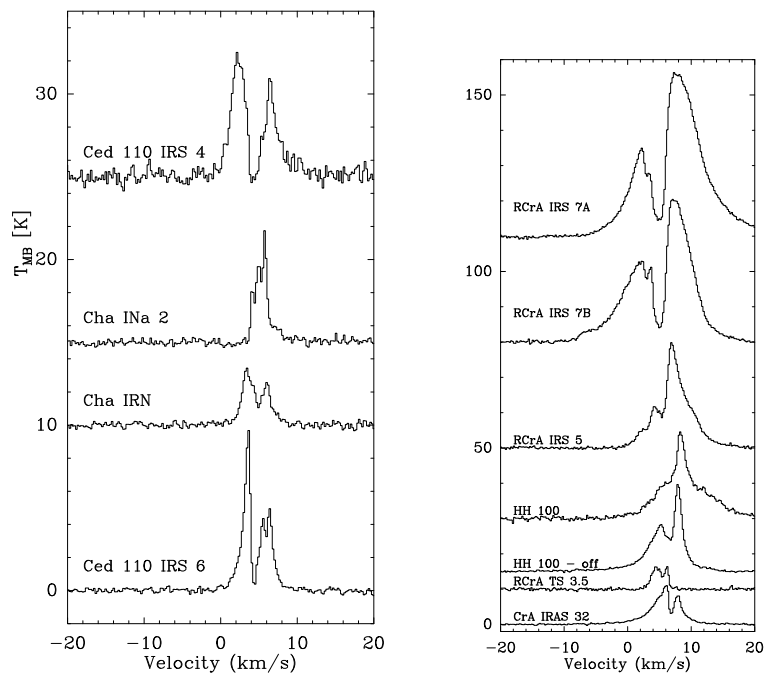


Figure 4.1 — ^{12}CO 3-2 spectra of the sources in Chamaeleon (*left*) and Corona Australis (*right*).

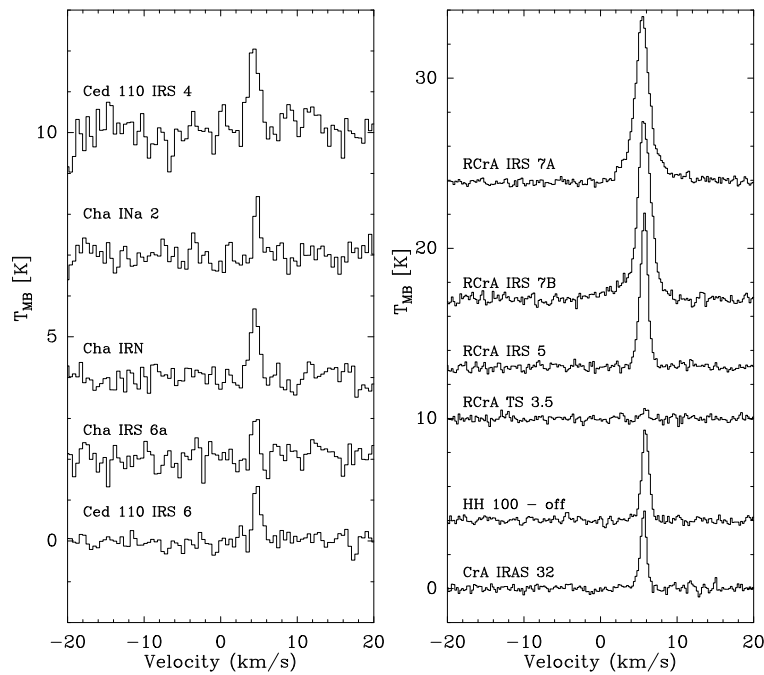


Figure 4.2 — C^{18}O spectra of the sources in Chamaeleon (*left*) and Corona Australis (*right*).

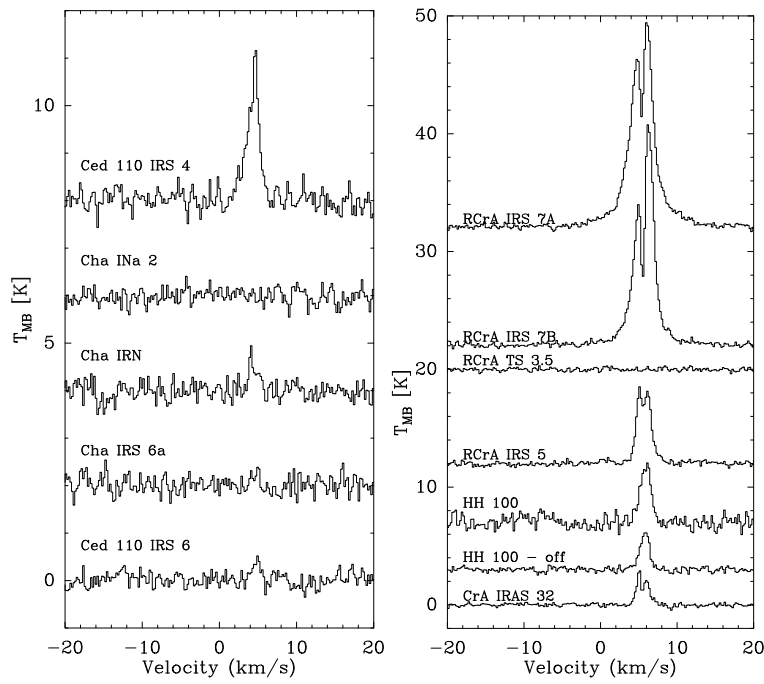


Figure 4.3 — HCO⁺ 4-3 spectra of the sources in Chamaeleon (*left*) and Corona Australis (*right*).

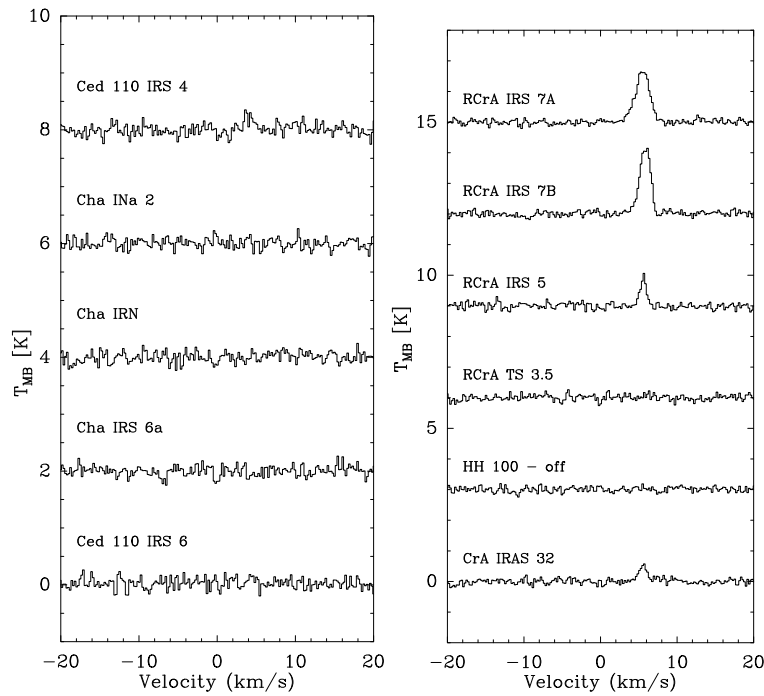


Figure 4.4 — H¹³CO⁺ 4-3 spectra of the sources in Chamaeleon (*left*) and Corona Australis (*right*).

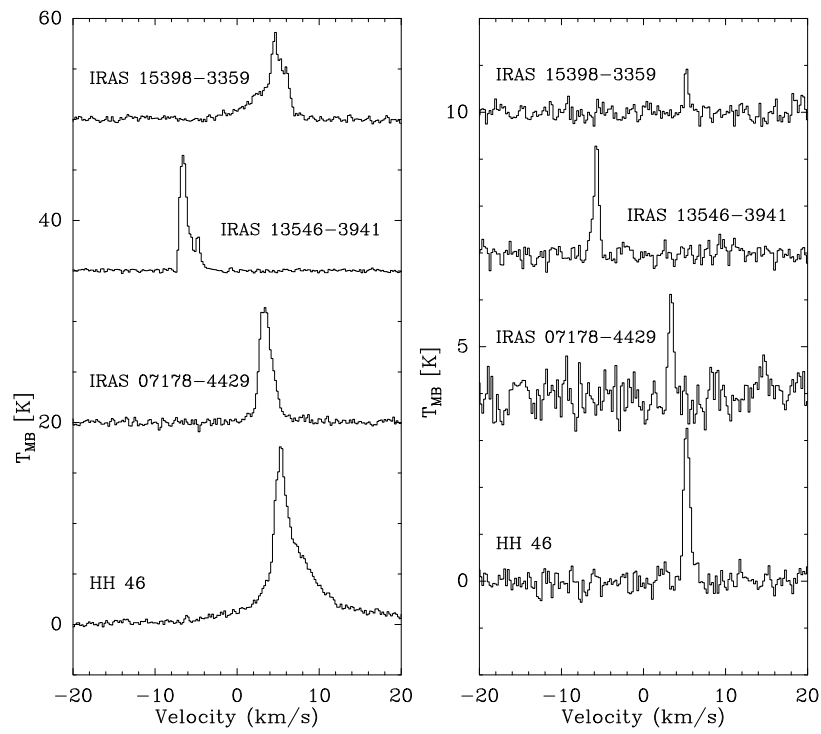


Figure 4.5 — ^{12}CO 3-2 (left) and C^{18}O 3-2 (right) spectra for the isolated sample.

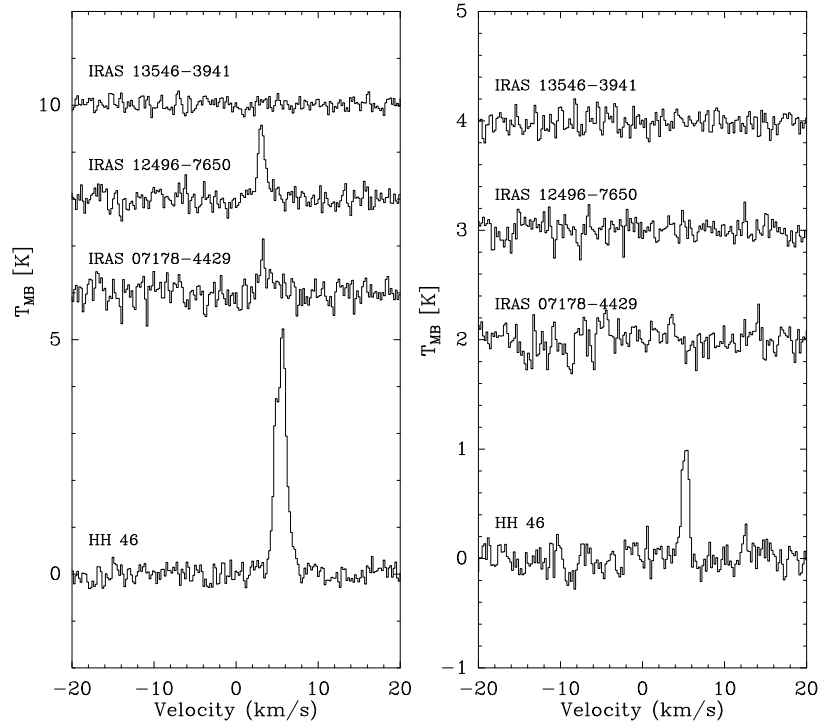


Figure 4.6 — HCO^+ 4–3 (*left*) and H^{13}CO^+ 4–3 (*right*) spectra for the isolated sample.

In this chapter we present results of CO and HCO^+ observations of a sample of embedded sources in the southern sky, with a focus on the Chamaeleon I and Corona Australis clouds, to identify basic parameters such as column density, presence and influence of outflowing material, presence of warm and dense gas and the influence of the immediate surroundings, in preparation for future Herschel and ALMA surveys or in-depth high resolution interferometric observations. In section § 4.2 we present the observations, for which the results are given in § 4.3 with a distinction between the clouds and isolated sources. Both the single spectra (§ 4.3.1) and maps (§ 4.3.2) are presented. In § 4.4 we perform the analysis of the observations, with the final conclusions given in § 4.5.

4.2 Observations

Observations of embedded sources in Chamaeleon, Corona Australis and a few isolated sources were carried using the APEX-2a (345 GHz, denoted as ‘2a’ hereafter Risacher et al. 2006) and the First Light APEX Submillimeter Heterodyne (460/800 GHz, denoted as FLASH hereafter Heyminck et al. 2006)) instruments mounted on APEX between August 2005 and July 2006. FLASH allows for the simultaneous observation of molecular lines in the 460 GHz and 800 GHz atmospheric windows. Typical beam sizes of APEX are $18''$, $14''$ and $8''$ for 345, 460 and 805 GHz with respective main beam efficiencies of 0.73, 0.6 and 0.43

Sources were selected for their far-IR and sub-mm properties and chosen from a sample of sources with rising infrared SEDs (Class I) observed with the InfraRed Spec-

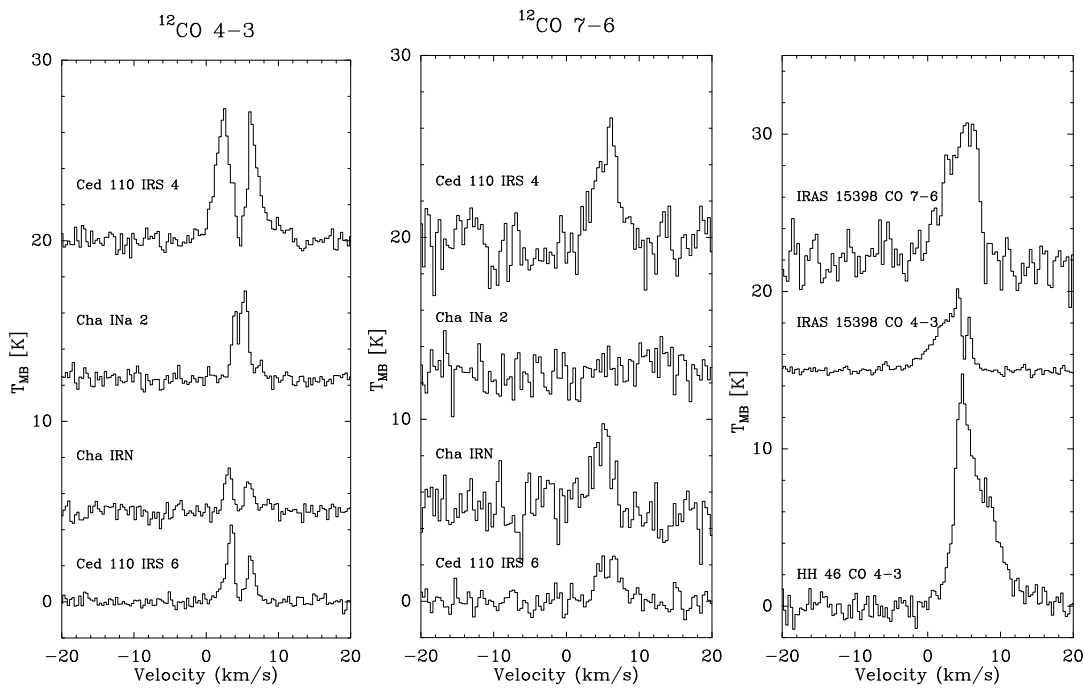


Figure 4.7 — ^{12}CO 4–3 (left) and 7–6 (middle) spectra of the sources in Chamaeleon, as well as the spectra of HH 46 and IRAS 15398-3359 taken with FLASH(right).

trograph (IRS) on *Spitzer* in the scope of the ‘Cores to disks’ (c2d) program (Evans et al. 2003), supplemented with other known Class I sources. Within the Chamaeleon I cloud, most sources are located in the Cederblad region (Persi et al. 2000; Hiramatsu et al. 2007). Cha IRS 6a is located $6''$ away from Ced 110 IRS 6 (\sim half a beam). The embedded YSOs in the Corona Australis region are mostly located in the small region around R CrA, called the Coronet (Wilking et al. 1986, 1997; Nutter et al. 2005), but two sources are located in the R CrA B region. In addition to the sources in these two star-forming regions, five embedded sources in other clouds are included. HH 46 is a Class I protostar famous for its well-characterized outflow (Heathcote et al. 1996; Stanke et al. 2006; Noriega-Crespo et al. 2004; Velusamy et al. 2007). IRAS 12496-7650 is one of the brightest protostars in the southern hemisphere and a potential driving source of HH 54 (Chapter 3). IRAS 07178-4429, IRAS 13546-3941 and IRAS 15398-3359 are also included (e.g., Bourke et al. 1995; Shirley et al. 2000; Haikala et al. 2006). Table 4.2 lists the sources of our sample and their properties.

Using 2a, observations were taken of the ^{12}CO 3–2 (345.796 GHz), C^{18}O 3–2 (329.331 GHz), HCO^+ 4–3 (356.734 GHz) and H^{13}CO^+ 4–3 (346.998 GHz) molecular lines of the entire sample at the source position. The ^{12}CO 4–3 (461.041 GHz) and 7–6 (806.652 GHz) transitions were observed with FLASH for the Chamaeleon I sample (Ced 110 IRS 4, Ced 110 IRS 6, Cha INa 2, Cha IRN, HH46, IRAS 12496-7650 and IRAS 15398-3359. The single spectra of CO 3–2, C^{18}O 3–2, CO 4–3 and 7–6 for IRAS 12496-7650 can be found in Chapter 3, but the integrated intensities are included here for completeness. Similarly, HH 46 is discussed more extensively in Chapter 5.

The 2a observations were smoothed to a spectral resolution of 0.2 km s^{-1} . The RMS

Table 4.2 — Source sample

Source	RA (h m s) [J2000]	Dec (d m s) [J2000]	Dist. (pc)	Lum. (L_{bol})	Ref. ^a	Notes ^c
Chamaeleon I						
Ced 110 IRS 4	11 06 47.0	−77 22 32.4	130	1	1,2,3	ISO-Cha 84
Ced 110 IRS 6	11 07 09.6	−77 23 04.3	130	0.6	1,3	ISO-Cha 92
Cha IRS 6a	11 07 09.9	−77 23 06.3	130	0.8	4	ISO-Cha 92+
Cha IRN	11 08 37.1	−77 43 51.0	130	5	3	ISO-Cha 150
Cha INa 2	11 09 36.6	−76 33 39.0	130	0.6	5	
Corona Australis						
RCrA IRS 5	19 01 48.0	−36 57 21.6	170	2	6	
HH 100 ^b	19 01 50.7	−36 58 10	170	15	6	
RCrA IRS 7a	19 01 55.2	−36 57 21.0	170	3.3 ^d	7	SMA 2
RCrA IRS 7b	19 01 56.2	−36 57 27.0	170	17 ^d	7	SMA 1
RCrA TS 3.5	19 02 07.1	−36 53 26.2	170	-		
CrA IRAS 32	19 02 58.7	−37 07 34.5	170	3.4		ISO-CrA 182
Isolated						
HH 46	08 25 43.8	−51 00 35.6	450	16	8,9,10	BHR 36
IRAS 07178-4429	07 19 21.8	−44 34 55.1	-	-	10,11	CG1/BHR 17
IRAS 12496-7650	12 53 17.2	−77 07 10.6	250	50	12	DK Cha, Cham II
IRAS 13546-3941	13 57 42.2	−39 56 21.0	630	-	10,11	CG12/BHR 92
IRAS 15398-3359	15 43 01.3	−34 09 15.0	130	0.92	2,13	B228, Lupus

^a References: 1. Luhman et al. (2008); 2. Froebrich (2005); 3. Persi et al. (2000); 4. Persi et al. (2001); 5. Persi et al. (1999); 6. Nisini et al. (2005); 7. Groppi et al. (2007); 8. Noriega-Crespo et al. (2004); 9. Velusamy et al. (2007); 10. Bourke et al. (1995); 11. Santos et al. (1998); 12. Chapter 3; 13. Evans et al. (2005)

^b Observations of HH 100 was erroneously pointed at these coordinates: RA 19h01m49.1s, Dec -36d58m16.0s. See text for further discussion.

^c e.g. other names and cloud location.

^d The estimated luminosities of the two RCrA IRS 7 sources are not well constrained, due to confusion of the total integrated flux at (sub-)mm wavelengths. The total luminosity of both sources ($20 L_{\odot}$) was used in the characterisation.

was found to be 0.15-0.2 K in 0.2 km s⁻¹ channels for HCO⁺ 4-3, ¹²CO 3-2 and C¹⁸O 3-2. H¹³CO⁺ spectra were rebinned to 0.5 km s⁻¹ for deriving the (upper limits on) integrated intensity. The RMS for the CO 4-3 observations is 0.35 K and for CO 7-6 1.4 K in channels of 0.3 km s⁻¹, significantly higher than the 2a observations.

In addition to single spectra, small (up to 80'' × 80'') maps were taken using the 2a instrument of ¹²CO 3-2 and HCO⁺ 4-3 for HH 46, Ced 110 IRS 4, IRAS 07178-4429, CrA IRAS 32, RCrA IRS 7, HH 100 and IRAS 13546-3941. With FLASH, similar maps were taken of the Cham. I sample, HH 46 and IRAS 12496-7650 in ¹²CO 4-3 and 7-6, but not of the RCrA sample. See Table 4.1. The RMS in the taken maps is generally a factor 5 or more higher than the single spectra. E.g., for the maps taken with the FLASH instrument the noise levels are on the order of 0.9 Kelvin for CO 4-3 in a 0.7

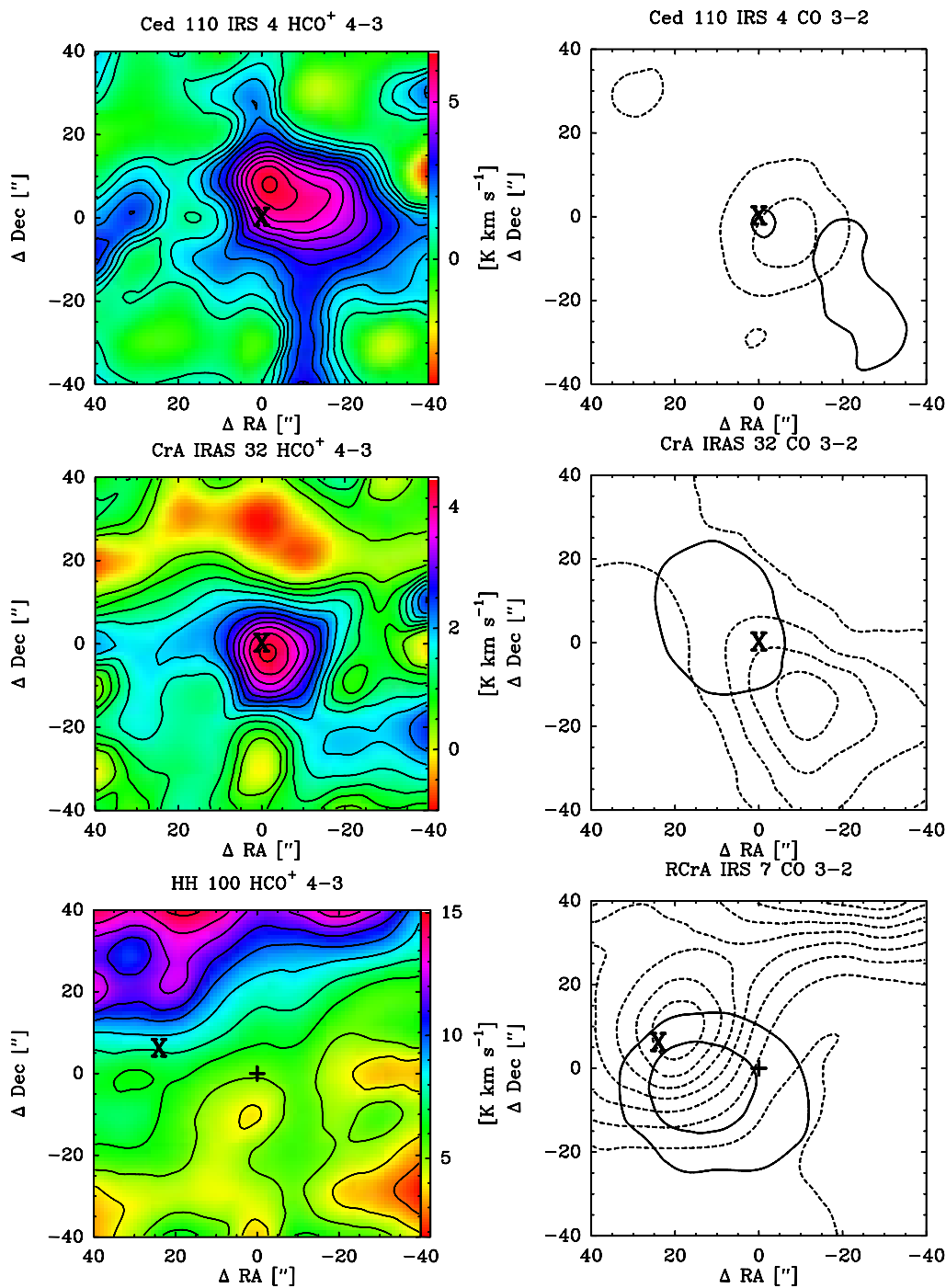


Figure 4.8 — HCO^+ 4-3 (left) and CO 3-2 (right) maps of Ced 110 IRS 4 (top), CrA IRAS 32 (middle) and HH 100 (bottom). The maps are $80'' \times 80''$ in size. HCO^+ 4-3 is integrated over the entire line. CO 3-2 shows the red- (dashed lines) and blue-shifted (solid lines) emission, derived by subtracting a gaussian fitted to the quiescent component. Contour levels for the CO 3-2 are at $3\sigma, 6\sigma, 9\sigma, \dots$. The IR position of HH 100 is marked with a 'X', while the pointed position HH100-off is marked with a plus sign.

km s⁻¹ channels, significantly higher than the noise levels found in the single spectra (0.35 K in a 0.3 km s⁻¹).

Observations were taken under normal to good weather conditions with the precipitable water vapor ranging from 0.4 to 1.0 mm. For both instruments, new Fast Fourier Transform Spectrometer (FFTS) units were used as backends, with over 16,000 channels available (Klein et al. 2006), allowing flexible observations up to a resolution of 60 kHz (0.05 km s⁻¹). Pointing was checked and found to be within 3'' for the 2a instrument. The pointing of FLASH was not as accurate with excursion up to 6'' for these observations. Calibration was done on hot and cold loads as well as on the sky. Total calibration errors are of the order of 20%. Offpositions of 1,800'' to 5,000'' in azimuth were selected. For some sources, emission in the CO 3–2 line in the off-position was seen, but this did not exceed 5 % of the source emission. During the reduction, it was discovered that the original pointing of HH 100 was incorrect and differed by ~20'' from the IR position. Throughout this chapter, the incorrect position will be referred to as 'HH 100-off', while 'HH 100' will refer to the actual source. Single-pixel spectra for this source at the incorrect position are shown, as they probe the cloud material in the RCrA region, but the true position of the source is included in the maps.

4.3 Results

4.3.1 Single spectra at source position

Spectra are shown in Figs. 4.1 - 4.6 (all spectra taken with 2a), and Fig. 4.7 (spectra taken with FLASH). The integrated intensities and peak temperatures at the source positions are given in Tables 4.3 (HCO⁺ and H¹³CO⁺ with 2a) and 4.4 (CO and C¹⁸O observations with 2a and FLASH observations).

In general the 3–2 line of ¹²CO cannot be fitted with single gaussians, because self-absorption is found at or around the source velocity V_{LSR} . This absorption is especially deep in RCrA IRS 7a and 7b with $\tau \gg 1$. Due to this absorption, the total integrated line strength of ¹²CO spectra is not a useful in the analysis of the quiescent molecular gas. For all sources in Corona Australis, except RCrA TS 3.5, and emission can be seen in the line wings of ¹²CO 3–2, up to 10-15 km s⁻¹ from the central source velocity. Line wings are seen in the line profiles of both HCO⁺ and C¹⁸O for RCrA IRS 7a and 7b. Due to the high peak temperatures of C¹⁸O, the assumption that C¹⁸O is optically thin at these location may not apply. See § 4.4.2 for further analysis of C¹⁸O.

Outflowing gas is seen for most spectra from sources in Corona Australis and some sources in Chamaeleon show signs of outflowing gas as well. Outflows will be further discussed in § 4.4.3. Self-absorption is seen in CO 4–3 for all sources, but is interestingly absent in all three detected CO 7–6 lines in Ced 110 IRS 4, Cha INa 2 and Cha IRN.

All C¹⁸O 3–2 lines can be fitted with single gaussians. The HCO⁺ lines, which can be used to trace the dense gas if one corrects for the contribution from the cloud, cover the widest range of antenna temperatures and include a variety of line profiles. For Cha INa2, no HCO⁺ 4–3 is seen down to 0.2 K, but the spectrum for RCrA IRS 7A peaks at $T_{\text{MB}}=18$ K. Note that the brightest spectra in Corona Australis all show self-absorption, indicating that the HCO⁺ 4–3 is optically thick. In addition, Ced 110 IRS 4, RCrA IRS 7a and 7b and CrA IRAS 32 have line profiles suggesting dense outflowing

gas. The H^{13}CO^+ 4–3 is only detected for 5 sources (RCrA IRS 7a and 7b, RCrA IRS 5, CrA IRAS 32 and Ced 110 IRS 4), although the detection of Ced 110 IRS 4 is only 3.4σ .

By fitting gaussian profiles to the optically thin lines of H^{13}CO^+ (preferred if detected) or C^{18}O , the systemic velocities of the source can be determined with an accuracy of 0.1 km s^{-1} .

All lines of sources in Corona Australis are significantly brighter than those seen in Chamaeleon. The sole exception is RCrA TS 3.5 which is only detected in ^{12}CO 3–2 and HCO^+ 4–3. C^{18}O intensities range from <0.3 (RCrA TS 3.5) to 23.0 K km s^{-1} (RCrA IRS 7b).

The embedded sources in Chamaeleon show weaker emission lines than their counterparts in Corona Australis, as can be seen from the intensity scales of the CO and HCO^+ figures. ^{12}CO spectra are self-absorbed for all sources, indicating that the lines are optically thick. C^{18}O emission is detected for all sources in Chamaeleon, with integrated intensities not greater than 3 K km s^{-1} . No H^{13}CO^+ is seen for any of the sources, while the main isotopologue HCO^+ is only detected for Ced 110 IRS 4 and Cha IRN with $>3\sigma$.

The CO 4–3 observations show detections for all sources, with peak temperatures ranging from $\sim 4\text{ K}$ for Cha IRN to $\sim 7\text{ K}$ for Ced 110 IRS 4. At 800 GHz, only Ced 110 IRS 4, Cha IRN and Ced 110 IRS 6 are detected in CO 7–6, with peak temperatures ranging from $\sim 3\text{ K}$ for Cha IRN to $\sim 10\text{ K}$ for Ced 110 IRS 4.

For the isolated sources of our sample clear detections in CO, HCO^+ and their isotopologues are found for HH 46 and IRAS 12496-7650. Line profiles also show outflow emission for both sources. IRAS 15398-3359 is detected in all its observed spectra (CO and C^{18}O only), and strong blue-shifted outflow emission is seen in all observations of ^{12}CO , regardless of the transition. Both IRAS 07178-4428 and IRAS 13546-3841 are detected in ^{12}CO 3–2 and C^{18}O 3–2, but only IRAS 07178-4428 is detected in HCO^+ 4–3.

4.3.2 Maps

The maps of the total integrated intensities of HCO^+ 4–3 can be found in Fig. 4.8 and 4.9, alongside outflow maps of ^{12}CO 3–2. No HCO^+ or outflowing gas was detected in the maps of IRAS 07178-4429 and IRAS 13546-3941. The only CO 7–6 maps that showed a detection outside the center of the maps in the CO 7–6 line were Ced 110 IRS 4 (§ 4.4.5.6) and HH 46 (§ 4.4.5.7).

The HCO^+ 4–3 and CO 3–2 maps for Ced 110 IRS 4 and CrA IRAS 32 (See Fig. 4.8) show spatially resolved cores, centered on the known IR position. For both sources, outflow emission is seen originating at the source position. The maps around RCrA IRS 7a and 7b (Fig. 4.9, sources marked with X and centered on RCrA IRS 7a) show a single core in the HCO^+ map that is almost $60''$ in size. However, the HCO^+ peaks only on RCrA IRS 7a, with no indication of HCO^+ emission associated with the RCrA IRS 7b source. In addition, the ^{12}CO 3–2 outflow is also centered on RCrA IRS 7a, suggesting it as the driving source. HH 100 (Fig. 4.8) shows no HCO^+ 4–3 core, but does have outflowing gas in the CO 3–2 map, originating at the IR position (marked with a X). HH 46 (Fig. 4.9) shows a nearly circular core in HCO^+ , but a strongly outflow-dominated emission profile in CO 3–2, with much stronger red-shifted than blue-shifted emission. IRAS 07178-4429 and IRAS 13546-3941 have no associated HCO^+ emission in any

off-position down to 0.5 K km s^{-1} in 0.9 km s^{-1} channels. The integrated intensity on source is 1.0 K km s^{-1} for IRAS 07178-4429, but no line was detected down to 0.15 K km s^{-1} on source for IRAS 13546-3941. The CO 4–3 integrated intensity maps show elongated spatial profiles for Ced 110 IRS 4, Ced 110 IRS 6 and Cha IRN, but no peak for Cha INa 2. IRAS 12496-7650 shows a round core, dominated by outflow emission (See § 4.4.5.1)

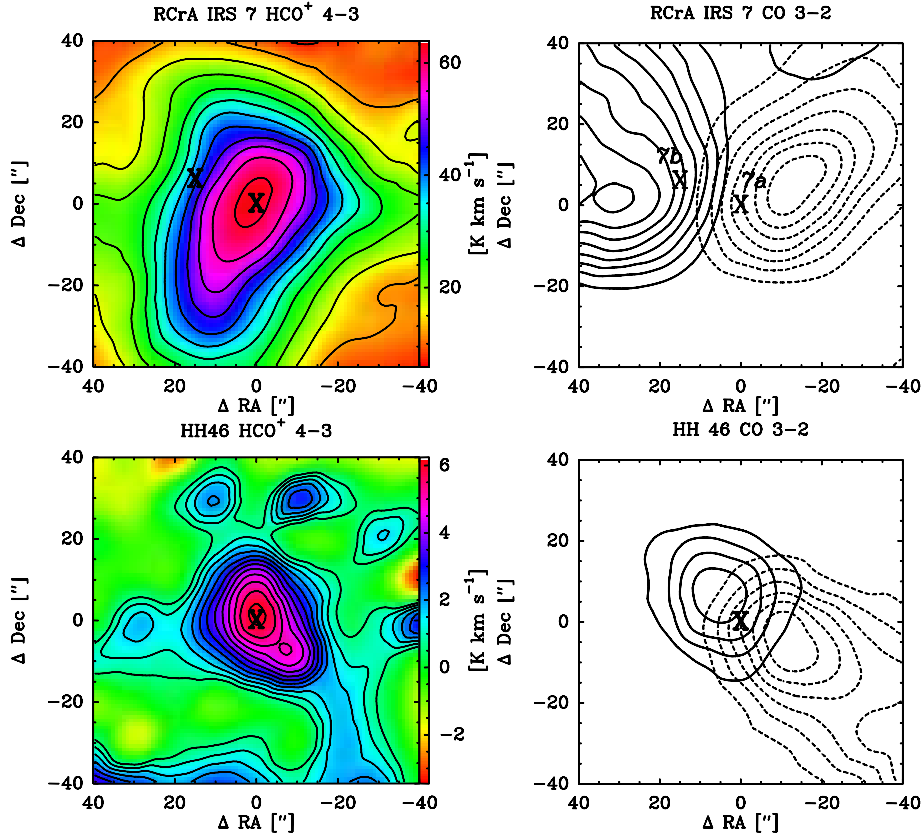


Figure 4.9 — HCO^+ 4–3 (left) and CO 3–2 (right) maps of RCrA IRS 7 (top) and HH 46 (bottom). The maps are $80'' \times 80''$ in size. HCO^+ 4–3 is integrated over the entire line. CO 3–2 shows the red- (dashed lines) and blue-shifted (solid lines) emission, derived by subtracting a gaussian fitted to the quiescent component. Contour levels for the CO 3–2 are at $3\sigma, 6\sigma, 9\sigma, \dots$. Both RCrA IRS 7a and IRS 7b are shown with X in the CO map, but the map is centered on RCrA IRS 7a.

4.4 Analysis

4.4.1 Envelope properties

Assuming the (sub-)mm emission is dominated by the cold dust in the protostellar envelope, the mass of a embedded YSO can be derived from the continuum observations (Shirley et al. 2000; Jørgensen et al. 2002). Using the recently released SCUBA Legacy archive (Di Francesco et al. 2008), an envelope mass was derived for Corona Australis (Nutter et al. 2005). Henning et al. (1993) observed fluxes at 1.3 mm for a large sample in Chamaeleon using the SEST, which are used here to constrain the masses of the very

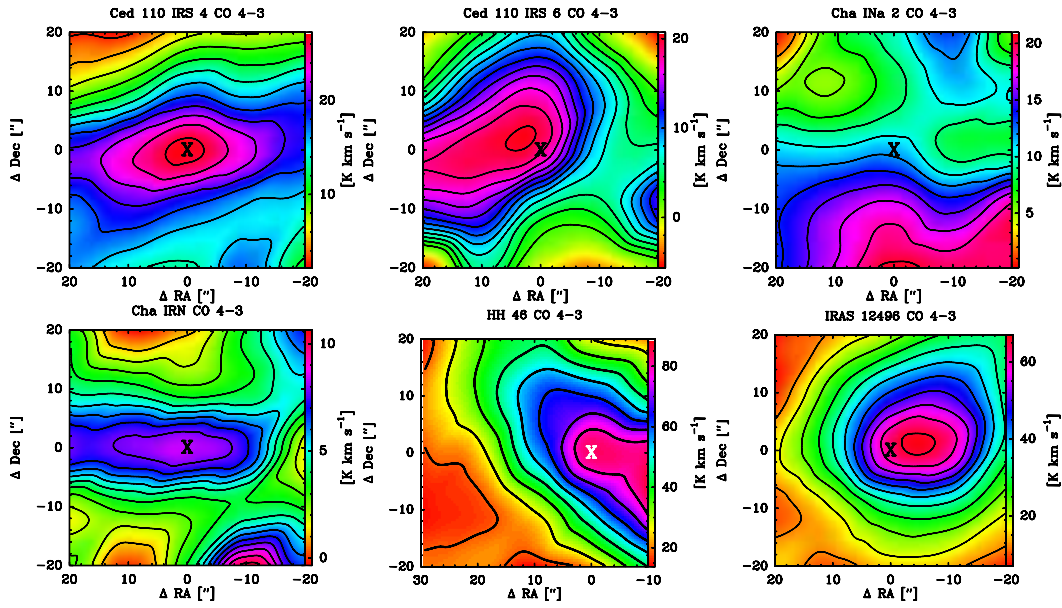


Figure 4.10 — CO 4–3 integrated intensity maps taken with FLASH of Ced 110 IRS 4, Ced 110 IRS 6 and Cha INa2 (*top row*), and Cha IRN, HH 46 and IRAS 12496-7650 (*bottom row*). Note that the noise levels in these maps are higher than in the spectra given in Fig. 4.7. Source positions are marked with ‘X’

southern sources and a dust emissivity $\propto \nu^{-3.5}$. All masses were derived using the relation

$$M_{tot} = S_{\nu} D^2 / \kappa_{\nu} B_{\nu}(T_d) \quad (4.1)$$

assuming an isothermal sphere of 20 K, a gas-to-dust ratio of 100 and a dust emissivity κ_{ν} of $0.02 \text{ cm}^2 \text{ g}^{-1}$ from (column 5, Ossenkopf & Henning 1994). The mass of HH 46 is estimated at $\sim 5 M_{\odot}$ using new LABOCA observations and radiative transfer modelling (Chapter 5) No mass could be derived for Cha IRS 6a, RCrA TS 3.5, IRAS 07178-4429, Cha INa2 and IRAS 13546-3941 as they were not detected or observed. The estimated envelope masses are given in Table 4.5.

With the assumption that H^{13}CO^+ 4–3 and C^{18}O 3–2 emission is optically thin, one can estimate the column densities of these molecules in the protostellar envelope. In this calculation, an excitation temperature of 20 K is adopted for the envelope and cloud material. Table 4.5 gives the column densities of H_2 , C^{18}O and H^{13}CO^+ , where the H_2 column density is derived from the C^{18}O column density assuming a $\text{H}_2/\text{C}^{18}\text{O}$ ratio of 5.5×10^6 (Wilson & Rood 1994). The H_2 column densities range from a few times 10^{22} cm^{-2} in Chamaeleon to a few times 10^{23} cm^{-2} in Corona Australis, all in a $18''$ beam. However, freeze-out of CO onto the interstellar grains make the adopted ratio of H_2 over CO uncertain. In very cold regions ($T < 15 \text{ K}$), abundances can be as much as two orders of magnitude lower than the assumed ISM abundance of 10^{-4} . For a more in-depth discussion about the influence of freeze-out, see Jørgensen et al. (2002).

The isotopologue observations of C^{18}O and H^{13}CO^+ also allow for an estimate of the average optical depth τ in the CO 3–2 and HCO^+ 4–3 lines (Table 4.5). Only quiescent emission is taken into account. Values range from $\tau = 4.5$ to < 2.3 for the ^{12}CO 3–2

Table 4.3 — HCO⁺ and H¹³CO⁺ results.

Source	HCO ⁺ 4-3		H ¹³ CO ⁺ 4-3		V_{LSR}^a (km s ⁻¹)
	$\int T_{\text{MB}}dV$ (K km s ⁻¹)	T_{MB} (K)	$\int T_{\text{MB}}dV$ (K km s ⁻¹)	T_{MB} (K)	
Chamaeleon					
Ced 110 IRS 4	4.0	3.1	0.38	0.25	4.3
Ced 110 IRS 6	0.5	0.4	<0.06	-	4.8
Cha IRS 6a	<0.2	-	<0.06	-	4.6
Cha IRN	0.87	0.95	<0.06	-	4.5
Cha INa 2	<0.2	-	<0.06	-	4.8
Corona Australis					
CrA IRAS 32	4.1	2.9	0.72	0.53	5.6
HH 100-off	4.8	3.2	<0.06	-	5.9
RCrA IRS 5	14.2	7.0	0.96	0.86	5.7
RCrA IRS 7a	63.7	17.4	3.8	1.6	5.5
RCrA IRS 7b	49.0	18.7	3.8	2.2	5.7
RCrA TS 3.5	<0.2	-	<0.06	-	5.9
Isolated					
HH 46	8.4	5.4	1.1	1.0	5.3
IRAS 07178-4429	1.0	0.6	< 0.08	-	3.4
IRAS 12496-7650	1.9	1.5	<0.06	-	1.9
IRAS 13546-3941	< 0.12	-	<0.06	-	-5.7
IRAS 15398-3359	-	-	-	-	5.2

^a The rest velocity V_{LSR} was determined by fitting gaussians to either the H¹³CO⁺ 4-3 (preferred) or C¹⁸O 3-2 lines (see Table 4.4).

transition and 2.5 to <0.3 for the HCO⁺ 4-3 transition. Interestingly, optical depths of ¹²CO are systematically higher in the Chamaeleon sources (mean $\tau = 4.3$) than in the Corona Australis (mean $\tau = 3.4$). For sources where outflow emission is detected, this optical depth estimate is a lower limit, since it may include optically thin outflow emission close to the line centers of CO 3-2 and HCO⁺ 4-3 lines.

A more likely possibility for the lower optical depths is that in the RCrA region, C¹⁸O 3-2 cannot be assumed to be optically thin. Test calculations using the RADEX radiative transfer code (van der Tak et al. 2007) indeed show that for these integrated intensities and derived column densities, C¹⁸O 3-2 has optical depths between 0.5 and 3 for typical cloud temperatures and densities of 15 K and 10⁴ cm⁻³ and various column densities between 10²² cm⁻² to 10²⁴ cm⁻². The region may also be warmer than this assumed here, due to the presence of the bright star R CrA. The low limit to the optical depth of HH 100-off shows that the HCO⁺ 4-3 emission from the RCrA cloud is optically thin.

Recent results in the Ophiuchus cloud show that at many locations throughout L 1688, multiple foreground layers are present, reddening more evolved sources (Chapter 2). The line profiles of C¹⁸O 3-2 could only be fitted with multiple gaussians, indicating the presence of multiple layers. In our southern sample, all C¹⁸O 3-2 lines

Table 4.4 — ^{12}CO and C^{18}O results

Source	^{12}CO 3–2		C^{18}O 3–2		CO 4–3		CO 7–6	
	$\int T_{\text{MB}}dV$ (K km s $^{-1}$)	T_{MB} (K)	$\int T_{\text{MB}}dV$ (K km s $^{-1}$)	T_{MB} (K)	$\int T_{\text{MB}}dV$ (K km s $^{-1}$)	T_{MB} (K)	$\int T_{\text{MB}}dV$ (K km s $^{-1}$)	T_{MB} (K)
Chamaeleon								
Ced 110 IRS 4	30.7	7.5	3.7	2.1	29.8	7.5	24.8	6.9
Ced 110 IRS 6	20.0	9.3	1.6	1.4	9.7	4.9	8.8	2.5
Cha IRS 6a	-	-	1.2	1.1	-	-	-	-
Cha IRN	11.1	3.5	2.3	1.8	6.5	3.0	14.0	5.2
Cha INa 2	11.3	6.7	1.3	1.6	10.0	4.7	<1.5	-
Corona Australis								
CrA IRAS 32	51.6	11.0	4.6	4.4	-	-	-	-
HH 100-off	102.6	24.7	6.3	5.2	-	-	-	-
RCrA IRS 5	144.2	29.9	11.4	8.7	-	-	-	-
RCrA IRS 7a	406.0	46.4	22.5	8.9	-	-	-	-
RCrA IRS 7b	332.7	40.4	23.0	10.0	-	-	-	-
RCrA TS 3.5	16.8	6.4	<0.3	-	-	-	-	-
Isolated								
HH 46 ^b	82.5	19.4	3.2	3.3	70.5	14.9	46.5	8.6
IRAS 07178-4429	24.0	11.4	1.7	2.3	-	-	-	-
IRAS 12496-7650 ^a	92.8	25	9.2	1.9	90.0	23	43.7	19.2
IRAS 13546-3941	16.3	11.4	1.8	2.3	-	-	-	-
IRAS 15398-3359	25.8	9.0	0.5	1.2	19.9	5.6	45.3	8.5

^a from Chapter 3.^b CO 7–6 from Chapter 5.

Table 4.5 — Overview of the envelope properties^a.

Source	M_{envelope} (M_{\odot})	$N(\text{H}_2)$ (10^{22} cm^{-2})	$N(\text{C}^{18}\text{O})$ (10^{15} cm^{-2})	$N(\text{H}^{13}\text{CO}^+)$ (10^{15} cm^{-2})	$\tau_{\text{CO}3-2}$	τ_{HCO^+4-3}
Chamaeleon						
Ced 110 IRS 4	0.07	5.0	8.3	1.4	4.2	1.9
Ced 110 IRS 6	0.04	3.3	5.5	-	-	-
Cha IRS 6a	-	0.26	0.43	-	-	-
Cha IRN	0.17	4.3	7.2	-	4.7	<1.5
Cha INa 2	-	3.8	6.3	-	4.1	-
Corona Australis ^b						
CrA IRAS 32	0.8	10.5	17.5	3.0	3.9	2.5
HH100-off	1.6	12.4	20.7	-	3.5	<0.3
RCrA IRS 5	1.7	20.7	35.1	4.8	3.7	1.6
RCrA IRS 7a	6.3 ^c	21.2	35.3	8.9	3.4	1.4
RCrA IRS 7b	6.3 ^c	23.8	39.7	12.3	3.6	1.7
RCrA TS 3.5	-	-	-	-	<2.3	-
Isolated						
HH 46	5.1	8.1	13.5	6.1	2.9	2.2
IRAS 07178-4429	-	5.5	9.2	-	3.7	<1.6
IRAS 12496-7650	0.4	3.0	5.0	-	<0.8	-
IRAS 13546-3941	-	5.5	9.2	-	4.1	-
IRAS 15398-3359	0.5	1.9	3.2	-	-	-

^a Columns 2, 3, and 4: Column densities of H_2 , C^{18}O and H^{13}CO^+ . The column density of H_2 is derived from the column density of C^{18}O . Columns 5 and 6: Optical depth of the CO 3–2 and HCO^+ 4–3 line.

^b Mass estimates in the RCrA region may be severely overestimated due to presence of cloud material.

^c RCrA IRS 7a and 7b cannot be distinguished in the submillimeter continuum.

can be fitted with single Gaussians indicating that no fore-ground layers are present, in contrast with Ophiuchus (Chapter 2). The fitted velocities can be found in Table 4.3.

4.4.2 Embedded or not?

In recent years, analysis of the physical structure of several Class I sources showed that some embedded sources are in fact not embedded, but either edge-on disks, such as CRBR 2422.8 (Brandner et al. 2000; Pontoppidan et al. 2005), or sources obscured by cloud material or neighbouring protostellar envelopes, such as IRS 46 (Lahuis et al. 2006). Theoretical models from Robitaille et al. (2006) and Crapsi et al. (2008) indeed show that edge-on disks can masquerade as embedded sources in their infrared SED due to the increased reddening. A recent survey of Class I sources in the Ophiuchus L 1688 region (Chapter 2) showed that the concentration of HCO^+ 4–3, combined with integrated intensities of HCO^+ 4–3 of at least 0.4 K km s^{-1} , can be used to identify truly embedded sources. Concentration parameters have been successfully applied in the analysis of submillimeter continuum observations (Johnstone et al. 2001; Walawender et al. 2005; Jørgensen et al. 2007), but rarely on molecular line emission maps. The concentration of HCO^+ is defined as:

$$C_{\text{HCO}^+} = 1 - \frac{1.13B^2 S_{\text{HCO}^+}}{\pi R_{\text{obs}}^2 T_{\text{MB}}}, \quad (4.2)$$

with S_{HCO^+} the spatially and spectrally integrated intensity $\int T_{\text{MB}} dV$ of HCO^+ over the entire envelope with radius R_{obs} , and T_{MB} the integrated intensity in the central beam. The FWHM from the spatial distribution integrated HCO^+ intensity is used as the observed core radius.

Although less reliable due to a lower critical density and contributions from outflows, the quiescent gas emission of CO 4–3, which is associated with the more central regions of protostellar envelopes can serve as a diagnostic of the warm dense gas in the inner envelop as well. The concentration parameters were investigated for Ced 110 IRS 4, CrA IRAS 32, HH 100, RCrA IRS 7, HH 46, IRAS 07178-4429 and IRAS 13546-3941 using spectra of HCO^+ 4–3 and for Ced 110 IRS 4, Ced 110 IRS 6, Cha IRN and Cha INa2 using CO 4–3 spectra. They are listed in Table 4.6. It was found that four sources (HH 100, RCrA IRS 7b, IRAS 07178-4429 and IRAS 13546-3941) have no associated HCO^+ core and thus no concentration. This may indicate that these sources are not embedded, but edge-on disks or background sources. Similarly, Cha INa2 shows no signs of centrally concentrated CO 4–3 emission. Since Cha INa2 has no detected HCO^+ on source, it is thus likely not to be an embedded YSO. All other sources have concentrations of ~ 0.7 and higher, as well as strong HCO^+ fluxes above 0.5 K km s^{-1} associated with the sources, characteristic of embedded sources.

The integrated intensities of the spectra in the off-positions show that it is possible to hide a protostellar envelope with small masses in a more massive molecular cloud with high column densities, as likely is the case for HH 100. RADEX (van der Tak et al. 2007) simulations show that smaller envelopes produce integrated intensities for

both $C^{18}O$ 3–2 and HCO^+ 4–3 emission that are similar to those produced by either the outer regions of heavier envelopes or large ($\sim 10^{23} \text{ cm}^{-2}$) cold cloud column densities. However, emission and concentration associated with the warmer envelope from the CO 4–3 and 7–6, provide a new tracer that is able to identify such envelopes. Both the integrated intensities of CO 4–3 and 7–6 of the quiescent envelope gas are at least a factor 2 brighter than the colder gas in the molecular cloud.

Table 4.6 — HCO^+ 4–3 and CO 4–3 concentrations

Source	C_{HCO^+}	$C_{CO(4-3)}$	Emb. ^b
Chamaeleon			
Ced 110 IRS 4	0.77	0.69	y
Ced 110 IRS 6	-	0.74	y
Cha IRN	-	0.72	y
Cha INa 2	-	n.c. ^a	n
Corona Australis			
CrA IRAS 32	0.78	-	y
HH 100	n.c. ^a	-	y(?) ^c
RCrA IRS 7a	0.68	-	y
RCrA IRS 7b	n.c. ^a	-	n(?) ^c
Isolated			
HH 46	0.79	-	y
IRAS 07178-4429	n.c. ^a	-	n
IRAS 13546-3941	n.c. ^a	-	n

^a n.c. = no core associated with source

^b An indicative conclusion about whether the source is embedded or not.

^c See §4.4.4

Table 4.7 — Temperature constraints of CO line wings ratios.

Source	CO 3–2/4–3		CO 4–3/7–6		T_{outflow} (K) Scenario 1 ^a		T_{outflow} (K) Scenario 2 ^b	
	Red	Blue	Red	Blue	Red	Blue		
Ced 110 IRS 4	1.0	1.2	3.5	-	50	40	170	160
Ced 110 IRS 6	2.2	1.7	-	-	<30	40	50	60
HH46	1.0	1.6-2.0	2.0	-	50	< 40	180	80
IRAS 12496	-	0.8	-	>4	-	50	-	<200
IRAS 15398	-	-	-	0.8	-	100	-	>200

^a Lines thermally excited ($n > n_{\text{cr}}$)

^b Lines subthermally excited (n assumed to be 10^4 cm^{-3})

Table 4.8 — Outflow parameters from the CO 3–2 mapping.

Source	i	Mass ^a (M _⊙)	ΔV_{\max}^b (km s ⁻¹)	R^b (AU)	$t_d^{b,c}$ (yr)	$\dot{M}^{b,d}$ (M _⊙ yr ⁻¹)	$F_{CO}^{a,e}$ (M _⊙ yr ⁻¹ km s ⁻¹)	$L_{\text{kin}}^{a,f}$ (L _⊙)
Red Lobe								
Ced 110 IRS 4	75	1.4e-2	4.0	2.4e3	2.8e3	4.2e-6	4.6e-5	7e-5
CrA IRAS 32	45	6.6e-2	6.3	9.3e3	7.1e3	9.3e-6	1.3e-4	5.5e-4
HH 100	60	3.6e-1	14.7	> 6.1e3	> 2.0e3	< 1.5e-4	< 4.9e-3	< 7.2e-2
RCrA IRS 7	45	1.1e0	23.0	> 1e4	> 2.1e3	< 4.3e-4	< 2.2e-2	< 5.0e-1
HH46	35	4.3e-1	9.5	> 2.5e4	> 1.2e4	< 3.2e-5	< 4.4e-4	< 3.1e-3
Blue Lobe								
Ced 110 IRS 4	75	5.8e-3	-4.2	-	-	-	-	-
CrA IRAS 32	45	1.7e-2	-5.4	4.6e3	4.0e3	4.3e-6	5e-5	1.8e-4
HH 100	60	4.7e-2	-9.7	4.6e3	2.2e3	2.1e-5	4.4e-4	2.9e-4
RCrA IRS 7	45	1.2e0	-15.8	> 5e3	> 1.5e3	< 7.9e-4	< 2.7e-2	< 2.9e-1
HH46	35	1.4e-1	-7.4	1.4e4	9.0e3	1.5e-5	1.7e-4	9.3e-4

^a corrected for inclination using the average correction factors of Cabrit & Bertout (1990).

^b not corrected for inclination.

^c Dynamical time scale : $t_d = R/V_{\max}$

^d Mass outflow rate : $\dot{M} = M/t_d$.

^e Outflow force : $F_{CO} = M V_{\max}^2 / R$

^f Kinetic luminosity : $L_{\text{kin}} = 0.5 M V_{\max}^3 / R$

4.4.3 Outflows

4.4.3.1 Temperatures

The ratios of emission in the line wings of CO 3–2, 4–3 and 7–6 line profiles at the central position in Table 4.4 are compared to model line ratios from van der Tak et al. (2007). The line wings are assumed to be optically thin and filling factors within the different beams the same in each line. Kinetic temperatures can be derived if outflow emission is detected in two of these three lines (Table 4.7). As seen from the diagnostic plots in Appendix C of van der Tak et al. (2007), the kinetic temperature depends on the local density. Such densities can be estimated from observations of HCO⁺, although large fore-ground emission can produce significant HCO⁺ intensities (see Chapter 2). Densities in the envelope can also be estimated from DUSTY modelling (Ivezić & Elitzur 1997). H₂ densities of a few times 10⁵ cm⁻³ are derived by Jørgensen et al. (2002) for distances of 1500-3000 AU (corresponding to 10-20'' at the distances of Chamaeleon and Corona Australis), but these drop to a few times 10⁴ cm⁻³ at a couple of thousand AU.

At densities above the critical density ($n > n_{\text{cr}}$, $n_{\text{cr}} = 5 \times 10^4$ cm⁻³ for CO 3–2), the gas is thermally excited. However, if densities are lower, the gas is subthermally excited and higher kinetic temperatures are needed to produce similar ratios of the line wings.

To estimate the temperatures, two scenarios are presented. In the first, it is assumed that the gas is thermally excited ($n > n_{\text{cr}}$) as densities in the envelope are near to, or

higher than, the critical density. This is applicable for all sources with the exception of HH 46, for which the central beam extends to about 4,500 AU in radius. The kinetic temperatures determined in this way are likely to be on the low side. A second scenario is considered by assuming the densities to be on the order of 10^4 cm^{-3} , closer to the assumed densities of the surrounding cloud or envelopes at larger radii. In the first scenario, outflow temperatures are on the order of 50 K. An exception is IRAS 15398-3359, which appears to be much hotter (100 K) (see § 4.4.5.5). If densities are lower, derived kinetic temperatures are on the order of 150 K, although for HH 46 (blue) and Ced 110 IRS 6 (both red and blue) the outflow could have temperatures of ~ 80 K.

Models by Hatchell et al. (1999) predict temperatures of the swept-up shells that produce the molecular line emission. For parameters typical of the Class 0 L 483 outflow temperatures on the order of 50 to 100 K in the inner few thousand AU from the star are found. Along the bulk of the outflow axis, temperatures are 100-150 K. Only near the bow shocks are higher temperatures in excess of a few hundred to thousand K predicted. The models depend on the local conditions such as dust cooling, density distribution and jet velocity, but most parameters have an influence of the order of a few tens of K on the temperature along most of the outflow, except for the region of the bow shock. The results in Table 4.7 agree well with the temperature predictions from Hatchell et al. (1999). The results suggest that jet velocities $> 100 \text{ km s}^{-1}$ are not present, with the exception of IRAS 15398-3359.

Although we assumed the line wings to be optically thin, this is not necessarily the case (e.g., Cabrit & Bertout 1992; Hogerheijde et al. 1998). A more in-depth discussion is presented in Chapter 5 about the influences of optical depths and different densities on the kinetic temperatures of the swept-up gas in the molecular outflow.

4.4.3.2 Other outflow parameters

For the five sources where outflow emission is seen in the ^{12}CO 3–2 spectral maps, it is possible to determine the spatial outflow parameters, such as outflow mass, maximum velocity and extent. Subsequently the dynamical time scales and average mass outflow rate, the outflow force (or momentum flux) and kinetic luminosity can be derived following a recipe detailed in Hogerheijde et al. (1998) with the assumption that the emission at the more extreme velocities is optically thin and that the material has a kinetic temperatures of 50-80 K. The inclination of the outflow with the plane of the sky influences the results and the derived values need to be corrected for their inclination using an average of the model predictions in Cabrit & Bertout (1990). For HH 46 the inclination has been constrained to 35° (Reipurth & Heathcote 1991; Micono et al. 1998). For the other sources, an inclination is estimated from the distance between the maximum contour levels in Figs. 4.8 and 4.9 (see Table 4.8).

The results in Table 4.8 show that most outflows have masses of $0.01\text{-}0.1 M_\odot$, with average mass loss rates between 4.4×10^{-4} to $2 \times 10^{-6} M_\odot \text{ yr}^{-1}$, and outflow forces of 4.6×10^{-5} to $2.7 \times 10^{-2} M_\odot \text{ yr}^{-1} \text{ km s}^{-1}$. The strongest outflow is RCrA IRS 7, which produces the most outflow force and the most kinetic luminosity. This is mainly caused by the emission detected at a high ΔV_{max} of 23 km s^{-1} , which for other sources is on the order of 4 to 9 km s^{-1} , almost an order of magnitude difference. Note that for HH 100 (red only), HH 46 (red only) and RCrA IRS 7 (red and blue), the quoted radius

is a lower limit, due to insufficient coverage. The resulting outflow force and kinetic luminosity are thus upper limits.

Hogerheijde et al. (1998) surveyed the outflows of Class I sources in the Taurus cloud. There, most sources produce weaker outflows than found in Table 4.8, with outflow forces on the order of a few times $10^{-6} M_{\odot} \text{ yr}^{-1} \text{ km s}^{-1}$. However, a few outflows peak as high as a few times $10^{-4} M_{\odot} \text{ yr}^{-1} \text{ km s}^{-1}$. A recent survey of the outflows present in the Perseus cloud, show momentum flux, F_{CO} of a few times $10^{-7} M_{\odot} \text{ yr}^{-1} \text{ km s}^{-1}$ to a few times $10^{-5} M_{\odot} \text{ yr}^{-1} \text{ km s}^{-1}$ (Hatchell et al. 2007a). However, these numbers were not corrected for inclination, which can account for at least a factor 5. The observed outflow forces above are all powerful outflows, especially HH 100 and RCrA IRS 7. Figure 5 of Hatchell et al. (2007a) show that most Class I outflows have lower outflow forces than the Class 0 sources. Most classical flows in the northern hemisphere were first discussed in Bontemps et al. (1996) using CO 2–1 observations with relatively large beams. Outflow forces ranged from a few times 10^{-7} to $10^{-4} M_{\odot} \text{ yr}^{-1} \text{ km s}^{-1}$, corrected for inclination and optical depth. In this chapter, a relation between the outflow forces, bolometric luminosities and envelope masses was empirically derived,

$$\log(F_{\text{CO}}) = -5.6 + 0.9\log(L_{\text{bol}}) \quad (4.3)$$

and

$$\log(F_{\text{CO}}) = -4.15 + 1.1\log(M_{\text{env}}) \quad (4.4)$$

Figure 4.11 shows a comparison between the observed outflows of Table 4.8 and the relations from Bontemps et al. (1996). One must conclude that, although the outflows found in our sample are all associated with Class I sources, they are all exceptionally strong outflows compared to the luminosity, but not with envelope mass. Outflow forces are one to two orders of magnitude higher than expected from equation (2). The relation with the envelope mass from (3) does fit our sample. This suggests that the outflow strength as measured through the swept-up material says more about the surroundings (i.e. the amount of matter that can be swept up) than about the intrinsic source and outflow properties.

4.4.4 Individual sources

4.4.4.1 IRAS 12496-7650

IRAS 12496-7650, also known as DK Cha, was previously observed with APEX (Chapter 3). An outflow was identified from the line profiles and it was concluded that the emission as seen with ISO-LWS (Giannini et al. 2001) has to originate on scales larger than $8''$ and not from the inner regions of a protostellar envelope around IRAS 12496-7650. Figure 4.12 reveals that the detected blue-shifted outflow is located only in the central $15''$ and is peaking strongly on the source. The lack of red-shifted emission reinforces the conclusion that the outflowing gas is viewed almost perfectly face-on and that our line of sight is straight down the outflow cone.

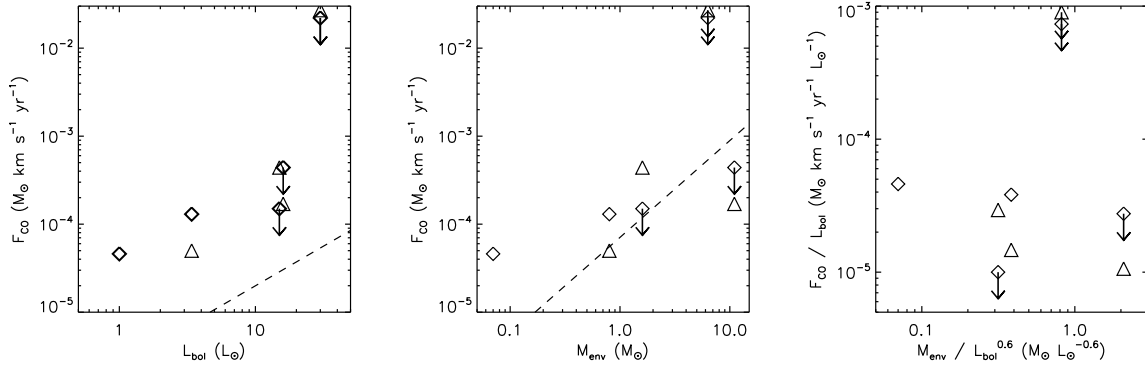


Figure 4.11 — CO outflow force F_{CO} versus the luminosity, L_{bol} (*left*), versus the envelope mass, M_{env} (*middle*), as well as a figure showing the $F_{\text{CO}}/L_{\text{bol}}$ versus $M_{\text{env}}/L_{\text{bol}}^{0.6}$, which should be free of most luminosity and distance effects following Fig. 7 of Bontemps et al. (1996) (*right*). Red outflows are shown with diamonds and blue outflows with triangles. The relation between F_{CO} , L_{bol} and M_{env} are shown with dashed lines.

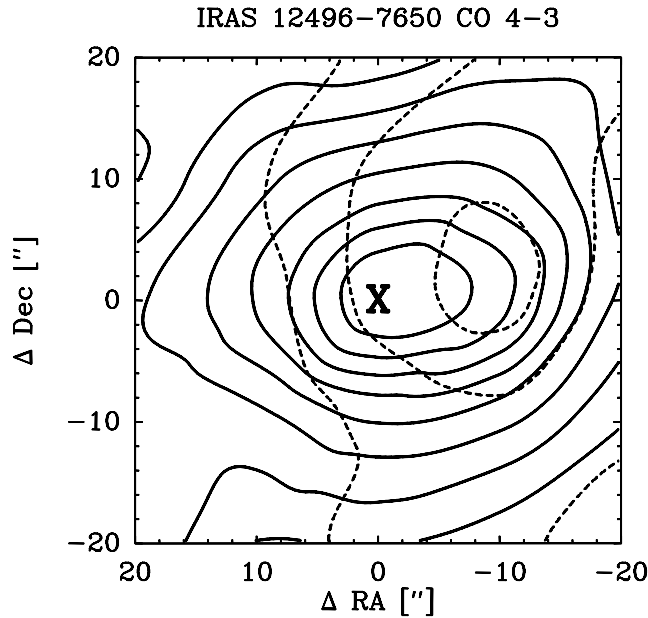


Figure 4.12 — CO 4-3 map of IRAS 12496-7650. The blue and red-shifted outflow emission are shown in *solid* and *dashed* contours respectively. Contours are in 3 K km s^{-1} .

4.4.4.2 RCrA IRS 7a and 7b

The sources RCrA IRS 7a and 7b are believed to be two embedded objects in a binary configuration with a separation of $\sim 30''$ (Nutter et al. 2005; Schöier et al. 2006). Using SMA interferometry and *Spitzer* results, Groppi et al. (2007) identified RCrA IRS 7b as a Class 0/Class I object, but since no IR counterpart to the disk seen in the SMA observations was found for RCrA IRS 7a, it was identified as Class 0 source. In this study, only a single outflow is found in Fig. 4.9, centered on RCrA IRS 7a. In addition, the HCO^+ 4-3 map shows a single core that is clearly peaking *only* on the position of RCrA

IRS 7a. No emission is found that peaks on the position of RCrA IRS 7b. From these results, it can be concluded that the envelope of the embedded source RCrA IRS 7a dominates. It is possible that RCrA IRS 7b is also embedded, and that a weaker envelope is being swamped by the contributions from RCrA IRS 7a and the cloud material, but it is also likely to be a Class II YSO, heavily obscured by the outflow, envelope and cloud material.

4.4.4.3 HH 100

An outflow is clearly detected at the IR position, with a north-south alignment for the red and blue-shifted emission. However, the submillimeter line emission around HH 100 do not provide a clear view of the physical structure of a potential protostellar envelope. No core is found in HCO⁺ 4–3 emission over the entire map. Due the large contributions of the cloud to the HCO⁺ emission ($\sim 5\text{--}10\text{ K km s}^{-1}$), it may be possible to hide a substantial envelope in this region (§ 4.3), but the lack of variation indicates that the emission must be optically thick. The SCUBA map from Nutter et al. (2005) confirms that this region is dominated by emission from the cloud around RCrA.

4.4.4.4 CrA IRAS 32

CrA IRAS 32 (known as SMM 8 in Nutter et al. (2005)) is located in the RCrA B region, but has little to no surrounding material. The small maps taken in CO 3–2 and HCO⁺ 4–3 reveal a very well-structured outflow, aligned in a NE (blue) to SW (red) direction around a spherical, barely resolved HCO⁺ core. However, the peak integrated intensity of 4.1 K km s^{-1} clearly indicates that this source is an isolated embedded protostar.

4.4.4.5 IRAS 15398-3359

The CO 4–3 and 7–6 (shown in Fig. 4.7) spectra of IRAS 15398-3359 show strong outflow-dominated line profiles with velocities up to $10\text{--}15\text{ km s}^{-1}$ from V_{LSR} . IRAS 15398-3359 is the only source that shows such strong outflow emission in CO 7–6 and temperature estimates in § 4.4.3 are significantly higher than for the other detected outflows. Additional spectral line mapping, such as C¹⁸O 3–2 and HCO⁺ 4–3, is needed to determine more properties of this southern source.

4.4.4.6 Ced 110 IRS 4

Ced 110 IRS 4 is the only source in the Cederblad region that shows clear evidence of both warm gas in CO 4–3 and 7–6, as well as an outflow in CO 3–2. Only the red-shifted outflow is detected for Ced 110 IRS 4 and centers on the same position as the core, suggesting a face-on outflow.

4.4.4.7 Ced 110 IRS 6

The single spectra of Ced 110 IRS 6 suggest that the outflowing gas of this source is unusually cold with temperatures of the order of $50\text{--}80\text{ K}$, as opposed to $>100\text{ K}$ for most other flows. The low HCO⁺ intensity for this source suggests that the ambient densities in this source are low. However, as no HCO⁺ map was taken, the densities

cannot be determined clearly. Additional observations of both CO 7–6 (to confirm the low temperature) and HCO^+ (to estimate the densities) are needed to fully characterize this embedded source.

4.4.4.8 HH 46

The HH 46 source is dominated by the red outflow lobe, pointed towards the southwest. It produces much brighter lines and extends to the edge of our CO 3–2 map (see Fig. 12), while the much weaker blue-shifted outflow lobe only extends 20'' from the driving source. The source is described in more detail in Chapter 5.

4.4.4.9 Cha INa 2

The CO 4–3 map of Cha INa 2 is the only map in Fig. 14 that does not show a peak at the source position. Although there is plenty of warm gas in the map as seen in the spectra of Fig. 7, it is unlikely that this is associated with the infrared source Cha INa 2. With the addition of an upper limit to the HCO^+ emission of 0.2 K km s^{-1} , Cha INa 2 is unlikely to be embedded. A more likely possibility is that Cha INa 2 is a photon dominated region (PDR).

4.4.4.10 IRAS 07178-4429 and IRAS 13546-3941

For both these isolated sources, no HCO^+ core is seen in the maps. In addition, both sources also show no variation or any outflow emission in their CO 3–2 emission maps down to 0.5 K km s^{-1} . We conclude that both these sources are likely not embedded, but the lack of warm gas observations cannot rule out very small envelopes.

4.5 Conclusions

In this chapter, we presented observations of CO, HCO^+ and their isotopologues, ranging in excitation from CO 3–2 to CO 7–6 of a sample of southern embedded sources to probe the molecular gas content in both the protostellar envelopes and molecular envelopes in preparation for future ALMA and Herschel surveys. The main conclusions are the following:

- HCO^+ 4–3 and CO 4–3 concentration confirm the presence of warm dense quiescent gas associated with 9 of our 15 sources.
- RCrA TS 3.5, RCrA IRS 7b, Cha INa2, IRAS 07178-4429, IRAS 13546-3941 are unlikely to be embedded YSOs due to either the lack of HCO^+ 4–3 emission or the lack of central concentration in HCO^+ 4–3, although the high column density around RCrA IRS 7b would be able to hide a substantial envelope.
- The outflows of Ced 110 IRS 4, Ced 110 IRS 6, CrA IRAS 32, RCrA IRS 7A, RCrA IRS 5, HH 100, HH 46, IRAS 12496-7650 and IRAS 15398-3359 were characterized using molecular line emission. The outflows detected in the spectral maps are all exceptionally strong with outflow forces almost two orders of magnitude higher than expected from their luminosities, following Bontemps et al. (1996). Outflows have temperatures on the order of 50-100 K, depending on the ambient densities.

These are similar to the temperatures predicted by Hatchell et al. (1999), with the exception of IRAS 15398-3359, which may be unusually warm.

- Neither Chamaeleon nor Corona Australis have foreground layers as found in Ophiuchus L 1688. All C¹⁸O 3–2 spectra can be fitted with single gaussians.
- The cloud material in the RCrA region has a large influence on the characteristics of the embedded sources in that region. A significant difference is seen with the lower column densities of a few times 10²² cm⁻² of the extended cloud in Chamaeleon I and the other Corona Australis regions to the few times 10²³ cm⁻² in RCrA.
- Although no HCO⁺ core was detected centered on HH 100, both red- and blue-shifted outflowing gas is present originating from the IR position. Further observations are needed to determine the envelope properties, although it is expected that the envelope mass is low.
- Of the binary RCrA IRS 7a and b, only RCrA IRS 7a is embedded. The HCO⁺ core observed in the map is only associated with RCrA IRS 7a, which also seems to be the origin of the bipolar outflow. No HCO⁺ core or outflowing gas is associated with RCrA IRS 7b.

Future observations using ALMA and Herschel will be able to probe the molecular emission associated with these YSOs at higher spatial resolution and higher frequencies. However, this study clearly shows that without detailed information about the immediate environment of a source, incorrect conclusions can be drawn from the spectral information. Comparison with single dish data, both continuum surveys and spectral line mapping, will be essential in analyzing the results obtained with future facilities.

Acknowledgements

TvK and astrochemistry at Leiden Observatory are supported by a Spinoza prize and by NWO grant 614.041.004. The APEX staff, in particular Michael Dumke, are thanked for their extensive support and carrying out the observations.

Chapter 5

Unraveling the structure of the molecular outflow and protostellar envelope of HH 46 using high- J CO observations

Abstract The spectacular outflow of HH 46/47 is driven by HH 46 IRS 1, an embedded Class I Young Stellar Object (YSO). Although much is known about this region from extensive optical and infrared observations, the properties of its protostellar envelope and molecular outflow are poorly constrained.

Our aim is to characterize the size, mass, density and temperature profiles of the protostellar envelope of HH 46 IRS 1 and its surrounding cloud material as well as the effect the outflow has on its environment.

The newly commissioned LABOCA and CHAMP⁺ arrays on the APEX telescope, combined with lower frequency line receivers, are used to obtain a large ($5' \times 5'$, 0.6×0.6 pc) continuum map and smaller ($80'' \times 80''$, $36,000 \times 36,000$ AU) heterodyne maps in various isotopologues of CO and HCO⁺. The high- J lines of CO (6–5 and 7–6) and its isotopologues, observed with CHAMP⁺, are used to probe the warm molecular gas in the inner few hundred AU and in the outflowing gas. The data are interpreted with continuum and line radiative transfer models.

Broad outflow wings are seen in CO low- and high- J lines at several positions, constraining the gas temperatures to a constant value of ~ 100 K along the red outflow axis and to ~ 60 K for the blue outflow. The derived outflow mass is of order $0.4\text{--}0.8 M_{\odot}$, significantly higher than previously found. The bulk of the strong high- J CO line emission has a surprisingly narrow width, however, even at outflow positions. These lines cannot be fit by a model of the HH 46 IRS envelope. We propose that it originates from photon heating of the outflow cavity walls by ultraviolet photons originating in outflow shocks and the accretion disk boundary layers. The envelope mass of $\sim 5 M_{\odot}$ is strongly concentrated towards HH 46 IRS with a density power law of -1.8 .

The fast mapping speed offered by CHAMP⁺ allows the use of high- J CO lines and their isotopes to generate new insights into the physics of the interplay between the molecular outflow and protostellar envelope around low-mass protostars.

T. A. van Kempen, E. F. van Dishoeck, R. Güsten, L. E. Kristensen, P. Schilke, M. R. Hogerheijde, W. Boland, B. Nefs, K. M. Menten, A. Baryshev, 2008, in prep

5.1 Introduction

The Young Stellar Object (YSO) HH 46 IRS 1 (RA= 08h25m43.9s, Dec =−51d00h36s (J2000)), located in an isolated Bok Globule ($D = 450$ pc) in the southern hemisphere (Schwartz 1977), is well-known for its spectacular outflow (Reipurth & Heathcote 1991), observed at both visible and infrared (IR) wavelengths with the *Hubble* and *Spitzer* Space Telescopes (e.g., Heathcote et al. 1996; Noriega-Crespo et al. 2004; Velusamy et al. 2007). Deep H α observations using the VLT have revealed bow shocks associated with the HH 46 outflow up to a parsec away from the central source (Stanke et al. 1999). Proper motion and radial velocity studies show that the outflow has an inclination of 35° with respect to the plane of the sky and flow velocities in atomic lines up to 300 km s^{-1} (Dopita et al. 1982; Reipurth & Heathcote 1991; Micono et al. 1998). The internal driving source was found to be HH 46 IRS 1 ($L = 16 L_\odot$), an embedded Class I YSO (Raymond et al. 1994; Schwartz & Greene 2003). Surprisingly, much less is known about the properties of the protostellar envelope and the molecular outflow. Chernin & Masson (1991) and Olberg et al. (1992) mapped this region using low excitation CO lines, which show that contrary to the optical flows, the red-shifted outflow lobe is much stronger than the blue-shifted one. Chernin & Masson (1991) theorised that a lack of dense material in the path of the blue-shifted flow is responsible for this.

Comparisons between dust emission and molecular emission lines at submillimeter wavelengths, together with self-consistent radiative transfer calculations have been extensively used to characterize the physical and chemical structure of Class 0 and Class I envelopes (Schöier et al. 2002; Jørgensen et al. 2002, 2005a; Maret et al. 2004). However, an essential component could not be probed with those data. The amount of warm ($T > 50$ K) gas within the protostellar envelope as well as the influence of the molecular outflow have not been constrained directly using observations of lower excited molecular lines in the 200 and 300 GHz bands. Although more complex molecules, such as H₂CO and CH₃OH emit at these frequencies from high energy levels (e.g. van Dishoeck et al. 1995; Ceccarelli et al. 2000), their more complex chemistry complicates their use as probes of the warm gas. Observations of CO at higher energies (up to 200 K) provide more reliable probes into the inner regions of envelopes and molecular outflows, but such lines have only been observed for a handful of sources (e.g., Hogerheijde et al. 1998; Parise et al. 2006; van Kempen et al. 2006). [C I] emission provides an important constraint on the strength of the radiation field within the outflows (Walker et al. 1993).

With the commissioning of the *Atacama Pathfinder Experiment* (APEX)¹ (Güsten et al. 2006), the CHAMP⁺ instrument (Kasemann et al. 2006; Güsten et al. 2008) allows observations of molecular emission lines in the higher frequency sub-millimeter bands of southern sources, like HH 46. CHAMP⁺ is the first array of its kind. With its 14 pixels, it is able to observe simultaneously in the 690 and 800 GHz atmospheric windows. This combination of dual-frequency observing and fast mapping speed, supplemented by

¹This publication is based on data acquired with the Atacama Pathfinder Experiment (APEX) in programs E-77.C-0217, X-77.C-0003, X-79.C-0101 and E-081.F-9837A. APEX is a collaboration between the Max-Planck-Institut für Radioastronomie, the European Southern Observatory, and the Onsala Space Observatory. APEX-1 was used during science verification in June 2008.

lower frequency single pixel data and a LABOCA continuum array map (Kreysa et al. 2003; Siringo et al. 2008), provides a large range of highly complementary tracers of both the gas and dust conditions in the inner and outer regions of the envelope, as well as the molecular outflow on scales of a few arcminutes. Spectral line maps provide key information that is essential in the analysis of embedded YSOs which single-pointed observations cannot offer (Boogert et al. 2002; van Kempen et al. 2008).

In this chapter, we present first results from CHAMP⁺ and LABOCA observations of the HH 46 IRS 1 source, supplemented by lower frequency line receivers. Observations of highly excited CO, HCO⁺ and their isotopologues are used to constrain the properties of the protostellar envelope and molecular outflow of HH 46. In § 5.2 the observations performed at APEX are presented. Resulting spectra and maps can be found in § 5.3. In § 5.4 the protostellar envelope, molecular outflow and close surrounding of HH 46 are characterized using a radiative transfer analysis. In addition, we discuss a possible scenario for the high-*J* CO emission. The final conclusions are given in § 5.5.

Table 5.1 — Overview of the observations

Line	Trans. J_u-J_l	E_u (K) (K)	Freq. (GHz)	Instrument	Beam ($''$)	Map
CO	2–1	16.6	230.538	APEX-1	28	y
	3–2	33.2	345.796	APEX-2a	18	y
	4–3	55.3	461.041	FLASH-I	14	y
	6–5	116.2	691.473	CHAMP ⁺ -I	9	y
	7–6	154.8	806.651	CHAMP ⁺ -II	8	y
¹³ CO	3–2	31.7	330.588	APEX-2a	18	n
	4–3	52.9	440.765	FLASH-I	14	n
	6–5	111.1	661.067	CHAMP ⁺ -I	9	y
	8–7	190.4	881.273	CHAMP ⁺ -II	8	n
C ¹⁸ O	3–2	31.6	329.331	APEX-2a	18	n
	6–5	110.6	658.553	CHAMP ⁺ -I	9	y
[C I]	2–1	62.3	809.342	CHAMP ⁺ -II	8	y
HCO ⁺	4–3	42.8	356.724	APEX-2a	18	y
H ¹³ CO ⁺	4–3	41.6	346.998	APEX-2a	18	n
870 μ m continuum				LABOCA	18	y

5.2 Observations

Molecular line observations were carried out with the CHAMP⁺ array (Kasemann et al. 2006) of CO and its isotopologues, ranging in transitions from $J=6-5$ to $J=8-7$, as well as [C I] 2–1. These observations were supplemented with low excitation line observations using APEX-1 (230 GHz, CO 2–1), APEX-2a (345 GHz, CO, C¹⁸O and ¹³CO 3–2, and HCO⁺ and H¹³CO⁺ 4–3) and FLASH (460 GHz, CO and ¹³CO 4–3). In addition, LABOCA was used to map the entire region at 870 μ m. See Table 5.1 for an overview of the observed emission lines for each instrument and the corresponding rest frequencies and upper level energies, together with their corresponding APEX beams. All

observations were done under excellent weather conditions with typical system temperatures of 2100 K for CHAMP⁺-I (SSB, 690 GHz), 7500 K for CHAMP⁺-II (SSB, 800 GHz), 1100 K for FLASH-I (DSB, 460 GHz), 290 K for APEX-1 and 230 K for APEX-2a (both SSB). The HH 46 protostar was spectrally mapped in CO 2–1, 3–2, 4–3, 6–5, 7–6 and HCO⁺ 4–3, as well as ¹³CO 6–5 and [C I] 2–1. The mapped area differs per line, ranging from 40'' × 40'' for CO 4–3 to 200'' × 200'' for CO 2–1, with most other lines covering 80'' × 80''. Observations were taken over a period of 2 years from July 2006 to June 2008 using Fast Fourier Transform Spectrometer (FFTS) (Klein et al. 2006) backends for all instruments, except CHAMP⁺, for which only the two central pixels were attached to the FFTS backends. Other CHAMP⁺ pixels were attached to the MPI Array Correlator System (MACS) backends. FFTS backends are able to reach resolutions of 0.12 MHz (0.045 km s⁻¹ at 800 GHz), while the MACS units were used at a resolution of 1 MHz (0.36 km s⁻¹ at 800 GHz). Beam efficiencies are 0.75 for APEX-1, 0.73 for APEX-2a, 0.7 for FLASH-I, 0.56 for CHAMP⁺-I and 0.43 for CHAMP⁺-II. Pointing was checked on nearby sources and found to be accurate within 3'' for the APEX-2a observations. For CHAMP⁺, pointing is accurate within ~5''. All observations were taken using position switching with off-positions in azimuth ranging from 600'' to 3600''.

LABOCA observed HH 46 during November 2007 using its 295 pixels in a spiral mode centered on the IR position using a position switch of 600'' arcseconds. Only the inner 5' × 5' of the 11' field of view was used. The field was integrated down to a noise level of 0.01 Jy/beam, averaged over the entire region. Due to the used spiral mode, the map contains a radial increase of noise towards the edge of the map. The continuum data were reduced with the BOA package².

5.3 Results

5.3.1 Single pixel spectra

Figure 5.1 shows the spectra taken at the position of HH 46 IRS 1 for all lines in Table 5.1. Integrated intensities, peak temperatures and estimated contributions from the blue- and red-shifted outflowing gas are given in Table 5.2. The latter are derived by subtracting the central part of the line profile, associated with the quiescent gas, with a single gaussian. Emission was detected for all lines with the exception of C¹⁸O 6–5 and ¹³CO 8–7. The quiescent gas component peaks at a V_{LSR} of 5.3 ± 0.1 km s⁻¹ and has a FWHM of 1–2 km s⁻¹ depending on the energy of the upper level. Since the detection of the [C I] 2–1 line is only 3.5 σ , a gaussian fit is overplotted in Fig. 5.1.

Integrated intensities range from 82.5 K km s⁻¹ for CO 3–2 to 1.1 K km s⁻¹ for H¹³CO⁺. All ¹²CO line profiles show contributions of a red-shifted outflow lobe within the beam, including the high excitation CO 7–6 line. Emission from the blue-shifted outflow lobe is much weaker and not found for CO 7–6. In the other lines, outflow emission is only detected for HCO⁺ 4–3, where a weak red-shifted wing is found.

²<http://www.astro.uni-bonn.de/boawiki>

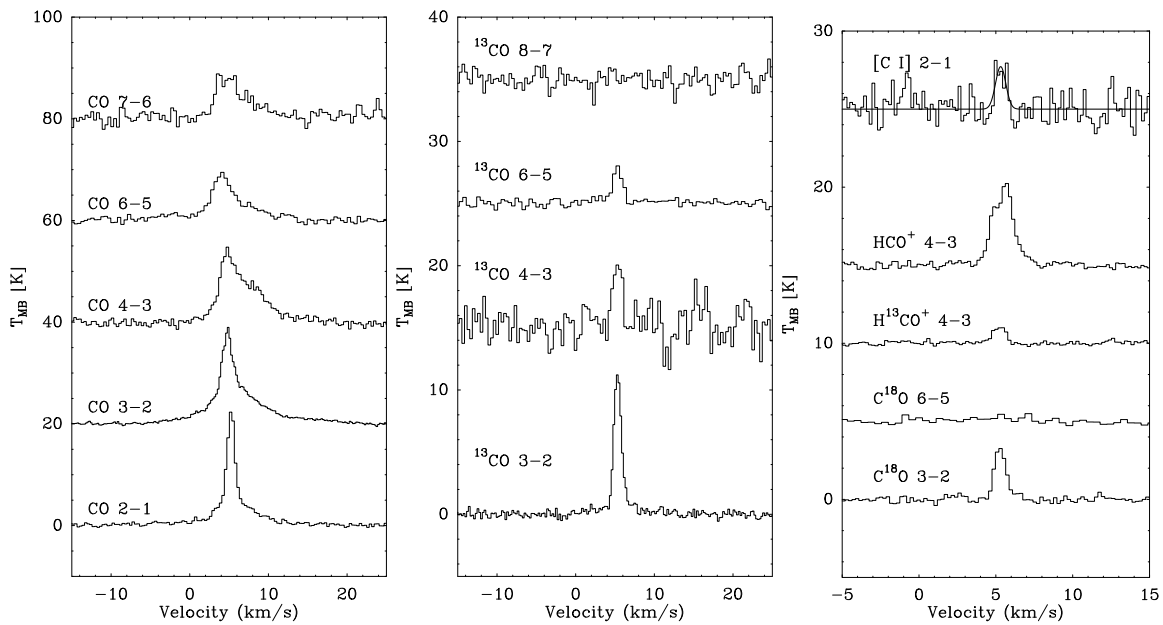


Figure 5.1 — Single spectra taken at the central position of HH 46 (all in order from *bottom to top*). *Left* : ^{12}CO 2–1, ^{12}CO 3–2, ^{12}CO 4–3, ^{12}CO 6–5 and ^{12}CO 7–6. *Middle* : ^{13}CO 3–2, ^{13}CO 4–3, ^{13}CO 6–5 and ^{13}CO 8–7. *Right* : C^{18}O 3–2, C^{18}O 6–5, H^{13}CO^+ 4–3, HCO^+ 4–3 and $[\text{C I}]$ 2–1. Spectra have been shifted vertically for easy viewing.

5.3.2 Maps

The resulting dust emission map ($5' \times 5'$) at $870 \mu\text{m}$ is shown in Fig. 5.2. The envelope is clearly resolved, considering the beamsize of $18''$ of the APEX dish. The envelope is slightly elongated on a south-west to north-east axis. South of HH 46, dust emission from the cold cloud is seen. The total integrated flux in a $120''$ diameter aperture around the source position is found to be 3.7 Jy. Reduction of archival SCUBA ($850 \mu\text{m}$) data of this region yielded a flux of 3.3 Jy (Di Francesco et al. 2008), a difference in flux well within the estimated calibration errors of both SCUBA and LABOCA. Using the formula in Shirley et al. (2000), the total mass in the $300''$ mapped area of the cloud is $8 M_{\odot}$, while the central $120''$ is associated with a mass of $3.7 M_{\odot}$, both with an assumed dust temperature of 20 K.

The integrated spectral line maps of CO 3–2, 7–6 and HCO^+ 4–3 (all $80'' \times 80''$) in Fig. 5.3 show a similar structure as the continuum maps (see also §5.4.1), although the elongation to the south-west is much more pronounced in the CO lines, with an integrated intensity of CO 3–2 of 65.6 K km s^{-1} seen in the $-20'', -20''$ off-position. As can be seen from the red- and blue-shifted velocity maps of CO 2–1, 4–3 and 6–5 in Fig. 5.4, the shape of the integrated intensity maps is largely due to the outflow contributions, especially for the low-excitation lines, even in the CO 2–1 map, for which a map of $200'' \times 200''$ was observed. This is in agreement with the results from Chernin & Mason (1991). In fact, the CO 3–2 line is so prominent that it can contribute significantly to the ‘continuum’ emission seen by LABOCA. The CO 3–2 line produces a flux density of 40 mJy/beam off source, equivalent to the LABOCA 4σ level. The total continuum emission seen at these positions is $\sim 12\text{--}15\sigma$. CO emission may thus contribute up to

Table 5.2 — Observed molecular line intensities^a.

Line	Transition	Central position				Off-position ^b	
		$\int T_{\text{MB}}dV^c$ (K km s ⁻¹)	T_{peak} (K)	Red (K km s ⁻¹)	Blue (K km s ⁻¹)	$\int T_{\text{MB}}dV^c$ (K km s ⁻¹)	T_{peak} (K)
CO	2-1	53.3	22.4	11.5	3.8	61.7	21.2
	3-2	82.5	19.4	28.0	13.4	65.6	19.8
	4-3	70.5	14.9	44.2	3.7	38.5	14.0
	6-5	42.6	9.5	11.7	5.7	34.6	8.8
	7-6	46.5	8.6	17.6	<3.7	25.3	5.9
¹³ CO	3-2	14.3	11.4	-	-	-	-
	4-3	8.0	5.5	-	-	-	-
	6-5	3.9	2.9	-	-	<0.6 ^d	-
	8-7	-	<0.9 ^c	-	-	-	-
C ¹⁸ O	3-2	3.2	3.3	-	-	-	-
	6-5	-	<0.5 ^d	-	-	-	-
[C I]	2-1	2.3	2.7	-	-	-	<1.8 ^d
HCO ⁺	4-3	8.5	5.4	1.4	-	-	<0.9 ^d
H ¹³ CO ⁺	4-3	1.1	1.0	-	-	-	-

^a Red and Blue shifted emission are calculated by subtracting the central part of the line profile with a gaussian with FWHM of 1.5-2 km s⁻¹.

^b Off-position : $\Delta\text{RA} = -20''$, $\Delta\text{Dec} = -20''$.

^c Velocity range used for integration: -5 km s⁻¹ to 15 km s⁻¹

^d Upper limit of 3σ in a 0.7 km s⁻¹ channel.

30% to the observed LABOCA emission in the outflow region.

In contrast, the elongation in the HCO⁺ 4-3 map is much less pronounced than in the CO low- J data. The map of [C I] 2-1 is not shown, since no lines were detected down to 1.8 K (3σ). In the map of ¹³CO 6-5, lines are only detected at the central position and at neighbouring pixels along the outflow.

Figure 5.5 shows the observed spectra within the central $80'' \times 80''$ of CO 3-2, taken with APEX-2a, and CO 6-5, taken with CHAMP⁺-I. Both are binned to square $10'' \times 10''$ pixels. The line profiles show an interesting distribution of emission, especially at the positions associated with the outflowing gas. The CO 3-2 spectra consist of a central gaussian originating in the cold envelope material surrounding the protostar, with a strong red-shifted outflow of up to 10 km s⁻¹ away from the source and cloud velocity in the south-east direction. The line profile at the source position has a quiescent component, flanked by both red- and blue-shifted emission. Interestingly, the CO 6-5 emission shows a quiescent component with relatively weak red-shifted emission at the off-positions. The central part of the line profile can be fitted with narrow ($\Delta V = 2-3$ km s⁻¹) gaussian profiles. At the central position, outflow emission in the CO 6-5 line is much more prominent, but a strong quiescent component is still present.

Figure 5.6 shows all spectra observed within the spectral line maps at the $(-20'', -20'')$ off-position. Peak temperatures and integrated intensities are given in Table 5.2. This off-position covers the red-shifted outflow seen prominently in the emission of the

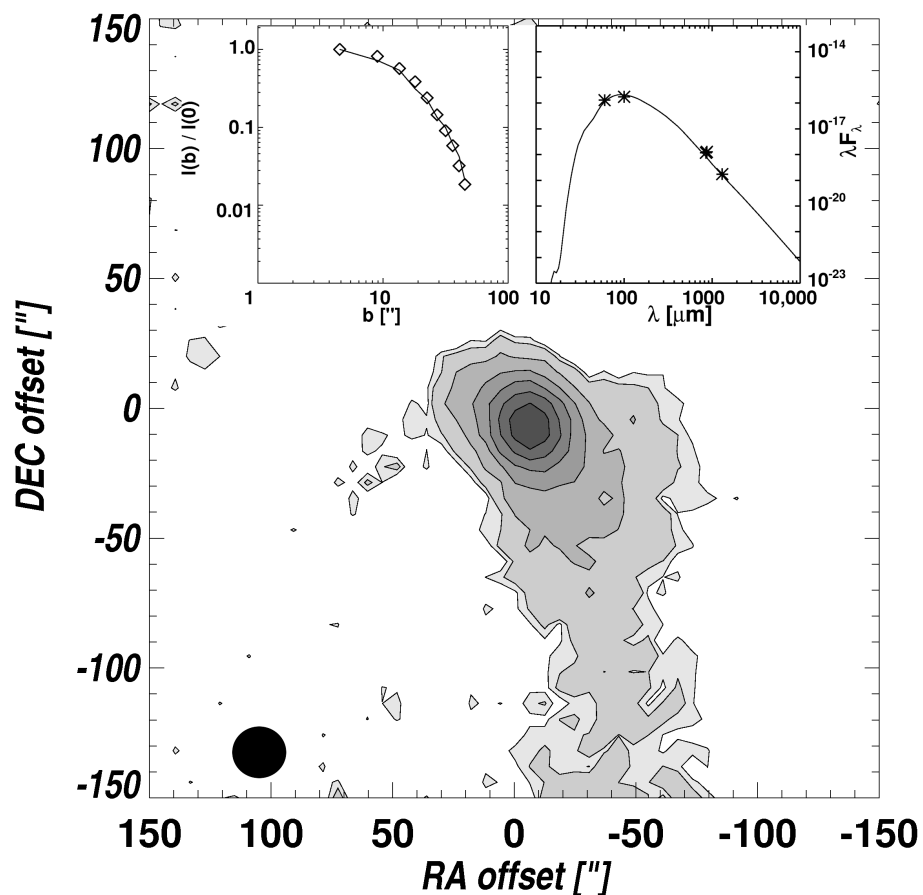


Figure 5.2 — Continuum map at $870 \mu\text{m}$ of HH 46 obtained with LABOCA with contour levels plotted in multiples of the 3σ noise level of 0.05 Jy/beam . *Left inset*: the radial profile going outwards from the IR position. *Right inset*: the SED from HH 46 from $10 \mu\text{m}$ to 10 mm . In both panels, the best-fitting DUSTY model is overplotted.

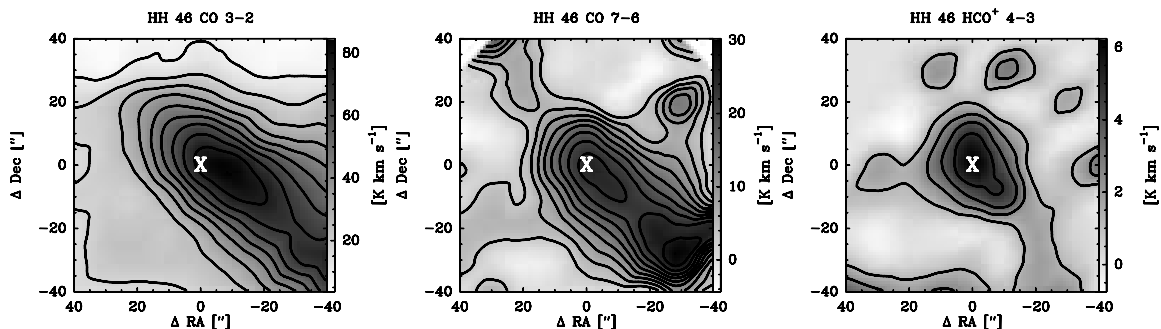


Figure 5.3 — From *left to right* : Spectrally integrated CO 3–2, 7–6 and HCO^+ 4–3 maps of HH 46 (see Table 5.2). Contour levels are at 3σ , 6σ , 9σ , ... ($\sigma = 1.5 \text{ K}$ for CO 3–2, 0.4 K for HCO^+ 4–3 and 0.8 K for CO 7–6) The position of the IR source is marked with a X. Note that the HCO^+ 4–3 map has higher noise levels than the central spectrum in Fig 5.1.

low-excitation CO 3–2 and 2–1 lines. Even CO 4–3 shows significant red-shifted outflow emission. The outflowing gas is still present in the high- J CO lines. However,

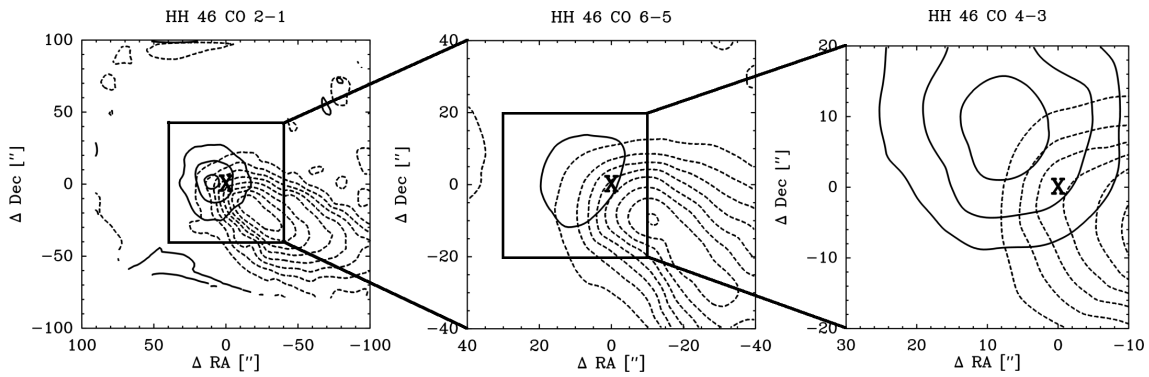


Figure 5.4 — Maps of HH 46 showing the outflowing gas. Solid lines show blue-shifted, dashed lines show red-shifted emission. Contours are drawn at 3σ , 6σ , 9σ , ... , with the exception of CO 2–1, where contours are drawn 3σ , 9σ , 15σ , 3σ levels are 0.4 K km s^{-1} , 1 K km s^{-1} and 1 K km s^{-1} for 2–1, 6–5 and 4–3 respectively. Blue- and red-shifted emission is derived by subtracting a central gaussian fitted to the quiescent central part of the line profiles. Velocities typically range from -5 to 1.5 km s^{-1} for the blue-shifted emission and 8 to 15 km s^{-1} for the red-shifted. Note that the images are at different spatial scales and progressively zoom in onto the central protostar from left to right. The position of the infrared source is marked in all maps with a ‘X’.

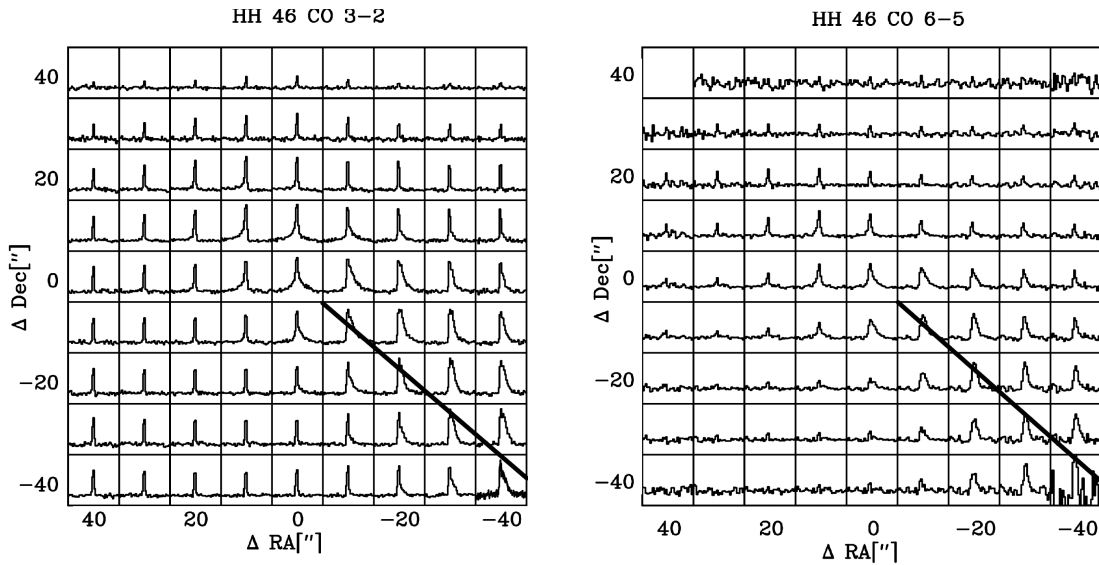


Figure 5.5 — Spectra of HH 46 of CO 3–2 (*left*) and CO 6–5 (*right*) in the $80'' \times 80''$ mapping area. Individual spectra are shown on a T_{MB} scale of -5 to 20 K for CO 3–2 and from -3 to 12 K for CO 6–5. Both axes are from -10 to 20 km s^{-1} . The black lines show the axis of the red outflow.

for both CO 6–5 and 7–6 a significant part of the emission (on the order of 70–80%) originates in a quiescent component. The isotopologue ^{13}CO 6–5 is not detected at the off-position, down to a 3σ level of 0.6 K in a 0.7 km s^{-1} bin. Similarly, no [C I] is detected down to 1.8 K and no HCO^+ 4–3 is detected down to 0.9 K , both 3σ in a 0.7 km s^{-1} bin.

Using the limits on the ^{13}CO 6–5 emission at both the central position and the se-

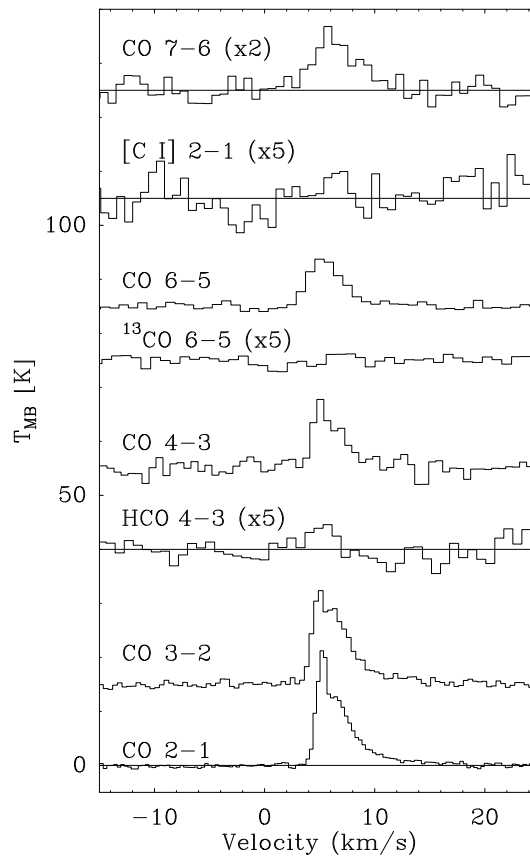


Figure 5.6 — Single spectra of (from *bottom to top*): CO 2–1, CO 3–2, HCO⁺ 4–3, CO 4–3, ¹³CO 6–5, CO 6–5, [C I] 2–1 and CO 7–6. All spectra are at an off-position in the red outflow lobe of $\Delta\text{RA}=-20''$ and $\Delta\text{Dec}=-20''$. The quiescent gas has a FWHM of 1.5 km s^{-1} centered at 5.3 km s^{-1} .

lected off-position, it is found that the quiescent component at the central position is optically thick ($\tau > 3$), while the quiescent emission at the outflow position is optically thin ($\tau < 0.4$), as no ¹³CO is detected between 0 and 10 km s^{-1} . This analysis assumes a ¹²CO:¹³CO ratio of 70:1 (Wilson & Rood 1994).

Although outflow emission heavily influences the line profiles of the CO 3–2 and 6–5 throughout the maps, positions south, south-east, and north of the (0,0) position are not affected by any outflowing gas, as seen in Fig. 5.5. About $30''$ to $40''$ north of HH 46, both the CO 3–2 and CO 6–5 are not detected. Even in the map of CO 2–1, no emission was found at these positions. It is concluded that the cold cloud material of the surrounding Bok globule does not extend to these scales. At positions south and south-east of HH 46, CO 3–2 emission is seen, but no CO 6–5 is detected there.

5.4 Envelope and surrounding cloud

5.4.1 Envelope - dust

Using the 1-D radiative transfer code DUSTY (Ivezić & Elitzur 1997), a spherically symmetric envelope model is constructed by fitting the radial profile of the $870 \mu\text{m}$ image and the SED simultaneously, determining the size, total mass, inner radius as well as

density and temperature profiles of the protostellar envelope. For a more thorough discussion of this method, see Jørgensen et al. (2002). DUSTY uses Y ($=R_{\text{outer}}/R_{\text{inner}}$), p , the power law exponent of the density gradient ($n \propto r^{-p}$), and τ_{100} , the opacity at 100 μm as its free parameters. For the SED, fluxes were used at 60 and 100 μm (IRAS, Henning et al. 1993), 850 μm (SCUBA archive, Di Francesco et al. 2008), 870 μm (LABOCA, this work) and 1.3 mm (SEST Henning et al. 1993). Since Velusamy et al. (2007) theorize that a shock position exists close to the star, no emission from MIPS at 24 μm or ISO-SWS (Nisini et al. 2002; Noriega-Crespo et al. 2004) was used. The radial profile was determined in directions away from the southwest outflow and cloud material, ignoring any emission in 90° to the south-west. Results for the best-fitting envelope model to the 16 L_\odot for the source luminosity can be found in Table 5.3. The corresponding fits are shown in the insets of Fig. 5.2.

The envelope contains a large amount of cold gas ($\sim 5.1 M_\odot$) within the outer radius of 20,800 AU (~ 0.1 pc), but with a significant fraction of the mass concentrated towards the inner envelope due to the steep density profile ($p=1.8$). The H_2 density at 1,000 AU is $2.4 \times 10^6 \text{ cm}^{-3}$.

Table 5.3 — Results from radiative transfer modelling for envelope properties

Best fit		Envelope Properties	
Y	700	$R_{\text{inner}}(250 \text{ K})$	30 AU
p	1.8	$R(30 \text{ K})$	533 AU
τ_{100}	2.6	$R(n_{\text{de}})$	6,100 AU
		R_{outer}	20,800 AU
		$n(1000 \text{ AU})$	$2.5 \times 10^6 \text{ cm}^{-3}$
		$M_{\text{env}} (> 10 \text{ K})$	$5.1 M_\odot$

5.4.2 Envelope - gas

The physical structure of the gas is best traced by optically thin emission that probes the quiescent envelope gas at high density (Jørgensen et al. 2005a). To that end, the temperature and density structure derived from the dust radiative transfer model was used a starting point for modeling the gaseous molecular lines with the RATRAN radiative transfer code (Hogerheijde & van der Tak 2000) with data files from the LAMDA database (Schöier et al. 2005). Two different models were run. In the first model, only freeze-out is taken into account, with an inner CO abundance X_0 of 2.7×10^{-4} with respect to H_2 and an outer CO abundance X_d of 10^{-5} . In the second model, the abundances are the same, except that a high abundance $X_0=2.7 \times 10^{-4}$ has been adopted for the outermost envelope regions where density is lower than $n_{\text{de}}=10^5 \text{ cm}^{-3}$. This so-called ‘drop’ abundance profile is motivated by the fact that at low densities, the timescales for freeze-out onto the grains are longer than the typical lifetimes of the cores of a few 10^5 yr. The abundances X_0 and X_d were derived by Jørgensen et al. (2002) and Jørgensen et al. (2005a) for a range of sources, based on emission from optically thin lines. Isotope ratios were taken from Wilson & Rood (1994) of 550 for $\text{CO}:\text{C}^{18}\text{O}$ and 70 for $\text{CO}:\text{C}^{13}\text{CO}$. The velocity field of the envelope is represented by a turbulent width of 0.8 km s^{-1} .

Table 5.4 gives the results for these models. For each model, the envelope contribution of both $\int T_{\text{MB}}$ and T_{peak} are given. The optically thin lines (C^{18}O 3–2 and 6–5, as well as the ^{13}CO 8–7) show that the inclusion of a higher abundance outer layer, as in a drop model, is necessary to increase the C^{18}O 3–2 emission to the observed levels. At the same time this does not change the emission of the C^{18}O 6–5 line. The adopted abundances of the drop abundance (Model 2) agree best with the observed intensities of the optically thin lines, including the upper limits on C^{18}O 6–5 and ^{13}CO 8–7 within the uncertainties.

Table 5.4 — Results from molecular line radiative transfer modelling.

Line	Model 1 ^a		Model 2 ^a		Obs.
	$\int T_{\text{MB}}$	T_{peak}^b	$\int T_{\text{MB}}$	T_{peak}^b	
CO 2–1	9.4	5.0/22.2	10.4	4.5/78.9	22.4
CO 3–2	8.0	4.7/22.5	7.1	3.8/55.8	19.4
CO 4–3	7.3	4.2/16.9	4.7	3.1/47.3	14.9
CO 6–5	6.8	3.4/4.8	5.1	2.7/5.2	9.5
CO 7–6	4.1	2.2	4.0	2.2	8.6
^{13}CO 3–2	4.6	3.7/3.8	5.9	3.6/10.7	11.4
^{13}CO 4–3	3.5	2.8	4.2	2.6/3.8	5.5
^{13}CO 6–5	1.9	1.2	1.9	1.2	2.9
^{13}CO 8–7	0.8	0.5	0.8	0.5	<0.9
C^{18}O 3–2	1.3	1.2	3.5	2.9	3.3
C^{18}O 6–5	1.0	0.7	1.0	0.7	<0.5
HCO^{+c} 4–3	3.5	2.3/11.8	2.8	2.5/8.3	5.4
$\text{H}^{13}\text{CO}^{+}$ 4–3	0.75	0.7	0.75	0.7	1.0

^a Model 1 has a jump abundance profile with X_0/X_d of $2.7 \times 10^{-4}/1 \times 10^{-5}$. Model 2 has a drop abundance profile with $X_0/X_d/X_0$ of $2.7 \times 10^{-4}/1 \times 10^{-5}/2.7 \times 10^{-4}$.

^b For some lines, the peak temperature is given as X/Y. The first value is the actual T_{peak} in the model profile. The second value refers to the peak of a gaussian fitted to the line wings of model profiles which show self-absorption. If only a single number is given, the modelled line is gaussian in nature and does not have self-absorption.

^c HCO^{+} abundances of X_0 and X_d are 2.0×10^{-8} and 3.0×10^{-9} .

The very optically thick low- J ^{12}CO (2–1, 3–2 and 4–3) lines cannot be fitted by either model due to the lack of self-absorption in the observed lines, which is strongly present in the modelled profiles. To obtain a rough correction for self-absorption, gaussian fits were made to the line wings of CO, similar to the one in Chapter 3. Such gaussian fits provide only upper limits to the peak emission of CO, as the true CO emission is best fitted with an infall velocity (Schöier et al. 2002).

Even with gaussian fits, the high- J (6–5 and higher) lines of both ^{13}CO and ^{12}CO are severely underproduced by almost a factor 3. Note that their model line profiles do not show self-absorption. The emission in these lines is almost identical in the drop or jump abundance models. Increasing or decreasing the CO abundances X_0 and X_d is not possible since the emission of optically thin lines such as C^{18}O 6–5 and 3–2 would then either be over- or underestimated. The main conclusion from the envelope models is therefore that an additional, relatively optically thin but hot component unobscured

by the warm envelope region is needed to account for this emission. The origin of this hot component producing narrow highly excited CO line emission will be discussed in § 5.6.

The integrated [C I] 2–1 intensity (2.3 K km s^{-1}) can be reproduced with a constant abundance ratio C/H_2 of $3\text{--}5 \times 10^{-7}$ (or about 0.1–3% of CO, depending on radius), typical for the densest molecular clouds. The [C I] line is optically thin, even for much higher abundances. A C abundance as high as 5×10^{-6} can be maintained by photodissociation of CO due to cosmic-ray induced UV photons deep inside the envelope (e.g., Flower et al. 1994).

HCO^+ 4–3 shows little to no difference between Model 1 and 2, because most of the emission traces gas denser than 10^5 cm^{-3} . There is a significant difference in T_{peak} from the line profile vs. gaussian fits for main isotope line because of self-absorption. The optically thin H^{13}CO^+ is slightly underproduced, similar to the C^{18}O 3–2 peak temperature.

5.4.3 Surrounding cloud material

The envelope of HH 46 is surrounded by cold, quiescent cloud material as evidenced by the LABOCA map and by the CO lines to the south-east (e.g., $20''$, $-40''$). If the cloud is assumed to be isothermal and homogeneous, the CO emission maps from 2–1 to 7–6 can be used to constrain its properties with the radiative transfer program RADEX (van der Tak et al. 2007)³. A line width of 1.2 km s^{-1} is used from the gaussian fits to the CO 3–2 emission at the off-positions. The ratios of CO 3–2/6–5 peak temperatures at these cold cloud positions are at least 20, since CO 6–5 is not detected. RADEX simulations show that the CO 6–5 line has to be sub-thermally excited, which can be done when the gas is at low densities or at very low ($T < 10 \text{ K}$) kinetic temperatures. The line ratios are best fitted by a cloud with a temperature of $\sim 14 \text{ K}$, a low density of a few times 10^3 cm^{-3} and a CO column density of $10^{17}\text{--}10^{18} \text{ cm}^{-2}$. The spatial distribution of the CO 3–2 and 6–5 lines also indicate that these cloud conditions extend homogeneously to at least $40''$ south of HH 46, the extent of both CO 3–2 and 6–5 maps. Maps of the optically thin C^{18}O 3–2, as have been done by van Kempen et al. (2008) for other sources, are needed to further constrain the column density and spatial structure of the surrounding cloud.

5.5 Outflow

5.5.1 Outflow temperature

The spectral line maps clearly reveal the red-shifted outflow to the south-west and the blue-shifted outflow to the north-east. The large difference in extent between the two outflow lobes, already noted by Olberg et al. (1992), is seen in all transitions, with the blue-shifted lobe producing much weaker emission. The brighter and larger outflow lobe seen with *Spitzer* (Noriega-Crespo et al. 2004; Velusamy et al. 2007) corresponds to the red-shifted outflow, which dominates the line profiles of CO. The lack of HCO^+ outflow wings as well as the absence of HCO^+ emission in most off-positions, suggest

³RADEX is available online at <http://www.strw.leidenuniv.nl/~moldata/radex.html>

Table 5.5 — Outflow properties of the red and blue outflow lobe).

Outflow properties							
	V_{\max}^a (km s ⁻¹)	R^a (AU)	$M^{b,c}$ (M _⊙)	$t_d^{a,d}$ (yr)	$\dot{M}^{a,e}$ (M _⊙ yr ⁻¹)	$F_{CO}^{b,f}$ (M _⊙ yr ⁻¹ km s ⁻¹)	$L_{\text{kin}}^{b,g}$ (L _⊙)
Red Lobe							
CO 2–1	14.2	5e4	0.8/2.9 ^h	2.6e4	9.1e-5	9.8e-4	1.2e-2
CO 3–2	14.0	>2.5e4	0.68	>1.3e4	4.2e-5	4.5e-4	5.4e-3
CO 4–3 ⁱ	11.0	-	>0.18	-	-	-	-
CO 6–5	10.5	>2.5e4	0.48	2.2e4	1.8e-5	1.1e-4	8.0e-4
CO 7–6	12.1	2.0e4	0.4	1.4e4	2.2e-5	1.7e-4	1.6e-3
Blue Lobe							
CO 2–1	0.5	1.2e4	0.24	1.2e4	1.6e-5	9.3e-5	6.0e-4
CO 3–2	0.3	1.6e4	0.24	1.5e4	1.3e-5	7.6e-5	5.0e-4
CO 4–3	1.7	1.1e4	0.19	1.5e4	1.1e-5	4.5e-5	2.2e-4
CO 6–5	0.5	1.1e4	7e-3	1.1e4	5.4e-7	3.0e-6	2.0e-5
CO 7–6	1.1	1.0e4	1e-2	1.2e4	8.6e-7	4.3e-6	2.4e-5

^a Actual LSR velocities; note that the quiescent gas is at $V_{\text{LSR}}=5.3$ km s⁻¹.

Velocities are not corrected for inclination.

^b Corrected for inclination using the average correction factors of Cabrit & Bertout (1990)

^c Constant temperature of 100 K assumed for red outflow and 70 K for blue outflow.

^d Dynamical time scale : $t_d = R/V_{\max}$

^e Mass outflow rate : $\dot{M} = M/t_d$, not corrected for swept-up gas.

^f Outflow force : $F_{CO} = MV_{\max}^2/R$

^g Kinetic luminosity : $L_{\text{kin}} = 0.5MV_{\max}^3/R$

^h 0.8 M_⊙ is derived for a temperature of 50 K. 2.9 M_⊙ is derived for a temperature of 100 K

ⁱ Outflow extends to far larger scales than map scale.

that the swept-up gas is at a density of a few times 10⁴ cm⁻³ or lower. The presence of a strong quiescent component at positions associated with the outflow is discussed in § 5.6.

The wings of the isotopic lines provide an upper limit to the optical depth, τ_{wing} , of the outflow. The ratio of T_{MB} of the ¹²CO 3–2/¹³CO 3–2 line wings at the source position is shown in Fig. 5.7 as a function of velocity. For a constant density of 3×10⁴ cm⁻³ the observed ratios correspond to τ_{wing} of 1.8 (ratio=10) and 1 (ratio=25). Fig. 5.7 shows that the line ratio increases for more extreme velocities, introducing a dependency of τ_{wing} on velocity. In addition, there is a large jump in τ_{wing} from 6 to 7 km s⁻¹, representing the transition between the optically thick quiescent and more optically thin shocked material. In the following analysis, it is assumed that all shocked outflow emission (>7 km s⁻¹, 1.7 km s⁻¹ with respect to the systemic velocity of 5.3 km s⁻¹) is optically thin for all transitions. The effects of the moderate optical depth of the lines are subsequently discussed.

Fig. 5.8 shows the ratios of the CO 3–2/6–5 main beam antenna temperatures of line wings as functions of velocity for four different positions along the red outflow

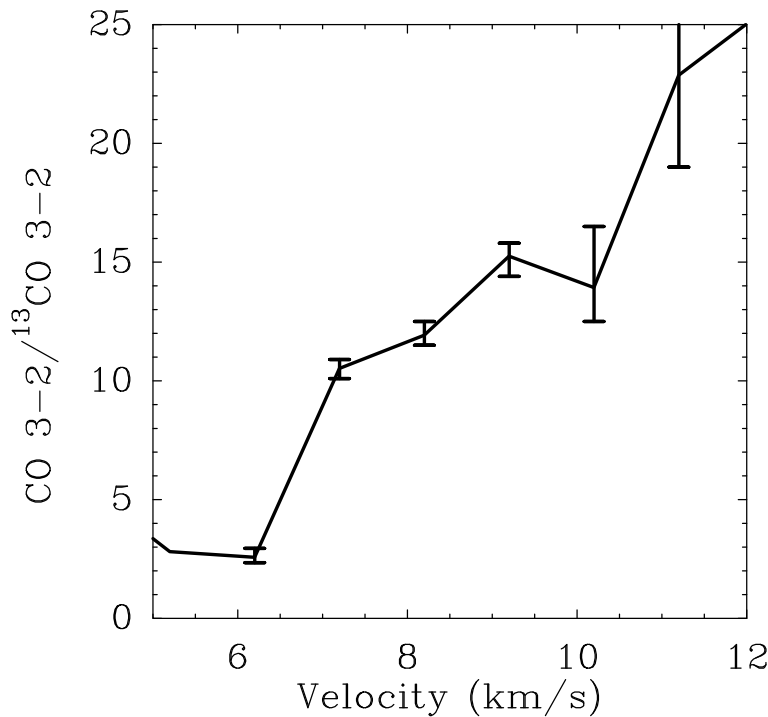


Figure 5.7 — The ratio of the main beam antenna temperatures of ^{12}CO with respect to ^{13}CO for the $J=3-2$ line at the (0,0) position. The ratios correspond to optical depths of 1.8 (ratio of 10) to 1.0 (ratio of 25).

axis ((0,0), (-20,-20), (-30,-30) and (-40'',-35'')). The CO 6–5 data have not been binned to the larger CO 3–2 beam, so the comparison assumes similar volume filling factors of the shocked gas. Ratios are only plotted if the emission in both wings is larger than 3σ . At most positions the ratios are rising at more extreme velocities, indicating a decrease of the excitation temperature T_{ex} of the swept-up gas with distance.

The kinetic temperature T_{kin} of the outflow can be derived by comparing the intensity ratios in the line wings from various transitions with model line intensities of van der Tak et al. (2007). With the density assumed to be constant at a few times 10^4 cm^{-3} , the observed 3–2/6–5 ratios of 2–3 correspond to kinetic temperatures of about 120 to 150 K. Outflow emission is slightly subthermally excited, especially the CO 6–5, with T_{ex} ranging from 85 to 120 K. The rising ratios observed at the more extreme velocities in Fig. 5.8 correspond to lower kinetic temperatures, but even the highest ratios of ~ 7 still indicate kinetic temperatures greater than 70 K. The variation of the optical depth with velocity, as seen in Fig. 5.7, could account for the rising ratios seen in Fig. 5.8, since a higher optical depth will result in a lower ratio for the same temperature. Even with the limit of $\tau_{\text{wing}}=1.7$, the inferred kinetic temperatures will drop by only 20% (see Fig. 4 of Jansen et al. (1996)).

Fig. 5.9 presents the kinetic temperatures as functions of position along the red outflow for a constant density of $2 \times 10^4 \text{ cm}^{-3}$. There is a clear trend towards lower temperatures at larger radii. Averaged between 7 and 9 km s^{-1} , temperatures drop from 170 K close to the source to 80 K at a distance 40''. However, the error bars, derived from the minimum and maximum ratio at velocities greater than 7 km s^{-1} show that

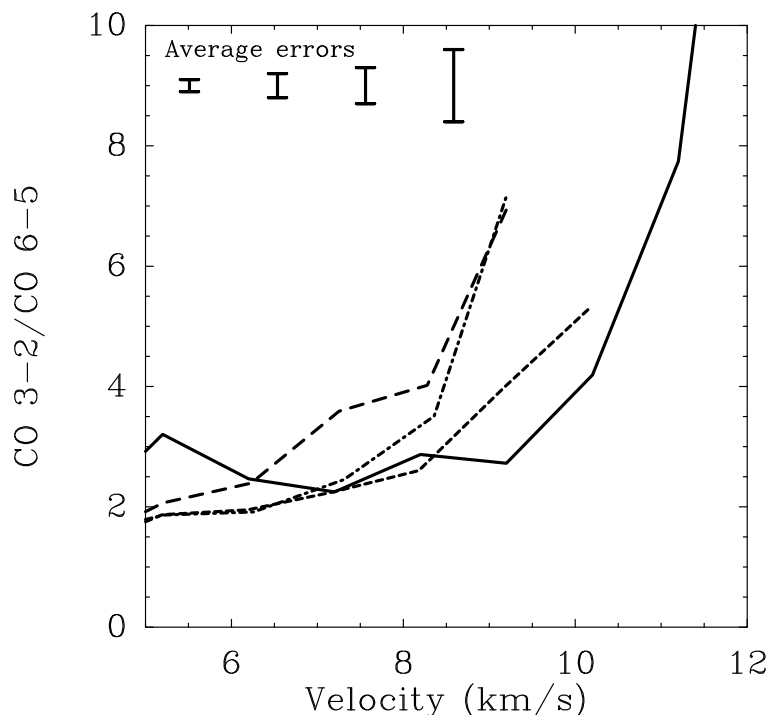


Figure 5.8 — The ratio of the ^{12}CO 3–2/ ^{12}CO 6–5 main beam antenna temperatures at various positions along the red outflow axis (*solid*:(0,0), *dashed*:(-20'',-20''), *dot-dashed*:(-30'',-30''), *long dash*:(-40'',-35'')) as functions of velocity. Average error bars at various velocities are given in the upper part of the figure at their respective velocity. They are applicable for all positions except (0,0), for which errors are a factor of 2 lower due to the longer integration time of CO 3–2 at the center position.

large variations are possible. In addition to the optical depth effects discussed above, it is also possible that the higher ratios at more extreme velocities and larger distances correspond to lower densities $n(\text{H}_2)$. The low density of a few times 10^3 cm^{-3} inferred for the surrounding cloud raises the inferred kinetic temperatures from 80 K to 100–120 K. Such a drop in density significantly would lower the T_{ex} . The current observational data cannot distinguish between these two possibilities, but both options are consistent with a high kinetic outflow temperature of ~ 100 K that is constant with distance from the source. This temperature is significantly higher than the T_{kin} and T_{ex} of ~ 15 K assumed by Olberg et al. (1992) for the CO 2–1/1–0 intensity ratios for the HH 46 outflow. Although some studies find T_{ex} that low (Bachiller et al. 2001), recent studies, at times including high- J CO, also find higher T_{ex} and T_{kin} (e.g. Hirano & Taniguchi 2001; Lee et al. 2002). While a cooler outflow component is not excluded, our data clearly show the presence of warmer outflow gas. Kinetic temperatures as low as 50 K would require outflow densities in excess of 10^5 cm^{-3} , which are excluded by the HCO^+ data.

In a similar analysis, the blue-shifted outflow has kinetic temperatures of 70 to 100 K with a lower limit of 50 K, somewhat cooler than the red lobe. In addition to a variation with velocity, the ratios also seem to vary with distance from the source. At larger distances, the CO 3–2/6–5 intensity ratio is almost a factor of 2 higher than at the source position.

Hatchell et al. (1999) use a swept-up shell model to predict kinetic temperatures

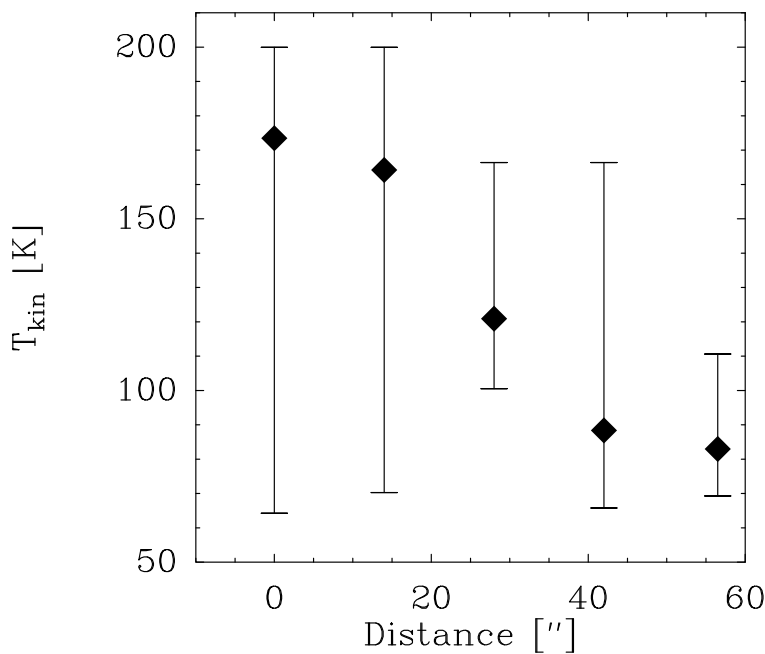


Figure 5.9 — The kinetic temperature of the outflow gas along the red outflow axis computed from the CO 3–2/6–5 line ratio for a constant density of $2 \times 10^4 \text{ cm}^{-3}$. Diamonds are the temperatures derived from the velocity-averaged ratios. The limits are determined from the minimum and maximum ratios between 7 and 11 km s^{-1} . The results are consistent with a constant temperature of $\sim 100 \text{ K}$ if variations in optical depth and density with distance are taken into account.

along the outflow axis and walls. Their predicted values of 50 to 100 K agree very well with our derived temperatures in both outflow lobes (Fig. 5.9). Such temperatures are much lower than calculated for entrainment models, which predict $> 1000 \text{ K}$ (e.g., Lizano & Giovanardi 1995). Arce & Goodman (2002) compare different outflow models and show that at least some flows are best explained with the jet-driven bow shock model. For a thorough review of outflow models, see Arce et al. (2007). The models from Hatchell et al. (1999) predict an almost constant temperature along most of the outflow axis with increasing temperatures near the bow shock, the main site of energy deposition. This is consistent with our constant temperature along the outflow axis, since the actual bow shock lies outside the area observed with CHAMP⁺.

5.5.2 Other outflow properties

Additional properties of both outflow lobes are derived from the molecular emission maps following the recipe outlined in Hogerheijde et al. (1998), in which the radii, masses, dynamical time scales, outflow force and kinetic luminosity are calculated (see Table 5.5). The results are corrected for the inclination of 35° found for this source (Reipurth & Heathcote 1991; Micono et al. 1998) using an average of the three correction factors from Cabrit & Bertout (1990) (their Figures 5–7). These factors range from 1.2 to 2.5, especially for the mass, and are introduced to account for the difference in observed V_{max} on the sky and the actual extreme velocities. Although excitation temperature variations are seen throughout the outflow that depend on velocity and

distance from the source, we assume an average excitation temperature of 100 K for the red outflow lobe and 70 K for the blue outflow lobe for the derivation of these parameters.

The resulting values can be uncertain up to an order of magnitude due to the variations in the covered area and thus in radius, especially for the CO 4–3 (observed with FLASH). The mass estimates of the low excitation CO lines (e.g., the CO 2–1) may be overestimated by up to a factor 4, due to the larger area covered and the assumption that the outflow is iso-thermal at 100 K. CO 2–1 may be dominated by cooler gas with temperatures down to, say, 50 K, lowering the mass estimate to a lower limit $0.8 M_{\odot}$, only 25% higher than the masses found for the high- J CO lines. Temperature differences are likely also responsible for the (smaller) difference in masses in the other lines.

Even with the uncertainties in covered area, the dynamical time scales for these outflows all converge on 10,000 to 20,000 years, with no difference between the red and blue outflow lobes. The values of Table 5.5 are similar to the results found in Cabrit & Bertout (1992) and Hogerheijde et al. (1998) for other Class I outflows and also agree with the results from Olberg et al. (1992) who find $L_{\text{kin}} = 4.5 \times 10^{-3} L_{\odot}$ and dynamical time scales of 4×10^4 yr. Although our dynamical time scales are a factor of 2 smaller, this can be accounted for by the smaller covered area in our observations.

The main discrepancy with older studies is that our outflow mass is up to an order of magnitude higher than that by Olberg et al. (1992). The origin of this difference is two-fold. First, Olberg et al. (1992) do not apply correction factors from Cabrit & Bertout (1990). Second, there is a large difference between assumed temperatures in the red lobe (15 K vs 100 K). Although Olberg et al. (1992) derive their temperature from the CO 1–0 and 2–1 emission, the presence and intensity of CO 4–3, 6–5 and 7–6 outflow emission strongly constrain temperatures to our higher value of 100 K. As illustrated by the CO 2-1 example, this can introduce a significant difference in the masses.

At first sight, there is no difference with the masses derived by Chernin & Masson (1991), but they assumed a similar temperature of 15–30 K as Olberg et al. (1992). However, Chernin & Masson (1991) took an optical depth of ~ 5 for the outflow emission, which is not confirmed by our observed lack of outflow emission in the ^{13}CO lines. For our observed maximum $\tau_{\text{wing}} = 1.7$, the outflow mass as derived from CO 3–2 would increase by a factor of 2 ($\approx \tau / (1 - e^{-\tau})$).

From the dust map, a total (envelope + cloud) mass of $8 M_{\odot}$ is derived (see § 5.3.2). The total outflow mass in Table 5.5 can be as high as $3.2 M_{\odot}$ and thus consist of a significant portion (40%) of that total mass. If the low mass for CO 2–1 is adopted, this percentage drops to 10%.

Bontemps et al. (1996) empirically derive a relation between the flow force, F_{CO} and bolometric luminosity

$$\log(F_{\text{CO}}) = 0.9 \log(L_{\text{bol}}) - 5.6 \quad (5.1)$$

and the envelope mass

$$\log(F_{\text{CO}}) = 1.1 \log(M_{\text{env}}) - 4.15 \quad (5.2)$$

Using the bolometric luminosity of $16 L_{\odot}$ and envelope mass of $\sim 5 M_{\odot}$, flow forces of between 3×10^{-5} and $4 \times 10^{-4} M_{\odot} \text{ yr}^{-1} \text{ km s}^{-1}$ are expected. The parameters for the red outflow lobe indeed show flow forces for most CO transitions that agree with these predictions. Only the flow force of CO 2–1 is a factor of 2.5 higher. If the lower mass of $0.8 M_{\odot}$ is used for this transition due to a lower outflow temperature of 50 K, the flow force similarly drops by a factor of 3.5, almost identical to the flow forces found for the CO 6–5 and 7–6.

The observed flow forces for the blue outflow lobe are up to two orders of magnitude lower than those of the red lobe. This ‘missing’ outflow force can be explained by assuming that the blue-shifted outflow escapes the envelope and surrounding cloud and thus interacts much less with the surrounding cloud due to a lack of cloud material in the path of this outflow lobe.

5.6 Origin of the quiescent high- J CO line emission

5.6.1 Photon heating of cavity walls

The analysis in § 5.4.2 shows that an envelope model derived from the dust emission is not able to fit the quiescent emission of the high-excitation lines by a factor of ~ 2.5 , even though the low-excitation optically thin lines are well-fitted with standard abundances. The limits on the C^{18}O 6–5, combined with the information that the ^{12}CO 6–5 emission from the envelope is optically thick, implies that an additional heating component must be present that produces quiescent emission. There are several constraints on this component. First, it cannot originate in the inner regions of the protostellar envelope or be obscured by the envelope itself, because emission from such a component cannot escape through the optically thick outer envelope emission. Second, it must be (nearly) optically thin, since the observed C^{18}O 6–5 limit is already reached by the envelope itself. Thus, it cannot contribute significantly in mass. Third, it must be extended since a similar warm quiescent component is also clearly seen at off-positions covering the red-shifted outflow through narrow ^{12}CO 6–5 emission, e.g. at positions $(-20''10'')$ and $(-20'', -20'')$ (see Fig. 5.5). Observations of ^{13}CO 6–5 at the off-position also confirm that this quiescent emission cannot be very optically thick ($\tau < 0.4$).

Spaans et al. (1995) investigated the influence of photon heating on the emission of high- J CO lines, in order to explain the bright but narrow ^{12}CO and ^{13}CO 6–5 single spectra observations of Class I sources (Hogerheijde et al. 1998). In this process ultraviolet (UV) photons heat the gas of the outflow cavity walls to temperatures of a few hundred K, but are unable to dissociate the CO molecules. The photons in this model originate in a $\sim 10,000$ K radiation field of the boundary layer in the accretion disk. It was proposed that dust present in the cavity scatters the UV photons towards the cavity walls. The turbulent velocity of the gas at the cavity walls is low, thus explaining the narrow width of the CO 6–5 and 7–6 lines. This extra warm gas due to photon heating could account for the differences in the observed ^{12}CO and ^{13}CO 6–5 emission on source and that modelled by just a protostellar envelope.

Although Spaans et al. (1995) only include photons created in the accretion disk and thus limit their Photon Dominated Region (PDR) to a central region of up to 4,000 AU in size, this model can be extended if additional sources of UV photons are in-

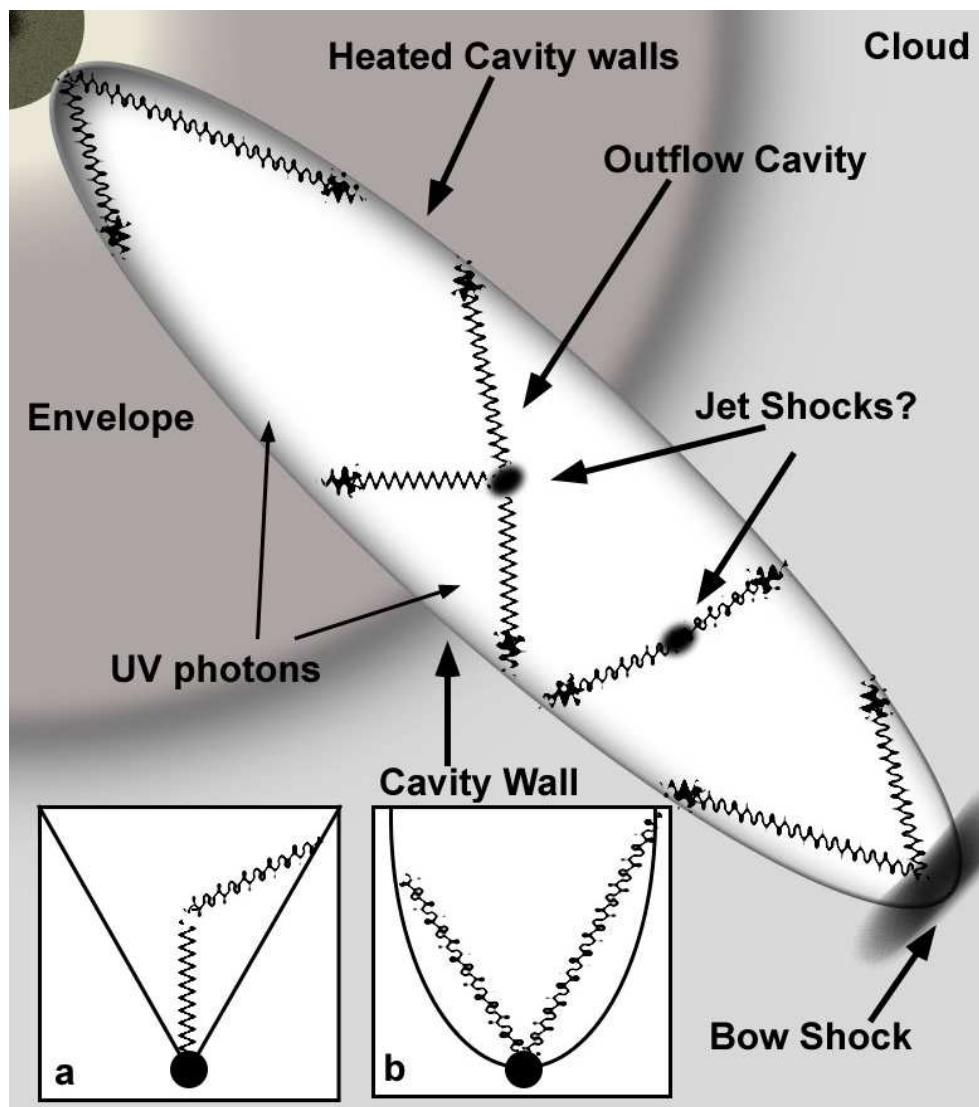


Figure 5.10 — Cartoon model of the HH 46 outflow on scales up to the bow shock ($\sim 60,000$ AU \times $\sim 60,000$ AU), illustrating the photon heating of the cavity walls that is responsible for the high- J CO emission. UV photons are created both in the accretion disk boundary layer, as well as the bow shock and illuminate the cavity walls. Illustrative paths of the UV photons are shown with wiggly lines. In inset **a**, the method of photon heating proposed by Spaans et al. (1995) using an outflow with constant opening angle is shown. There, dust must scatter UV photons to produce significant irradiation of the cavity walls. In inset **b**, a parabolic shape of the outflow cavity allows many more UV photons to directly impact the outflow cavity walls. Due to the expected long mean free path of UV photons within the outflow cavity ($\sim 65,000$ AU), scenario **b** is assumed to be the more likely scenario. See the text for more information.

cluded. Such photons can be produced at bow shock positions of the outflow if J -shocks are present there (Neufeld & Dalgarno 1989). Velusamy et al. (2007) show that apart from the $24 \mu\text{m}$ hotspot of HH 47C, two additional $24 \mu\text{m}$ emission spots can be found within the outflow cavity of HH 46/47, that likely originate in the jet (see Fig. 3 in Velusamy et al. 2007). These positions produce additional UV photons, creating a much more extended PDR. The bow shock at the position of HH 47C, the two new

jet/shock positions and the accretion shock boundary layer combined are excellent sources of the necessary UV photons. Figure 5.10 shows a schematic overview of the red-shifted outflow cavity and the proposed process of photon heating within the HH 46/47 outflow. § 5.6.2 presents constraints on the UV field, while in § 5.6.3 discusses the path of the UV photons in more detail.

5.6.2 Constraining the UV field

The temperature of the cavity walls can be derived from the radiation field originating from these shocks. The radiation field G_0 at the cavity walls can be characterized by

$$G_0 = \sum G_0^i f^i \quad (5.3)$$

with G_0^i the radiation field originating at each shock position i and f^i a geometric dilution factor to account for the difference in the UV emitting surface to the total illuminated surface of the cavity walls. A dissociative shock i produces $3 \times 10^7 (v_s/100 \text{ km s}^{-1})^3 (n_0)$ photons $\text{cm}^{-2} \text{ s}^{-1}$ assuming all energy is emitted at 10 eV (Neufeld & Dalgarno 1989). This is equivalent of a G_0^i of 30,000 assuming a density n_0 of 10^4 cm^{-3} and a shock velocity v_s of 220 km s^{-1} , derived for the bow shock (Fernandes 2000). The average factor of f^i over all shocks is assumed to be 0.005, meaning that the working surface of each shock is $\sim 1/200$ in size compared to the cavity surface. However, not all shocks will have as high velocity as 220 km s^{-1} . It is more likely that the velocities of the secondary shocks within the cavity are much lower. But similarly, the size of the working surfaces of the shocks, and thus the f^i can be larger, resulting in a similar overall strength G_0 , but of a different ‘color’. With four spots, the cavity walls are illuminated by a total G_0 equaling ~ 600 with an uncertainty of a factor of 2 to 3 due to the uncertainty in the f^i . Using the results from Kaufman et al. (1999, their Figure 1), the PDR surface temperature is then constrained to 250–400 K, sufficient to produce the observed lines.

The lack of detected [C I] 2–1 at the outflow positions indicates that the penetrating UV photons are not able to dissociate CO significantly, constraining the color temperature of the radiation field. Neufeld & Dalgarno (1989) show that shocks with velocities less than 90 km s^{-1} do not produce CO dissociating photons. If all shocks have $v_s \approx 80 \text{ km s}^{-1}$ the estimated G_0^i drops by a factor ~ 20 . In that case, the total G_0 is not sufficient to heat the cavity walls to surface temperatures of 250–400 K, but only to about 100 K. Lower velocities are likely for the shocks observed inside the cavity, but the main bow shock position has $v_s = 220 \text{ km s}^{-1}$ (Fernandes 2000) and should thus produce CO dissociating photons. Because this position lies outside the area observed with CHAMP⁺, a possible scenario is that such photons are created in the shock, but cannot propagate towards the observed area of the cavity walls, for example if they are used to dissociate H₂ and CO close to the bow shock position. Additional observations at the bow shock position of [C I] are needed to confirm this scenario. Also, observations of far-IR CO lines, such as are possible with the *HIFI* and *PACS* instruments on *Herschel*, are needed to constrain the exact temperature of CO gas at the cavity walls. Note that the UV radiation from the accretion boundary layer of the disk consists of a $\sim 10,000 \text{ K}$ continuum with strong Lyman α radiation superposed (Bergin et al. 2003; van Zadelhoff et al. 2003), and thus also lacks CO dissociating photons.

Slow ($v_s = 5\text{--}10 \text{ km s}^{-1}$) C-type shocks along the outflow cavity walls are able to generate similar amounts of CO emission (Draine & Roberge 1984). However, the narrow nature of the line profile, as well as the presence of CO 6–5 emission over the entire area traced by the IR outflow, make this scenario less likely than the photon heating, although it could contribute some.

5.6.3 Importance of the outflow geometry

To illuminate a larger area of the cavity wall than possible by direct irradiation Spaans et al. (1995) invoked scattering of the UV photons by the dust present in the outflow cavity, even though such scattering dominated by anisotropic, mainly forward scattering. With a constant opening angle (see inset **a** of Fig. 5.10), only a very small area of the envelope wall will be directly impacted by UV photons. However, with densities of a few 100 cm^{-3} the mean free path of a UV photon until its first scattering event is $\sim 65,000 \text{ AU}$, with the assumption that on average an A_v of 1 produces a single scattering event (Draine 2003). This is significantly larger ($\sim 150''$ on the sky) than the area covered by the outflow cavity.

A parabolic shape of the outflow cavity in the regions near the envelope, as seen in inset **b** of Fig. 5.10, allows much more UV radiation from the accretion boundary layer to illuminate the cavity walls at larger distances of a few thousand AU. A more quantitative description of outflow shapes and its effect on the illumination of the outflow walls is beyond the scope of this chapter.

5.7 Conclusions

In this chapter, we characterize the structure of protostellar envelope and the molecular outflow associated with HH 46 IRS 1, as well as its immediate surrounding cloud material, through dust and molecular line maps. CO lines are observed ranging in transitions from 2–1 to 7–6, including isotopologues. The three distinct components can be best described by the following model:

- **Envelope** - The envelope of HH 46 with $\sim 3\text{--}5 M_\odot$ is one of the most massive ones found for a Class I low-mass protostar, but is densely concentrated toward the center ($n \propto r^{-1.8}$). The C^{18}O line emission from the envelope can be best fitted with a drop abundance of $2.7 \times 10^{-4} / 1 \times 10^{-5}$ above/below 30 K and below/above 10^5 cm^{-3} . However, such abundances are unable to reproduce the observed ^{12}CO and ^{13}CO 6–5 and 7–6 emission. The dense envelope itself is best traced by the HCO^+ 4–3 emission, which has very little outflow contribution and shows a spherical distribution. Densities in the inner few hundred AU of the envelope are high ($> 10^7 \text{ cm}^{-3}$), with high optical depths of the HCO^+ 4–3 and all ^{12}CO lines. A C/ H_2 abundance of a few times 10^{-7} is found, which can be maintained by photodissociation of CO by cosmic ray induced UV photons.
- **Surrounding cloud** - The surrounding cloud does not extend further than $\sim 30''$ north of HH 46 IRS 1 where even no low excitation CO emission is found. Cloud conditions include a low density of a few times 10^3 cm^{-3} , derived from limits on

the CO 6–5 emission at positions such as (30'', -20''). The total column of CO is $\sim 10^{18} \text{ cm}^{-2}$.

- **Outflow** - The red-shifted molecular outflow, extending at least 40'' from the source, produces strong molecular line wings up to CO $J=7-6$ and heats the surrounding cloud and envelope significantly close to the star. Spatially, the red-shifted outflow lobe corresponds to the bright infrared outflow lobe from Noriega-Crespo et al. (2004). Optical depth of the CO 3–2 outflow wing is less than 1.7. Kinetic temperatures of the red-shifted outflow are of order 100–150 K close to the star for flow densities of $2 \times 10^4 \text{ cm}^{-3}$, but drop to 80 K further from the central source if densities and optical depth remain constant. However, the data are also consistent with a constant kinetic temperature in the covered area if densities decrease to a few 10^3 at a distance $>40''$ from the central source, as found for the surrounding cloud.

Temperatures of both outflow lobes are significantly higher than the previously derived temperature of 15 K, but agree well with the model predictions of Hatchell et al. (1999) for a swept-up shell model. The high temperature causes the observed outflow mass to be significantly higher (almost an order of magnitude) than derived in older studies such as Olberg et al. (1992). For each lobe, outflow parameters like outflow force and kinetic luminosity are independently derived from all CO transitions, and agree within an order of magnitude with each other. The red lobe confirms the empirically derived relation between the force of a molecular outflow and the bolometric luminosity. The blue lobe does not. The lack of material in the path of the blue-shifted molecular outflow is responsible for the different parameters between the red and blue lobes.

- **Origin of high- J CO** - The emission seen in the higher excitation CO transition has three main origins.
 1. The dense envelope produces optically thick emission in both CO 6–5 and 7–6, originating in the warm ($T > 50 \text{ K}$) inner envelope, accounting for roughly 1/3 of the observed line intensities on source.
 2. High- J CO emission is detected in the red- and blue-shifted outflow wings at some positions along the outflow axis.
 3. The bulk of the high- J CO emission has narrow lines and is produced by photon heating. UV photons originating in the bow shocks, jet shocks and accretion boundary layer heat the cavity walls up to a few hundred K. The lack of strong associated [C I] emission indicates that the UV photons do not photodissociate CO, suggesting shock velocities lower than 90 km s^{-1} such as could be present inside the cavity. Although the velocity of the bow shock has been observed to be as high as 220 km s^{-1} , these photons apparently do not reach the observed area of the cavity walls in our map.

This chapter shows that the addition of the high- J CO emission lines as observed with CHAMP⁺ provides new insights into the physical structure of the protostellar enve-

lope and molecular outflow of HH 46. The presence of narrow line emission in the high- J CO lines throughout the outflow suggests that photon heating is an important process in HH 46. The high- J isotopic CO lines, in particular those of C¹⁸O 6–5, have been key in constraining the envelope model. Future high-frequency observations using CHAMP⁺ and, in the long run, ALMA band 9, will provide unique constraints on the interaction between outflow and envelope.

Acknowledgements

TvK and astrochemistry at Leiden Observatory are supported by a Spinoza prize and by NWO grant 614.041.004. CHAMP⁺ is built with NWO grant 600.063.310.10. TvK is grateful to the APEX staff for carrying out the bulk of the low-frequency observations and Friedrich Wyrowski for extensive help with the CHAMP⁺ observations. Carlos de Breuck is thanked for providing the APEX-1 observations on a very short notice within the science verification project E-81.F-9837A. We appreciate the input of Steve Doty into an illuminating and essential discussion about outflow cavity shapes. We are grateful for support from Ronald Stark throughout construction of CHAMP⁺.

Chapter 6

The warm gas within young low-mass protostars: using CHAMP+ to observe extended high- J CO in envelopes and outflows

Abstract Embedded Young Stellar Objects (YSOs) have warm ($50 < T < 200$ K) gas in bipolar outflows, heated by shocks, and in the inner regions of the protostellar envelope, heated by the central star. The characteristics of this warm gas are often inferred from the emission of the cold gas, complex molecules or spectral energy distributions, but few direct observations exist. Since warm gas reveals much about the heating processes within the inner regions of protostars, such observations provide unique insights into the physical structure at $\sim 1'$ scales. We aim to characterize the warm gas within protostellar objects, and disentangle contributions from the (inner) envelope, bipolar outflows and the quiescent cold cloud. High- J CO maps (^{12}CO $J=6-5$ and $7-6$) of the immediate surroundings (up to 10,000 AU) of eight YSOs were obtained with the CHAMP+ array mounted on APEX. In addition isotopologue observations of ^{13}CO $6-5$ and $[\text{C I}]$ $2-1$ were taken. A strong quiescent narrow ^{12}CO $6-5$ and $7-6$ emission is seen for all protostars. In the case of HH 46 and Ced 110 IRS 4, the on-source emission originates in material heated by UV photons scattered in the outflow cavity and not just by passive heating in the inner envelope. Warm quiescent gas is also present in the outflows, heated by UV photons from shocks, as clearly evidenced by BHR 71 for which quiescent emission becomes stronger at more distant outflow positions. Shock-heated warm gas is only detected for Class 0 flows and the more massive Class I sources of L 1551 IRS 5 and HH 46. Outflow temperatures, estimated from the CO $6-5$ and $3-2$ line wings, are ~ 100 K, close to model predictions, with the exception of the L 1551 IRS 5, for which temperatures < 50 K are found. The capabilities of the CHAMP+ array to observe small ($\sim 1' \times 1'$) regions in the 650 and 850 GHz atmospheric bands provide a unique probe into the heating and physical structure of the inner few thousand AU.

T. A. van Kempen, E. F. van Dishoeck, R. Güsten, L. E. Kristensen, M. R. Hogerheijde, F. Wyrowski, P. Schilke, W. Boland & K. M. Menten, in prep

6.1 Introduction

Low-mass ($M < 3 M_{\odot}$) Stage 0 and Stage 1 protostars (Robitaille et al. 2006) have two distinct components. First, they are surrounded by a protostellar envelope, consisting of a reservoir of gas and dust, which can feed the star and disk. The envelope can be divided into cold ($T \sim 10 - 20$ K) outer regions and a warm ($T > 50$ K) inner region (Adams et al. 1987; Shirley et al. 2000; Schöier et al. 2002; Shirley et al. 2002; Jørgensen et al. 2002; Whitney et al. 2003a; Robitaille et al. 2006). Second, most, if not all, embedded protostars have molecular outflows (Bachiller & Tafalla 1999). These outflows have been observed to have a wide variety in intensity, collimation and affected area, from the strong and large outflows seen for L 1448, L 1551 IRS 5 and HH 46 (Bachiller et al. 1994; Heathcote et al. 1996, Chapter 5) to the weak outflows, as found for TMR 1 and TMC-1 (Cabrit & Bertout 1992; Hogerheijde et al. 1998). Such molecular outflows are observed to influence the evolution of the envelope (e.g., Arce & Sargent 2005).

Envelope models can be constructed using either a 1-D or 2-D self-consistent dust radiative transfer calculation, and are tested using observations of the cold dust (e.g. Shirley et al. 2002; Jørgensen et al. 2002) and/or the Spectral Energy Distribution (SED) (e.g. Whitney et al. 2003b,a; Robitaille et al. 2006; Crapsi et al. 2008). Combining heterodyne observations with radiative transfer calculations, one can in turn analyze line emission of a large range of molecules and determine their origin and excitation conditions, both in the inner and outer regions of protostellar envelopes as well as in circumstellar disks and fore-ground components (e.g. Boogert et al. 2002; Jørgensen 2004; Maret et al. 2004; Brinch et al. 2007; Lee et al. 2007). Envelope models predict that the inner regions are warm ($T > 100$ K), dense ($n(\text{H}_2) > 10^6 \text{ cm}^{-3}$) and relatively small ($R < 500$ AU). Most molecular lines trace the colder gas, but a few lines, such as the high- J CO lines, directly probe the warm gas. The atmospheric windows at 650 and 850 GHz are the highest atmospheric windows in which observations of CO up to energy levels of ~ 150 K can be routinely carried out. Unfortunately, few studies have successfully observed CO transitions or its isotopologues in these atmospheric windows due to the excellent weather conditions necessary. In addition, such studies are often limited to single spectra of only a handful of YSOs (e.g. Schuster et al. 1993, 1995; Hogerheijde et al. 1998; Ceccarelli et al. 2002; Stark et al. 2004; Parise et al. 2006, Chapter 3 and 4). The lack of spatial information on the warm gas distribution prevented an in-depth analysis. Comparison between such ground-based high- J CO observations and far-IR CO transitions (CO 15–14 and higher) do not always agree (see Chapter 3).

Complex molecules such as H_2CO and CH_3OH , emit in high excitation lines at longer wavelengths, and have been observed to have surprisingly high abundances in low-mass protostars (e.g. van Dishoeck et al. 1995; Blake et al. 1995; Ceccarelli et al. 2000; Schöier et al. 2002; Maret et al. 2004; Jørgensen 2004; Bottinelli et al. 2004, 2007). Unfortunately, the abundances of these molecules are influenced by the gas-phase and grain surface chemistry, complicating their use as tracers of the physical structure (e.g., Bisschop et al. 2007). It has been proposed that the emission of such molecules originates inside a hot core region, a chemically active area close to the star, coinciding with the passively heated warm inner region of the protostellar envelope where ices have evaporated (Ceccarelli et al. 2000; Bottinelli et al. 2004, 2007). However, to fully under-

stand the origin of these complex organics, knowledge of the structure of the warm gas is an essential ingredient.

Warm gas near protostars can have different origins than passive heating alone. Outflow shocks passing through the envelope can be a source of heat. Quiescent gas, heated by X-rays of UV, is present in the inner envelope. For example, Stauber et al. (2004) show that significant amounts of Far Ultra-Violet (FUV) or X-ray photons are necessary to reproduce the line intensities and the derived abundances of molecules, such as CO^+ , CN , SH^+ and NO in both high and low-mass protostars. Spaans et al. (1995) investigated photon heating of outflow cavity walls to reproduce the observed line intensities and widths of ^{12}CO 6–5 and ^{13}CO 6–5 in Class I sources (Hogerheijde et al. 1998). In Chapter 5, an extension of this model is proposed in which a Photon Dominated Region (PDR) at the outflow/envelope cavity walls is present in the HH 46 outflow cavity to explain the relatively strong and quiescent high- J CO emission. The emission of [C I] can constrain the color and extent of the more energetic photons. Apart from the accretion disk, UV photons are also produced by the shocks in the outflow cavity and the outflow bow shock. All these models provide different predictions for the spatial extent of the warm gas ($\sim 1'$ for the outflow to $< 1''$ for a passively heated envelope), as well as the different integrated intensities and line profiles of the high- J CO transitions.

The most direct tracers of the warm ($50 < T < 200$ K) gas are thus the high- J CO lines. So far, studies to directly detect the warm gas components through these lines have rarely been able to disentangle the envelope and outflow contributions. Far Infrared (IR) transitions of even higher- J CO, the far-IR CO lines, have been observed using the ISO-LWS instrument to trace the inner regions (e.g., Ceccarelli et al. 1998; Giannini et al. 1999; Nisini et al. 1999; Giannini et al. 2001; Nisini et al. 2002), but could not unambiguously constrain the origin of the warm gas emission, due to the limited spatial and spectral resolution.

The Chajnantor plateau in northern Chile and the site of the recently commissioned Atacama Pathfinder Experiment (APEX)¹ is currently the only site able to perform routine observations within the high frequency atmospheric windows at high ($\leq 10''$) spatial resolutions. The CHAMP⁺ instrument, developed by the MPIfR and SRON Groningen, is the only instrument in the world able to simultaneously observe molecular line emission in the 650 and 850 GHz atmospheric windows on arcminute spatial scales and is thus ideally suited to probe the warm gas directly through observations of the 6–5, 7–6 and 8–7 transitions of CO and its isotopologues with 7–9'' angular resolution (Kasemann et al. 2006; Gusten et al. 2008). CHAMP⁺ has 14 pixels (7 in each frequency window) and is thus capable of fast mapping of the immediate surroundings of embedded YSOs. The *Herschel Space Observatory* will allow observations of far-IR CO lines at spectral and spatial resolution similar to submillimeter ground-based facilities ($\sim 10''$). Note also that the beam of Herschel is comparable or smaller than the field of view of CHAMP⁺ at its longer wavelengths ($\sim 500\mu\text{m}$). Thus the CHAMP⁺ data obtained here provide information of the distribution of warm gas within the Herschel

¹This publication is based on data acquired with the Atacama Pathfinder Experiment (APEX). APEX is a collaboration between the Max-Planck-Institut fur Radioastronomie, the European Southern Observatory, and the Onsala Space Observatory.

Table 6.1 — Adopted Champ⁺ settings

Setting	Lines	Freq. (GHz)	Mode
A	¹² CO 6–5	691.4730	OTF/Hexa
A	¹² CO 7–6	806.6652	OTF/Hexa
B	¹³ CO 6–5	661.1067	Hexa
B	[C I] 2–1	809.3435	Hexa
C	C ¹⁸ O 6–5	658.5533	Stare
C	¹³ CO 8–7	881.2729	Stare

beams.

In this chapter, we present observations of CO and its isotopologues using CHAMP⁺ for eight embedded YSOs. §6.2 presents the sample and observations. The resulting spectral maps are shown in §6.3. §6.4 discusses the envelope and outflow structure, while the heating within protostellar envelopes and molecular outflows is analyzed in §6.5. §6.6 investigates the relation between the emission of more complex molecules and the emission of high-*J* CO. Final conclusions are given in §6.7.

6.2 Sample and observations

6.2.1 Observations

The sample was observed using the CHAMP⁺ array on APEX (Kasemann et al. 2006). CHAMP⁺ observes simultaneously in the 650 GHz (450 μ m, CHAMP⁺-I) and 850 GHz (350 μ m, CHAMP⁺-II) atmospheric windows. The array has 7 pixels for each frequency, arranged in a hexagon of 6 pixels around 1 central pixel, for a total of 14 pixels. During the observations, the backend consisted of 2 FFTS units in the central pixel, and 12 MACS units in the other pixels. The FFTS units are capable of observing up to a resolution of 0.04 km s⁻¹ (0.12 MHz) and the MACS units to a spectral resolution of 0.37 (1 MHz), both at a frequency of 806 GHz. The observations were done during three observing runs in June 2007, October–November 2007 and July 2008 in three different line settings, see Table 6.1. Note that in July 2008, all pixels were attached to FFTS units and no MACS backends were used. For mapping purposes, the array was moved in a small hexagonal pattern to provide a fully Nyquist sampled map or in an on-the-fly (OTF) mode. The ‘hexa’ pattern covers a region of about 30'' \times 30''. For some sources, a slightly larger area was mapped in a small OTF (40'' \times 40'') map in ¹²CO 6–5/7–6. At the edge of the maps, noise levels are often higher due to the shape of the CHAMP⁺ array. NGC 1333 IRAS 2, TMR 1 and RCrA IRS 7 were observed using the hexa mode and have smaller covered areas. Due to the different beams at 690 and 800 GHz, small differences exist between the areas covered in CO 6–5 and 7–6. For the C¹⁸O 6-5 /¹³CO 8–7 (setting C), a stare mode was used to increase the S/N within the central pixel. A position switch of 900'' was used for all settings, except for the stare setting C, which used a beam-switching of 90''.

Table 6.2 — The sample of sources observed with CHAMP+.

Source	RA (J2000)	Dec (J2000)	D (pc)	L_{bol} (L_{\odot})	T_{bol} (K)	Class
NGC 1333 IRAS 2	03:28:55.2	+31:14:35	250	12.7	62	0
L1551 IRS 5	04:31:34.1	+18:08:05.0	160	20	75	1
TMR 1	04:39:13.7	+25:53:21	140	3.1	133	1
HH 46	08:25:43.8	-51:00:35.6	450	16	102	1
Ced 110 IRS 4	11:06:47.0	-77:22:32.4	130	0.8	55	1
BHR 71	12:01:36.3	-65:08:44	200	11	60	0
IRAS 12496-7650	12:53:17.2	-77:07:10.6	250	24	326 ^b	1
RCrA IRS 7A ^c	19:01:55.2	-36:57:21.0	170	-	-	0
	Sett. ^a	Ref. Cont.		Ref.CO		
NGC 1333 IRAS 2	A	1,2,3,4,5,6,7		vii		
L1551 IRS 5	A	2,8,9,10,11,12		i		
TMR 1	AB	13,14,15,16		i		
HH 46	ABC	1,17,18		ii,iii		
Ced 110 IRS 4	AB	7,19,20,21,22		iii,iv		
BHR 71	AB	17,23,24,25		v		
IRAS 12496-7650	AB	26, this work		iii,viii		
RCrA IRS 7A ^c	A	1,7,27,28		iii, viii		

^a Observed settings with CHAMP+. See Table 6.1

^b IRAS 12496-7650 is likely to be viewed face-on and thus has strong IR emission and a high T_{bol} . See Chapter 4

^c RCrA IRS 7 is a binary. Pointing was chosen to be on RCrA IRS 7A, believed to be the main embedded source, following results from Chapter 4 and Groppi et al. (2007). RCrA IRS 7B is located 15'' to the east. At mid- and far-IR wavelengths, the source is heavily confused with RCrA. Therefore, no reliable T_{bol} and L_{bol} could be derived.

Continuum References: 1: Di Francesco et al. (2008) 2: Motte & André (2001) 3: Gutermuth et al. (2008) 4: Enoch et al. (2006) 5: Hatchell et al. (2007b) 6: Sandell & Knee (2001) 7: Froebrich (2005) 8: Chandler & Richer (2000) 9: Reipurth et al. (2002) 10: Osorio et al. (2003) 11: Liu et al. (1996) 12: Butner et al. (1991) 13: Kenyon et al. (1994) 14: Hogerheijde et al. (1999) 15: Furlan et al. (2008) 16: Terebey et al. (1993) 17: Henning & Launhardt (1998) 18: Chapter 5 19: Reipurth et al. (1993) 20: Luhman et al. (2008) 21: Lehtinen et al. (2001) 22: Lehtinen et al. (2003) 23: Evans et al. (2007) 24: Bourke et al. (1997) 25: Bourke (2001) 26: Henning et al. (1993) 27: Nutter et al. (2005) 28: Groppi et al. (2007)

CO references : i: Hogerheijde et al. (1998) ii: Chapter 4 iii: Chapter 5 iv: Hiramatsu et al. (2007) v: Parise et al. (2006) vi: Knee & Sandell (2000) vii: Giannini et al. (2001) viii: Giannini et al. (1999)

Beam efficiencies were derived using observations on planets and are 0.56 for CHAMP⁺-I and 0.43 for CHAMP⁺-II. Typical single side-band system temperatures are 700 K for CHAMP⁺-I and 2100 K for CHAMP⁺-II. The 12-m APEX dish produces a beam of 9'' at 650 GHz and 7'' at 850 GHz. Pointing was checked on various planets and sources and was found to be within 3''. Calibration of the sources was done against similar observations, as well as hot and cold loads and estimated to be within 30% for both

Table 6.3 — Properties of the ^{12}CO lines^a.

Source	Offpos. (",")	V_{LSR} km s ⁻¹	CO 6–5				
			$\int T_{MB}dV$ K km s ⁻¹	T_{peak} K	red K km s ⁻¹	blue K km s ⁻¹	RMS ^b K
NGC 1333 IRAS 2	0,0	7.0	34.3	6.8	8.9	13.2	0.6
	0,20	7.0	43.7	9.8	20.0	-	0.6
	-20,-20	7.0	36.3	7.6	2.2	11.0	0.7
L 1551 IRS 5	0,0	6.2	16.5	3.6	3.2	3.6	0.1
	-20,-20	6.0	14.2	3.2	2.0	5.3	0.2
	10, 20	6.5	12.3	3.0	4.2	1.7	0.2
TMR 1	0,0	4.5	23.4	8.1	2.5	5.2	0.3
HH 46	0,0	4.4	45.3	9.3	10.6	10.4	0.3
	-20,-20	4.4	33.4	9.1	11.1	-	0.5
Ced 110 IRS4	0,0	3.5	20.8	7.8	-	4.8	0.4
BHR 71	0,0	-4.5	38.6	5.2	9.1	12.7	0.4
	10, -40	-4.5	96.3	16.5	-	68.1	1.0
	0, 40	-4.5	75.8	13.0	41.5	-	1.0
IRAS 12496-7650	0,0	1.8	22.1	5.9	-	-	0.5
RCRA IRS 7A ^c	0,0	5.7	337.9	36.3	33.6	10.9	0.3

Source	Offpos. (",")	V_{LSR} km s ⁻¹	CO 7–6				
			$\int T_{MB}dV$ K km s ⁻¹	T_{peak} K	red K km s ⁻¹	blue K km s ⁻¹	RMS ^b K
NGC 1333 IRAS 2	0,0	7.0	29.2	6.3	8.8	5.2	1.7
	0,20	7.0	65.8	10.1	27.8	5.2	1.7
	-20,-20	7.0	-	-	-	-	3.5
L 1551 IRS 5	0,0	6.2	17.8	4.5	2.4	4.5	0.4
	-20,-20	6.0	8.4	5.2	-	3.5	0.6
	10, 20	6.5	12.6	3.4	5.0	3.2	0.5
TMR 1	0,0	4.5	19.8	10.1	1.5	1.8	0.7
HH 46	0,0	4.4	34.2	8.4	-	9.9	0.8
	-20,-20	4.4	29.8	6.2	15.7	-	1.0
Ced 110 IRS4	0,0	3.5	23.1	7.1	-	-	1.0
BHR 71	0,0	-4.5	36.6	4.4	5.4	-	0.7
	10, -40	-4.5	41.5	7.0	5.6	17.2	2.8
	0, 40	-4.5	54.7	9.1	27.0	-	3.0
IRAS 12496-7650	0,0	1.8	19.9	6.1	-	-	1.4
RCRA IRS 7A ^c	0,0	5.7	407.6	46.3	29.0	22.2	0.7

^a Red is the redshifted outflow lobe calculated from -10 to -1.5 km s⁻¹ with respect to the source velocity. Blue is the blueshifted outflow lobe calculated from +1.5 to +10 km s⁻¹ with respect to the source velocity.

^b 1σ in a 0.8 km s⁻¹ channel.

^c Outflowing gas refers to emission in -20 to -8 km s⁻¹ and +8 to +20 km s⁻¹ from line center.

frequencies. The difference in CO 7–6 emission of 60% for IRAS 12496-7650 in Chapter 4 and this chapter can be accounted for by the respective calibration and pointing errors of FLASH and CHAMP⁺. A factor of 2 difference is found with the observations of TMR 1 in Hogerheijde et al. (1998). Since a similar factor of 2 is seen between the observations of T Tau in Schuster et al. (1995) and Hogerheijde et al. (1998), it is most

likely that the side-band ratio for the observations taken by Hogerheijde et al. (1998) were incorrectly calibrated. Currently, the data taken in July 2008 (L 1551 IRS 5 ^{12}CO 6–5 and 7–6 and TMR 1 ^{13}CO 6–5 and [C I] 2–1), have a de-rotation problem in the calibrator data. Although these data are presented for completeness, the corresponding maps are subject to change.

6.2.2 Sample

The sample consists of eight well-known and well-studied embedded protostars, with a slight bias toward the southern sky. A variety of protostars in mass, luminosity, evolutionary stage and parental cloud is included. All sources have been studied in previous surveys of embedded YSOs in the sub-mm (e.g., Jørgensen et al. 2002, 2004; Groppi et al. 2007). More information on southern sources can be found in Chapters 3 (IRAS 12496-7650), 4 (IRAS 12496-7650, RCrA IRS 7 and Ced 110 IRS 4) and 5 (HH 46). Table 6.2 gives the parameters of each source and its properties. References to previous continuum studies (column 7) include infrared (IR) photometry and (sub)millimeter dust continuum, and studies of CO emission (column 8) include both submillimeter and far-IR lines.

6.2.3 Spectral energy distribution

For all sources, SED information was acquired from the literature, ranging from near-IR to the (sub-)mm. Spitzer-IRAC (3.6, 4.5, 5.6, 8.0 μm), Spitzer-MIPS (24, 70 and 160 μm), submillimeter photometry from JCMT-SCUBA (Di Francesco et al. 2008), SEST-MAMBO and IRAM-30m are all included, if available. For sources with no reliable Spitzer fluxes, IRAS fluxes at 12, 25, 60 and 100 μm were used. In addition to the obtained fluxes, the bolometric luminosity and temperature, L_{bol} and T_{bol} were calculated using the mid-point method (Dunham et al. 2008). The results can be found in Table 6.2. Note that due to a lack of mid- and far-IR fluxes with sufficient spatial resolution, the derived values for IRAS 12496-7650 and Ced 110 IRS 4 are highly uncertain, with expected errors of 50%, while no T_{bol} and L_{bol} could be determined for RCrA IRS 7. For other sources, errors are on the order of 10-20%.

Table 6.4 — CO isotopologue and [C I] properties at the source position.

Source	^{13}CO 6–5			^{13}CO 8–7	C^{18}O 6–5	[C I] 2–1
	$\int T_{\text{MB}}dV$ K km s $^{-1}$	T_{peak} K	FWHM km s $^{-1}$	$\int T_{\text{MB}}dV$ K km s $^{-1}$	$\int T_{\text{MB}}dV$ K km s $^{-1}$	$\int T_{\text{MB}}dV$ K km s $^{-1}$
TMR 1 ^b	4.3	1.9	2.0	-	-	2.9
HH 46	3.9	3.1	1.5	<0.3 ^a	<0.15 ^a	2.3
Ced 110 IRS4	5.2	2.1	2.3	-	-	2.5
BHR 71	1.4	1.5	0.8	-	-	<0.6 ^a
IRAS 12496-7650	3.8	1.7	2.1	-	-	<0.6 ^a

^a 1σ level in a 0.7 km s $^{-1}$ bin.

^b TMR 1 data suffer from a de-rotational problem in the calibration data and are subject to change.

6.3 Results

6.3.1 Maps

Figure 6.1 to 6.8 show the integrated intensity and the red- and blue-shifted outflow maps of CO 6–5, as well as the spectra at the central position of all observed emission lines. Both the integrated intensity and outflow maps were spatially rebinned to a resolution of $10''$. Figures 6.9 to 6.12 show the CO 6–5 and 7–6 spectra taken in the inner $40'' \times 40''$ of all the sources, also binned to square $10'' \times 10''$ bins.

Table 6.3 presents the intensities of both CO lines. Here, the total integrated emission, the peak main beam temperature, the emission in the red and blue outflow wings shown in the outflow maps and the noise levels are given for the central position, as well as clear outflow positions. The limits for the red and blue outflow were chosen to be -10 to -1.5 km s^{-1} with respect to the source velocity for the blueshifted emission and $+1.5$ to $+10$ km s^{-1} with respect to the source velocity for the redshifted emission for most sources. These limits were chosen after examination of the profiles of the spectra and subtracting gaussians that were fitted to the central 3 km s^{-1} of the profile. For all sources, except RCrA IRS 7, the difference in the blue- and red-shifted emission between the two methods was less than 5 %. The outflowing gas of RCrA IRS 7 was derived by limiting the red- and blue-shifted emission to -20 to -8 and $+8$ to $+20$ km s^{-1} . This corresponds to a $\text{FWHM} \approx 8$ km s^{-1} for the quiescent material. Broad line widths are also seen for the rarer isotopologues C^{18}O and C^{17}O , for which line widths of 3 km s^{-1} is seen, much wider than typically observed for these species (Schöier et al. 2006). Noise levels (see Table 6.3) differ greatly between sources and even within single maps.

^{12}CO 6–5 and 7–6 was detected at the central position of all sources, ranging from 16.5 K km s^{-1} ($T_{\text{peak}}=3.6$ K) for L 1551 IRS 5 for CO 6–5 to 407.6 K km s^{-1} ($T_{\text{peak}}=46.3$ K) for RCrA IRS 7A for the CO 7–6 line. All maps show extended emission, except for IRAS 12496-7650, which shows unresolved emission in the CO 7–6 transition. However, the scales on which extended emission is seen varies significantly, with detections at all mapped positions for RCrA IRS 7 to only 1 or 2 for IRAS 12496-7650, TMR 1 and Ced 110 IRS 4. All sources except RCrA IRS 7 and NGC 1333 IRAS 2 show spectra with a single peak over the entire map, while the latter two have spectra that are self-absorbed.

Figures 6.9 to 6.12 clearly identify the variation of the line profiles across the maps, especially when outflowing gas is present, such as in the maps of NGC 1333 IRAS 2, BHR 71, HH 46 and RCrA IRS 7. The sources for which little to no shocked emission is seen do show spatially resolved CO 6–5 and 7–6 emission, but always quiescent narrow emission and located close to the central pixel, except in the case of L 1551 IRS 5.

6.3.2 Outflow emission

From the outflow maps in Fig. 6.1 to 6.8, it can be concluded that the contributions from shocks within the bipolar outflows to the warm gas differ greatly from source to source. RCrA IRS 7, NGC 1333 IRAS 2, HH 46, L 1551 IRS 5 and BHR 71 produce spatially resolved flows, but TMR 1, IRAS 12496-7650 and Ced 110 IRS 4 do not have warm shocked gas that result in high- J CO in any of the off-positions. Small shocks on the

source position are seen, but are generally weak. For all sources in the sample, outflow emission has been detected in low ($J_{\text{up}} \leq 3$) excitation CO lines, although such flows have large differences in spatial scales, ranging from tens of arcminutes to the central twenty arcseconds (e.g. Moriarty-Schieven & Snell 1988; Fridlund et al. 1989; Cabrit & Bertout 1992; Bachiller et al. 1994; Bourke et al. 1997; Hogerheijde et al. 1998; Parise et al. 2006, Chapter 4). Table 6.3 gives the integrated intensities of the CO emission at selected off-positions for the outflowing gas.

6.3.3 Isotopologue observations at the central position

For HH 46 transitions of ^{13}CO $J=6-5$ and $8-7$ and C^{18}O $J=6-5$ as well as [C I] $2-1$ were observed (see Table 6.1 and 6.2). TMR 1, Ced 110 IRS 4, IRAS 12496-7650 and BHR 71 were observed in ^{13}CO $6-5$ and [C I] $2-1$. The results at the central position can be found in Fig. 6.1 to 6.8, as well as Table 6.4. All ^{13}CO $6-5$ spectra can be fitted with single gaussians. However, the width of the gaussians varies with a FWHM of ~ 1.2 km s^{-1} for HH 46 and BHR 71 to ~ 2.2 km s^{-1} for Ced 110 IRS 4 and IRAS 12496-7650. [C I] $2-1$ is detected for TMR 1, HH 46 and Ced 110 IRS 4 ($\sim 3\sigma$). No line was found for IRAS 12496-7650 and BHR 71 down to a 1σ limit of 0.6 K in 0.7 km s^{-1} bins. Integrated line strengths are on the order of 3 K km s^{-1} with widths of 0.75 km s^{-1} . ^{13}CO $8-7$ and C^{18}O $6-5$ were observed towards HH 46 only, but not detected down to a 1σ level of 0.15 and 0.3 in a 0.7 km s^{-1} channel.

6.3.4 ^{13}CO 6-5 and [C I] 2-1 maps

For ^{13}CO $6-5$ and [C I] $2-1$ maps were also obtained. Spectra at the central position are given in Figs. 6.1 to 6.8. Integrated intensity maps are presented in Fig. 6.13 (^{13}CO $6-5$) and Fig. 6.14 ([C I] $2-1$). It is seen that such observations are often dominated by centrally located unresolved emission, but not always peaked at the source. Both HH 46 and BHR 71 also show some isotopic emission associated with the outflow. For HH 46, ^{13}CO $6-5$ is only detected off-source for the blue outflow, where part of the outflow is unobscured by cloud or envelope (see Chapter 5).

6.4 Envelope

6.4.1 Envelope models

In order to investigate whether high- J CO emission can be reproduced by a passively heated envelope, the properties of the protostellar envelopes were calculated by modelling 850 μm continuum images and SED information. The 1-D dust radiative transfer code DUSTY described in Ivezić & Elitzur (1997) (Schöier et al. 2002; Jørgensen et al. 2002). Although NGC 1333 IRAS 2, L1551 IRS 5 and TMR 1 were included in a similar study by Jørgensen et al. (2002), new fluxes from Spitzer (e.g., Luhman et al. 2008; Gutermuth et al. 2008, see Table 6.2) have since come available and must be included. To constrain the models both the SED from ~ 50 μm to 1.3 mm and the spatial distribution of the sub-mm continuum emission at 850 μm were used, with the exception of BHR 71 and Ced 110 IRS 4, for which no 850 μm map is available. A normalized radial emission profile with a power law index of 1.5 is assumed for these two sources. The

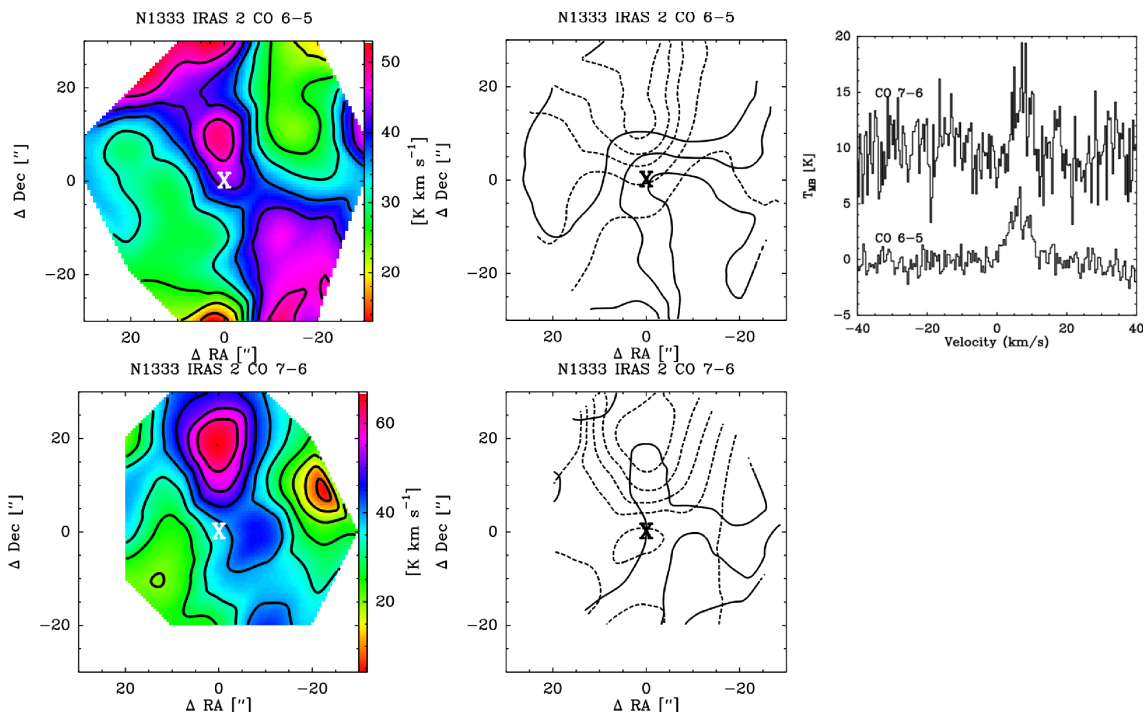


Figure 6.1 — Maps of CO 6–5 (*top row*) and CO 7–6 (*bottom row*) of NGC 1333 IRAS 2. The left-most image shows the total integrated intensity over the line. The middle figures show the outflow contributions from the red (*dashed lines*) and blue (*solid lines*) outflow. Contours are in increasing levels of 4 K km s⁻¹ for both transitions. The outflow contributions are calculated by only including emission greater or smaller than ± 1.5 km s⁻¹ from the central velocity. The right-most image at the top row shows the ¹²CO spectra at the central position.

radial profiles of L 1551 IRS 5, RCrA IRS 7A, NGC 1333 IRAS 2 and TMR 1 were obtained from 850 μm images of the processed SCUBA archive (Di Francesco et al. 2008). For HH 46 and IRAS 12496-7650, recent data from LABOCA at 870 μm were used (see Chapter 5 and Appendix B).

The parameters of the best-fitting envelope models can be found in Table 6.5, together with the corresponding physical parameters of the envelope. The three main parameters of DUSTY, Y , the ratio over the inner to outer radius, p , the power law exponent of the density profile $n \propto r^{-p}$ and $\tau_{100\mu\text{m}}$, the opacity at a 100 μm , are scaled by the L_{bol} and the distance, D given in Table 6.2, to get the physical properties of each source. Fig. 6.15 shows the best-fitting model of each source of the radial profiles of the 850 μm images and the SEDs of the entire sample.

The inner radii of the protostellar envelopes range from 5 to 35 AU corresponding to $T_{\text{d}} = 250$ K. Compared to the models from Jørgensen et al. (2002), sources have comparable masses, although differences exist in individual cases due to the new Spitzer fluxes. Most sources also show a steep profile with all sources having $p \geq 1.7$, with the exception of Ced 110 IRS 4, which has a $p=1.4$.

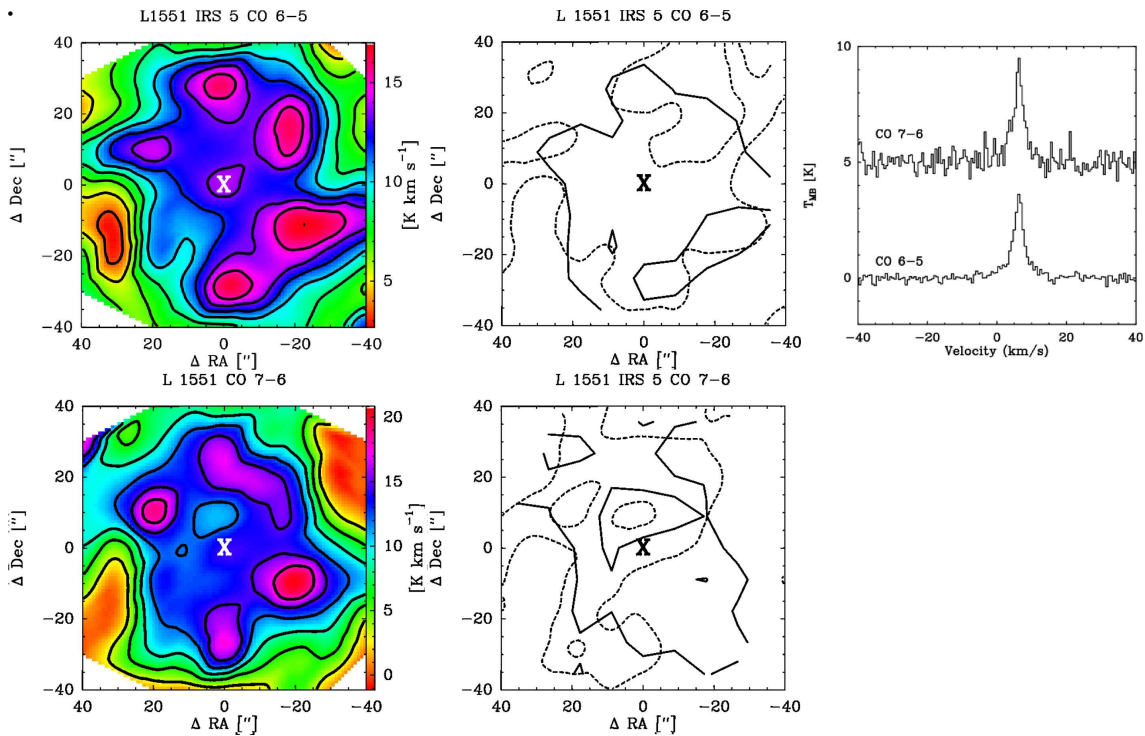


Figure 6.2 — Maps of CO 6–5 (*top row*) and CO 7–6 (*bottom row*) of L 1551 IRS 5. The left-most image shows the total integrated intensity over the line. The middle figures show the outflow contributions from the red (*dashed lines*) and blue (*solid lines*) outflow. Contours are in increasing levels of 2 K km s⁻¹ for both transitions. The outflow contributions are calculated by only including emission greater or smaller than ± 1.5 km s⁻¹ from the central velocity. The right-most image at the top row shows the ¹²CO spectra at the central position. Note that L 1551 IRS 5 data suffer from a de-rotation problem in the calibrator data and are subject to change. In particular the ‘clumpy pattern’ should not be trusted.

Table 6.5 — Inferred envelope properties from the DUSTY models.

Source	Y	p	τ_{100}	R_{inner} (AU)	R_{outer} (10 ⁴ AU)	$n_{1000\text{AU}}$ (10 ⁴ cm ⁻³)	$M_{\text{env}}(< R_{\text{outer}})$ (M _⊙)
RCrA IRS 7A	700	2.0	0.2	24.7	5.9	13	0.9
NGC 1333 IRAS 2	1500	1.9	1.8	31.3	1.6	140	2.2
L 1551 IRS 5	500	1.7	0.3	26.5	1.3	33	0.6
TMR 1	2400	1.9	0.2	9.5	2.3	5.4	0.1
IRAS 12496-7650	2500	2.2	0.2	35.7	8.9	8.7	0.3
HH 46	700	1.8	2.6	30.0	2.1	250	5.1
BHR 71	1300	1.9	0.2	15.6	2.0	8.5	0.2
Ced 110 IRS 4	1400	1.4	0.5	5	0.7	51	0.6

6.4.2 CO emission within protostellar envelopes

Using the best-fit envelope temperature and density structure derived from the dust emission, the CO emission and line profiles from the protostellar envelopes were in turn simulated with the self-consistent 1D molecular line radiative transfer code RATRAN (Hogerheijde & van der Tak 2000) using data files of the LAMDA database

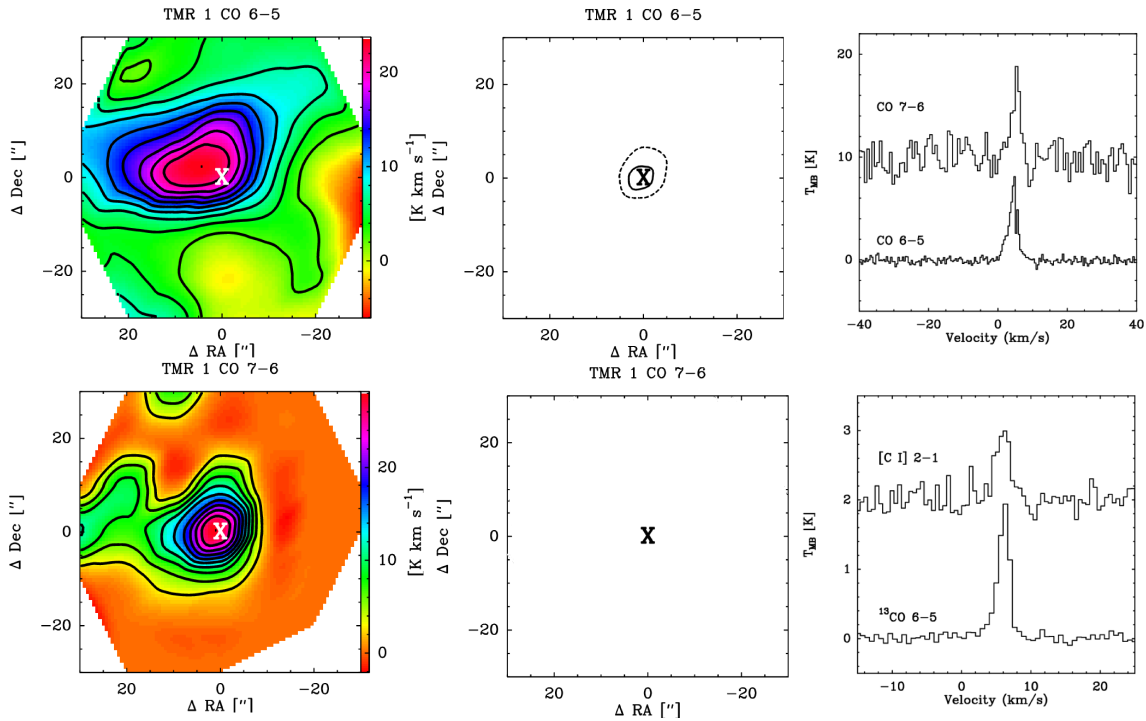


Figure 6.3 — Maps of CO 6–5 (top row) and CO 7–6 (bottom row) of TMR 1. The left-most image shows the total integrated intensity over the line. The middle figures show the outflow contributions from the red (dashed lines) and blue (solid lines) outflow. Contours are in increasing levels of 1 K km s^{-1} for both transitions. The outflow contributions are calculated by only including emission greater or smaller than $\pm 1.5 \text{ km s}^{-1}$ from the central velocity. The right-most image at the top row shows the ^{12}CO spectra at the central position, while the right-most image at the bottom row shows the spectra of the observed isotopologues and [C I] 2–1 at the central position.

(Schöier et al. 2005). CO abundances with respect to H_2 are taken from Jørgensen et al. (2005b). A ‘drop’ abundance with $X_0 = 2.7 \times 10^{-4}$ and $X_d = 10^{-5}$ is adopted. A ‘drop’ abundance consists of a warm ($T > T_{\text{freeze}}$) inner region with the high abundance X_0 and a region with $T < T_{\text{freeze}}$ and $n > n_{\text{de}}$ where CO is frozen out to a low abundance X_d . In the outer region ($n < n_{\text{de}}$), the abundance is again high at X_0 because freeze-out timescales become longer than the typical life-times of protostars. In our models, $T_{\text{freeze}} = 30 \text{ K}$ and $n_{\text{de}} = 10^5 \text{ cm}^{-3}$ are adopted, following the conclusions of Jørgensen et al. (2005b). There, the derived abundances are based upon the emission of low-excitation optically thin lines such as C^{18}O lines (both 2–1 and 3–2, 1–0 is often dominated by the very cold cloud material) and C^{17}O . Chapter 5 showed that contrary to the low- J CO lines there is little difference between ‘jump’ and ‘drop’ abundances for the emission of in high- J transitions. A static velocity field is assumed with a turbulent width of 1 km s^{-1} . Due to the static nature of the velocity field, excessive self-absorption is seen in line profiles of CO lines up to the 8–7 transition. The total area of a gaussian fitted to the line wings is used in those cases to derive an upper limit. This is a very strict limit as the true CO emission associated with the envelope is best fitted by a infall velocity (Schöier et al. 2002), producing integrated intensities between the two limits. However, Schöier et al. (2002) show that the envelope emission modelled with an infall velocity

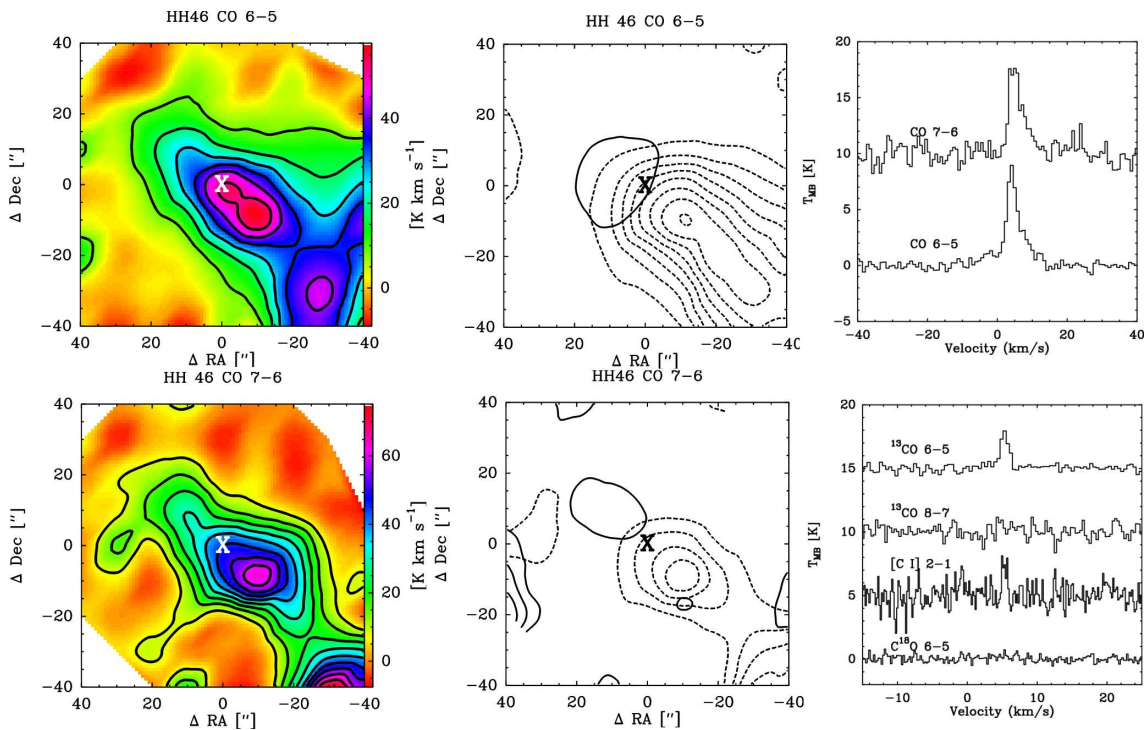


Figure 6.4 — CO 6–5 (left) CO 7–6 (middle) maps and spectra of the central position of HH 46. The left-most image shows the total integrated intensity over the line. The middle figures show the outflow contributions from the red (dashed lines) and blue (solid lines) outflow. Contours are in increasing levels of 2 K km s^{-1} for CO 6–5 and 3 K km s^{-1} for CO 7–6. The outflow contributions are calculated by only including emission greater or smaller than $\pm 1.5 \text{ km s}^{-1}$ from the central velocity. The right-most image at the top row shows the ^{12}CO spectra at the central position, while the right-most image at the bottom row shows the spectra of the observed isotopologues and [C I] 2–1 at the central position.

is in the worst case only a factor 2 greater than the intensity derived from the static envelope. The lower limit is derived from the actual modelled integrated intensity with the static velocity field.

Figure 6.16 shows the resulting integrated intensities produced by the model protostellar envelopes of all CO lines from $J=1-0$ up to $J=19-18$. All transitions were convolved with a $10''$ beam used for CHAMP⁺, except the three lowest transitions, which are convolved with a beam of $20''$. Such beams are typical for single-dish submillimeter telescopes. $10''$ will also be the approximate beam for several transitions covered by the PACS and HIFI (Band 6 and 7) instruments on Herschel at the higher frequencies. Overplotted are the observed line strengths of various CO lines of different studies, including the far-IR high- J CO lines of Giannini et al. (1999) and Giannini et al. (2001), assuming that all flux observed by the ISO-LWS in its $80''$ beam originates in a $10''$ region. See Table 6.2 for the references used.

The low- J CO emission can often be completely reproduced by the envelope models, as they are dominated by the colder gas in the outer regions of the envelopes. For HH 46, Ced 110 IRS 4 and RCrA IRS 7, the observed quiescent emission in the CO 6–5 and 7–6 lines is clearly brighter than the modelled envelope emission, even for the ^{13}CO 6–5 lines (see Table 6.6). For RCrA IRS 7, the difference is almost an order magnitude.

Table 6.6 — ^{13}CO model predictions

Source	$\int T_{\text{MB}} dV$		T_{peak}	
	Mod.	Obs.	Mod.	Obs.
TMR 1	3.6	4.3	1.9	1.9
IRAS 12496-7650	7.2	3.3	3.6	1.6
HH 46	1.9	3.9	1.2	2.9
BHR 71	4.7	1.4	2.7	1.2
Ced 110 IRS 4	2.3	5.2 ^a	1.2	1.9

^a Possible outflow contribution, see Fig. 6.5 and 6.13, estimated to be at 25% of total integrated intensity.

Table 6.7 — Outflow kinetic temperature estimates^a.

Source	Ratio ^b	$T_{\text{kin}}(\text{Blue})$	Ratio ^b	$T_{\text{kin}}(\text{Red})$
	K	K		
RCRA IRS 7	1	>200	2.5	160
NGC 1333 IRAS 2	-	-	-	-
L 1551 IRS 5 ^c	>8	<50	9	40
TMR 1 ^d	1.5	180	>4	120
IRAS 12496-7650	>8	<65	-	-
HH 46 ^e	6	100	3	140
BHR 71	-	-	-	-
Ced 110 IRS 4	3	140	>7	<80

^a Estimated with an ambient density of 10^4 cm^{-3} . Kinetic temperatures at different densities can be derived by comparing the ratio with the diagnostic plots of van der Tak et al. (2007).

^b CO 3–2/6–5 line wing ratio. Ratios are averaged over velocity and distance from the source. See Chapter 5 for more discussion.

^c CO 4–3/6–5 ratio.

^d Optical depth of 8 inferred for ^{12}CO 3–2 wings (Hogerheijde et al. 1998).

^e See Chapter 5.

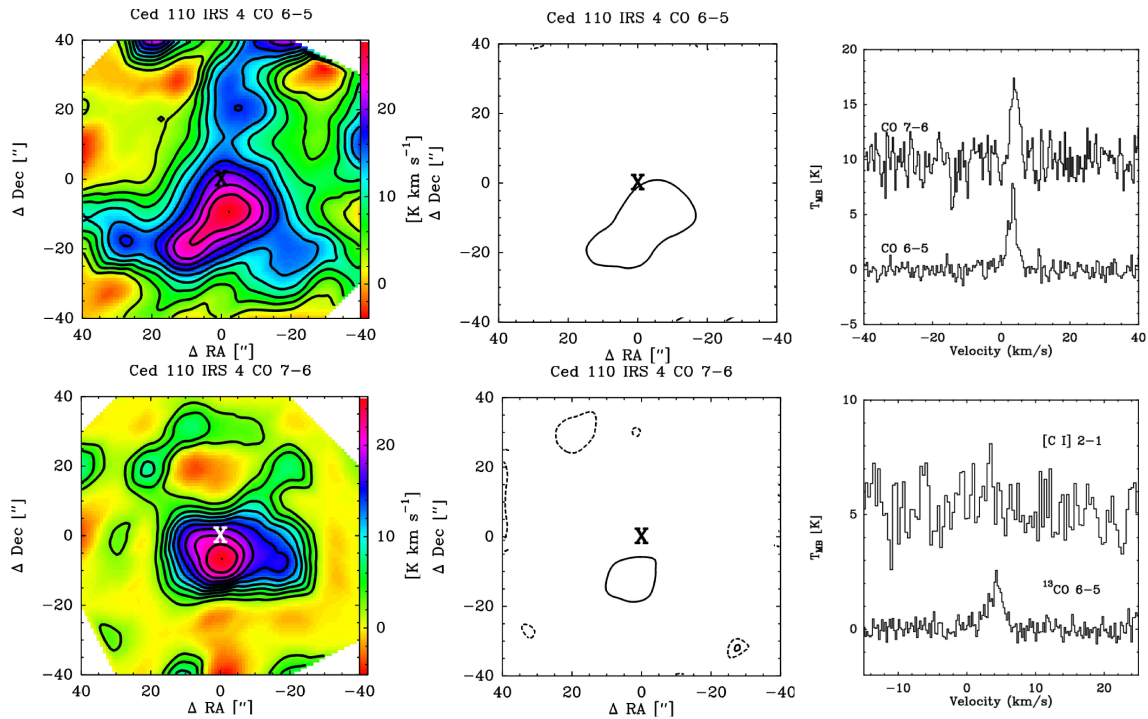


Figure 6.5 — Maps of CO 6–5 (*top row*) and CO 7–6 (*bottom row*) of Ced 110 IRS 4. The left-most image shows the total integrated intensity over the line. The middle figures show the outflow contributions from the red (*dashed lines*) and blue (*solid lines*) outflow. Contours are in increasing levels of 3 K km s^{-1} for both transitions. The outflow contributions are calculated by only including emission greater or smaller than $\pm 1.5 \text{ km s}^{-1}$ from the central velocity. The right-most image at the top row shows the ^{12}CO spectra at the central position, while the right-most image at the bottom row shows the spectra of the observed isotopologues and [C I] 2–1 at the central position.

In those cases, the observed emission is 3 to 5 times as bright as would be expected from just envelope emission. In Chapter 5, the quiescent CO 6–5 and 7–6 emission of HH 46 was attributed to ‘photon heating’ (Spaans et al. 1995), both by UV from the accretion disk and shocks inside the outflow cavity. Fig. 6.16 clearly shows that this method of heating likely applies to other sources. The envelopes of both IRAS 12496-7650 and L 1551 IRS 5 can account for all the emission detected in the ^{12}CO 6–5 and 7–6 lines. Similar to ^{12}CO , a much stronger ^{13}CO 6–5 intensity is observed for HH 46 and Ced 110 IRS 4 than can be produced by a passively heated envelope (see Table 6.6). Deep C^{18}O 6–5 spectra are needed to fully pin down the envelope models (see Chapter 5). Giannini et al. (1999) and Giannini et al. (2001) report emission of high- J CO (14–13 to 19–18) lines at far-IR of NGC 1333 IRAS 2, IRAS 12496-7650 and RCrA. For RCrA, RCrA IRS 7 is within the beam, but the emission is probably dominated by emission from RCrA itself. Fluxes in excess of $10^{-20} \text{ W cm}^{-2}$ are seen for both IRAS 12496-7650. They assumed that the flux originates within the central $3''$ ($\sim 0.002 \text{ pc}$). It is very clear from Fig. 6.16 that such observed emission cannot be produced by a passively heated envelope. A more likely explanation is that the CO emission detected with ISO-LWS is either located outside the inner $10''$ as is the likely case for IRAS 12496-7650 (see Chapter 3) or associated with an energetic outflow.

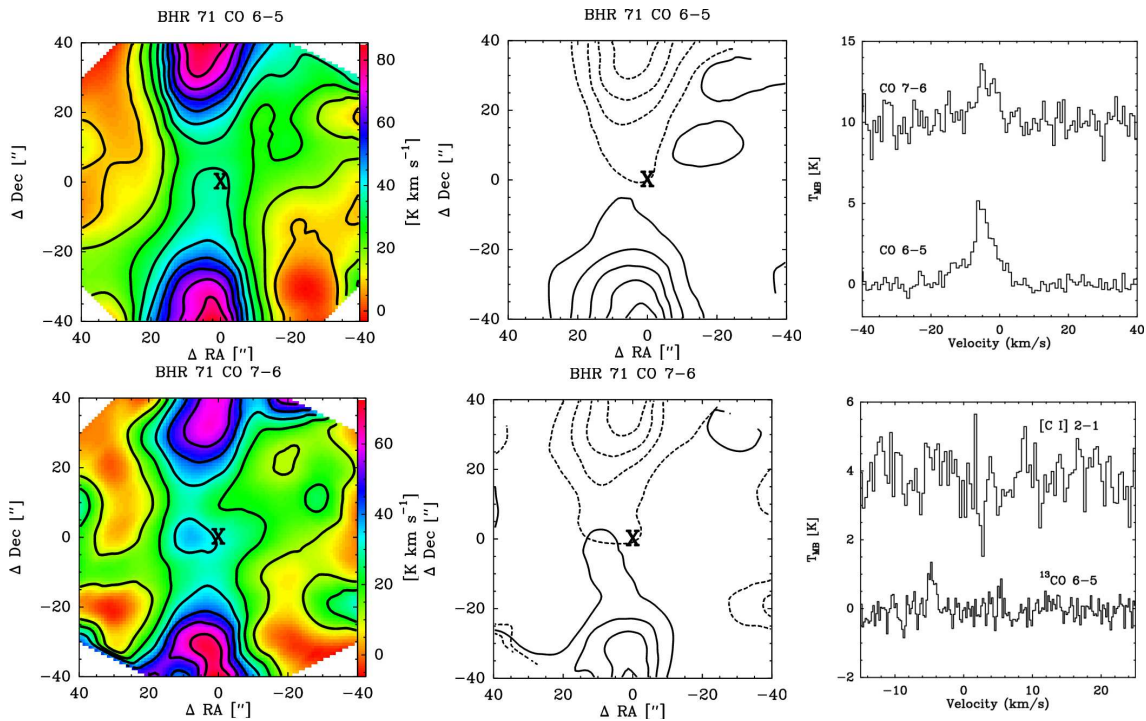


Figure 6.6 — Maps of CO 6–5 (top row) and CO 7–6 (bottom row) of BHR 71. The left-most image shows the total integrated intensity over the line. The middle figures show the outflow contributions from the red (dashed lines) and blue (solid lines) outflow. Contours are in increasing levels of 10 K km s^{-1} for CO 6–5 and 5 K km s^{-1} for CO 7–6. The outflow contributions are calculated by only including emission greater or smaller than $\pm 1.5 \text{ km s}^{-1}$ from the central velocity. The right-most image at the top row shows the ^{12}CO spectra at the central position, while the right-most image at the bottom row shows the spectra of the observed isotopologues and [C I] 2–1 at the central position.

6.5 Outflows

6.5.1 Shocks

Bachiller & Tafalla (1999) propose an evolutionary sequence of outflows around low-mass protostars, with young deeply embedded YSOs (Class 0) producing highly collimated and energetic outflows, and with more evolved embedded YSOs (Class I) producing outflows which show less energetic shocks and a wider opening angle. Observations of the shocked ^{12}CO 6–5 and 7–6 gas in the outflow directions confirm the scenario that the shocks within the vicinity of the protostar grow weaker in energy over time. The Class 0 sources (NGC 1333 IRAS 2, BHR 71 and RCrA IRS 7) all show shocked warm gas in their CO 6–5 and 7–6 lines, in both blue- and red-shifted outflow. Of the Class I sources, only HH 46 shows shocked gas in its red-shifted outflow. L 1551 IRS 5, one of the most-studied molecular outflows (Moriarty-Schieven & Snell 1988; Bachiller et al. 1994), shows little emission in the high- J line associated with outflow shocks. Although several spectra do show a small outflow wing, the integrated emission in the wings is not higher than a few σ . All other Class I flows show no sign of shocked warm gas. HH 46 and L 1551 IRS 5, even though classified as Class I, have massive envelopes of a few M_{\odot} , more characteristic of Class 0 (Jørgensen et al. 2002). L 1551 IRS 5 is believed to be older and consist of several successive ejecta events

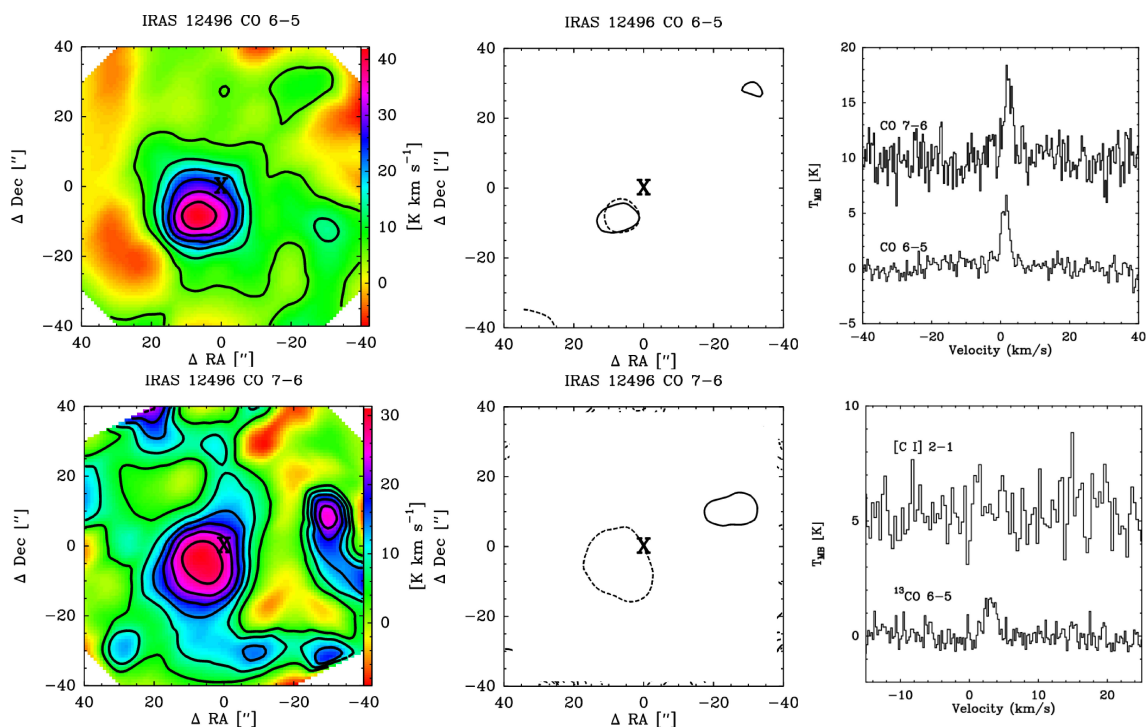


Figure 6.7 — Maps of CO 6–5 (*top row*) and CO 7–6 (*bottom row*) of IRAS 12496-7650. The left-most image shows the total integrated intensity over the line. The middle figures show the outflow contributions from the red (*dashed lines*) and blue (*solid lines*) outflow. Contours are in increasing levels of 3 K km s^{-1} for both transitions. The outflow contributions are calculated by only including emission greater or smaller than $\pm 1.5 \text{ km s}^{-1}$ from the central velocity. The right-most image at the top row shows the ^{12}CO spectra at the central position, while the right-most image at the bottom row shows the spectra of the observed isotopologues and [C I] 2–1 at the central position.

(Bachiller et al. 1994; White et al. 2000). Quiescent gas at known outflow positions, thought to be related to photon heating, is detected for HH 46 and L 1551 IRS 5 which is discussed in depth in § 6.6.

Figure 6.17 shows the maximum outflow velocities of the ^{12}CO 6–5 and 3–2 lines vs the bolometric temperature, envelope mass and outflow force. A clear absence of warm high-velocity material is seen for sources with a higher bolometric temperature. Only the cold outflow (Chapter 3) of IRAS 12496-7650 is seen at higher T_{bol} . Similarly, there is also a clear relation between the mean outflow force of both red and blue outflow lobes, and the maximum velocity seen in both ^{12}CO 3–2 and ^{12}CO 6–5. Outflow forces are derived from the spatial scales and velocities of low-excitation CO line emission (1–0, 2–1 and 3–2) (Cabrit & Bertout 1992; Bourke et al. 1997; Hogerheijde et al. 1998, and Chapters 4 and 5).

6.5.2 Temperatures of the swept-up gas

The excitation temperature of the outflowing swept-up gas can be derived from the ratios of different CO line wings. As an example, Fig. 6.18 shows the CO 3–2 from Chapter 4 and 5 and CO 6–5 from this Chapter overplotted on the same scales for a few sources. The CO 6–5 data have not been binned to the larger CO 3–2 beam, so the

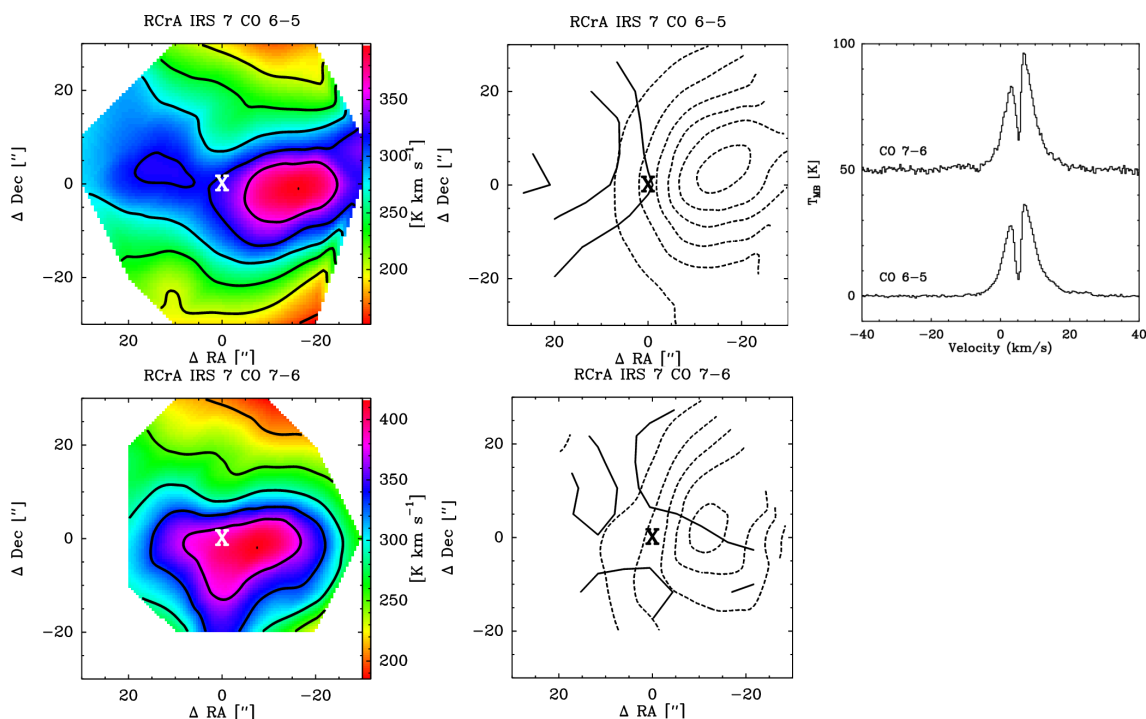


Figure 6.8 — Maps of CO 6–5 (*top row*) and CO 7–6 (*bottom row*) of RCrA IRS 7a. The left-most image shows the total integrated intensity over the line. The middle figures show the outflow contributions from the red (*dashed lines*) and blue (*solid lines*) outflow. Contours are in increasing levels of 10 K km s^{-1} for both transitions. The outflow contributions are calculated by only including emission greater or smaller than $\pm 8 \text{ km s}^{-1}$ from the central velocity. The right-most image at the top row shows the ^{12}CO spectra at the central position.

comparison assumes similar volume filling factors of the shocked gas. If the density is known this excitation temperature can be related to the kinetic temperature using the diagnostic plots produced by the RADEX radiative transfer code (van der Tak et al. 2007).

As can be seen from the temperature analysis of HH 46 in Chapter 5, there are many uncertainties. The ratios depend on the velocity, the optical depth of the line wings and the ambient density at different distances from the source. For HH 46, a drop in temperature was observed if the density remains constant, but a scenario is proposed in which the density is lower at larger radii will result in a constant kinetic temperature with distance. Following the conclusions from Hatchell et al. (1999) and Chapter 5, we assume that the kinetic temperatures of the outflowing gas are nearly constant along the observed outflow axis and thus provide a median temperature of the bulk of the flow.

Table 6.7 gives the median temperatures using the extreme velocities of the line wings $> 3\sigma$, assuming the line wings are optically thin and with an ambient cloud density of 10^4 cm^{-3} . CO 3–2 spectra can be found in Hogerheijde et al. (1998) (TMR 1, L 1551 IRS 5), Knee & Sandell (2000) (NGC 1333 IRAS 2), Parise et al. (2006) (BHR 71), Chapter 3 (IRAS 12496-7650), 4 (RCrA IRS 7, Ced 110 IRS 4) and 5 (HH 46).

The main error on these temperature estimates is the optical depth in the outflow

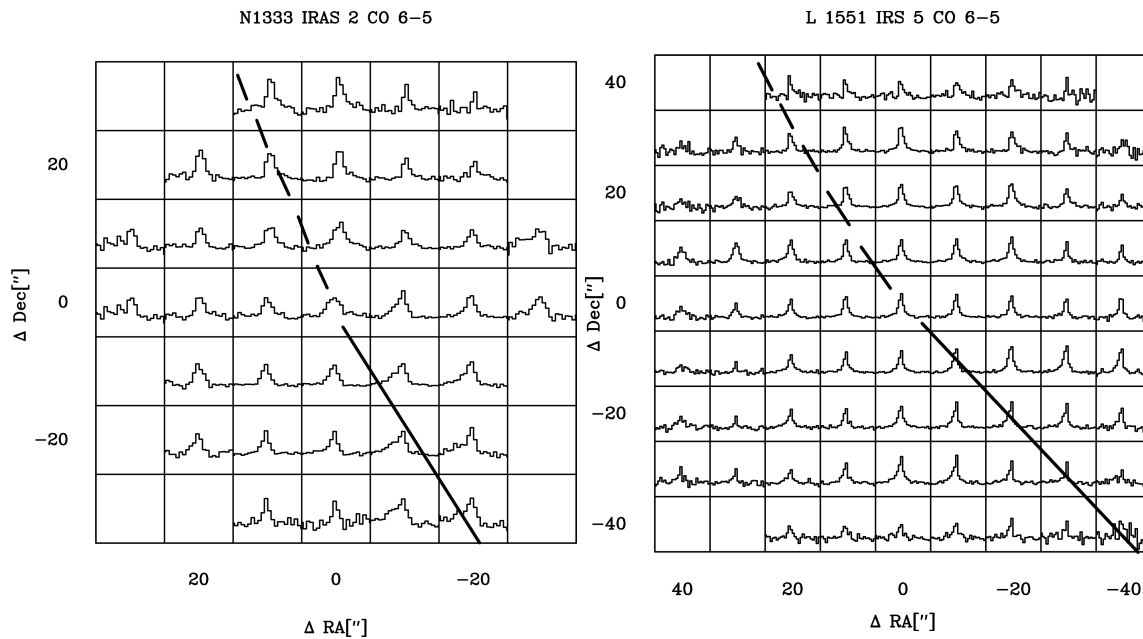


Figure 6.9 — Spectra of ^{12}CO 6–5 over an area of $40'' \times 40''$ of NGC 1333 IRAS 2 (*left*) and L 1551 IRS 5 (*right*). NGC 1333 IRAS 2 was observed using the hexa mode, so the covered area is slightly smaller than that of L 1551 IRS 5 taken in OTF mode. For all spectra in both sources, horizontal axes range from -10 to 25 km s^{-1} and vertical axes from -5 to 12 K . For both sources, the main outflow axis of the red and blue are shown with a *dashed* and *solid* lines. Note that the L 1551 IRS 5 data suffers from a de-rotation problem in the calibrator data and are subject to changes.

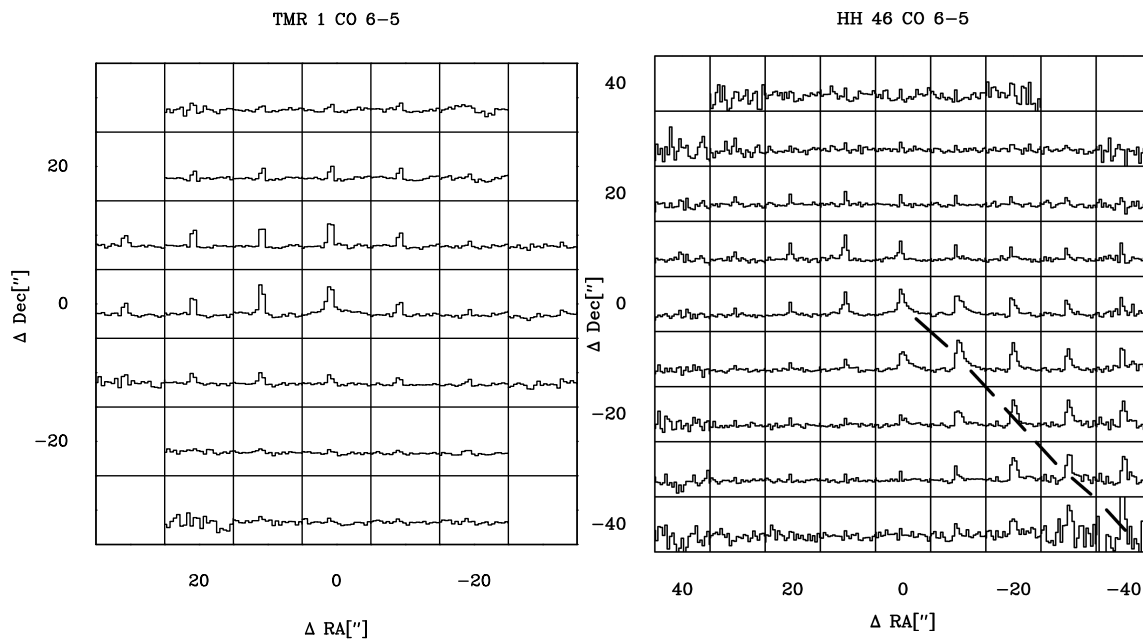


Figure 6.10 — Spectra of ^{12}CO 6–5 over an area of $40'' \times 40''$ of TMR 1 (*left*) and HH 46 (*right*). TMR 1 was observed using the hexa mode, so the covered area is slightly smaller than that of HH 46 taken in OTF mode. For all spectra in both sources, the horizontal axes range from -10 to 20 km s^{-1} with vertical axes from -5 to 12 K . For HH 46, the red outflow axis is shown with a *dashed* line.

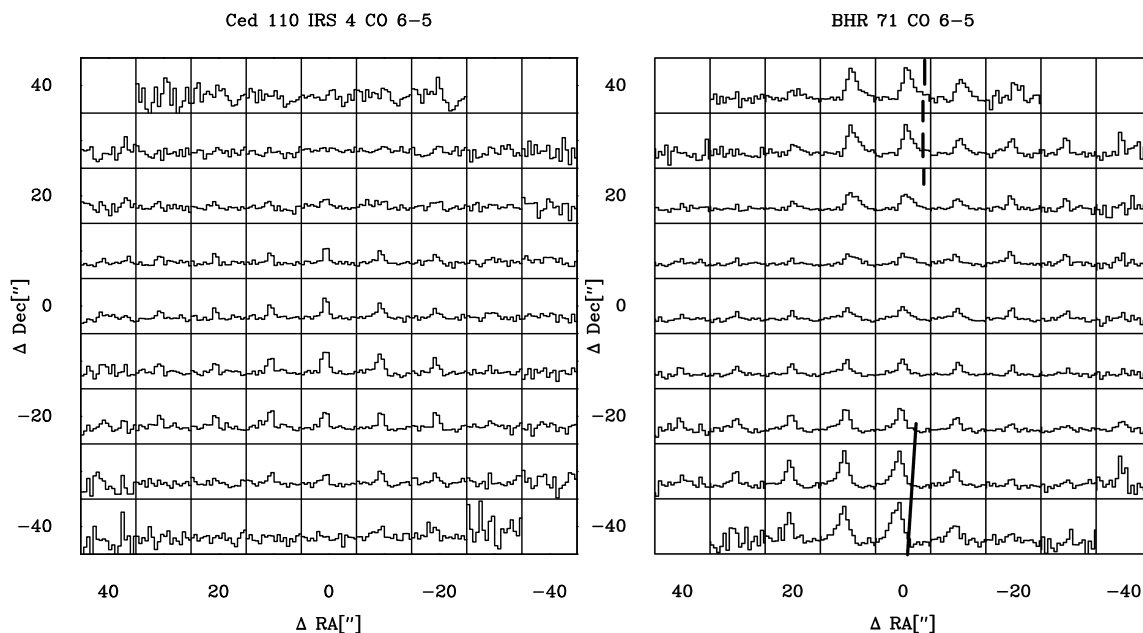


Figure 6.11 — Spectra of ^{12}CO 6–5 over an area of $40'' \times 40''$ of Ced 110 IRS 4 (*left*) and BHR 71 (*right*). For Ced 110 IRS 4, the horizontal axes are -10 to 25 km s^{-1} with vertical axes from -4 to 10 K . For BHR 71, horizontal axes are -20 to 10 km s^{-1} with vertical axes -5 to 15 K . For BHR 71, the main outflow axis of the red and blue are shown with a *dashed* and *solid* lines.

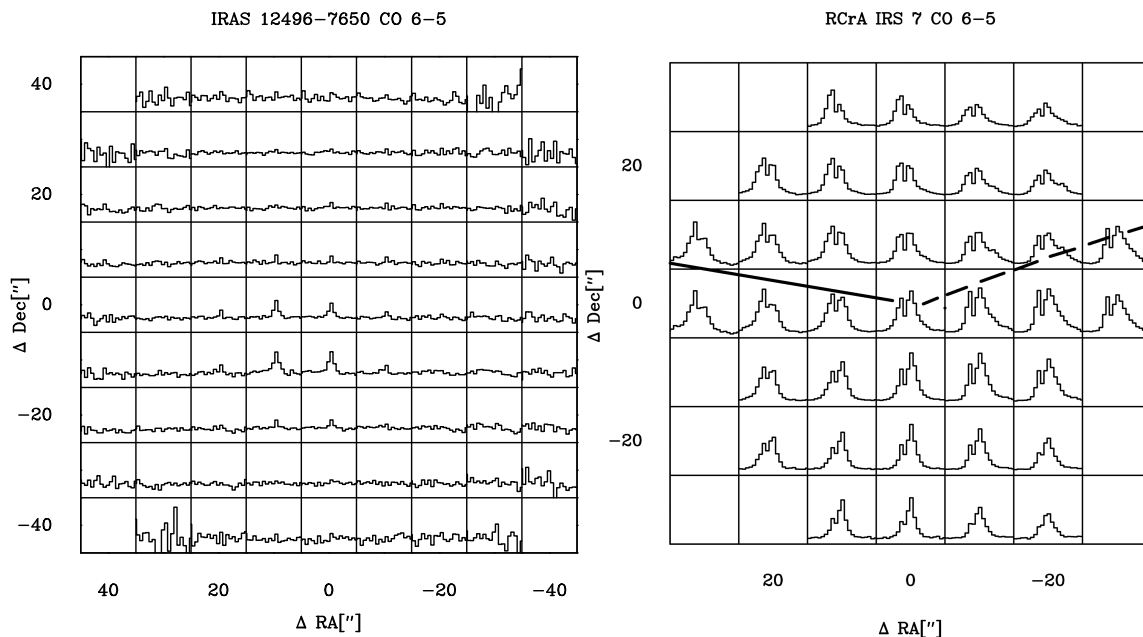


Figure 6.12 — Spectra of ^{12}CO 6–5 over an area of $40'' \times 40''$ of IRAS 12496-7650 (*left*) and RCrA IRS 7A (*right*). RCrA IRS 7A was observed using the hexa mode, so the covered area is slightly smaller than that of IRAS 12496-7650 taken in OTF mode. For all spectra, the horizontal axes are -15 to 15 km s^{-1} with vertical axes from -5 to 15 K for IRAS 12496-7650 and from -10 to 25 km s^{-1} and -5 to 50 K for RCrA IRS 7. For RCrA IRS 7, the main outflow axis of the red and blue lobes are shown with a *dashed* and *solid* lines.

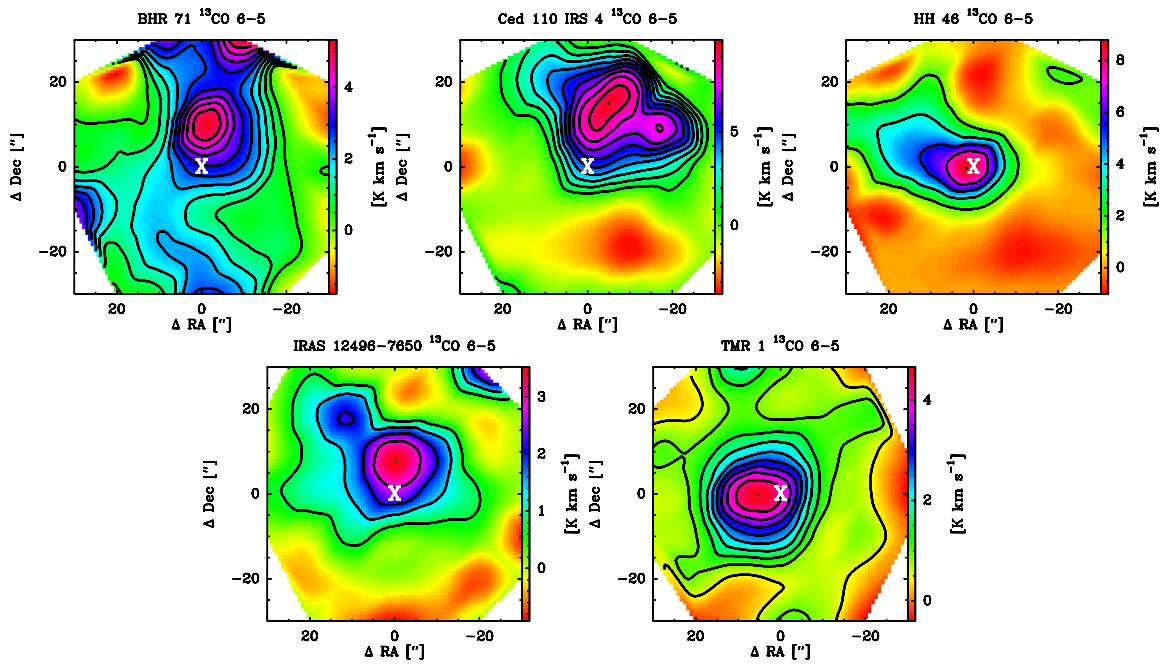


Figure 6.13 — ^{13}CO 6–5 integrated intensity maps of BHR 71 (*upper left*), Ced 110 IRS 4 (*upper middle*), HH 46 (*upper right*), IRAS 12496-7650 (*lower left*) and TMR 1 (*lower middle*). Note that the TMR 1 data suffer from a de-rotation problem in the calibrator data and are subject to change.

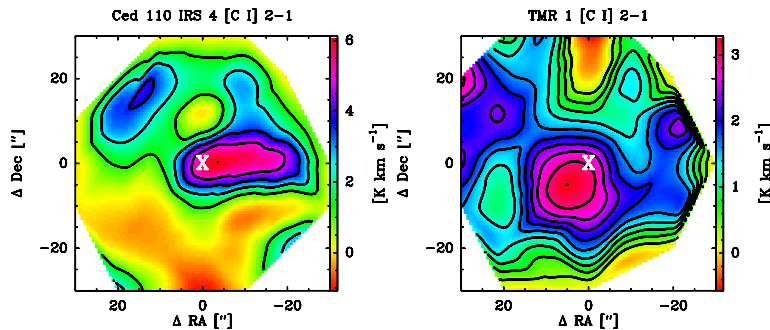


Figure 6.14 — [C I] 2–1 integrated intensity maps of Ced 110 IRS 4 (*left*) and TMR 1 (*right*). Note that the TMR 1 data suffer from a de-rotation problem in the calibrator data and are subject to change.

wings. Deep ^{13}CO 3–2 observations show that outflows can be optically thick. Hogerheijde et al. (1998) find optical depths in the ^{12}CO 3–2 line wings, τ_{wing} , on the order of 10, while in Chapter 5 $\tau_{\text{wing}}=1-1.8$ is found for HH 46. Even if the optical depths are assumed to be similar in CO 3–2 and CO 6–5, kinetic temperatures can be almost 50% lower. A theoretical study by Hatchell et al. (1999) using a jet-driven bow shock model suggests that the kinetic temperatures of molecular outflows are typically of order of 50-150 K along the axis and rising towards the the location of the bow shock and overall with higher jet velocities. The temperatures found in Table 6.7 agree very well with these predicted temperatures. For several outflows, e.g. IRAS 12496-7650 (blue) or Ced 110 IRS 4 (red), temperatures are significantly lower. The lowest outflow temperatures are found for the flows of L 1551 IRS 5. Fig. 6.19 shows the CO 6–5 and 4–3 line profiles

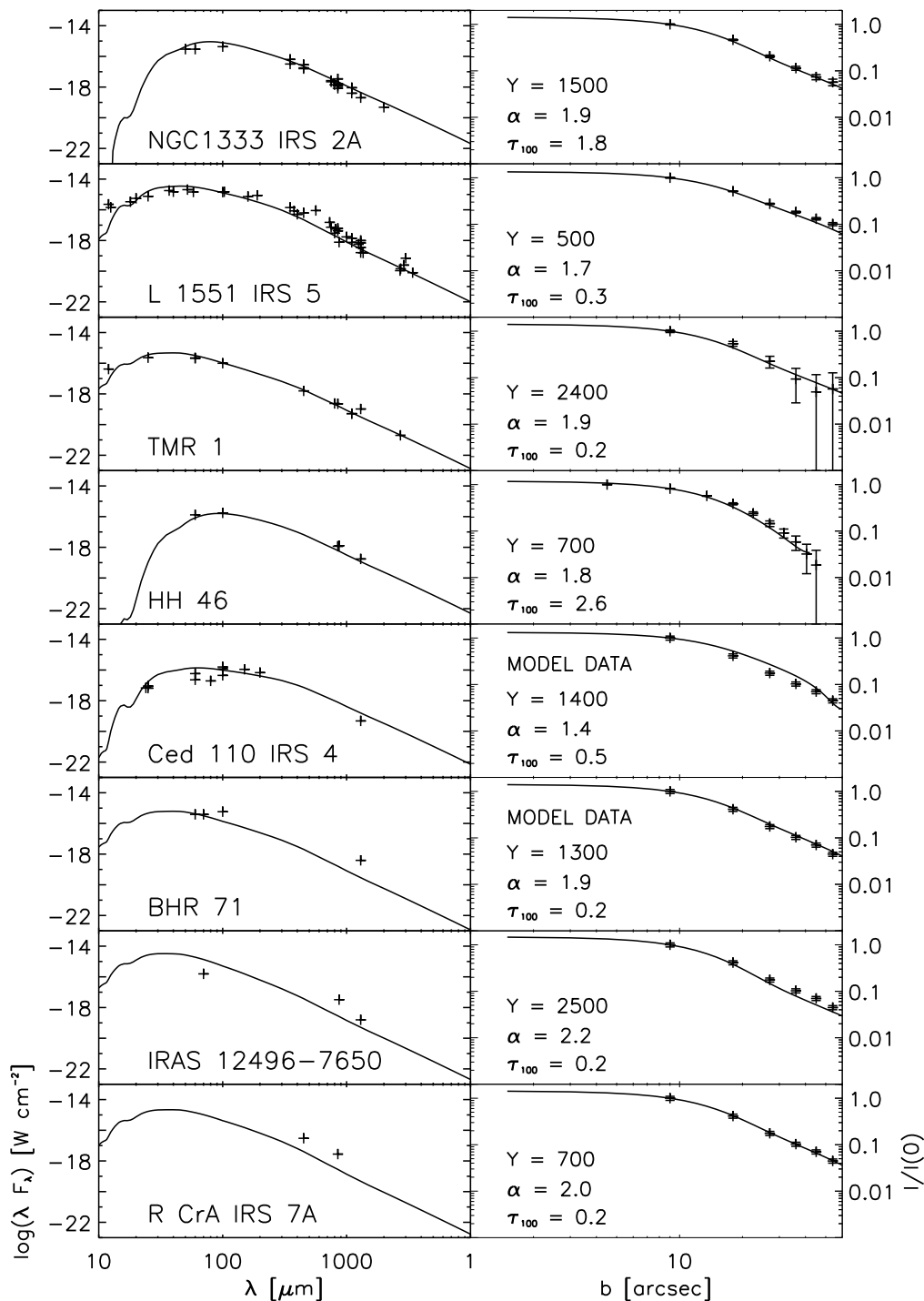


Figure 6.15 — The SEDs and radial profiles at $850 \mu\text{m}$ of the sample. Overplotted is the best-fitting envelope model. For Ced 110 IRS 4 and BHR 71, the model spatial $850 \mu\text{m}$ profile is plotted since data are lacking.

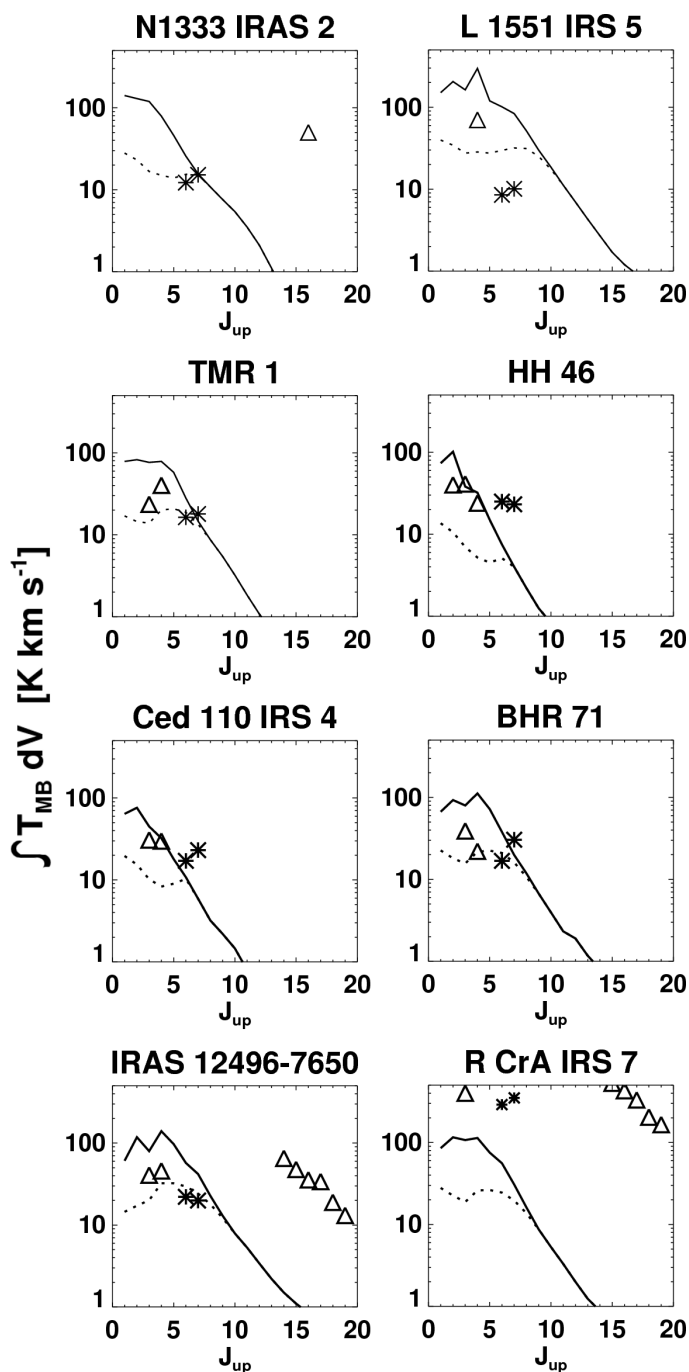


Figure 6.16 — The contribution of the envelope to CO lines at the source position with J_{up} ranging from 1 to 19. Integrated emission is shown with dashed and solid lines. Dashed lines are modelled lines which show excessive self-absorption. Solid lines represent gaussian fitted to the line wings of the envelope model and thus represent the strict upper limit to the CO line emission from the protostellar envelope. Beam-sizes were taken to be $10''$ for all transitions except for $J_{\text{up}} \leq 3$, for which a beam of $20''$ was used. Stars indicate the integrated quiescent emission of the lines observed with CHAMP⁺ from Table 6.3, corrected for red- and blue-shifted emission, while triangles are literature data (see Table 6.2).

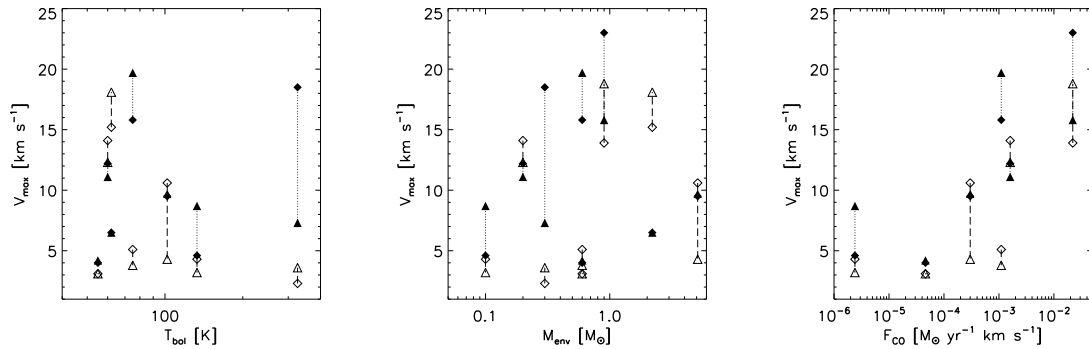


Figure 6.17 — V_{\max} of ^{12}CO 6–5 and 3–2 vs. T_{bol} (left), envelope mass (middle) and outflow force. Triangles represent the blue outflows and diamonds the red outflows. Open symbols are the CO 6–5 lines and filled symbols the CO 3–2 lines. Outflow force from Cabrit & Bertout (1992); Hogerheijde et al. (1998) (NGC 1333 IRAS 2, L 1551 IRS 5 and TMR 1), Bourke et al. (1997) (BHR 71) and Chapters 4 (Ced 110 IRS 4, IRAS 12496-7650, RCrA IRS 7) and 5 (HH 46). CO 3–2 from Parise et al. (2006) (BHR 71), Hogerheijde et al. (1998) (TMR 1, L 1551 IRS 5), Knee & Sandell (2000) (NGC 1333 IRAS 2), Chapter 3 (IRAS 12496-7650) and Chapter 4 (HH 46, RCrA IRS 7 and Ced 110 IRS 4).

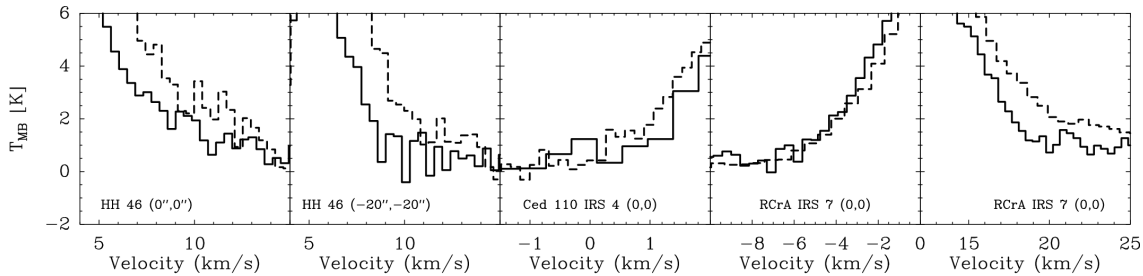


Figure 6.18 — Line wings of CO 6–5 (solid) and CO 3–2 (dashed) for HH 46 (red wing at central position and in the red outflow), Ced 110 IRS 4 (blue at the central position), RCrA IRS 7A (red and blue at the central position).

at the center position (CO 4–3 from Hogerheijde et al. 1998). CO 4–3/6–5 ratios are on the order of 8 or higher. At an assumed density of 10^4 cm^{-3} , this corresponds to kinetic temperatures of 50 K and lower. If both line wings are optically thin, densities must be lower than 10^3 cm^{-3} to produce temperatures of $\sim 100 \text{ K}$, observed at other flows.

6.6 Heating processes in the molecular outflow and protostellar envelope

As discussed in § 6.4, several sources show quiescent, narrow ^{12}CO 6–5 and 7–6 emission that is more intense than can be produced by an envelope model. Moreover, strong narrow high- J CO emission is observed off-source along outflow axes for most sources. In Chapter 5, we proposed that for HH 46 the quiescent narrow-line ^{12}CO 6–5 and 7–6 emission originates within the outflow cavity walls heated to 250-400 K by a G_0 , the enhancement factor with respect to the standard interstellar radiation field, of a few hundred, with the UV photons created in the outflow shocks and accretion boundary layer near the central protostar. This heating method was first proposed by Spaans

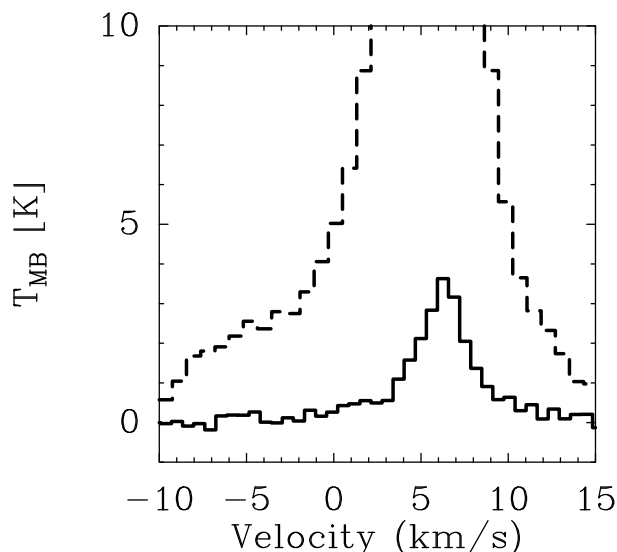


Figure 6.19 — CO 4–3 (*dashed*) from Hogerheijde et al. (1998) overplotted with CO 6–5 (*solid*) from the central position of L 1551 IRS 5. The very high CO 4–3/6–5 ratio in both red and blue outflow indicates that the temperatures in this outflow are very low.

et al. (1995), but Chapter 5 shows that it applies to both the inner envelope/outflow walls as well as outflow cavity walls much further from the central star, due to jet shocks within the outflow cavities. The data presented in this chapter show that photon heating is present in other protostars, especially in outflow cavities (e.g. L 1551 IRS 5 § 6.2). But even in sources with little to no outflow, such as Ced 110 IRS 4, relatively strong ^{12}CO 6–5 and 7–6 is seen at positions not associated with the central protostar, see Fig. 6.16.

The origin of such quiescent high- J CO emission was shown to be physically different from both the thermal emission of the protostellar envelope (see § 6.4), emission from shocks present at the working surfaces of outflows (Reipurth & Raga 1999; Raga et al. 2007), or swept-up gas, that is accelerated to velocities of a few km s^{-1} (Bachiller et al. 1994; Bachiller & Tafalla 1999).

Slow ($v_s = 5 - 10 \text{ km s}^{-1}$) C-shocks may produce similar quiescent levels of CO 6–5 and 7–6 emission in outflows (Draine & Roberge 1984; Spaans et al. 1995). However, the presence of quiescent ^{12}CO 6–5 and 7–6 emission in the envelopes of TMR 1 and Ced 110 IRS 4, both of which show little to no spatially resolved outflow emission in CO 3–2 (Hogerheijde et al. 1998, and Chapter 4), is more easily explained with the photon heating scenario than with slow C-shocks. In addition, the narrow line widths for other sources argue against this scenario.

6.6.1 Envelope and outflow of BHR 71

The proposed model that photon heating takes place both in the outflow cavities and near the envelope is clearly illustrated by the observations of BHR 71. At the north and south position of the outflow, shocked gas is clearly detected, but almost no shocked gas is seen near the central star. Quiescent gas is observed both within the envelope and the outflow. In the ^{12}CO 7–6 map, the photon heating in the envelope can strongly

be identified from the central contour. BHR 71 is the only source for which the quiescent emission at the outflow position is (much) brighter than that seen at the position of the envelope. It is likely that strong shocks are present in the main outflow. The main outflow (Bourke et al. 1997) is clearly detected at the edges of the map, but the secondary weaker outflow, associated with the IRS2 position, as seen by Parise et al. (2006) is not detected down to the noise levels. Shocked CO 6–5 and 7–6 emission is also only seen at relatively low levels in the inner 20'' and strongly increases at 40'' away from the source for both outflows.

6.6.2 The ‘fossil’ outflow of L 1551 IRS 5

The outflow of L 1551 IRS 5 has been considered an example of an older outflow, due to its large size (Moriarty-Schieven & Snell 1988; Fridlund et al. 1989), large opening angle (Bachiller et al. 1994) and other submillimeter properties (Cabrit & Bertout 1992; Bachiller et al. 1994; Hogerheijde et al. 1998). White et al. (2000) constructed a detailed model from a wide variety of space- and ground-based IR continuum and spectroscopic observations, including a wide opening angle of the outflow ($\sim 50^\circ$). This view is clearly confirmed by the low derived temperatures of 40 to 50 K of the shocked gas, which is much cooler than in other sources. The emission at the off-position is dominated by a quiescent component, originating on the cavity walls. Comparison of the peak temperatures of CO 4–3 (Hogerheijde et al. 1998), 6–5 and 7–6, shows that L 1551 IRS 5 has a relatively much lower T_{peak} at high- J transitions than other sources that have a strong quiescent component in their outflow cavity, such as HH 46. This can be indicative of a lower G_0 at the cavity walls, resulting in a lower gas temperature of the surface PDR (~ 100 K vs 250–400 K) (Kaufman et al. 1999, their Figure 1). It can also be possible that the ambient density is much lower, thus subthermally exciting the CO 6–5 and 7–6, although kinetic temperatures are just as high.

6.6.3 The PDR of RCrA IRS 7

The lines of RCrA IRS 7 are an order of magnitude stronger than those of equivalent sources in different clouds. Even at off-positions at the edge of the observed area, integrated intensities larger than 300 K km s^{-1} are seen. Even with the high luminosity of $\sim 20\text{--}30 L_\odot$, these integrated intensities cannot originate from heating by RCrA IRS 7 itself. A likely explanation is the proximity of the A5 star RCrA ($L_{\text{bol}} = 130 L_\odot$). RCrA was observed by ISO-LWS, and many strong high- J CO lines (CO 14–13 to 21–20) were detected in the large beam of ISO (Lorenzetti et al. 1999; Giannini et al. 1999). Models were put forward with the emission originating in relatively small (~ 0.002 pc), dense ($> 10^6 \text{ cm}^{-3}$) and hot ($T > 300 - 1000$ K) regions (Giannini et al. 1999). However, the spatial distribution of the CO 6–5 and 7–6 seen in Fig. 6.8 does not agree with this hypothesis. A much more likely explanation is that RCrA itself irradiates the outer edges of the cloud and envelope around RCrA IRS 7a, creating a PDR at its surface, much like the case of intermediate mass sources in Orion (Jørgensen et al. 2006).

6.6.4 Presence of [C I] 2–1

A limit on the amount of FUV/X-ray emission that is available to dissociate CO and H₂ can be derived from the presence of the [C I] 2–1. Theoretical studies show that the dissociation of CO can only occur at 912–1100 Angstrom. (van Dishoeck & Black 1988) The absence of strong [C I] 2–1 emission in the outflow cavities of most protostars suggests that the radiation field in outflows does not produce sufficiently energetic radiation, but still heats the cavity walls to a few hundred K (Chapter 4). This would also limit the shock velocities to $<90 \text{ km s}^{-1}$, since higher shock velocities produce CO and H₂ dissociating photons (Neufeld & Dalgarno 1989).

[C I] is detected in the inner 10'' for HH 46, TMR 1 and Ced 110 IRS 4 at levels of 2 K km s⁻¹. For IRAS 12496-7650 and BHR 71, no [C I] 2–1 was detected. The low emission in all sources can be accounted for by a C abundance of a few times 10⁻⁶ with respect to H₂. Such abundances can be maintained by low UV levels produced by cosmic ray radiation (Flower et al. 1994).

6.7 Conclusions

In this chapter, we have presented the first ¹²CO 6–5 and 7–6 maps of a sample of 8 low-mass protostars with a large range of luminosities, evolution and densities, as well as several isotopologue and [C I] observations. All observations have been carried out with the CHAMP⁺ instrument. The main conclusions of this chapter are

- Warm gas, as traced by ¹²CO 6–5 and 7–6, is present in all observed protostars at the central position. Envelope models show that for HH 46 and Ced 110 IRS 4, passive heating of the envelope is insufficient to explain the observed ¹²CO 6–5, 7–6 and ¹³CO 6–5 lines. Heating of the envelope/outflow boundary layer by UV photons, as detailed in Spaans et al. (1995) and in Chapter 5, can explain the observed differences.
- Photon heating of the cavity walls also takes place for the outflow cavities of several other Class 0 and Class I protostars, as seen at positions off-source of BHR 71, NGC 1333 IRS 2, HH 46 and L 1551 IRS 5. The necessary UV photons are created by internal jet shocks and the bow shock where the jet interacts with the ambient medium, in addition to the accretion boundary layer. The distribution of the quiescent CO 6–5 and 7–6 emission of BHR 71, with narrow emission stronger at larger distances from the source, confirms the hypothesis that UV photons necessary for the heating can originate both from accretion near the star and in outflow shocks. We propose that photon heating is present in all outflows.
- The lack of [C I] 2–1 emission in the outflow constrains the production of energetic CO dissociative photons in the shocks. The observed [C I] emission at the source position can be accounted for by a low atomic C abundance that is maintained by cosmic ray induced UV photodissociation of CO.
- Shocked ¹²CO 6–5 and 7–6 gas only exist in large quantities in flows of more massive sources (NGC 1333 IRAS 2, BHR 71, HH 46 and RCrA IRS 7), while low-mass flows do not show much shocked gas that emits in the ¹²CO 6–5 and 7–6 lines. Within the proposed model of Bachiller & Tafalla (1999), the outflows of Class I are more evolved and are driven with much less energy, producing far

weaker shocks.

- Kinetic temperatures of ~ 100 K are found for most flows. Such temperatures agree with expected conditions of jet driven modelled flows (Hatchell et al. 1999). Only the flows of L 1551 IRS 5 are much colder (< 50 K), in agreement with the ‘fossil’ nature of the flow.
- A relation between the outflow force and the maximum velocity of ^{12}CO 6–5 emission is noted. Protostars with the lowest outflow force also produce the least amount of CO 6–5 and 7–6 at the high velocities.
- The very strong intensities at all positions of RCrA IRS 7, an order of magnitude higher than can be produced by passive heating, must be due to a significant PDR region near the source. Likely, RCrA itself heats the outside of the RCrA IRS 7 envelope and cloud region.

The spatially resolved observations taken with the CHAMP⁺ instrument of ^{12}CO 6–5, 7–6, the isotopologue lines ^{13}CO 6–5 and [C I] 2–1 provide a unique insight in the structure and physical processes of the inner regions of low-mass protostars, as well as the energetics of outflowing gas and the interaction between the outflow and envelope at the cavity walls. Deep C^{18}O 6–5 will be able to improve on this analysis. In the future, the Herschel Space Telescope will be able to map high- J CO lines in the far-IR between 60 and 600 μm with the PACS and HIFI instruments. Comparison with this data set and future interferometric observations obtained with ALMA or the SMA will play a crucial role in characterizing the center regions of embedded YSOs.

Acknowledgements

TvK and astrochemistry at Leiden Observatory are supported by a Spinoza prize and by NWO grant 614.041.004. The staff at APEX and many members of the Bonn submillimeter group are thanked for the excellent support during observations. The help of Bas Nefs with the LABOCA map around IRAS 12496-7650, obtained during the science verification of the LABOCA instrument in collaboration with Renée Liseau, is greatly appreciated. CHAMP⁺ is constructed with funds from NWO grant 600.063.310.10. We thank Ronald Stark for continued support of the CHAMP⁺ project.

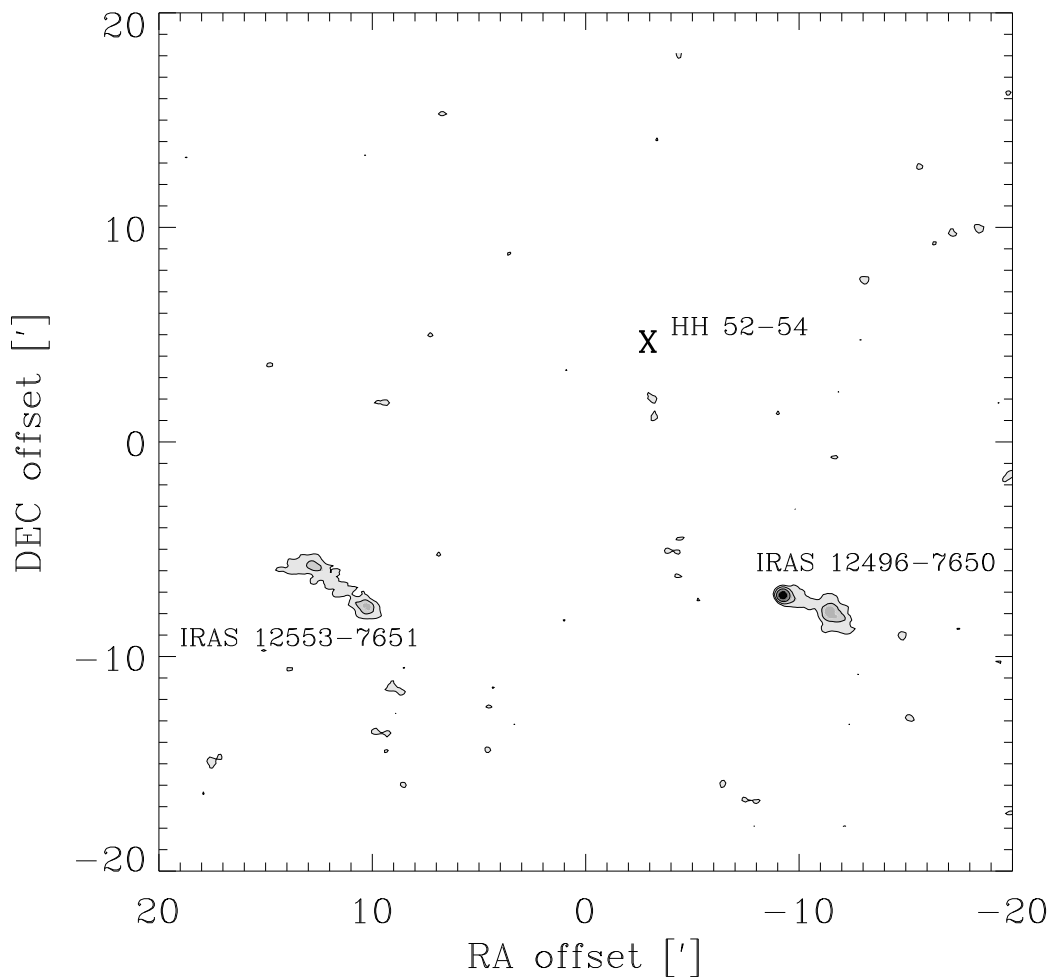


Figure A.1 — The LABOCA map of the Chamaeleon II region near IRAS 12496-7650. Both IRAS 12496-7650, IRAS 12553-7651 and HH 52-54 are indicated on the map. The position of HH 52-54, its position is indicated with an 'X'

A.1 Chamaeleon II LABOCA map

Since it was not possible to efficiently map southern protostars at submillimeter wavelengths until the advent of APEX, such sources have had little attention. LABOCA, the $870\ \mu\text{m}$ 295-element bolometer array mounted on APEX (Kreysa et al. 2003; Siringo et al. 2008), allows for the first time for extensive submillimeter continuum observations of southern protostars. Continuum observations of HH 46 are presented in Chapter 5, but during the science verification of LABOCA, we also observed an extensive region in Chamaeleon II, in the neighbourhood of IRAS 12496-7650. Results are presented in this appendix.

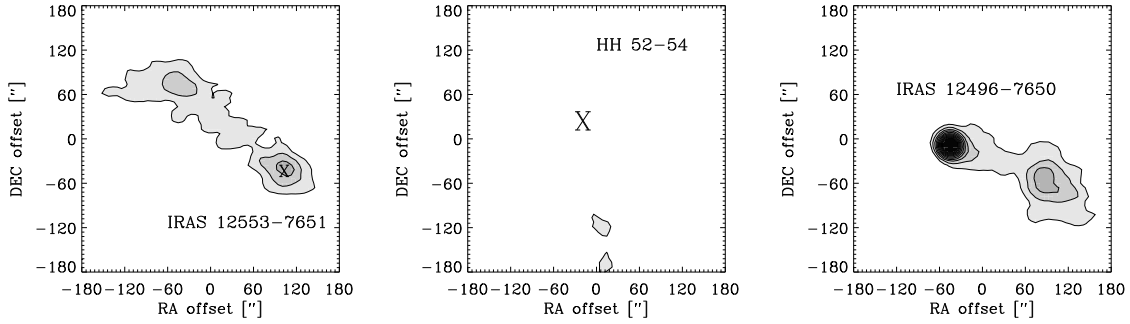


Figure A.2 — Zooms of the areas covered by IRAS 12553-7651 (*left*, IR position marked with ‘X’), HH 52-54 (*middle*) and IRAS 12496-7650 (*right*).

A.1.1 Observations

Observations were carried out during the science verification phase of the LABOCA instrument during May and July 2007. The 295 pixels together form an almost circular field of view of $11.6'$. The beam of the 12-meter APEX dish at this wavelength is $18.5''$. Although pixels do not fully sample the sky due to their separation, a fully sampled map can be attained by OTF-mapping. For the Cha II region, a region of $40' \times 40'$ was mapped, centered on a point between the IRAS 12496-7650 and the HH 52-54 sources. Calibration was carried out on Saturnus and Jupiter, and skydips were taken to characterize the opacity of the sky. The weather was stable with PWV (precipitable water vapor) ranging from 0.5 to 1.5 mm during both observations. Data were subsequently reduced with the BOA² reduction software.

A.1.2 Results

Fig. A.1 shows the submillimeter emission of the entire map with levels of $3\sigma, 6\sigma, 9\sigma, \dots$ with 1σ levels of ~ 20 mJy/beam. The brightest peak emission is associated directly with the IR position of IRAS 12496-7650. Fig. A.2 shows the blowups of three regions (IRAS 12496-7650, IRAS 12553-7651 and HH 52-54). Resulting fluxes in an area with diameter of $120''$ can be found in Table A.1. No emission was found down to a limit of 65 mJy at the position of HH 52-54. In addition, little to no large-scale emission is seen for the Cha II cloud.

Table A.1 — Extracted fluxes from LABOCA

Source	Flux Jy ($120''$)
IRAS 12496-7650	9.4
HH 52-54	$<0.065^a$
IRAS 12553-7651	4.2

^a 3σ level in Jy/beam.

²[http:// www.astro.uni-bonn.de/boawiki](http://www.astro.uni-bonn.de/boawiki)

Chapter 7

Modeling water emission from low-mass protostellar envelopes

Abstract Within low-mass star formation, water vapor plays a key role in the chemistry and energy balance of the circumstellar material. The Herschel Space Observatory will open up the possibility to observe water lines originating from a wide range of excitation energies. Our aim is to simulate the emission of rotational water lines from envelopes characteristic of embedded low-mass protostars. A large number of parameters that influence the water line emission are explored: luminosity, density, density slope, and water abundances. Both dust and water emission are modeled using full radiative transfer in spherical symmetry. The temperature profile is calculated for a given density profile. The H₂O level populations and emission profiles are in turn computed with a non-LTE line code. The results are analyzed to determine the diagnostic value of different lines, and are compared with existing observations. Lines can be categorized in: (i) optically thick lines, including ground-state lines, mostly sensitive to the cold outer part; (ii) highly excited ($E_u > 200 - 250$ K) optically thin lines sensitive to the abundance in the hot inner part; and (iii) lines which vary from optically thick to thin depending on the abundances. Dust influences the emission of water significantly by becoming optically thick at the higher frequencies, and by pumping optically thin lines. A good physical model of a source, including the correct treatment of dust, is a prerequisite for inferring the water abundance structure and possible jumps at the evaporation temperature from observations. The inner warm ($T > 100$ K) envelope can be probed by highly excited lines, while a combination of excited and spectrally resolved ground state lines probes the outer envelope. Observations of H₂¹⁸O lines, although weak, provide even stronger constraints on abundances.

T. A. van Kempen, S. D. Doty, E. F. van Dishoeck and M. R. Hogerheijde, 2008, *A&A* 487, 975-991

7.1 Introduction

Low-mass ($M < 3 M_{\odot}$) young stellar objects (YSOs) form through gravitational collapse of cloud cores. Most of their mass is accreted over periods of less than 10^6 years (André et al. 2000; Myers et al. 2000). These early stages of low-mass star formation, the so-called Class 0 and Class I stages, are characterized by the presence of centrally condensed envelopes that veil the central protostars and disks (Lada 1987; André et al. 1993). The envelopes also contain most of the mass ($M \sim 0.1\text{--}1 M_{\odot}$) of the total system until the emergence of the central star and disk (Adams et al. 1987; Shirley et al. 2000; Jørgensen et al. 2002). Water plays a pivotal role in these early evolutionary stages. First, the high dipole moment of H_2O makes its rotational lines excellent coolants of warm gas in the inner region of protostellar envelopes, allowing material to continue collapsing at higher temperatures (Goldsmith & Langer 1978; Neufeld & Kaufman 1993; Ceccarelli et al. 1996). Second, water is one of the dominant reservoirs of the non-refractory oxygen budget in dense clouds (van Dishoeck et al. 1993). The partitioning of gaseous oxygen between H_2O , OH and O, as well as the ratio between H_2O gas and ice, affect the chemistry of all other oxygen-containing molecules including the complex organics (Charnley et al. 1992). The evaporation point of H_2O ice in interstellar space is around 100 K (Fraser et al. 2001), so only the small warm inner regions of protostellar envelopes are likely to contain fractional abundances of water vapor as high as 10^{-4} with respect to H_2 , perhaps even exceeding that of CO (e.g., Ceccarelli et al. 1996; van Dishoeck & Blake 1998; Boonman et al. 2003). In colder regions, water is the main ingredient of icy grain mantles as shown by infrared spectroscopy (e.g., Whittet et al. 1983; Smith et al. 1989; Boogert et al. 2002; Pontoppidan et al. 2004), with gas-phase water abundances that are orders of magnitudes lower. This abundance jump makes water an excellent tracer of warm, dense gas and a unique probe into the inner region close to the forming star.

Observations of interstellar gas-phase water from the ground are limited by the large amounts of water vapor in the Earth's atmosphere. Water maser lines at radio wavelengths longward of 3 mm (100 GHz), such as at 22 GHz, are readily seen, even from low-mass embedded YSOs (e.g., Furuya et al. 2003; Park & Choi 2007), but are constrained to small hot spots and are often variable in nature (Felli et al. 2007). They provide little information about the general physical and chemical evolution during star formation (Elitzur et al. 1989). One of the few exceptions of a non-masing water line observable from the ground is the 183 GHz $J = 3_{13} - 2_{02}$ transition, which can be used to trace widespread water emission under exceptional conditions (e.g., Cernicharo et al. 1990, 1996; Doty 2000). Observations of deuterated water can also be done from the ground, in particular through the HDO $1_{01} - 0_{00}$ 464 GHz, $3_{12} - 2_{21}$ 225 GHz, and $2_{11} - 2_{12}$ 241 GHz lines (e.g., Turner et al. 1975; Jacq et al. 1990; Helmich et al. 1996; Stark et al. 2004; Parise et al. 2005) and the D_2O $1_{10} - 1_{01}$ 316 GHz line (Butner et al. 2007), but the large uncertainties in the D/H ratio owing to fractionation make such observations a poor tracer of water itself. The H_2^{18}O isotopologue can be detected as well, but only through its high excitation temperature ($E_{\text{up}} = 193$ K) $3_{13}\text{--}2_{20}$ transition at 203 GHz (e.g., Jacq et al. 1988; Gensheimer et al. 1996; van der Tak et al. 2006).

To observe water emission lines systematically for a wide range of energy states,

one has to turn to space-based observatories. Gaseous water has been detected in a number of starforming regions using the Infrared Space Observatory (ISO), the Submillimeter Wave Astronomy Satellite (SWAS), and ODIN (e.g., Helmich et al. 1996; Harwit et al. 1998; Nisini et al. 1999; Ceccarelli et al. 1999; Snell et al. 2000; Bergin & Snell 2002; Maret et al. 2002; Nisini et al. 2002; Boonman et al. 2003; Bergin & Melnick 2005; Ristorcelli et al. 2005; Cernicharo & Crovisier 2005). However, due to large beams, low spectral resolution, or a combination of both, such observations were unable to accurately resolve the water abundance profile and trace the origin of the water emission, especially for low-mass YSOs. Two instruments onboard the Herschel Space Observatory¹ can be used for future observations of rotational water lines at unprecedented sensitivity, resolution and spectral coverage (Ceccarelli et al. 2001). The *Heterodyne Instrument for the Far Infrared* (HIFI) (de Graauw & Helmich 2001) and *Photodetector Array Camera and Spectrometer* (PACS) (Poglitsch et al. 2001) provide high spectral (up to 125 kHz) and spatial (20'' at 1 THz) resolution, which will allow a thorough analysis of water emission through a much wider range of observable transitions. In addition, the high sensitivity of the instrument will allow observations of various lines at low abundance, such as the optically thin isotopologues of water, in particular H₂¹⁸O. However, to infer abundances from such observations, detailed radiative transfer calculations are needed.

Several modeling efforts have been carried out to analyze the observed water lines, based either on models of shocks at high and low velocities (e.g., Kaufman & Neufeld 1996; Giannini et al. 2001; Nisini et al. 2002) or on thermal emission from the envelope itself (e.g., Maret et al. 2002; Boonman et al. 2003). As pointed out by van der Tak et al. (2006), the high water abundance combined with its high dipole moment and its susceptibility to far-infrared emission from dust results in high optical depths make this molecule particularly difficult to model. As a result, no systematic parameter studies have been carried out yet. We present here a parameter study of the water emission from low-mass protostellar envelopes using a full radiative transfer method including the effects of dust that is applied to realistic physical models of low-mass YSOs. Specific predictions for Herschel are made by convolving the computed emission with the Herschel observing beams. Poelman & van der Tak (2007) present similar models for high-mass protostars.

This chapter is organized as follows. § 7.2 presents the physical and molecular parameters necessary to accurately model water. § 7.3 takes an in-depth look at a single Class 0 source, L 483, and explores the effects of possible water abundance profiles. § 7.4 presents the results from the range of parameters that influence water emission. § 7.5 investigates the influence of dust on water line fluxes and profiles, which is often ignored. § 7.6 gives an analysis of a selected sample of observed water lines from ISO, SWAS, and ODIN to test the models and to infer implications for observations with future instruments such as HIFI and PACS. Final conclusions and recommendations can be found in § 7.7.

¹see <http://herschel.esac.esa.int/>

7.2 Model

The modeling has been carried out in two stages. First, the dust radiative transfer is calculated for a given power-law density profile (§ 7.2.1). This produces dust temperature profiles for given density structures. Subsequently, water level populations and line emission profiles are modeled using the line radiative transfer code RATRAN (§ 7.2.2) (Hogerheijde & van der Tak 2000), with the assumption that the gas temperature is equal to that of the dust. For an overview of the steps, see van Dishoeck (2003) (Figure 2). Our method refers to the ‘empirical method’ presented there. See Table 7.1 for an overview of the parameters.

7.2.1 Physical structure of the envelope model

7.2.1.1 Dust radiative transfer

Our protostellar envelope models are taken to be spherically symmetric, with the protostar located at the center. It has been shown that this assumption is valid for analyzing both the continuum and line emission down to scales of a few hundred AU (e.g., Shirley et al. 2000; Jørgensen et al. 2002; Schöier et al. 2002; Jørgensen et al. 2005a). The density n at radius r within the protostellar envelope is described by

$$n(r) = n_0(r/r_0)^{-p}, \quad (7.1)$$

with the power-law exponent p and density n_0 at a reference radius r_0 as parameters. Within the context of protostellar collapse theories, both parameters depend on the age of the system and on the original core conditions, such as its initial mass.

Both the gas and dust temperatures inside the envelope are also often described by a power-law profile. However, this approximation fails at small radii where the dust becomes optically thick (e.g., Doty & Leung 1994; Jørgensen et al. 2002; Young & Evans 2005). The actual temperature structure depends on a combination of the density structure and the central source luminosity, and a dust radiative transfer calculation is needed to determine it. The radiation is produced by the energy released through accretion of material onto the protostar.

The continuum radiative transfer through the envelope was calculated using the spherically symmetric dust radiative transfer code DUSTY (Ivezić & Elitzur 1997). DUSTY is a scale-free 1-D code that uses the ratio Y of the outer over inner radius, $R_{\text{out}}/R_{\text{in}}$, the dust opacity τ at $100 \mu\text{m}$, the temperature at R_{in} , and the power-law index of the density profile p as its variables. Results are then scaled by using the luminosity and distance of specific sources. The inner edge of our envelope R_{in} was set at the radius where the temperature of the envelope reaches 250 K. Material closer to the star is assumed to be located in a disk, which is not taken into account. In addition, we assume that the disk has no influence on the temperature and density distribution of the envelope. The exact inner radius in AU depends on the luminosity, which differs for each model, and R_{in} is typically a few tens of AU, much smaller than the Herschel beams (see Table 7.2). In all our models, Y is taken to be 200. Values of R_{out} are a few thousand to ten thousand AU, greater than the Herschel beam ($20''$ at 1113 GHz) at all but the lowest frequencies, but generally less than the values given in Jørgensen et al. (2002). The adopted dust opacity’s are the often-used OH tables, column 5 of

Ossenkopf & Henning (1994) throughout. Figure 7.1 shows a typical temperature and density profile.

7.2.1.2 Gas radiative transfer

The gas temperature is taken to be equal to the dust temperature for the entire spatial extent of our model, and the gas:dust mass ratio is taken to be 100:1. Warm dense gas can efficiently cool through the emission of excited molecular and atomic lines such as CO, H₂O, OH, and [O I] (Giannini et al. 2001). Water can also heat the gas through far-infrared pumping followed by collisional de-excitation (e.g., Ceccarelli et al. 1996). As a result, dust and gas temperatures can differ slightly, especially in the 100-200 K range (e.g., Ceccarelli et al. 2000; Maret et al. 2002); however, at densities of 10^7 cm^{-3} or higher, the gas and dust in the warm inner region couple efficiently. At low densities ($<10^5 \text{ cm}^{-3}$) and temperatures ($<50 \text{ K}$), any differences between gas and dust temperature depend on the source parameters (e.g., luminosity, total envelope mass) and the external interstellar radiation field (ISRF). Doty & Neufeld (1997) show in their Figure 12 that these differences are generally small, about 10 K or less for low-mass YSOs, and typically only exist at radii greater than 2000 AU. Boonman et al. (2003) show that for high-mass YSOs, the water line emission for a full radiative transfer calculation of the gas temperature differs negligible from that calculated using the $T_{\text{dust}} = T_{\text{gas}}$ assumption.

Our choice of $R_{\text{out}}=200 R_{\text{in}}$ assumes that water vapor at larger radii does not contribute to the total water line emission due to the low densities ($< 10^5 \text{ cm}^{-3}$) and temperatures ($<15 \text{ K}$) in these regions. This assumption mostly affects the transitions leading to the ground states. Any such material is able to absorb water emission for optically thick lines, and lead to weak emission lines in observations taken with a beam that is much larger than our adopted source sizes. However, such extended envelope material is almost indistinguishable from any larger scale cloud complexes not directly related to the source. Such contributions from large-scale clouds need to be taken into account on a source-by-source basis, but are beyond the scope of this work. The protostellar envelopes are assumed to be shielded from strong external radiation fields by surrounding molecular cloud material. If directly exposed to outside radiation, the temperature in the outer envelopes is affected by the ISRF, but material is not heated by more than 40 K for the ISRF found within the Orion starforming region (Jørgensen et al. 2006). Low-mass starforming regions are expected to have significantly lower ISRF. External radiation is not considered for these models.

7.2.1.3 Grid parameters

To limit the model complexity, the wide range of parameters was reduced to four variables (see Table 7.1). The density at 1000 AU, $n_0(\text{H}_2)$ and the exponent of the density power law p are two of these. Jørgensen et al. (2002) observed many low-mass YSOs and inferred densities at 1000 AU between 1×10^5 to $5 \times 10^6 \text{ cm}^{-3}$. Accordingly, three values, 0.4×10^6 , 1×10^6 , and $5 \times 10^6 \text{ cm}^{-3}$ were chosen to sample this range, and p was chosen to be either 1.5 or 2.0. The stellar variables are reduced to a single variable, the luminosity. Models using luminosities of 2, 7, and 25 L_{\odot} are explored to represent

Table 7.1 — Parameters for low-mass protostellar envelopes

Variables	
$n_{\text{H}_2}(1000 \text{ AU}) (10^6 \text{ cm}^{-3})$	0.4, 1, 5
p	1.5, 2.0
Luminosity (L_{\odot})	2, 7, 25
X_0 (water)	$10^{-4}, 10^{-6}$
X_d (water)	$10^{-6}, 10^{-7}, 10^{-8}$
Fixed Parameters	
Distance	150 pc
Stellar temperature	5000 K
Gas temperature	$= T_{\text{dust}}$
R_{in} (inner radius)	250 K
R_{out} (outer radius)	$200 R_{\text{in}}$
r_0	1000 AU
Water freeze-out	100 K
$o : p$ ratio H_2O^a	3:1
$o : p$ ratio H_2	1:1
Dust properties	OH 5 ^b
Velocity dispersion ΔV	1.67 km s^{-1}

^aFor the L483 models, ortho-, and para-water were modeled independently. See § 7.3 ^bSee Ossenkopf & Henning (1994) column 5

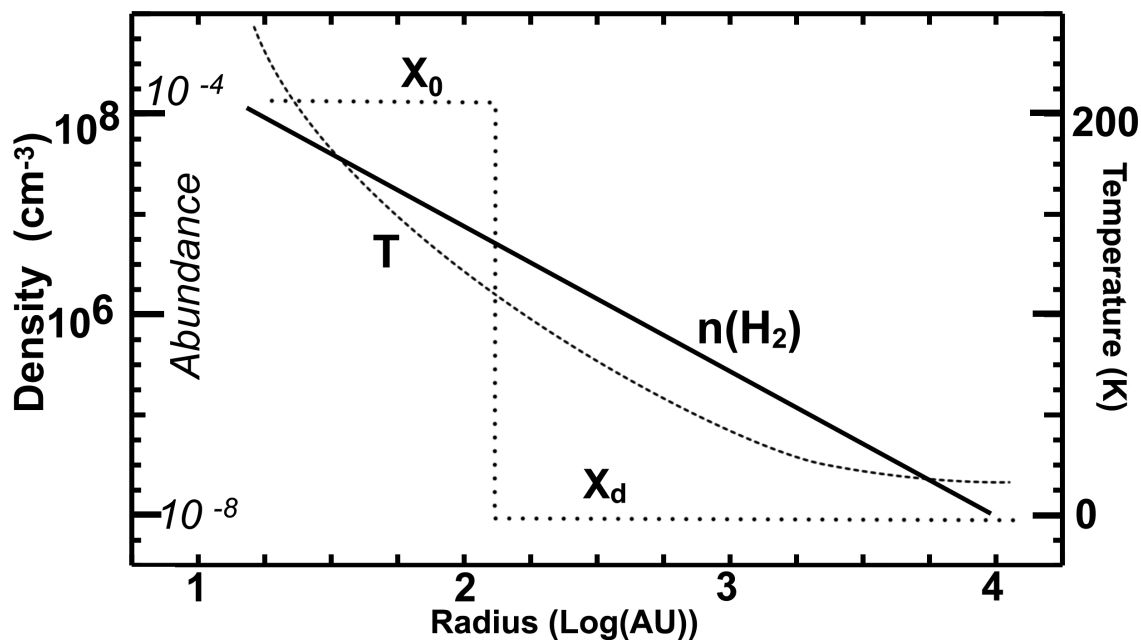
the wide range of luminosities observed in low-mass protostars. Although the surface temperature of the protostar cannot be derived directly, it is assumed to be around 5000 K for low-mass young stars, regardless of the luminosity or age. Test models show that, due to the reprocessing of stellar photons into IR/thermal photons very close to the star, the stellar effective temperature has little influence on the modeling. The final variable is the gas-phase water abundance, to be discussed below. Table 7.1 summarizes all the adopted parameters. The resulting masses and inner and outer radii for each envelope model can be found in Table 7.2.

7.2.2 H₂O line modelling

Because of the gradient in temperature, the water abundance X with respect to H_2 is expected to vary within YSO envelopes. Previous studies of low- and high-mass YSOs used a variety of H_2O observations with ISO-LWS, ISO-SWS, and/or SWAS to constrain the water abundance profile in protostellar envelopes to have a ‘jump’ in abundance at a characteristic temperature around 100 K (e.g., Maret et al. 2002; Boonman et al. 2003; van der Tak et al. 2006). Such ‘jumps’ have also been confirmed by ground-based observations of other molecules such as CH_3OH and H_2CO (e.g., van der Tak et al. 2000; Ceccarelli et al. 2000; Schöier et al. 2002; Jørgensen 2004; Maret et al. 2004). The abundance of water in the inner region X_0 is high for two reasons. First, most water exists in the gas phase above 100 K, the temperature at which water ice evaporates from the grains. Second, gas-phase reactions of atomic oxygen with molecular hydrogen drive all oxygen into water at high temperatures ($T > 230 \text{ K}$) (Charnley

Table 7.2 — The masses and inner radii of the model envelopes.

L_{bol}	$n_{\text{H}_2}(r_0)$	M_{env}	R_{in}	$R_{100\text{K}}$
L_{\odot}	10^6 cm^{-3}	M_{\odot}	AU	AU
$p = 1.5$				
2	0.4	0.06	8.22	23
2	1	0.15	8.22	23
2	5	0.76	8.22	23
7	0.4	0.15	15.3	42
7	1	0.39	15.3	42
7	5	1.93	15.3	42
25	0.4	0.40	29	80
25	1	1.01	29	80
25	5	5.04	29	80
$p = 2$				
2	0.4	0.07	8.22	21
2	1	0.18	8.22	21
2	5	0.90	8.22	21
7	0.4	0.13	15.3	38
7	1	0.33	15.3	38
7	5	1.65	15.3	38
25	0.4	0.24	29	72
25	1	0.63	29	72
25	5	3.15	29	72

**Figure 7.1** — Example of the physical structure of a model envelope with the density (solid), temperature (dashed), and abundance (dotted) displayed versus radius. The adopted parameters are $n_0(\text{H}_2)=10^6 \text{ cm}^{-3}$, $p=1.5$, and $L = 2 L_{\odot}$.

et al. 2001). However, in regions where the temperature drops below 100 K, water is mostly frozen out onto the grains, and only trace amounts of gaseous water are present with an abundance X_d .

Accordingly, ‘jump’ abundances are assumed for all models with X_0 , the abundance of the warm inner region, taken to be 10^{-4} or 10^{-6} , and X_d , the abundance in the cold outer region, taken to be 10^{-6} , 10^{-7} , or 10^{-8} . These values cover the range of inferred abundances from observations to date for embedded protostars. Although beam-averaged H_2O abundances below 10^{-8} have been observed for B 68 and Oph-D (Bergin & Snell 2002), such clouds are starless. At the extremely low temperatures of <15 K, virtually all heavy elements are frozen out. Abundances as low as 10^{-11} were tested by Boonman et al. (2003), but models with outer abundances of 10^{-8} were preferred in fitting the combined SWAS and ISO-LWS data. One combination of abundances is a constant abundance at 10^{-6} , included to investigate the differences between ‘jump’ and constant abundance profiles. A finer grid of abundances within this range is explored for the L 483 model. Figure 7.1 includes the assumed abundance structure. Our models do not consider a so-called ‘drop’ abundance profile (see Schöier et al. 2004), in which the abundance in the outermost part is higher due to longer timescales for freeze-out at lower densities and due to photodesorption of ices (Bergin & Melnick 2005). Such an abundance profile would result in more self-absorption in the ground-state lines, equivalent to absorption caused by the cold fore-ground material not associated with the protostellar system.

The effects of micro-turbulence within the envelope are represented by a velocity dispersion FWHM, $\Delta V = 1.67 \text{ km s}^{-1}$ ($b = 1 \text{ km s}^{-1}$, with b the Doppler parameter), consistent with the typical line widths observed for optically thin rotational emission in low-mass YSO envelopes (Jørgensen et al. 2002, 2004, 2005a). For a more thorough discussion of the effects of the choice of this value, see § 7.5.2. An infall velocity profile was included, based on the velocity profiles for collapsing clouds as found by Shu (1977). This velocity profile was scaled to a velocity of 4 km s^{-1} at the inner radius R_{in} . At radii of a few hundred AU, the micro-turbulent velocity dominates over the infall velocity, which is the scale probed mostly by single-dish observations (e.g., Jørgensen et al. 2004). H_2 is assumed to be in a 1:1 ortho to para ratio. Water itself is in 3:1 ortho to para ratio. Collisional rate coefficients for both ortho- and para- H_2O with ortho- and para- H_2 were obtained from the LAMDA database (Schöier et al. 2005) based on calculations by Green et al. (1993) for temperatures in the range from 20 to 2000 K. New rate coefficients have recently been published (Phillips et al. 1996; Dubernet & Grosjean 2002; Grosjean et al. 2003; Faure et al. 2007)², but those new calculations often do not include a wide enough range of temperatures or the higher excited energy levels, needed for the analysis of YSOs. Test models using different published rate coefficients show that absolute line fluxes may differ up to 30% (Poelman & van der Tak 2007). Even greater differences are found at low temperatures ($T < 20$ K) and densities ($n(\text{H}_2) < 10^4 \text{ cm}^{-3}$) for the ground-state line intensities and profiles (e.g. Poelman & Spaans 2005; Dubernet et al. 2006). However, the general trends found in this chapter remain valid for different rate coefficients. . For a general discussion of uncertainties

²The rate coefficients from Faure et al. (2007) only became available once most of the models had been run

Table 7.3 — Key water lines observable with Herschel HIFI and PACS.

Transition	Freq. (GHz)	Wavelength (μm)	E_{up} (K)	Beam ^a ($''$)
HIFI				
Ortho-H ₂ O transition				
1 ₁₀ -1 ₀₁	556.93607	538.66147	61.0	39
2 ₁₂ -1 ₀₁	1669.90496	179.65094	114.4	13
2 ₂₁ -2 ₁₂	1661.00802	180.61322	194.1	13
3 ₁₂ -2 ₂₁	1153.12682	260.16219	249.4	19
3 ₁₂ -3 ₀₃	1097.36505	273.38213	249.4	21
3 ₂₁ -3 ₁₂	1162.91187	257.97312	305.3	19
Para-H ₂ O transition				
1 ₁₁ -0 ₀₀	1113.34306	269.45872	53.4	21
2 ₀₂ -1 ₁₁	987.92670	303.66625	100.8	21
2 ₁₁ -2 ₀₂	752.03323	398.91854	136.9	30
2 ₂₀ -2 ₁₁	1228.78902	244.14281	195.9	19
3 ₃₁ -4 ₀₄	1893.68681	158.42113	410.4	13
4 ₂₂ -3 ₃₁	916.17164	327.44956	454.3	25
4 ₂₂ -4 ₁₃	1207.63890	248.41863	454.3	19
5 ₂₄ -4 ₃₁	970.31524	309.17787	598.8	21
PACS				
Ortho-H ₂ O transition				
2 ₁₂ -1 ₀₁	1669.90496	179.65094	114.4	13
2 ₂₁ -1 ₁₀	2773.97691	108.14798	194.1	8
2 ₂₁ -2 ₁₂	1661.00802	180.61322	194.1	13
3 ₀₃ -2 ₁₂	1716.76979	174.74678	196.8	12
4 ₁₄ -3 ₀₃	2640.47434	113.61595	323.5	8
Para-H ₂ O transition				
2 ₂₀ -1 ₁₁	2968.74895	101.05267	195.9	7
3 ₁₃ -2 ₀₂	2164.13230	138.62371	204.7	10
4 ₀₄ -3 ₁₃	2391.57290	125.44046	319.5	9

^a taken from <http://herschel.esac.esa.int/home.shtml>

in molecular data, see Schöier et al. (2005).

The excitation and radiative transfer of the rotational water lines were calculated using the spherically symmetric version of the RATRAN code (Hogerheijde & van der Tak 2000). First, level populations were computed for all H₂O levels with energies up to 2000 K for the model envelope using full Monte Carlo radiative transfer. Individual iterations use a convergence criterion of 10^{-6} on the relative error of the fractional population for the solution of the statistical equilibrium. Iterations continue with increasing amounts of photons, until the greatest relative difference between fractional populations over all cells and all levels of three subsequent iterations is less than 1/6. In practice this means that the vast majority of cells and levels are converged to much smaller relative errors. Far-infrared radiation from the dust and CMB are included in the H₂O excitation and line formation. This inclusion makes it possible to investi-

gate infrared pumping, self-absorption of a line, and absorption against the dust continuum. Even though many levels are very sparsely populated, tests show that it is necessary to include the higher levels to obtain an accurate population distribution throughout the model.

The populations are then used to reconstruct detailed line profiles through ray-tracing, which can be convolved with any beam or area. It can also be used to make velocity maps of the source. The adopted spectral resolution is 0.05 km s^{-1} . RATRAN was benchmarked against many codes (van Zadelhoff et al. 2002). Furthermore, it was part of a recent benchmark test³ for line modeling of H_2O (van der Tak et al. 2005).

Although level populations were calculated for all levels up to $E_{\text{up}}=2000 \text{ K}$, only lines with an upper energy level below 500 K were selected for the presentation of results (see Table 7.3). Both H_2O and H_2^{18}O were modeled with a focus on lines that fall into the Herschel wavelength range. The $^{16}\text{O}:^{18}\text{O}$ isotope ratio was assumed to be 550:1, the ratio in the local ISM (Wilson & Rood 1994). All generic models are placed at 150 pc , the typical distance of most nearby low-mass starforming regions such as Ophiuchus, Taurus, and Chameleon. Results were convolved with the appropriate Herschel beams and given in main beam temperatures. For reference, the typical sensitivities expected with HIFI (5σ , 0.5 hr , 0.5 km s^{-1} resolution) are 60 mK for 557 GHz , 180 mK at 1130 GHz , and 600 mK at 1669 GHz . For PACS, limiting line fluxes (5σ , 0.5 hr , point source) range from $6 \times 10^{-18} \text{ W m}^{-2}$ to $35 \times 10^{-18} \text{ W m}^{-2}$ ⁴. To convert from main beam temperatures T_{MB} to fluxes S_ν in Jy ($10^{-26} \text{ W m}^{-2} \text{ Hz}^{-1}$), use the formula

$$S_\nu = 2.65 \times 10^8 \times T_{\text{MB}}(\text{K}) \times \theta_0^2(') \times \lambda^{-2}(\mu\text{m}). \quad (7.2)$$

This assumes a source size equivalent to the beam size. For sources smaller than the beam, a correction needs to be taken into account. The Herschel beam θ_0 ranges from $40''$ ($0.66'$) at 557 GHz ($539 \mu\text{m}$) to $7''$ ($0.12'$) at 3000 GHz ($100 \mu\text{m}$) (see Table 7.3).

7.3 Example : L 483

7.3.1 Physical structure

As an illustrative model, the isolated Class 0 source L 483, (Motte & André 2001) located at 200 pc , was modeled to investigate the sensitivity of the water line intensities to different abundances. This source has been studied extensively by Jørgensen et al. (2002) and Jørgensen (2004) and its physical and chemical structure is well-constrained through continuum and line data from (sub)millimeter single-dish telescopes and interferometers. The well-determined envelope and source parameters ($L_{\text{bol}} = 9 L_\odot$ and $n_0(\text{H}_2)=1 \times 10^6 \text{ cm}^{-3}$) are roughly in the middle of our parameter range, making L 483 an excellent test-case for modeling water emission. Only the inferred density slope, $p=0.9$, is somewhat flatter than for other sources, but this does not influence the model trends. For CO, a jump abundance at an evaporation temperature of $T \approx 30 \text{ K}$ was found to explain the observed molecular lines. Any compact disk is constrained to a mass of $0.012 M_\odot$ using interferometer observations with the Sub-Millimeter Array

³see <http://www.sron.rug.nl/~vdtak/H2O/>

⁴Calculated with Hspot, see <http://herchel.esac.esa.int/>

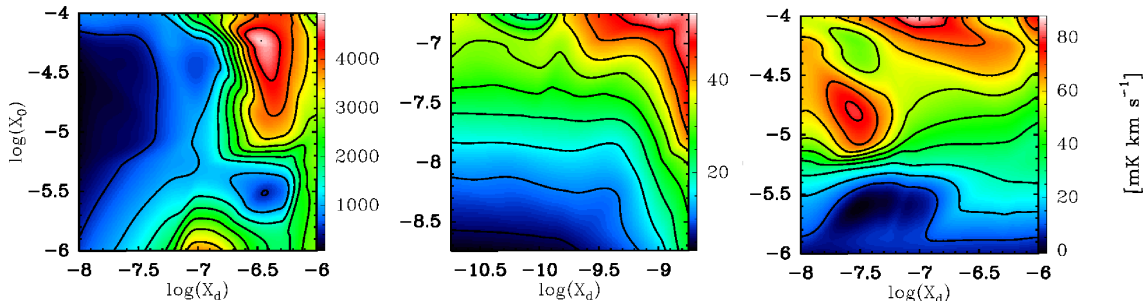


Figure 7.2 — Contour plots of the integrated water line intensity for the L 483 models, plotted as functions of X_d and X_0 . *left* : the o- H_2O $1_{10}-1_{01}$ line (557 GHz), showing a strong dependence on X_d ; *middle* : the p- H_2^{18}O $2_{02}-1_{11}$ line (995 GHz), showing a clear cut between the dependency on X_d or X_0 , depending on the abundance profile; *right* : the p- H_2O $5_{24}-4_{31}$ line (970 GHz), showing a strong dependence on X_0 .

(Jørgensen et al. 2007), negligible compared to the total estimated envelope mass of $4.4 M_\odot$ out to the 10 K radius of 10,000 AU. In addition, this source has been observed with ISO-LWS (Giannini et al. 2001). The best-fit parameters from the dust radiative transfer ($Y=1400$, $p=0.9$, $\tau_{100}=0.3$), which fit both the SED and the spatial extent of the SCUBA continuum data, determine the physical structure of the envelope. R_{in} (at $T=250$ K) is 9.9 AU for this rather shallow density profile, and R_{out} is $\sim 10,000$ AU. The radius where water freezes out onto the grains ($T=100$ K) is located at 35 AU. This L 483 model was used to explore a wider variety of water abundances than the generic models. Specifically, values of 1×10^{-4} , 5×10^{-5} , 1×10^{-5} , 5×10^{-6} , and 1×10^{-6} were used for X_0 and 1×10^{-6} , 5×10^{-7} , 1×10^{-7} , 5×10^{-8} , and 1×10^{-8} for X_d . All other parameters were kept fixed. Ortho- and para-water were modeled separately, and water abundances are given for ortho- or para-water individually instead of the combined total water abundance with the used 3:1 ortho to para ratio. This allows independent probes of the ortho to para ratio. Thus, X_0 and X_d refer to either ortho- or para- H_2O , depending on the line in question.

7.3.2 Results

In Table 7.4 the integrated emission of both H_2^{16}O and H_2^{18}O lines, observable with Herschel-HIFI (see Table 7.3), are presented for the reference grid of L 483, whereas Table 7.5 presents the peak temperatures. Detailed contour plots of all HIFI lines as functions of X_0 and X_d are presented in Fig. 7.2 the online appendix. Many of the trends discussed below are similar to those found for AFGL 2591, as discussed in Poelman & van der Tak (2007). Overall, lines are found to belong to three categories. First, all excited H_2^{18}O and several H_2O highly excited ($E_{\text{up}} > 200$ K) lines are completely optically thin. They have Gaussian profiles with widths that depend on the turbulent width. Due to the freeze-out of water onto grains below 100 K, these optically thin lines probe the inner warm dense region. For the model where water has a constant abundance of 10^{-6} , emission from the warm dense inner region still dominates and is optically thin (either due to the low population of the highly excited states or the low abundance of H_2^{18}O). A good example is the H_2O $5_{24}-4_{31}$ 970 GHz line shown in Fig. 7.2 (*right*).

Table 7.4 — Integrated intensities, $\int T_{\text{MB}}dV$ [K km s⁻¹], for H₂O and H₂¹⁸O lines for L 483 models with various abundances. Negative values indicate strong (self-) absorbed lines.

Transition $X_d =$	$X_0 = 10^{-4}$			$X_0 = 10^{-5}$			$X_0 = 10^{-6}$		
	10^{-6}	$\frac{10^{-4}}{10^{-7}}$	10^{-8}	10^{-6}	$\frac{10^{-5}}{10^{-7}}$	10^{-8}	10^{-6}	$\frac{10^{-6}}{10^{-7}}$	10^{-8}
Ortho-H ₂ O transitions									
1 ₁₀ -1 ₀₁	2.7	2.4	0.83	2.8	1.0	8.8(-2)	9.5	3.8	0.57
2 ₁₂ -1 ₀₁	-0.2	-0.13	0.27	-0.35	-0.38	-0.33	3.0	0.23	-0.05
2 ₂₁ -2 ₁₂	1.7	0.27	0.20	0.17	0.32	0.11	1.7	0.37	0.12
3 ₁₂ -2 ₂₁	0.8	0.17	0.10	0.47	0.12	7.8(-2)	0.95	0.20	7.1(-2)
3 ₁₂ -3 ₀₃	0.8	0.29	0.13	0.43	0.22	6.0(-2)	0.94	0.39	7.4(-2)
3 ₂₁ -3 ₁₂	1.3	0.35	0.11	0.73	0.26	5.4(-2)	1.5	0.46	8.2(-2)
Para-H ₂ O transitions									
1 ₁₁ -0 ₀₀	-6.5(-3)	1.23	-0.17	-0.12	5.2(-2)	0.29	3.12	1.4	-0.13
2 ₀₂ -1 ₁₁	1.1	0.59	0.26	1.4	0.6	0.45	0.6	1.4	0.26
2 ₁₁ -2 ₀₂	0.85	0.73	0.16	0.99	0.6	0.34	0.96	1.1	0.15
2 ₂₀ -2 ₁₁	0.38	0.61	0.18	0.45	0.50	0.31	0.38	0.83	0.13
3 ₃₁ -4 ₀₄	4.4(-2)	6.3(-2)	6.3(-2)	1.9(-2)	1.9(-2)	2.7(-2)	3.7(-3)	1.9(-3)	1.3(-3)
4 ₂₂ -3 ₃₁	5.0(-2)	6.8(-2)	3.7(-2)	5.2(-2)	5.6(-2)	5.1(-2)	1.8(-2)	1.5(-2)	9.7(-3)
4 ₂₂ -4 ₁₃	0.21	8.6(-2)	5.3(-2)	0.25	8.3(-2)	8.0(-2)	0.24	0.10	5.8(-3)
5 ₂₄ -4 ₃₁	6.0(-2)	8.8(-2)	5.5(-2)	3.2(-2)	4.3(-2)	5.5(-2)	4.0(-3)	5.9(-3)	3.3(-3)
Ortho-H ₂ ¹⁸ O transitions									
1 ₁₀ -1 ₀₁	-3.3(-2)	-5.6(-3)	2.3(-2)	-4.0(-2)	-2.0(-2)	5.2(-3)	-1.9(-2)	-2.4(-2)	-3.9(-4)
2 ₁₂ -1 ₀₁	-0.13	-3.3(-2)	1.2(-2)	-0.13	-4.5(-2)	-6.7(-4)	-0.12	-4.9(-2)	-5.2(-3)
2 ₂₁ -2 ₁₂	4.1(-3)	4.2(-3)	3.7(-3)	1.8(-3)	9.6(-4)	9.3(-4)	1.0(-3)	1.3(-4)	1.1(-4)
3 ₁₂ -2 ₂₁	5.6(-2)	6.0(-2)	5.9(-2)	3.6(-3)	3.0(-3)	3.0(-3)	5.9(-4)	1.39(-4)	1.2(-4)
3 ₁₂ -3 ₀₃	2.5(-2)	2.6(-2)	2.5(-2)	8.5(-3)	6.9(-3)	6.8(-3)	2.0(-3)	4.6(-4)	3.8(-4)
3 ₂₁ -3 ₁₂	1.7(-2)	1.9(-2)	1.8(-2)	4.5(-3)	3.6(-3)	3.5(-3)	1.0(-3)	2.1(-4)	1.7(-4)
Para-H ₂ ¹⁸ O transitions									
1 ₁₁ -0 ₀₀	-0.21	-7.7(-2)	8.7(-3)	-0.16	-8.8(-2)	-4.7(-3)	-0.21	-9.3(-2)	-1.2(-2)
2 ₀₂ -1 ₁₁	5.3(-2)	4.0(-2)	3.8(-2)	4.4(-2)	2.0(-2)	1.8(-2)	2.5(-2)	4.7(-3)	3.1(-3)
2 ₁₁ -2 ₀₂	2.5(-2)	1.9(-2)	1.9(-2)	2.0(-2)	7.9(-3)	7.6(-3)	9.6(-3)	1.5(-3)	1.1(-3)
2 ₂₀ -2 ₁₁	1.7(-2)	1.4(-2)	1.4(-2)	1.6(-2)	6.5(-3)	6.2(-3)	7.2(-3)	1.0(-3)	6.9(-4)
3 ₃₁ -4 ₀₄	9.2(-5)	1.2(-4)	1.2(-4)	5.7(-6)	4.6(-6)	4.6(-6)	5.1(-7)	2.5(-7)	2.3(-7)
4 ₂₂ -3 ₃₁	6.3(-4)	8.4(-4)	8.5(-4)	2.8(-5)	2.3(-5)	2.3(-5)	9.1(-7)	6.7(-7)	6.4(-7)
4 ₂₂ -4 ₁₃	2.5(-2)	3.0(-2)	3.0(-2)	1.5(-3)	1.2(-3)	1.2(-3)	4.8(-5)	3.5(-5)	3.4(-5)
5 ₂₄ -4 ₃₁	7.1(-5)	1.1(-4)	1.1(-4)	1.6(-6)	1.3(-6)	1.3(-6)	4.6(-8)	4.2(-8)	4.0(-8)

In this and subsequent tables, the notation $A(B)$ indicates $A \times 10^B$.

The ground state lines of both H₂¹⁸O and H₂O, together with most H₂O excited lines with energies below 200 K, provide a strong contrast with the optically thin lines. These lines only probe the outer region. Even an abundance of water as low as 10^{-8} in the cold outer envelope produces a high enough column for these lines to become optically thick. The extremely high optical depth ($\tau > 25$) and the absorptions into the dust further prevent the integrated intensity from probing the entire envelope. Thus, these lines trace the outer abundance X_d , and self-absorption and absorption of the dust

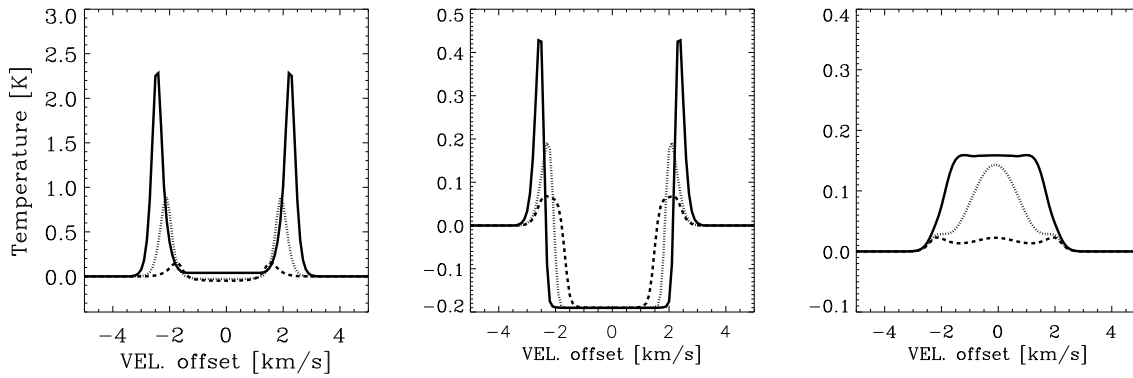


Figure 7.3 — H_2O spectra for an abundance X_0 of 10^{-5} for the $1_{10}-1_{01}$ (557 GHz, *left*), $2_{12}-1_{01}$ (1669 GHz *middle*), and $3_{12}-3_{03}$ (1097 GHz *right*) lines. Lines are shown for X_d of 10^{-6} (solid), 10^{-7} (dot), and 10^{-8} (dash).

continuum are commonly found in their line profiles. However, most optically thick lines have wings that are either optically thin or less optically thick. These wings may be able to probe the inner region up to the boundary layer around $T = 100$ K. See the $1_{10}-1_{01}$ line in Fig. 7.2 (*left*), Table 7.5 and the spectra in Fig. 7.3 and 7.4 (discussed in § 7.3.4).

Finally, some lines are optically thick for a high X_0-X_d combination, but are optically thin at low abundances. It is not known a-priori if these lines originate within the cold outer envelope or the warm dense inner regions. Examples are several of the highly excited H_2O lines, but such dependencies are also seen for lowly excited H_2^{18}O lines. Fig. 7.2 (*middle*) shows an example with the $p\text{-H}_2^{18}\text{O}$ $2_{02}-1_{11}$ line. It can be seen that, depending on the total column of water, this line either traces X_d at high columns or X_0 at lower columns. For the H_2^{18}O lines, a clear dividing line between dependency on X_0 or X_d lies at $X_d(\text{H}_2^{18}\text{O}) < 10^{-9.5}$ (see online appendix). Such a division is less clear for H_2^{16}O . The dust can become optically thick, especially at high frequencies, so the higher frequency lines will not be able to probe the inner region at all. For the L 483 models, this only takes place at frequencies higher than 1500 GHz, but see § 7.5 for further discussion. In the following, individual H_2O and H_2^{18}O lines are discussed in more detail.

7.3.3 Integrated emission

7.3.3.1 H_2O

The main isotopologue of water, H_2^{16}O , is optically thick in most transitions considered here. All lines with $J_{\text{up}} = 1$ and 2 are optically thick and trace the outer cold envelope. Most other lines trace either the warm inner or cold outer envelope. The integrated intensities of these ‘hybrid’ lines depend sensitively on the precise abundance parameters of the L 483 reference model. In particular, the radius where the line turns optically thick is comparable to that where the one where the temperature reaches 100 K for this model. These are the $2_{21} - 2_{12}$, $3_{12} - 2_{21}$, $3_{12} - 3_{03}$, $3_{21} - 3_{12}$ and $4_{22} - 4_{13}$ lines. At low abundances of X_d , they depend more on X_0 . If the abundance in the outer region is larger than 5×10^{-8} , they depend on X_d instead. The integrated intensities range from

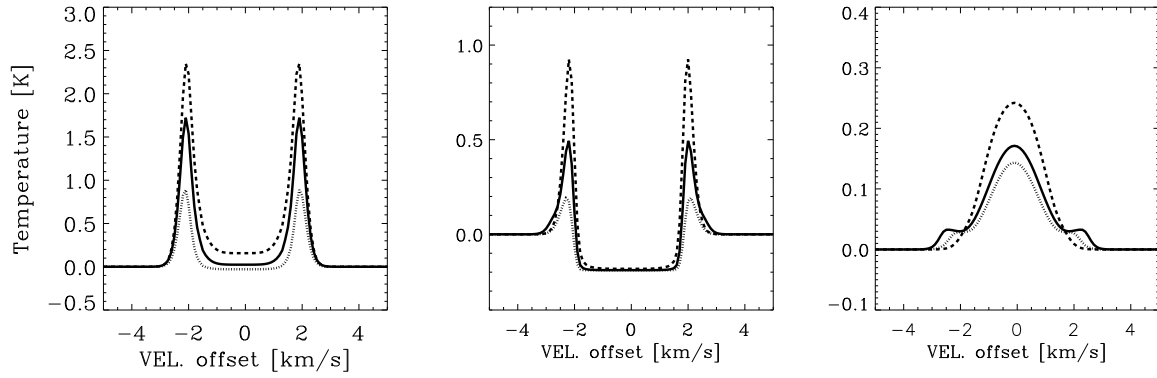


Figure 7.4 — H_2O spectra for an abundance X_d of 10^{-7} for the $1_{10}-1_{01}$ (557 GHz left), $2_{12}-1_{01}$ (1669 GHz middle), and $3_{12}-3_{03}$ (1097 GHz right) lines. Lines are shown for X_0 of 10^{-4} (solid), 10^{-5} (dot), and 10^{-6} (dash).

several hundreds of mK km s^{-1} in absorption to a few K km s^{-1} in emission, with peak brightness from 100 mK to 1 K, readily detectable with HIFI. The group of highly excited para-lines have peaks up to a few tens of mK, requiring much longer integration times.

Dependencies of the line strengths on abundances are not linear. An exception is whenever the line is completely optically thin over the entire profile. This is not the case for most lines and parts of the line profile will be optically thin and parts optically thick, causing complicated dependencies. For instance, the total integrated intensity of the 557 GHz line depends sensitively on the inner and outer abundances. Abundance combinations of $10^{-4}/10^{-6}$ produce lines with less total emission than $10^{-6}/10^{-6}$. The $10^{-6}/10^{-6}$ combination contains less water emission originating from the warm inner regions, but more dust continuum is able to escape the inner regions in the $10^{-6}/10^{-6}$. This influences the population distribution in the outer region, resulting in less central absorption. Since absorption is a major feature within this line profile, the total integrated line intensity effectively goes up.

7.3.3.2 H_2^{18}O

Because of the low abundance of the H_2^{18}O isotopologue, most of its lines are optically thin. Only the three transitions connecting to the ground levels of ortho- and para- H_2^{18}O - $1_{11} - 0_{00}$, $1_{10} - 1_{01}$, and $2_{12} - 1_{01}$ - have optical depths higher than 5 for all abundances. However, excited lines with $J_{\text{up}}=2$ are optically thick in their line centers for $X_0 > 10^{-5}$. The integrated intensities of these H_2^{18}O lines range from a few hundred mK km s^{-1} in absorption to a few tens of mK km s^{-1} in emission, whereas peak temperatures range from a few mK to a few tens of mK, thus requiring long integration times. Due to the low abundance, the dependence on either X_0 or X_d is much more evident than for H_2^{16}O (see Fig.7.2 for example). The optically thick ground-state lines accurately trace X_d , while optically thin excited lines only depend on X_0 . The few optically thick excited lines trace X_0 as well, since the $\tau = 1$ surface lies within the 100 K radius. Higher excitation H_2^{18}O lines are not very strong, in the range of a few micro-K to a few milli-K, too weak to be detectable with HIFI in reasonable integration times.

Table 7.5 — Peak temperatures [K] of H₂O lines for L 483 models of various abundances. Negative values primarily indicate absorption into the dust continuum.

Transition $X_d =$	$X_0 = 10^{-4}$			$X_0 = 10^{-5}$			$X_0 = 10^{-6}$		
	10^{-6}	$\frac{10^{-4}}{10^{-7}}$	10^{-8}	10^{-6}	$\frac{10^{-5}}{10^{-7}}$	10^{-8}	10^{-6}	$\frac{10^{-6}}{10^{-7}}$	10^{-8}
Ortho-H ₂ O transitions									
1 ₁₀ -1 ₀₁	2.8	2.1	0.65	2.8	1.1	0.2	5.4	2.8	0.5
2 ₁₂ -1 ₀₁	0.45	0.35	0.25	0.3	-0.13	-0.13	1.9	-0.13	0.25
2 ₂₁ -2 ₁₂	1.1	0.1	0.05	0.2	0.1	3.8(-2)	1.6	0.21	4.5(-2)
3 ₁₂ -2 ₂₁	0.28	6.5(-2)	2.4(-2)	0.18	4.5(-2)	2.1(-2)	0.36	0.1	2.4(-2)
3 ₁₂ -3 ₀₃	0.27	0.12	4.1(-2)	0.12	0.1	1.5(-2)	0.4	0.17	2.8(-2)
3 ₂₁ -3 ₁₂	0.5	0.18	4.1(-2)	0.33	0.13	1.5(-2)	0.55	0.26	3.2(-2)
Para-H ₂ O transitions									
1 ₁₁ -0 ₀₀	1.5	1.3	-9(-2)	0.45	0.45	0.45	1.6	1.25	0.13
2 ₀₂ -1 ₁₁	1.6	0.55	8(-2)	1.1	0.4	0.18	0.9	1.0	8(-2)
2 ₁₁ -2 ₀₂	0.8	0.22	7(-2)	0.38	0.18	0.16	0.45	0.38	7.5(-2)
2 ₂₀ -2 ₁₁	0.4	0.28	7.5(-2)	0.12	0.24	0.17	0.1	0.35	7(-2)
3 ₃₁ -4 ₀₄	2.8(-2)	2.2(-2)	2.2(-2)	1(-2)	1(-2)	1.9(-2)	2.5(-3)	1.5(-3)	8(-4)
4 ₂₂ -3 ₃₁	2.8(-2)	2(-2)	1(-2)	2.3(-2)	2.4(-2)	1.5(-2)	1.2(-2)	1(-2)	6(-3)
4 ₂₂ -4 ₁₃	0.16	2.4(-2)	1.4(-2)	0.12	2.7(-2)	1.7(-2)	0.12	4.5(-2)	2.2(-2)
5 ₂₄ -4 ₃₁	2.2(-2)	2.6(-2)	1.6(-2)	1.8(-2)	1.9(-2)	2.4(-2)	2.5(-3)	3.5(-3)	2(-3)

7.3.4 Line profiles

A number of characteristic line profiles are presented in Figures 7.3 and 7.4. The continuum has been subtracted so that the profiles can be readily compared on the same scale. The total profile contains valuable information about the envelope structure and velocity profile, none of which can be determined using the integrated line intensity alone. As seen in the examples, there is a wide variety of model profiles depending on a number of parameters. First, the excitation energy of the upper state, the total water column density and the critical density of the line in question will determine whether an emission line is optically thick, thin or a combination of both. Most lines show a combination, with optically thin wings around an optically thick line center. Second, the width depends on the systematic and turbulent velocity. Third, water in the colder outer envelope will absorb photons and scatter the radiation, causing an absorption feature. Finally, the optical depth of dust itself blocks line emission at frequencies above 1500 GHz originating in the inner region. In the following these profile shapes are discussed in more detail.

The profiles of optically thin lines are Gaussian and are good tracers of the velocity profile. Optically thin lines always trace the inner warm region, where the higher excitation states are populated. The ratio of the line wing over the peak temperature can vary, depending on the excitation energy of the line. Higher excitation lines are broader, while low excitation lines have a narrower peak with very weak line wings. An example in Figure 7.4 is the 3₁₂-3₀₃ 1097 GHz line, which is completely optically thin for $X_0=10^{-6}$. The line center becomes optically thick at $X_0=10^{-5}$ and thus decreases, but the optically thin line wings are noticeably higher in emission. At $X_0=10^{-4}$, the

optically thick line center is brighter than at 10^{-5} due to the high abundance, but still weaker than the optically thin emission at $X_0=10^{-6}$.

The profiles of optically thick lines are much more complicated. Their wings can either be optically thick or thin, depending on the abundances and frequency of the line. This gives rise to three different profiles.

- Lines with a Gaussian line center, but with enhanced line wings. A characteristic ‘bump’ can be seen at velocities where the line profile changes from optically thick to thin when going to more extreme velocities. The line center is optically thick, but is heavily pumped by the line radiation coming from water in the warmer regions further inwards in the envelope. This behavior is often called ‘effectively optically thin’. Such lines trace the inner abundance X_0 , unless optically thick dust veils the inner region. An example is seen by the $3_{12} - 3_{03}$ 1097 GHz line with an X_0 of 10^{-4} in Figure 7.4.
- ‘Flat top’ lines, where the center of the line is optically thick, but not self-absorbed. The center of the line is dominated by emission from a small region with a specific temperature. Line wings are optically thin. Material at larger radii is unable to cause self-absorption, and there is not enough material deeper within the envelope to make such a line ‘effectively optically thin’. Optically thick dust can prevent warmer regions from influencing the line at higher frequencies. An example is given by the $3_{12} - 3_{03}$ 1097 GHz line with $X_d = 10^{-6}$ in Figure 7.3.
- Deeply (self)-absorbed lines with most of the emission in the line wings. Absorption into the dust occurs, and is stronger for high frequency lines, where the dust continuum is higher. All three ground state lines show such profiles. Examples are the $1_{10}-1_{01}$ and $2_{12}-1_{01}$ lines in Figs. 7.3 and 7.4. Both the depth and the width of the absorption vary, as do the line wing strengths:

(i) Absorption depth: If dust is optically thick (e.g., at 1669 GHz), the depth is independent of both X_0 and X_d as long as $\tau \gg 1$, and only depends on the radius where the dust turns optically thick, setting the continuum level. In Figure 7.3 and 7.4 (*middle*) the 1669 GHz continuum-subtracted line is always at -0.2 K. If dust is optically thin (e.g., the 557 GHz $1_{10}-1_{01}$ line), the depth v of the absorption depends on both X_d and X_0 and is caused by self-absorption of the water in the cold outer region against the warm emission. Indeed, it is found that water at around 70–90 K acts as a warm background emitter and water at 20 K as the cold absorber.

(ii) Absorption width: again there is a difference between high and low optical depths of dust. For 1669 GHz the width of the absorption depends on X_d , but not on X_0 . For 557 GHz, there is no dependence on abundance. The width of the absorption is the same for varying X_0 (the temperature at which the water emits changes little), and even though the profiles appear different for different X_d , this can be attributed to the changing absorption depth, not width.

(iii) Line wing strength: the strength of the line wing, which often contains the bulk of the line emission, is determined by the optical depth of the dust and gas.

Most often, the peaks seen in the wings of the ground-state lines are still optically thick. The wings trace both X_d (see $1_{10}-1_{01}$ and $2_{12}-1_{01}$ lines in Fig. 7.3, left, middle), which still contain large columns of the gas, and X_0 ($1_{10}-1_{01}$ and $2_{12}-1_{01}$ Fig. 7.4, left, middle), although in that case the relation is not straightforward. Line pumping from the warm gas further inwards is the main origin of the dependency from $X_0=10^{-4}$ to 10^{-5} . However, if X_d and X_0 are low enough, the line wings turn optically thin and are significantly enhanced (Fig 7.3) because higher temperatures are probed. This behavior is seen for a X_d/X_0 combination of $10^{-7}/10^{-6}$ where the line wings are brighter than for X_d/X_0 combinations of $10^{-7}/10^{-4}$ and $10^{-7}/10^{-5}$.

7.3.5 HIFI diagnostic lines

Although the beams for HIFI and the accompanying dilution factors are large compared to the physical size of the warm gas (see Table 7.3), the inner warm region is detectable through the higher excited states. The outer cold envelope is completely transparent for these lines. Considering the expected sensitivities of HIFI, a combination of different lines can constrain the water abundance profile. The H_2^{18}O $2_{02}-1_{11}$ 994 GHz line in HIFI Band 4 is mostly optically thin and traces X_0 , except at H_2^{16}O X_d abundances higher than 5×10^{-6} . However, the line is weak (a few tens of mK) and needs at least a few hours of integration to be detected. A possible alternative is the high excitation H_2^{16}O $3_{12}-3_{03}$ line in HIFI Band 4, which can be detected in roughly an hour of integration. It traces X_0 at high X_0 abundances, but for X_0 lower than 10^{-5} , emission coming from the colder outer part dominates, thus tracing X_d . This emission originates in the region with temperatures ranging from 70–100 K. Once the inner abundance X_0 is well-constrained, ground-state lines can in turn be used to constrain the abundance in the outer region. The bright wings of the 557 GHz line (HIFI Band 1) are detectable within a few minutes, but the entire line profile is needed for proper analysis (see § 7.3.4). The dependence on X_d can be traced most accurately using the line profiles of the $1_{11}-0_{00}$ 1113 GHz para- H_2O and 1101 GHz para- H_2^{18}O lines in Band 4, but resolving these profiles requires much longer integration times than the 557 GHz line. The 1667 GHz $2_{12}-1_{01}$ ortho- H_2O line in Band 6 is intrinsically brighter, but will take almost an hour of integration due to the low sensitivity of HIFI at this frequency. In addition, dust can become optically thick at this high frequency so that the line profile only traces the structure in the outer envelope.

The optically thick H_2^{16}O $2_{02}-1_{11}$ 988 GHz line, with its optically thin H_2^{18}O counterpart are the best candidates for determining the optical depth of water, but the H_2^{18}O lines require significant integration time (see above). An alternative is provided by comparison between of the 548 GHz H_2^{18}O and 557 GHz H_2^{16}O ground-state lines, but H_2^{18}O is still optically thick so that detailed modeling is required. The $1_{11}-0_{00}$ 1113 GHz, $2_{02}-1_{11}$ 988 GHz, and $2_{11}-2_{02}$ 752 GHz para- H_2O lines are well-suited to probing the physical structure of the envelope. Due to their different excitation energies and optical depths, these lines probe different environments within the protostellar envelope, and their line ratios are not affected by the uncertain ortho/para ratio.

7.3.6 Comparison with ISO-LWS data

The source L 483 was observed with ISO-LWS (Giannini et al. 2001). The para $2_{20-1_{11}}$ line at 2968 GHz ($101 \mu\text{m}$) was detected with a flux of $8.6 \pm 1.0 \times 10^{-20} \text{ W cm}^{-2}$ and the ortho $2_{12-1_{01}}$ line at 1670 GHz ($179.5 \mu\text{m}$) was found to have an upper limit of $4.3 \times 10^{-20} \text{ W cm}^{-2}$. The low LWS resolving power of $\lambda/\Delta\lambda = 200$ ($\sim 1500 \text{ km s}^{-1}$) was insufficient for determining the effect of any self-absorption or disentangling outflow components from quiescent envelope material. The best-fitting LVG model for the high- J CO lines gave a component of gas with $T=850\text{--}1800 \text{ K}$; it is expected that this hot gas contributes significantly to the water emission (Giannini et al. 2001).

The above models, corrected for the ISO beam of $80''$, are compared to the observed intensity. Our models show a strong absorption into the dust for both lines with optically thin line wings. Integrated intensities range from 7×10^{-22} up to $17 \times 10^{-20} \text{ W cm}^{-2}$ for the $2_{20-1_{11}}$ line and from $0.9 \times 10^{-20} \text{ W cm}^{-2}$ to $16 \times 10^{-20} \text{ W cm}^{-2}$ for the ortho $2_{12-1_{01}}$ line for different X_0 - X_d combinations. The best fit, using both the detection and upper limit, is found for an outer abundance of 10^{-7} and an inner abundance between 10^{-6} and 10^{-5} . The detected line is reproduced within 30%, while the upper limit is only 50% higher than the intensity produced by the model. For lower values of X_d , around 10^{-8} , the integrated emission in our model is almost an order of magnitude lower than the observed $2_{20-1_{11}}$ line. Such low outer abundances are found for cold regions in the envelopes around high-mass YSOs (Boonman et al. 2003), but appear inconsistent with the data for this low-mass YSO, unless the detected emission originates fully in the outflow. Higher inner abundances cannot be ruled out. However, the self-absorption in the models becomes stronger, resulting in a worse fit to the detected line and upper limit.

Other water lines within the ISO-LWS domain were not detected. The derived upper limits were found to be at least a factor 5 higher than fluxes predicted from all possible models. At short ($> 80 \mu\text{m}$) wavelengths, the difference is a few orders of magnitude. Since all lines are unresolved, no conclusion can be reached as to whether the detected water emission is dominated by outflow contributions or by thermal excitation within the circumstellar envelope with a high abundance. This example illustrates the need for spectrally and spatially resolved data of a number of lines to disentangle the different physical components.

7.4 General parameter study

Table 7.6 and Figures 7.5 and 7.6 present the results for a grid probing the parameters from Table 7.1 for a constant abundance combination of 10^{-4} for X_0 and 10^{-7} for X_d . Results for the full grid, including all probed abundances, can be found in the online appendix. The main variables of the grid - the luminosity, the density, and the density profile steepness - are discussed within this section. The dependence on abundance mirrors the behavior seen for the L 483 model discussed in § 7.3. For most combinations of envelope parameters, the H_2^{16}O transitions studied here are optically thick, sometimes with optically thin line wings. For H_2^{18}O lines, most transitions are optically thin, although the three ground state lines are optically thick at line center. The only optically thin H_2^{16}O lines are those for which the upper level of the transition has an

Table 7.6 — Integrated intensities, $\int T_{\text{MB}}\Delta V$ [K km s⁻¹], for H₂O lines in the wide parameter grid for an abundance combination of $X_0 = 10^{-4}$ and $X_d = 10^{-7}$.

Transition	Integrated Intensity ($\int T_{\text{MB}}\Delta V$ [K km s ⁻¹])					
	Lum. (w. $n_0 = 10^6$ cm ⁻³)			Dens. (w. $L = 7 L_\odot$)		
	2	7	25	0.4	1	5
$p = 1.5$						
Ortho-H ₂ O transitions						
1 ₁₀ -1 ₀₁	0.37	0.95	0.70	0.43	0.95	2.1
2 ₁₂ -1 ₀₁	0.35	0.36	-1.2	0.30	0.36	-4.4
2 ₂₁ -2 ₁₂	0.29	0.87	1.5	0.60	0.87	0.74
3 ₁₂ -3 ₀₃	0.21	0.60	1.5	0.38	0.60	0.89
3 ₁₂ -2 ₂₁	0.21	0.67	1.6	0.40	0.67	0.84
3 ₂₁ -3 ₁₂	0.37	1.1	2.7	0.59	1.1	1.7
Para-H ₂ O transitions						
1 ₁₁ -0 ₀₀	0.13	1.0	0.31	0.43	1.0	1.6
2 ₀₂ -1 ₁₁	0.58	1.5	3.0	0.72	1.5	1.1
2 ₁₁ -2 ₀₂	0.34	1.0	2.0	0.41	1.0	2.7
2 ₂₀ -2 ₁₁	0.31	1.0	2.3	0.47	1.0	1.4
3 ₃₁ -4 ₀₄	4.3(-2)	0.15	0.58	0.18	0.15	1.3(-3)
4 ₂₂ -3 ₃₁	4.1(-2)	0.13	0.48	0.13	0.13	9.6(-2)
4 ₂₂ -4 ₁₃	9.5(-2)	0.26	0.74	0.18	0.26	2.3(-3)
5 ₂₄ -4 ₃₁	5.0(-2)	0.15	0.57	0.16	0.15	8.7(-2)
$p = 2.0$						
Ortho-H ₂ O transitions						
1 ₁₀ -1 ₀₁	0.12	0.24	0.19	0.10	0.24	0.82
2 ₁₂ -1 ₀₁	0.89	-1.6	-3.1	0.71	-1.6	-5.0
2 ₂₁ -2 ₁₂	0.13	0.14	0.15	0.13	0.14	-1.4
3 ₁₂ -3 ₀₃	0.12	0.47	1.3	0.35	0.47	0.51
3 ₁₂ -2 ₂₁	0.13	0.48	1.2	0.29	0.48	0.49
3 ₂₁ -3 ₁₂	0.20	0.87	2.1	0.45	0.87	1.2
Para-H ₂ O transitions						
1 ₁₁ -0 ₀₀	0.30	9.4(-2)	0.23	0.52	9.4(-2)	9.0(-2)
2 ₀₂ -1 ₁₁	0.65	1.4	3.1	0.90	1.4	1.8
2 ₁₁ -2 ₀₂	0.46	0.94	2.1	0.56	0.94	2.2
2 ₂₀ -2 ₁₁	0.32	0.78	2.1	0.54	0.78	1.3
3 ₃₁ -4 ₀₄	-3.7(-3)	-6.7(-3)	0.13	7.1(-2)	-6.7(-3)	-1.2(-3)
4 ₂₂ -3 ₃₁	1.0(-2)	5.9(-2)	0.31	9.3(-2)	5.9(-2)	2.3(-3)
4 ₂₂ -4 ₁₃	4.7(-2)	0.19	0.74	0.22	0.19	8.1(-2)
5 ₂₄ -4 ₃₁	8.3(-3)	6.5(-2)	0.34	0.11	6.5(-2)	-6.9(-3)

Column 2 to 4 show the luminosity variation with a density of 10^6 cm⁻³. Column 5 to 7 show the variation of density with a luminosity of $7 L_\odot$.

excitation temperature above 200–250 K, specifically the lines with $J = 3$ and higher. These lines are only optically thin if the densities are low enough, $<10^7$ cm⁻³, and abundances are low, $X_0 < 10^{-5}$ and $X_d < 10^{-7}$. For typical low-mass envelopes, such

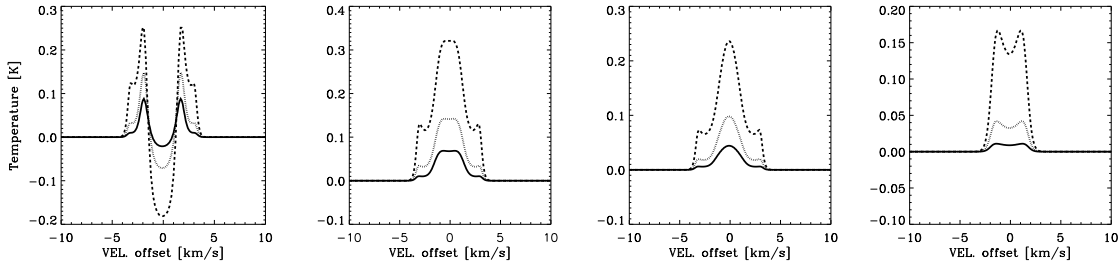


Figure 7.5 — Examples of the luminosity dependence of line profiles for a model with $p=1.5$, $X_0=10^{-4}$, $X_d=10^{-8}$, $n_0(\text{H}_2)=10^6 \text{ cm}^{-3}$. From left to right are shown the $1_{11}-0_{00}$ 1113 GHz, $2_{02}-1_{11}$ 988 GHz, $2_{11}-2_{02}$ 752 GHz, and $3_{31}-4_{04}$ 1893 GHz lines. Luminosities are 2 (solid), 7 (dot), and 25 (dash) L_\odot . These lines reflect the different characteristic line profiles discussed in § 7.3.4. It can be seen that the line shapes stay the same with increasing luminosity, while the line strengths and depths of the absorption are stronger at higher luminosities.

densities are only encountered within the inner region, where enhanced abundances are found. Thus, because many higher excited H_2^{16}O lines become optically thick only in the very dense warm inner region, they are still good tracers of the inner region (see § 7.3.3.1 and Fig. 7.4 right). For high densities and thus higher envelope masses, the larger dust column plays a major role by heavily influencing the water line emission. This is discussed in § 7.5.

7.4.1 Luminosity

Figure 7.5 shows four lines for various luminosities. For all lines, both the line strength and the absorption features are stronger for higher luminosities. For optically thin lines, a best fit can be found with a slope that has a power-law index of ~ 0.8 , i.e. $I \propto L^{0.8}$. Figure 7.7 shows two such power laws for the $2_{20}-2_{11}$ 1228 GHz line that differentiate between the exact conditions and correspond to $0.45L^{0.8}$ and $0.15L^{0.8}$. The slope of the power law is determined by the temperature profile, which determines the amount of warm gas present in the dense inner region, and the filling factor of this warm gas within the beam. This filling factor is not readily apparent, since models have different values for R_{in} and different radii where $T=100 \text{ K}$ is reached depending on luminosity and density profile (see Table 2). The peak temperatures of these optically thin lines naturally follow a similar dependence. Even for lines that display an optically thick line center (e.g., the $3_{31}-4_{04}$ line in Fig. 7.5), the peak temperatures depend on luminosity in a similar way to the completely optically thin lines.

For optically thick lines, a more complex dependency is seen in Fig. 7.5 (e.g., the $1_{11}-0_{00}$ line). For such self-absorbed lines, the wings (which are optically thin) increase with L , while any absorption features also become more prominent. Although the peak temperatures do not follow the proposed power law of the optically thin lines, they will become easier to detect for more luminous sources.

7.4.2 Density

Figure 7.6 shows four lines for a range of densities, varying by more than an order of magnitude, corresponding to envelope masses ranging from 0.15 to 1.93 M_\odot . The

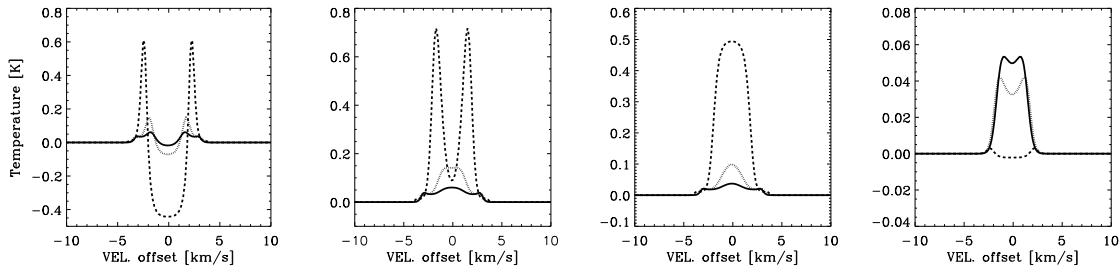


Figure 7.6 — Examples of the density dependence of line profiles for a model with $p=1.5$, $X_0=10^{-4}$, $X_d=10^{-8}$, $L=7 L_\odot$. From left to right are shown the $1_{11}-0_{00}$ 1113 GHz, $2_{02}-1_{11}$ 988 GHz, $2_{11}-2_{02}$ 752 GHz, and $3_{31}-4_{04}$ 1893 GHz lines. Densities are 4×10^5 (solid), 10^6 (dot), and 5×10^6 (dash) cm^{-3} . For most lines, the higher density, and thus higher water column, increases the emission, although absorption features are also enhanced. For the $3_{31}-4_{04}$ line at 1893 GHz, the dust becomes optically thick at lower temperatures (i.e. larger radii) within the envelope for higher densities.

density at 1000 AU has a strong influence on the water line emission. For optically thin lines, models with a constant p and constant luminosity show that a power law with an index of 0.75 accurately describes the dependence of line strengths on $n_0(\text{H}_2)$ (see Fig. 7.7). For optically thick lines, the line will decrease in strength at higher densities, since the emission from the warm inner part is veiled behind a larger, cold water column.

A higher density can also result in the dust becoming optically thick. This has an effect on the higher excited lines at high frequencies. For example, the optically thin $3_{31}-4_{04}$ 1893 GHz line (see Fig. 6, right) decreases by nearly two orders of magnitude in strength when the density increases from 0.4×10^6 to $5 \times 10^6 \text{ cm}^{-3}$. The dust is optically thin in the low-density models and optically thick at high density. Since the emission of this higher excitation line originates in the warm inner region, optically thick dust can obscure over 99% of the emission of this high frequency line (see § 7.5).

7.4.3 Density profile index

The steepness of the power law used to define the density distribution, p , also influences water line emission. Table 7.6 shows that lines differ subtly between $p=2$ and $p=1.5$. The line intensities of models with $p=2$ are lower by a factor ranging from 0.5 to 3 than those for models with $p=1.5$. Absorption features also differ in their depths for similar models with only p varied. This is caused by differing temperature profiles within the Herschel beams. Assuming equal $n_0(\text{H}_2)$ at 1000 AU, the warm ($T > 100$ K) region is significantly smaller for a model with $p=2$ than for $p=1.5$. Although local densities are higher by almost an order of magnitude, the beam dilution is too severe to overcome such small regions.

7.4.4 H_2^{18}O

The models were also calculated for the isotopologue H_2^{18}O . Similar to the L 483 models, transitions connected with the ground state lines are optically thick for all models. H_2^{18}O excited lines with $J_{\text{up}} = 2$ and 3 do have optically thick centers for some combinations of abundance, luminosities and/or densities, but are optically thin at densities below 10^6 cm^{-3} . Higher excitation H_2^{18}O lines are always optically thin. The best-fit

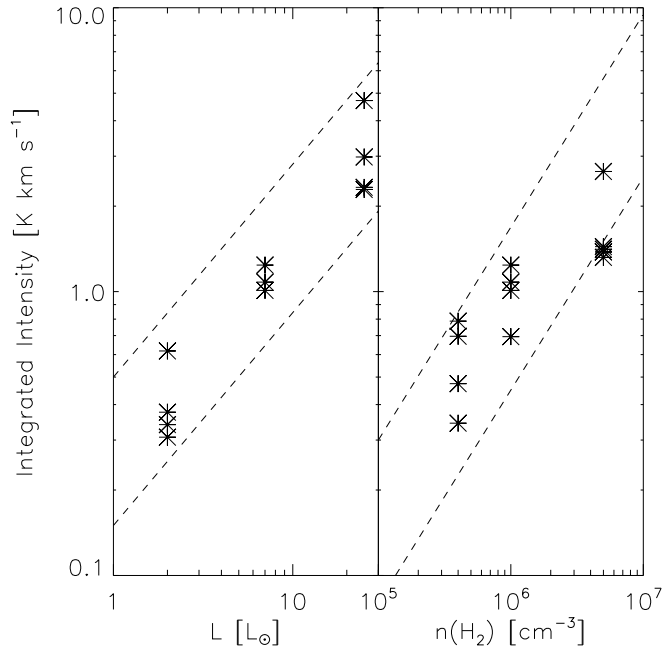


Figure 7.7 — The modeled integrated intensity of the optically thin $2_{20-2_{11}}$ 1228 GHz line for $X_0=10^{-4}$. Intensities are shown for the 3 different values of X_d for a constant density of 10^6 cm^{-3} (left) and for a constant luminosity of $7 L_\odot$ (right). Power laws with indices of 0.8 (left) and 0.75 (right) are overplotted. In the right panel, at $5 \times 10^6 \text{ cm}^{-3}$, this line becomes optically thick for $X_d=10^{-6}$, with its intensity dropping below the relation.

power law slopes for the optically thin H_2^{18}O lines are the same as those for H_2^{16}O . Of course, these conclusions are limited by the optical depth of dust at the frequency of the line, since H_2^{18}O lines at high frequencies are affected by dust. The precise frequency depends on the combination of luminosity and the density profile (§ 7.5). Results for H_2^{18}O can be found in the online appendix.

7.4.5 Line profiles

The H_2O line profiles shown in Figs. 7.5 and 7.6 all contain optically thin and optically thick parts as discussed in § 7.3.4. Since the line wings of most transitions are optically thin, a ‘bump’ is present in these wings at the velocity for which that particular line becomes optically thick. This velocity depends solely on the total column of water at this velocity and not on the luminosity. The height of this bump is determined by both the luminosity and the density profile. The line center changes according to the actual optical depth of both the dust and the water itself. Line centers can (i) be effectively thin and show a Gaussian profile, (ii) be dominated by a small region and be flat-topped, (iii) show a self-absorption feature determined by the optical depth of the line alone, (iv) have absorption into the dust continuum.

7.4.6 Model limitations

Our spherically symmetric envelope models have several limitations, which can affect the interpretation of observed line strengths.

- The presence of a large velocity gradient, such as seen in infall and rotation of envelopes around high-mass stars, can significantly broaden the water line and simultaneously make it less optically thick. The velocity field in these models was taken to be small, with an average infall velocity of 4 km s^{-1} at R_{in} . For low-mass sources, such an infall velocity combined with a turbulent width of 1 km s^{-1} has been shown to accurately reproduce observed emission line profiles (Jørgensen 2004).
- Outflow contributions. No outflow contribution has been taken into account in our models. It is assumed that emission from outflow material can be identified with sufficient spectral resolution in observational data with Herschel-HIFI. However, material heated by outflow shocks in high-density regions will not necessarily be accelerated to high velocities. This material can add significantly to the emission of water lines, but requires a detailed shock model to quantify it (e.g., Kaufman & Neufeld 1996). In addition, outflow cavities allow emission from the high-density regions of the inner envelope to escape along paths with much lower density than encountered in the cold outer envelope.
- Large extended molecular cloud or fore-ground cloud contributions can both emit rotational water lines or absorb radiation coming from the protostellar envelope. This is especially likely for the three transitions connected to the ground-states of ortho- and para-water. For example, for a cloud column density of 10^{22} cm^{-2} and an assumed water abundance of 10^{-8} with a gas density of 10^5 cm^{-3} , the ground state ortho- H_2O 557 GHz line will have an intensity of 50 mK if the emission fills the beam. The optical depth of this line is large enough, $\tau \approx 20$, to absorb radiation coming from behind this cloud. Results from SWAS and ODIN (See § 7.6.2) indeed do not show the deep absorption in the 557 GHz line, seen in Figs. 7.3–7.6. It is likely that extended cold cloud material dominates close ($< 0.5 \text{ km s}^{-1}$) to the line center in these data due to the much larger observing beams than Herschel. For excited lines, emission and optical depth in a fore-ground cloud are negligible. At high ($> 1 \text{ THz}$) frequencies, the dust within such cloud complexes can, however, absorb the emission from excited water.
- A large massive gas disk can contribute to the emission of water. However, most gas within disks is at low ($T \sim 30 \text{ K}$) temperatures. Most of the water will be frozen out, except in the inner few AU and in the warm surface layers. In addition, high dust columns can completely obscure frequencies above 1 THz. Water emission from disks is thus expected to be orders of magnitude lower for lines at all frequencies, except for the transitions connected to the ground state below 1 THz. However, the small angular size of disks causes much of the emission to be diluted to much lower values (a few mK) within the Herschel beam than commonly found for envelopes (a few 100 mK to a few K).

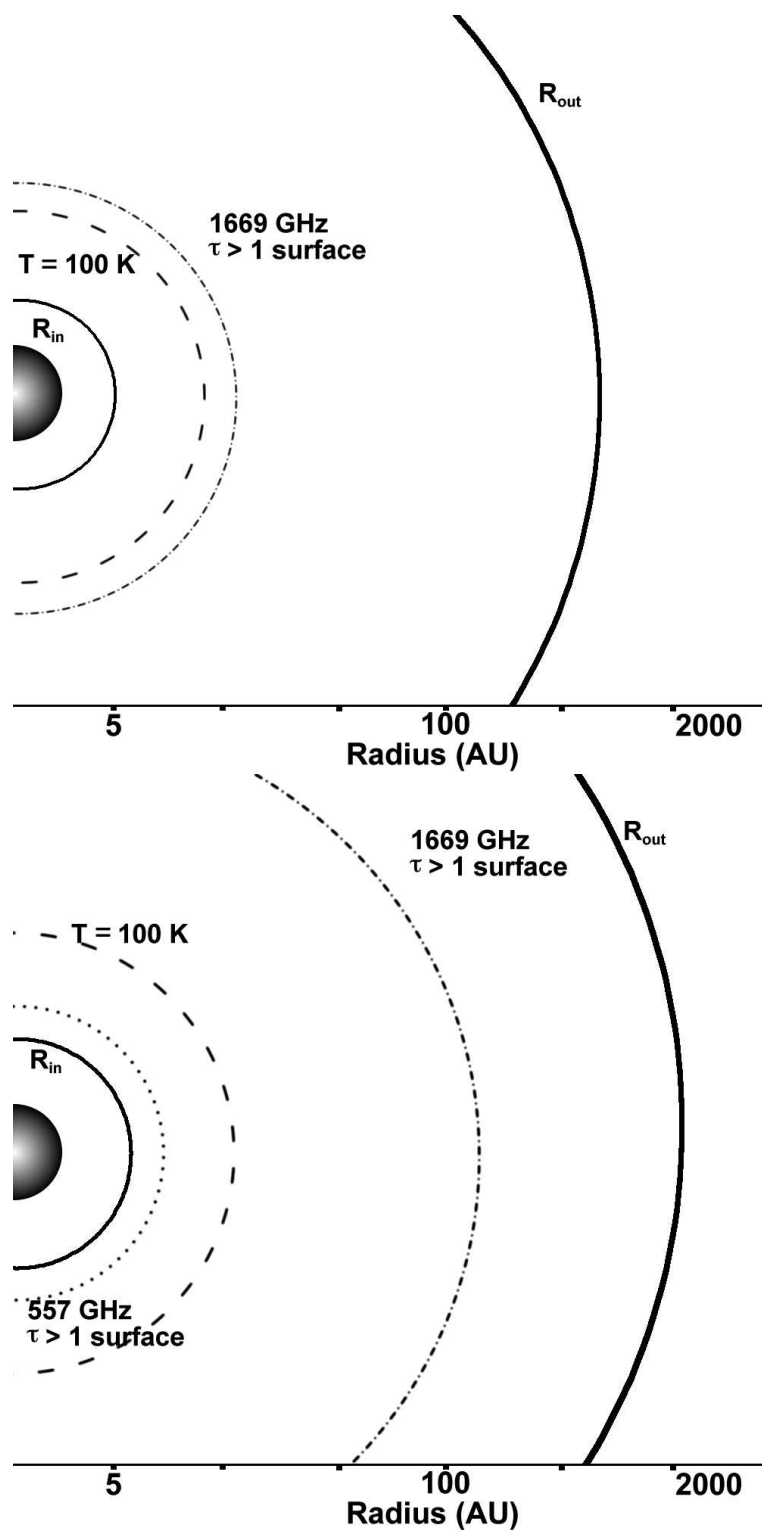


Figure 7.8 — Cartoon of protostellar envelope models. For two different models, the $\tau = 1$ surfaces at 557 and 1669 GHz for the dust are shown. A model with low-density ($n_0(\text{H}_2) = 4 \times 10^5 \text{ cm}^{-3}$, $M = 0.15 M_{\odot}$) is shown in the top panel; here the 557 GHz line contour is absent, since dust is optically thin throughout the envelope at this frequency. A model with a high density ($n_0(\text{H}_2) = 5 \times 10^6 \text{ cm}^{-3}$, $M = 1.93 M_{\odot}$) is shown in the bottom panel. The long-dashed line indicates the $T = 100 \text{ K}$ contour. In both models, the 1669 GHz line is unable to probe the inner warm region, regardless of its own optical depth, since the dust $\tau = 1$ surface lies far outside the $T = 100 \text{ K}$ radius.

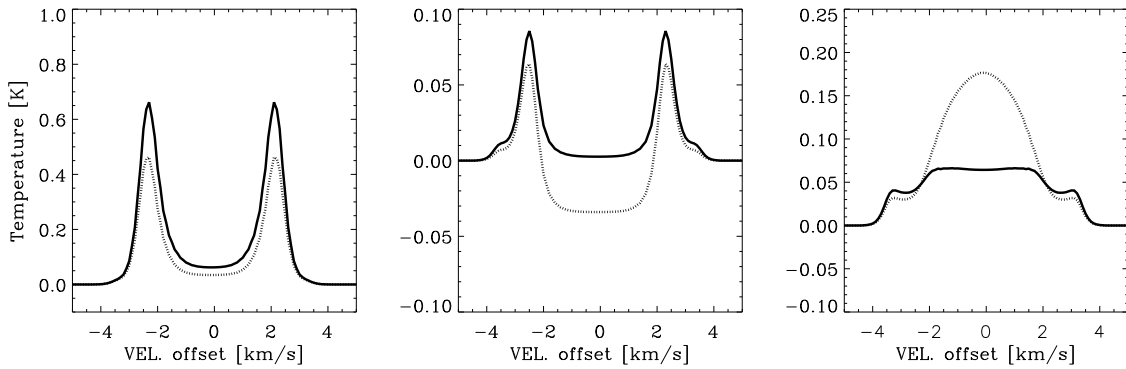


Figure 7.9 — Example spectra of the $1_{10}-1_{01}$ 557 GHz line (*left*), $2_{12}-1_{01}$ 1669 GHz line (*middle*) and $3_{12}-3_{03}$ 1097 GHz line (*right*) for a model with $p=1.5$, $L = 7 L_{\odot}$ and $n_{\text{H}_2}=1 \times 10^6 \text{ cm}^{-3}$. The solid lines represent the spectra with no dust within the envelope, while the dotted line shows the same line with dust included in the model. The influence of dust can be clearly seen. The peaks of the optically thick lines are reduced in strength, the depth of the absorption changes, and the optically thin lines are significantly pumped by far-infrared radiation.

7.5 Effects on H₂O excitation and line formation: dust and micro-turbulence

7.5.1 Dust

The presence of dust in protostellar envelopes influences water emission lines significantly in two ways, as can be seen in Table 7.7. First, the dust can become optically thick, preventing water emission from deep in the envelope to escape. Second, the far-infrared radiation can pump the water lines. Dust becomes optically thick at specific columns, depending on the value of the opacity, κ , at a given frequency (see Fig 5c in Ossenkopf & Henning (1994) for the precise relation). Since $\kappa_{\nu} \propto \nu^{\beta}$, with the dust opacity index β typically 1.5, this is especially likely at higher frequencies. Column 4 of Table 7.8 shows the total gas and dust column densities needed to reach a dust optical depth equal to 1 for each line.

Figure 7.8 illustrates this effect in a cartoon for two different envelope models. Two models, one with low density (low $M_{\text{env}} \approx 0.15 M_{\odot}$) and one with high density (high $M_{\text{env}} \approx 1.93 M_{\odot}$), are compared for two ground-state lines. The dust at 557 GHz only becomes optically thick for the more massive envelope due to very high column densities, while the low-density model remains optically thin throughout. The $\tau = 1$ surfaces correspond to temperatures well over 100 K. Since the 557 GHz water line is optically thick at lower columns, the dust will have no effect on this line, except for weakening the line due to dust absorption. Even the H₂¹⁸O column is large enough to prevent the dust opacity from influencing the 548 GHz line. In contrast, the dust at 1669 GHz becomes optically thick at a much smaller column, which corresponds to a radius and temperature much farther out into the envelope. The actual radius depends on the model in question. In the low-density model, the dust only turns optically thick at radii close to the 100 K water evaporation radius, while dust in the high-density model already obscures the line in the outer regions of the envelope. Optically thin lines at this frequency will not be able to probe the warm inner region, since the optically thick

Table 7.7 — Integrated intensity and peak brightness of lines with and without dust for a model with $p=1.5$, $L = 7 L_{\text{bol}}$ and $n_{\text{H}_2}=1 \times 10^6 \text{ cm}^{-3}$.

Transition	Dust		No Dust	
	Intensity [K km s ⁻¹]	T_{peak} [K]	Intensity [K km s ⁻¹]	T_{peak} [K]
1 ₁₀ -1 ₀₁	0.95	0.47	1.41	0.65
2 ₁₂ -1 ₀₁	-2.6(-2)	0.26	0.16	0.39
3 ₁₂ -3 ₀₃	0.67	0.18	0.39	0.06

dust effectively absorbs all water line emission.

Figure 7.9 shows example spectra of the 1₁₀-1₀₁ line at 557 GHz, 2₁₂-1₀₁ line at 1669 GHz and the 3₁₂ – 3₀₃ line at 1097 GHz for a model with $L=7 L_{\odot}$, $n_{\text{H}_2}=1 \times 10^6 \text{ cm}^{-3}$, $p=1.5$, $X_0=10^{-4}$, and $X_d=10^{-7}$, with and without dust. The spectra with dust are significantly weaker by up to 50%, even for optically thin dust at 557 GHz, since dust within the line of sight absorbs the water line photons. Lines that are optically thin at a frequency where optically thick dust exists are weaker by factors up to a few or more if dust is present, due to less water being ‘visible’. Optically thin lines can be pumped by far-infrared dust radiation coming from the region at radii larger than the $\tau = 1$ surface of the dust at the frequency of the line.

For each envelope model, the column density of dust depends on a combination of luminosity L (through the location of R_{in} , Table 2) and envelope structure parameters n_0 and p . If the $\tau = 1$ surface is approximated as a hard surface where all water photons are absorbed, a typical temperature can be extracted for each combination of L , n_0 , and p . This temperature is the upper limit to which water lines can probe for each model before dust becomes optically thick. Table 7.8 presents the $\tau = 1$ temperatures for four astronomically distinct models, based on the results from Table 6 of Jørgensen et al. (2002). Model 1, with $L=7 L_{\odot}$, $p=1.5$, and $n_0=5 \times 10^6 \text{ cm}^{-3}$, corresponds to a very young Class 0 YSO, which is dominated by a large, cold, and massive protostellar envelope. A good example is the well-studied NGC 1333 IRAS 4B source in the Perseus molecular cloud. Lines with a frequency above 1600 GHz are unable to probe the region with $T > 100$ K. Dust is optically thin throughout the envelope for frequencies lower than a 1000 GHz. Model 2, with $L=7 L_{\odot}$, $p=2$ and $n_0=5 \times 10^6 \text{ cm}^{-3}$, has similar parameters but its mass is more centrally condensed. Due to the very high column densities, dust becomes optically thick at all frequencies above 700 GHz, making it even more difficult to probe the central warm region than in Model 1. Highly excited water lines are effectively shielded from observers within this envelope at all frequencies. The third model, $L=2 L_{\odot}$, $p=2$, $n_0=4 \times 10^5 \text{ cm}^{-3}$, corresponds to a more evolved source with a low luminosity and a small envelope with most of the mass concentrated in the center due to a steep density profile. The relative amount of warm gas in this envelope is significantly higher. Such a model would correspond to most Class I sources, e.g., TMC-1A. The last model included has $L=25 L_{\odot}$, $p=1.5$, and $n_0=1 \times 10^6 \text{ cm}^{-3}$ which corresponds to a higher luminosity source, but with a low total mass. The mass of the envelope is distributed over larger radii and the luminosity is higher. For these last two models, dust will not hide the inner parts of the envelope at all. Only the very warm region

Table 7.8 — The dust properties at selected water line frequencies for four typical models. The column density N_{H_2} required to produce $\tau = 1$ for the dust at each frequency is given with the corresponding radii and temperatures.

Transition	Freq. GHz	κ_{OH5} 10^{-2} $\text{cm}^2\text{g}^{-1a}$	N_{H_2} 10^{23} cm^{-2}	r and T ($\tau_{\text{dust}} = 1$)							
				Model 1 ^c		Model 2 ^d		Model 3 ^e		Model 4 ^f	
				AU	K	AU	K	AU	K	AU	K
Ortho-H ₂ O transitions											
1 ₁₀ -1 ₀₁	556	4.56	54.8	- ^b	-	-	-	-	-	-	-
2 ₁₂ -1 ₀₁	1669	32.7	7.6	45	97	62	73	9	188	-	-
2 ₂₁ -2 ₁₂	1661	32.3	7.2	48	92	63	72	10	179	-	-
3 ₁₂ -3 ₀₃	1097	17.3	14.5	-	-	32	111	-	-	-	-
3 ₁₂ -2 ₁₂	1153	18.5	13.5	15	240	34	107	-	-	-	-
3 ₂₁ -3 ₁₂	1162	18.7	13.3	16	217	35	105	-	-	-	-
Para-H ₂ O transitions											
1 ₁₁ -0 ₀₀	1113	17.7	14.1	-	-	33	109	-	-	-	-
2 ₀₂ -1 ₁₁	987	14.4	17.3	-	-	27	128	-	-	-	-
2 ₁₁ -2 ₀₂	752	8.45	29.5	-	-	16	213	-	-	-	-
2 ₂₀ -2 ₁₁	1228	20.0	12.4	18	185	37	101	-	-	-	-
3 ₃₁ -4 ₀₄	1893	40.9	6.1	64	78	74	65	12	154	-	-
4 ₂₂ -3 ₃₁	916	12.2	20.4	-	-	38	99	-	-	-	-
4 ₂₂ -4 ₁₃	1207	19.6	12.7	17	193	23	144	-	-	-	-
5 ₂₄ -4 ₃₁	970	13.9	17.9	-	-	26	131	-	-	-	-

^a Total gas and dust

^b - indicates that the dust is optically thin throughout the entire envelope

^c See text, $L=7 L_{\odot}$, $p=1.5$, $n_0=5 \times 10^6 \text{ cm}^{-3}$

^d See text, $L=7 L_{\odot}$, $p=2$, $n_0=5 \times 10^6 \text{ cm}^{-3}$

^e See text, $L=2 L_{\odot}$, $p=2$, $n_0=4 \times 10^5 \text{ cm}^{-3}$

^f See text, $L=25 L_{\odot}$, $p=1.5$, $n_0=1 \times 10^6 \text{ cm}^{-3}$

($T > 150 \text{ K}$) is veiled near the inner radius of Model 3.

7.5.2 Micro-turbulence

The structure of micro-turbulence, defined in our models as a velocity dispersion, during the embedded phases of star formation is not well known, and theoretical models do not yet agree on a correct treatment. A good review of the theoretical considerations and problems is given in Ward-Thompson & Buckley (2001, their § 3.2). Jørgensen (2004) concludes that the inclusion of micro-turbulence as a velocity dispersion gives a more accurate reproduction of line intensities and profiles as opposed to the inclusion of infall (Jørgensen et al. 2005a). Ward-Thompson & Buckley (2001, § 4.6) test different values of micro-turbulence, as well as different power-law values for the variation of micro-turbulence with radius. This results in a large variation in the molecular line profiles of CS and HCO⁺. Similarly, Fig. 7.10 shows that the choice of the velocity dispersion can have a strong effect on all water lines, both optically thick and thin. All three lines (557, 1669, and 1097 GHz) show large differences in both line profile and

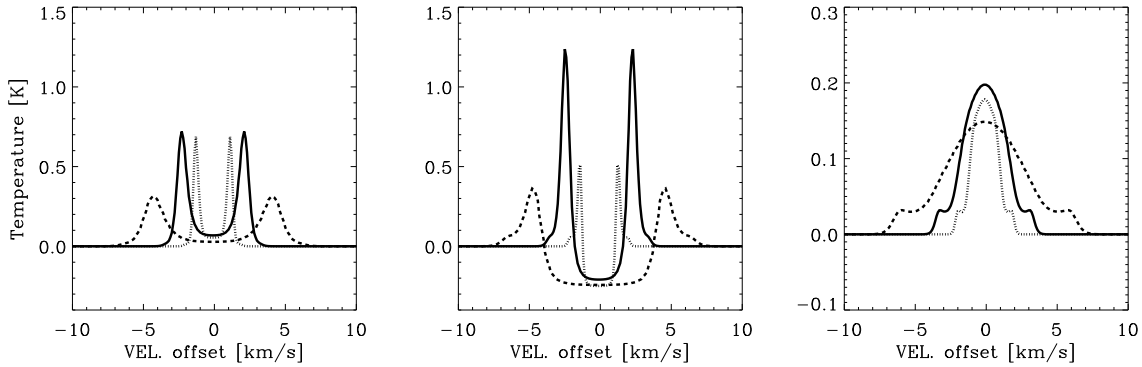


Figure 7.10 — Example spectra of the $1_{10}-1_{01}$ 557 GHz line (*left*), $2_{12}-1_{01}$ 1669 GHz line (*middle*), and $3_{12}-3_{03}$ 1097 GHz line (*right*) for a model with $p=1.5$, $L = 7 L_{\odot}$, and $n_{\text{H}_2}=1 \times 10^6 \text{ cm}^{-3}$. The dotted line is for a model with $\Delta V = 0.83 \text{ km s}^{-1}$. The solid line for $\Delta V = 1.67 \text{ km s}^{-1}$, and the dashed line for $\Delta V = 3.34 \text{ km s}^{-1}$. The large effect of micro-turbulence for all lines can be seen clearly.

in total integrated emission up to a factor of 3, when the velocity dispersion is varied between 0.83 ($b=0.5$), 1.67 ($b=1$) and 3.34 ($b=2$) km s^{-1} . Absorption both into the continuum and in the line are broader for higher values of micro-turbulence, while peak separation increases with increased velocity dispersion. Optically thin lines and line wings broaden if b is larger. Such effects are similar to those found by Ward-Thompson & Buckley (2001)

For molecular lines in low-mass protostellar envelopes, Ward-Thompson & Buckley (2001) and Jørgensen et al. (2005a) both adopt a constant value for the micro-turbulence with radius. In our case, a velocity dispersion, $\Delta V \sim 1.67 \text{ km s}^{-1}$ ($b=1 \text{ km s}^{-1}$), has been chosen to best reproduce line emission for a wide variety of molecules in sources such as L483, including CO, CS, but also complex molecules such as H_2CO and CH_3OH , tracing both the warm and cold regions. We recommend that for the modeling of water lines from specific sources, the velocity dispersion for the cloud in question be adopted as derived from other molecular lines.

7.6 Observational studies

The conclusions presented in previous paragraphs can be compared to current observational studies. However, due to the approximations used within the models and the unique combinations of parameters for individual sources, it is recommended that these models be used only as a starting point for interpreting water emission of protostellar envelopes from specific sources. As discussed in § 7.4.6, there are several factors that will complicate any analysis of observed water lines. To compare the envelope models presented above with any individual observation other than those from Herschel, the line intensities have to be corrected for the actual beam size of the telescope.

7.6.1 ISO-LWS

Water has been detected in several low-mass YSOs (both Class 0 and Class I) with ISO-LWS such as NGC 1333 IRAS 2/4, IRAS 16293-2422, Elias 29, L 1448, L 483, and SSV 13 (e.g., Liseau et al. 1996; Ceccarelli et al. 1999; Nisini et al. 1999; Giannini et al. 2001; Maret et al. 2002). Up to 14 water lines were detected, ranging from 180.5 μm to 67.3 μm . In most sources the total number of lines is significantly lower, but sufficient for proving the existence of water. For example, only a single line was detected for the Class I source Elias 29 (Ceccarelli et al. 1999).

As an illustration, we consider the case of NGC 1333 IRAS4A/B, for which Maret et al. (2002) report the emission of 14 water lines, together with high-J CO, OH, [O I], and [C II]. A model was put forward to explain the origin of these FIR lines using a collapsing envelope model without an outflow. Based on the model developed by Ceccarelli et al. (1996), the envelope and stellar parameters were derived from the best fit model to the 14 water lines. The water abundances in the envelope were found to include a jump at 100 K with a best fit of $X_0=5\times 10^{-6}$ and $X_d=5\times 10^{-7}$. A lower inner abundance is excluded by their model results, but a higher X_0 abundance of the order of 5×10^{-5} cannot be excluded.

The physical parameters derived by Jørgensen et al. (2002) and abundances proposed by Maret et al. (2002) correspond best with our model to $n_0=10^6\text{ cm}^{-3}$, $L=7L_\odot$, and $p=1.5$ with abundances 10^{-6} for X_0 and $10^{-6}/10^{-7}$ for X_d . However, our predicted line strengths differ from the observed and predicted line strengths in Maret et al. (2002), especially for low excitation lines. Our $2_{21}-2_{12}$ and $2_{12}-1_{01}$ predictions are 0.5×10^{-20} and $1.1\times 10^{-20}\text{ W cm}^{-2}$ for the $10^{-6}/10^{-7}$ abundance combination within the ISO-LWS beam, significantly lower than the observed values of 11 and $27\times 10^{-20}\text{ W cm}^{-2}$. Although an inner abundance of 10^{-4} produces brighter lines for the presented models, these lines are still an order of magnitude lower than the observed fluxes in Maret et al. (2002). The most likely explanation is the different treatment of dust between the two models, which lowers the fluxes of the high-frequency lines in our case. However, this also suggests that our models can only explain the ISO-LWS fluxes if there are cavities in the envelopes through which the photons can escape. Recent results with the Spitzer Space Telescope show numerous spectrally unresolved water lines from 20 to 30 μm , which suggest that NGC 1333 IRAS 4B is indeed viewed almost face-on, allowing the ro-vibrational lines to escape the protostellar system unhindered along the outflow axis (Watson et al. 2007). This can also help the longer wavelength lines coming from the inner envelope. Another possibility is that significant contributions come from large-scale outflows. This is confirmed by SWAS (see § 7.6.2).

7.6.2 SWAS

SWAS⁵ observed only the ground-state transition of o-H₂O at 557 GHz and o-H₂¹⁸O at 548 GHz. Although the beam of SWAS (3.3'x4.5') is significantly larger than for ISO-LWS, the increased spectral resolution of better than 1 km s^{-1} spectrally resolves most lines in starforming regions.

⁵See <http://cfa-www.harvard.edu/swas/> for more info

SWAS observed the NGC 1333 IRAS4 region (Neufeld et al. 2000; Bergin et al. 2003) where, contrary to the analysis of Maret et al. (2002), they observed a wide (24.4 km s^{-1}) and bright ($\int T_A^* dV = 0.5 - 1.9 \text{ K km s}^{-1}$) line. It was concluded that these lines originate within the outflow of one or more sources inside the NGC 1333 region. The model proposed by Maret et al. (2002) would have produced a narrow ($<4 \text{ km s}^{-1}$) and weak ($0.02\text{-}0.04 \text{ K km s}^{-1}$) 557 GHz line for each source contained within the beam. Our grid gives a typical integrated intensity within a SWAS beam of $\int T_{\text{MB}} dV = 0.5 \text{ K km s}^{-1}$ for a X_0/X_d combination of $10^{-4}/10^{-6}$ with a typical line width of 6 km s^{-1} .

Ashby et al. (2000) report on SWAS data for B335, an isolated Class 0 source with a 3σ upper limit of $<0.06 \text{ K km s}^{-1}$. Evans et al. (2005) used a wide variety of molecular emission lines to model the chemistry and physical structure of this source. The low luminosity ($4.5 L_\odot$) and low density ($4 \times 10^5 \text{ cm}^{-3}$) found by Evans et al. (2005) indicate that this class 0 source would be represented best by a model with $p=1.5$, $L=2 L_\odot$ and $n_0(\text{H}_2)=4 \times 10^5 \text{ cm}^{-3}$. Our predicted 557 GHz line strength corrected for the much larger SWAS beam is $0.02\text{-}0.06 \text{ K km s}^{-1}$ for outer abundances from 10^{-8} to 10^{-6} , just below the upper limits from SWAS. The only model that would have been detectable with SWAS has a constant abundance of 10^{-6} . The high jump abundance model with $X_0=10^{-4}$ and $X_d=10^{-6}$ cannot be ruled out, since most of the line is self-absorbed. A similar conclusion holds for most other Class 0 sources detected with SWAS.

Using the SWAS archive⁶, upper limits were found on several Class I sources, including RCrA IRS 5 and 7. Only upper limits of 20–50 mK in peak temperature could be derived. These observed limits are higher by up to an order of magnitude than the predictions presented in § 7.4 for models that would fit the physical parameters of Class I sources. The cold envelope material is constrained to $10''\text{-}30''$, a small region within the SWAS beam. Thus, our models are consistent with the scarce observational data on Class I sources.

In summary, both the ISO and SWAS data stress the need for Herschel Space Observatory data to properly constrain the origin of the observed H_2O emission and distinguish large-scale and outflow contributions from the emission originating in the quiescent gas of the protostellar envelope.

7.7 Summary and conclusions

This chapter presents several models that examine the excitation of water and its oxygen-18 isotopologue in envelopes around low-mass protostars, with parameters covering the entire range of luminosity and envelope characteristics of observed Class 0 and I sources. A model for the Class 0 source L 483 was used to illustrate the dependence of rotational water lines on the water abundances in the inner ($T > 100 \text{ K}$) region X_0 and outer ($T < 100 \text{ K}$) region X_d . In turn, a broader grid of models was explored for the full range of parameters and likely abundances. The main conclusions follow.

- The strengths and line shapes of all rotational water lines are sensitive to the physical parameters of the envelope. Thus, an accurate physical model, including a well-constrained density profile, is a necessary pre-requisite to modeling the water emission and derive abundances.

⁶See <http://lambda.gsfc.nasa.gov/product/swas/> for more information

- Ground-state lines from both H_2^{16}O and H_2^{18}O become optically thick at low water columns. Even though water abundances are expected to be very low in the outer envelope (10^{-8} with respect to H_2), the ground-state lines are still dominated by emission from the cold ($T < 30$ K) outer ($r > 1000$ AU) envelope. Ground-state line profiles are characterized by a double-peak feature with an absorption around narrow, optically thin emission line wings. The total integrated intensity cannot be used to trace the water abundance. Spectrally resolving the ground state lines is essential if these lines are to be used as probes for the water abundance.

- Higher excitation lines ($E_{\text{up}} > 150$ K) are usually dominated by emission coming from the warm inner region. At very high excitation ($E_{\text{up}} > 200 - 250$ K), the lines are optically thin. Although these lines are weak (< 0.4 K km s $^{-1}$), they provide valuable information about the characteristics of the warm gas present in the inner regions of the protostellar envelopes. Power laws with an index of 0.8 and 0.75 were found to accurately represent the dependence of optically thin lines on luminosity and density.

- H_2^{18}O is a reliable alternative tracer of the abundances in both the warm ($T > 100$ K) and cold ($T < 100$ K) regions of the envelope. However, such lines are weaker with predicted peak temperatures of only a few tens of mK, requiring long integration times.

- The presence of dust strongly influences the emission of most water lines. The optical depth of dust, which depends on the luminosity (due to varying R_{in} in our models) and density profile parameters, can prevent optically thin water lines from escaping the inner envelope, resulting in orders of magnitude reduction of the water fluxes. In addition, even optically thin dust absorbs up to 50% of the total line emission. Furthermore, the far-infrared continuum can pump optically thin water lines.

- The value of the micro-turbulent velocity dispersion and the structure of any systematic velocity field can significantly influence the line profiles and intensities of all water lines. The adoption of a micro-turbulent width that is constant with radius, as inferred from line profile fits of other molecules such as CS and HCO^+ , is expected to produce the best-fitting H_2O line profiles, but the actual values need to be determined on a source-by-source basis. To conclude, although water is a complex molecule to model, total intensities and line profiles of rotational water transitions can be used to constrain essential information about the protostellar envelope. The increased sensitivity and resolution, both spectrally and spatially available with HIFI and PACS on Herschel compared with previous missions, will provide the technology to observe water lines covering a wide range of excitations for the water molecule. The increased spectral resolution will be essential for locating the origin of warm gaseous water and understanding the structure of low-mass protostellar envelopes. Abundances in both the cold outer region and the warm inner region are best probed by a combination of lines and must include detailed line profiles.

Acknowledgements

T.v.K. would like to thank Dieter Poelman, Floris van der Tak, and Antonio Crapsi for valuable discussion concerning YSO envelope modeling and RATRAN. T.v.K. and astrochemistry at Leiden Observatory are supported by a Spinoza grant and by grant 614.041.004 from the Netherlands Organization for Scientific Research (NWO).

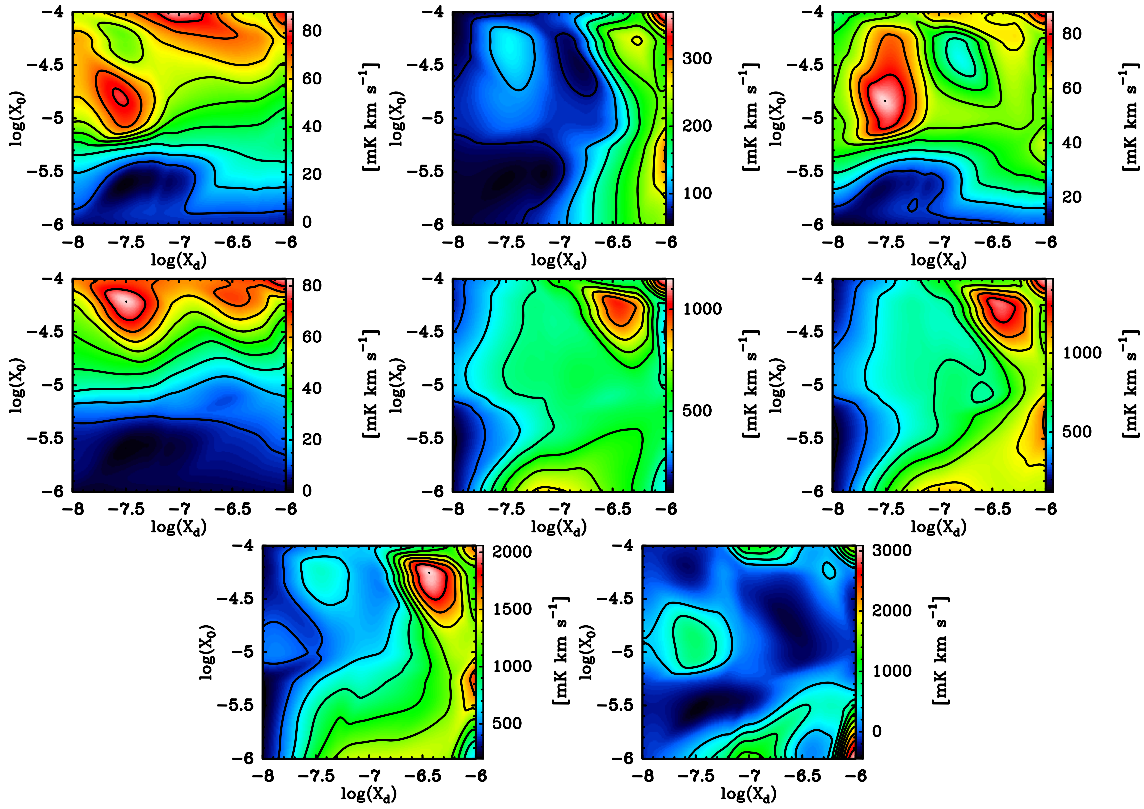


Figure A.1 — Contour plots of the integrated intensity of the L 483 models as a function of inner (X_0) and outer (X_d) for all para- H_2O lines. Upper row (from left to right): $5_{24}\text{-}4_{31}$, $4_{22}\text{-}4_{13}$ and $4_{22}\text{-}3_{31}$. Middle row: $3_{31}\text{-}4_{04}$, $2_{20}\text{-}2_{11}$ and $2_{11}\text{-}2_{02}$. Lower row: $2_{02}\text{-}1_{11}$ and $1_{11}\text{-}0_{00}$.

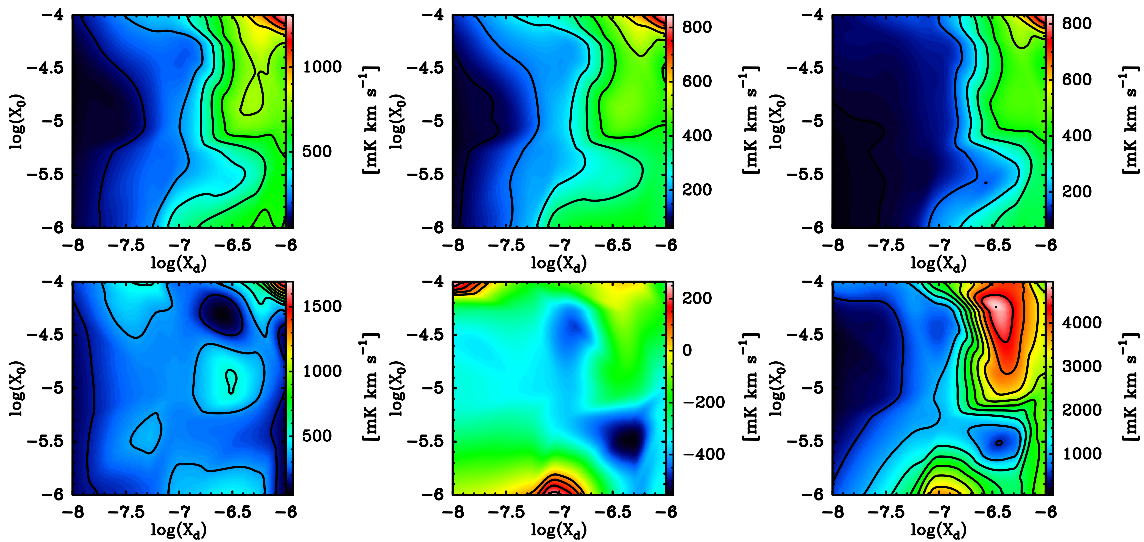


Figure A.2 — Contour plots of the integrated intensity of the L 483 models as a function of inner (X_0) and outer (X_d) for all ortho- H_2O lines. Upper row (from left to right): $3_{21}\text{-}3_{12}$, $3_{12}\text{-}3_{03}$ and $3_{12}\text{-}2_{21}$. Lower row: $2_{21}\text{-}2_{12}$, $2_{12}\text{-}1_{01}$ and $1_{10}\text{-}1_{01}$.

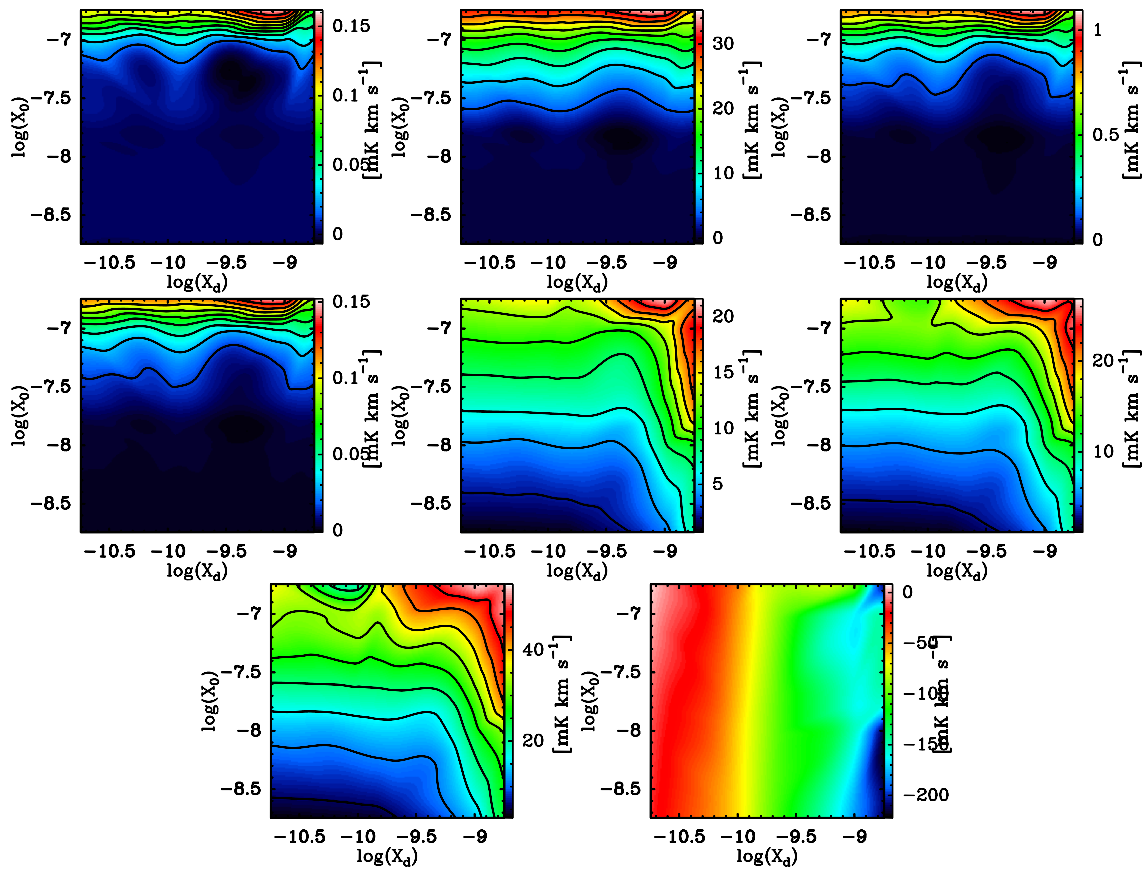


Figure A.3 — Contour plots of the integrated intensity of the L 483 models as a function of inner (X_0) and outer (X_d) for all para- H_2^{18}O lines. Upper row (from left to right): 5₂₄-4₃₁, 4₂₂-4₁₃ and 4₂₂-3₃₁. Middle row: 3₃₁-4₀₄, 2₂₀-2₁₁ and 2₁₁-2₀₂. Lower row: 2₀₂-1₁₁ and 1₁₁-0₀₀.

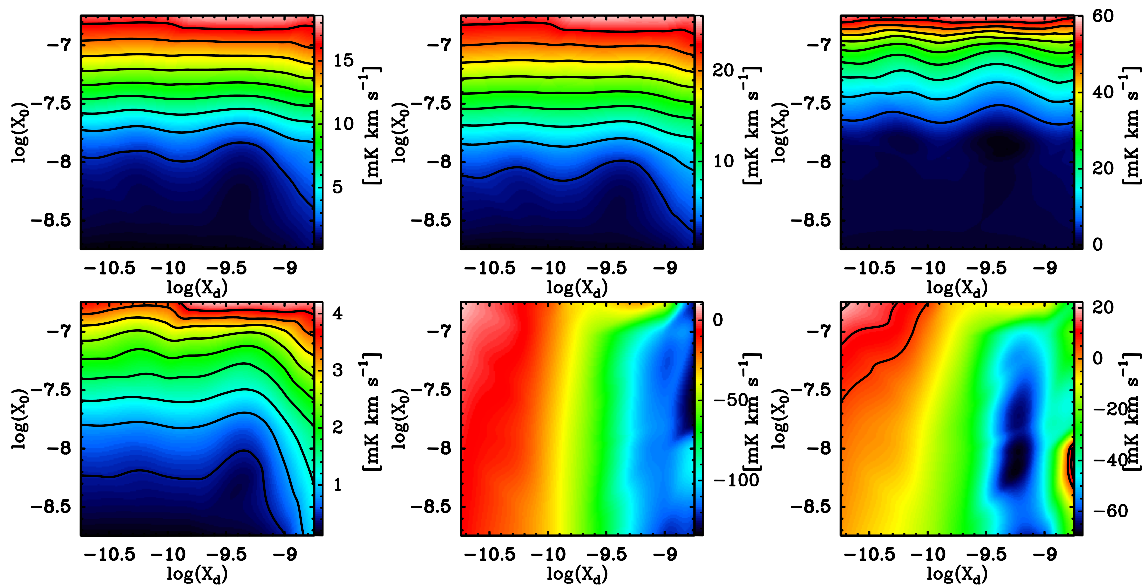


Figure A.4 — Contour plots of the integrated intensity of the L 483 models as a function of inner (X_0) and outer (X_d) for all ortho- H_2^{18}O lines. Upper row (from left to right): 3₂₁-3₁₂, 3₁₂-3₀₃ and 3₁₂-2₂₁. Lower row: 2₂₁-2₁₂, 2₁₂-1₀₁ and 1₁₀-1₀₁.

Table A.1 — Integrated intensities, $\int T_{\text{MB}}\Delta V$ [K km s⁻¹], for H₂O lines in the wide parameter grid for all abundances. Ortho lines for $p=1.5$

Density (cm ⁻³)	Integrated Intensity $\int T_{\text{MB}}\Delta V$ [K km s ⁻¹]																	
	$L = 2$ (L _☉) Abundance ^d						$L = 25$ (L _☉) Abundance ^d						$L = 7$ (L _☉) Abundance ^d					
	1a	1b	1c	2a	2b	2c	1a	1b	1c	2a	2b	2c	1a	1b	1c	2a	2b	2c
	$1_{10}-1_{01}$																	
4×10 ⁵	0.68	0.27	4.7(-2)	2.1	0.18	6.2(-2)	1.2	0.55	0.27	1.3	0.23	0.14	4.1	0.43	0.12	0.59	0.19	9.1(-2)
1×10 ⁶	2.7	2.7	0.37	0.24	2.9	0.64	0.16	6.2	0.70	0.48	2.2	0.54	0.29	2.5	0.95	0.17	1.8	0.56
5×10 ⁶	3.6	2.3	0.22	3.9	2.1	1.7	11.2	1.9	0.33	15.0	2.0	0.16	8.6	2.1	0.22	3.6	3.9	0.43
	$2_{12}-1_{01}$																	
4×10 ⁵	2.9(-2)	7.2(-2)	-2.5(-2)	2.1	-1.3(-2)	4.2(-2)	0.26	0.82	0.92	0.11	-0.37	0.28	5.0	0.30	0.19	-0.24	-0.21	2.48(-3)
1×10 ⁶	3.7	-0.35	3.6(-2)	1.2	-0.21	-0.17	1.0	-1.2	-0.14	-1.7	-1.7	-0.75	-0.43	-0.36	-0.54	-0.83	-0.80	0.88
5×10 ⁶	-1.3	-1.1	-1.7	-1.4	-1.6	-3.6(-2)	-9.1	-9.1	-7.5	-5.5	-9.1	-7.7	-3.9	-4.4	-3.8	-3.9	-3.6	-3.7
	$2_{21}-2_{12}$																	
4×10 ⁵	0.20	0.51	0.16	0.40	0.17	7.4(-2)	1.4	1.2	1.2	0.73	0.67	0.65	1.2	0.60	0.45	0.41	0.32	0.17
1×10 ⁶	4.8	0.29	0.25	0.13	0.42	0.14	6.3	1.5	1.6	0.42	1.2	0.67	2.3(-2)	0.87	0.46	0.20	0.55	0.38
5×10 ⁶	-0.29	0.16	0.10	-0.59	-0.30	0.48	-5.1	-2.0	1.0	2.0	-2.0	0.42	-1.3	-0.74	0.50	-0.54	-0.69	0.29
	$3_{12}-3_{03}$																	
4×10 ⁵	0.26	0.18	8.3(-2)	0.32	0.11	5.8(-2)	2.0	1.1	0.91	1.7	0.75	0.77	0.95	0.38	0.25	0.65	0.26	0.18
1×10 ⁶	0.82	0.21	9.1(-2)	0.37	0.22	6.9(-2)	8.3	1.5	0.92	3.1	1.3	0.69	1.1	0.60	0.25	1.3	0.47	0.23
5×10 ⁶	0.57	0.32	6.9(-2)	0.69	0.28	8.8(-2)	4.3	2.7	0.92	4.1	2.5	0.77	1.9	0.89	0.23	0.98	0.95	0.23
	$3_{12}-2_{21}$																	
4×10 ⁵	0.19	0.19	8.3(-2)	0.31	0.10	5.2(-2)	1.5	1.1	0.70	1.4	0.69	0.44	0.83	0.40	0.24	0.47	0.26	0.14
1×10 ⁶	0.93	0.21	0.12	0.33	0.23	9.2(-2)	5.8	1.6	1.1	2.1	1.4	0.69	0.78	0.67	0.29	0.71	0.50	0.30
5×10 ⁶	0.37	0.37	0.12	0.33	0.30	0.18	2.4	2.9	1.5	3.3	2.5	1.3	1.1	0.84	0.42	1.0	0.99	0.42
	$3_{21}-3_{12}$																	
4×10 ⁵	0.328	0.302	0.103	0.575	0.155	5.604(-2)	2.84	1.4	0.753	2.67	0.929	0.672	1.52	0.592	0.308	0.867	0.372	0.152
1×10 ⁶	1.44	0.317	0.16	0.633	0.372	0.118	12.1	2.69	1.28	4.49	2.29	0.832	1.53	1.09	0.374	1.59	0.824	0.398
5×10 ⁶	0.785	0.609	0.157	0.809	0.547	0.236	7.34	5.44	2.28	9.35	5.17	2.05	2.8	1.64	0.60	1.96	1.85	0.612

^a The abundance combinations are as follows: **1**: $X_0 = 10^{-4}$, **2**: $X_0 = 10^{-6}$ and **a**: $X_d = 10^{-6}$, **b**: $X_d = 10^{-7}$, **c**: $X_d = 10^{-8}$
Note: A(B) = A × 10^B

Table A.2 — Integrated intensities, $\int T_{\text{MB}}\Delta V$ [K km s⁻¹], for H₂O lines in the wide parameter grid for all abundances, Ortho lines for $p=2.0$

Density (cm ⁻³)	Integrated Intensity $\int T_{\text{MB}}\Delta V$ [K km s ⁻¹]																	
	$L = 2 (L_{\odot})$ Abundance ^a						$L = 25 (L_{\odot})$ Abundance ^a						$L = 7 (L_{\odot})$ Abundance ^a					
	1a	1b	1c	2a	2b	2c	1a	1b	1c	2a	2b	2c	1a	1b	1c	2a	2b	2c
	$1_{10} - 1_{01}$																	
4×10^5	0.37	5.1(-2)	0.23	1.2	5.1(-2)	0.11	0.45	0.28	0.25	0.63	0.25	0.19	1.5	0.10	0.20	1.6	0.69	0.11
1×10^6	2.4	2.4	0.12	0.19	1.1	0.27	0.11	2.8	0.19	0.41	0.85	0.19	0.28	2.8	0.24	0.11	3.3	0.16
5×10^6	4.0	2.2	0.36	5.0	1.7	0.59	14.0	1.6	-6.2(-2)	4.5	2.4	1.2	9.0	0.82	0.78	7.3	0.89	0.11
	$2_{12} - 1_{01}$																	
4×10^5	-0.27	-0.43	0.43	0.35	-0.43	-0.10	-0.98	-0.73	9.6(-2)	-0.68	-0.79	-0.11	0.27	-0.71	0.17	5.7(-2)	0.42	-0.31
1×10^6	-0.16	-0.89	-0.47	-0.53	-0.80	-0.62	-1.3	-3.08	-1.4	-3.2	-3.1	-1.8	-0.88	-1.6	-1.3	6.3(-3)	-1.7	-0.88
5×10^6	-1.1	-1.5	-1.9	-0.62	-2.1	-1.7	-7.2	-9.3	-8.4	-10.4	-8.7	-6.5	-3.2	-5.0	-3.6	-3.6	-4.9	-4.2
	$2_{21} - 2_{12}$																	
4×10^5	-0.11	-6.6(-3)	0.11	3.6(-2)	-1.4(-2)	6.3(-2)	0.47	0.94	0.91	0.22	0.77	0.46	0.57	0.13	0.20	1.2	0.55	0.17
1×10^6	-0.23	-0.13	6.2(-2)	-0.35	2.6(-2)	0.11	0.14	0.15	0.53	-0.95	1.9(-2)	0.41	0.28	0.14	0.20	-0.23	-0.13	0.18
5×10^6	-0.58	-0.58	8.5(-4)	-0.93	-0.7	5.6(-3)	-4.8	-3.07	-0.36	-6.3	-3.2	-1.1	-2.1	-1.4	-0.18	-1.0	-1.5	-0.11
	$3_{12} - 3_{03}$																	
4×10^5	0.23	0.13	6.3(-2)	0.25	0.13	5.2(-2)	2.0	1.1	0.70	1.6	0.98	0.54	0.88	0.35	0.20	1.1	0.43	0.16
1×10^6	0.31	0.12	4.6(-2)	0.29	0.16	4.7(-2)	2.9	1.3	0.63	2.6	1.2	0.53	1.2	0.47	0.15	0.85	0.39	0.15
5×10^6	0.19	0.15	2.9(-2)	0.18	0.16	3.2(-2)	2.4	1.9	0.44	3.1	1.9	0.56	0.78	0.51	0.14	1.06	0.47	0.13
	$3_{12} - 2_{21}$																	
4×10^5	0.18	9.3(-2)	8.9(-2)	0.19	8.1(-2)	7.1(-2)	1.18	0.99	0.73	1.2	0.97	0.53	0.69	0.29	0.23	0.83	0.46	0.19
1×10^6	0.20	0.13	7.3(-2)	0.21	0.16	6.8(-2)	2.1	1.2	0.86	1.4	1.1	0.73	0.80	0.48	0.20	0.73	0.40	0.23
5×10^6	0.20	0.14	6.7(-2)	0.15	0.11	7.3(-2)	2.7	1.6	0.80	0.89	1.8	0.98	0.48	0.49	0.28	0.76	0.55	0.24
	$3_{21} - 3_{12}$																	
4×10^5	0.29	0.14	0.13	0.35	0.13	0.10	2.3	1.6	0.93	2.4	1.6	0.65	1.3	0.45	0.33	1.6	0.77	0.26
1×10^6	0.45	0.20	0.11	0.41	0.27	0.10	4.4	2.1	1.2	3.4	2.0	1.1	1.6	0.87	0.30	1.5	0.73	0.35
5×10^6	0.49	0.35	0.11	0.48	0.33	0.1	6.3	4.0	1.5	4.9	4.3	1.8	1.7	1.2	0.49	1.9	1.3	0.43

^a The abundance combinations are as follows: **1:** $X_0 = 10^{-4}$, **2:** $X_0 = 10^{-6}$ and **a:** $X_d = 10^{-6}$, **b:** $X_d = 10^{-7}$, **c:** $X_d = 10^{-8}$
Note: A(B) = A $\times 10^B$

Table A.3 — Integrated intensities, $\int T_{\text{MB}}\Delta V$ [K km s⁻¹], for H₂O lines in the wide parameter grid for all abundances. Para lines for $p=1.5$

Density (cm ⁻³)	Integrated Intensity $\int T_{\text{MB}}\Delta V$ [K km s ⁻¹]																	
	$L = 2$ (L _⊙) Abundance ^d						$L = 25$ (L _⊙) Abundance ^d						$L = 7$ (L _⊙) Abundance ^d					
	1a	1b	1c	2a	2b	2c	1a	1b	1c	2a	2b	2c	1a	1b	1c	2a	2b	2c
	$1_{11}-0_{00}$																	
4×10 ⁵	0.50	0.23	9.0(-2)	3.0	0.22	6.9(-2)	1.4	0.52	0.48	2.8	0.20	0.14	0.64	0.43	0.18	1.0	0.26	9.4(-2)
1×10 ⁶	1.0	1.0	0.13	0.15	0.62	0.38	0.13	1.5	0.31	0.28	1.2	1.2	4.7(-2)	1.5	1.0	0.19	2.9	5.4(-3)
5×10 ⁶	1.5	-1.6(-2)	4.0(-2)	1.9	0.19	0.22	-0.45	-1.8	-0.70	6.2	-1.1	-2.3	0.88	1.6	-0.66	3.1	0.9	-0.55
	$2_{02}-1_{11}$																	
4×10 ⁵	0.65	0.32	0.12	3.8	0.31	9.0(-2)	3.2	1.6	0.87	2.8	1.2	0.43	1.2	0.72	0.28	1.3	0.62	0.19
1×10 ⁶	1.3	0.58	0.24	1.0	0.64	0.22	6.7	3.0	1.3	3.9	3.1	0.99	2.0	1.5	0.53	1.7	1.2	0.46
5×10 ⁶	1.7	0.76	0.60	1.6	0.82	0.6	6.8	5.2	4.3	15.1	4.6	4.2	5.1	1.1	1.9	3.4	1.1	1.9
	$2_{11}-2_{02}$																	
4×10 ⁵	0.37	0.17	6.2(-2)	1.4	0.17	4.8(-2)	2.3	1.0	0.51	2.4	0.78	0.26	0.78	0.41	0.16	0.87	0.36	1.0(-1)
1×10 ⁶	0.75	0.34	0.13	0.60	0.39	0.12	4.9	2.0	0.79	3.5	2.4	0.62	1.5	1.0	0.29	1.4	0.72	0.26
5×10 ⁶	1.3	0.82	0.47	1.4	0.85	0.48	10.4	6.5	5.0	25.7	6.8	4.4	4.9	2.7	1.8	3.9	2.3	1.8
	$2_{20}-2_{11}$																	
4×10 ⁵	0.31	0.18	8.8(-2)	1.1	0.15	4.7(-2)	2.3	1.1	0.69	2.2	0.74	0.22	0.70	0.47	0.18	0.79	0.34	9.4(-2)
1×10 ⁶	0.62	0.31	0.13	0.38	0.34	0.11	4.7	2.3	0.94	3.0	2.3	0.59	1.2	1.0	0.36	1.1	0.69	0.25
5×10 ⁶	0.37	0.45	0.33	0.44	0.47	0.33	3.9	4.1	4.3	16.8	4.5	3.8	1.4	1.4	1.4	2.7	1.3	1.4
	$3_{31}-4_{04}$																	
4×10 ⁵	5.9(-2)	5.8(-2)	5.7(-2)	4.6(-3)	1.8(-3)	1.7(-3)	0.57	0.56	0.56	1.4(-2)	8.0(-3)	7.6(-3)	0.18	0.18	0.18	7.4(-3)	4.0(-3)	3.8(-3)
1×10 ⁶	4.7(-2)	4.2(-2)	4.1(-2)	7.4(-3)	3.8(-3)	3.4(-3)	0.60	0.58	0.58	4.7(-2)	2.6(-2)	2.6(-2)	0.16	0.15	0.15	1.8(-2)	1.0(-2)	9.8(-3)
5×10 ⁶	1.1(-3)	-7.8(-4)	-9.6(-4)	2.6(-3)	6.8(-4)	5.0(-4)	0.20	8.1(-2)	6.9(-2)	0.2	6.9(-2)	5.5(-2)	2.9(-2)	1.3(-3)	-1.5(-3)	3.6(-2)	9.6(-3)	7.6(-3)
	$4_{22}-3_{31}$																	
4×10 ⁵	4.8(-2)	4.2(-2)	4.2(-2)	2.2(-2)	1.0(-2)	9.8(-3)	0.56	0.56	0.56	9.7(-2)	6.2(-2)	6.0(-2)	0.15	0.13	0.13	4.4(-2)	2.8(-2)	2.7(-2)
1×10 ⁶	4.9(-2)	4.1(-2)	4.3(-2)	3.1(-2)	1.7(-2)	1.6(-2)	0.59	0.48	0.47	0.27	0.18	0.17	0.16	0.13	0.12	9.0(-2)	5.6(-2)	5.3(-2)
5×10 ⁶	4.0(-2)	1.9(-2)	1.5(-2)	3.5(-2)	1.4(-2)	1.1(-2)	0.87	0.39	0.31	0.78	0.31	0.23	0.22	9.6(-2)	6.8(-2)	0.19	8.0(-2)	5.2(-2)
	$4_{22}-4_{13}$																	
4×10 ⁵	0.15	6.6(-2)	5.1(-2)	0.18	5.7(-2)	4.5(-2)	1.0	0.64	0.63	1.1	0.54	0.51	0.37	0.18	0.15	0.39	0.17	0.15
1×10 ⁶	0.20	9.5(-2)	5.1(-2)	0.19	8.4(-2)	4.3(-2)	2.2	0.74	0.55	2.0	0.75	0.60	0.58	0.26	0.15	0.53	0.24	0.15
5×10 ⁶	0.14	6.6(-2)	2.3(-2)	0.13	6.4(-2)	2.1(-2)	3.4	1.8	0.66	3.4	1.8	0.60	0.86	0.41	0.15	0.87	0.41	0.15
	$5_{24}-4_{31}$																	
4×10 ⁵	5.0(-2)	5.0(-2)	5.0(-2)	6.7(-3)	6.6(-3)	0.59	0.61	0.62	3.6(-2)	2.6(-2)	2.7(-2)	0.16	0.16	0.16	2.0(-2)	1.6(-2)	1.5(-2)	4.3(-2)
1×10 ⁶	5.0(-2)	5.0(-2)	5.1(-2)	1.9(-2)	1.4(-2)	1.4(-2)	0.58	0.57	0.57	0.14	0.12	0.12	0.17	0.15	0.15	5.2(-2)	4.3(-2)	4.3(-2)
5×10 ⁶	2.6(-2)	1.8(-2)	2.0(-2)	1.2(-2)	1.1(-2)	0.54	0.39	0.37	0.43	0.27	0.25	0.14	8.8(-2)	7.9(-2)	0.12	6.3(-2)	5.6(-2)	4.3(-2)

^a The abundance combinations are as follows: **1**: $X_0 = 10^{-4}$, **2**: $X_0 = 10^{-6}$ and **a**: $X_d = 10^{-6}$, **b**: $X_d = 10^{-7}$, **c**: $X_d = 10^{-8}$
Note: A(B) = A × 10^B

Table A.4 — Integrated intensities, $\int T_{\text{MB}}\Delta V$ [K km s⁻¹], for H₂O lines in the wide parameter grid for all abundances for para p = 2.0

Density (cm ⁻³)	Integrated Intensity $\int T_{\text{MB}}\Delta V$ [K km s ⁻¹]																	
	$L = 2$ (L_{\odot}) Abundance ^d						$L = 25$ (L_{\odot}) Abundance ^d						$L = 7$ (L_{\odot}) Abundance ^d					
	1a	1b	1c	2a	2b	2c	1a	1b	1c	2a	2b	2c	1a	1b	1c	2a	2b	2c
	$1_{11-0_{00}}$																	
4×10^5	3.9	0.11	9.3(-2)	0.51	0.26	8.4(-2)	0.7	0.43	0.38	2.8	0.24	0.22	0.29	0.52	0.15	1.4	0.17	0.12
1×10^6	0.34	0.34	0.30	0.10	0.71	0.30	0.12	0.44	0.23	8.1(-2)	0.21	-0.11	3.6(-3)	0.66	9.4(-2)	8.3(-2)	1.6	2.7
5×10^6	1.7	0.98	-0.26	0.91	0.44	-0.10	-1.9	2.0	-1.8	-3.5	0.16	-2.1	-0.2	-9.0(-2)	-0.18	6.1	-0.49	-0.57
	$2_{02-1_{11}}$																	
4×10^5	2.9	0.40	0.18	0.76	0.4	0.18	2.8	1.9	0.95	2.9	1.7	0.74	1.2	0.90	0.40	1.9	0.8	0.35
1×10^6	0.90	0.66	0.31	0.86	0.65	0.29	4.1	3.1	1.6	3.6	2.8	1.5	1.9	1.4	0.65	1.8	1.6	0.62
5×10^6	1.4	0.94	0.46	1.36	0.68	0.47	2.2	3.8	2.7	7.6	3.57	2.6	0.77	1.8	1.1	5.5	1.6	1.2
	$2_{11-2_{02}}$																	
4×10^5	1.3	0.24	9.8(-2)	0.46	0.26	9.4(-2)	1.9	1.1	0.54	2.2	1.0	0.43	0.79	0.56	0.21	1.16	0.49	0.19
1×10^6	0.66	0.46	0.19	0.66	0.45	0.19	3.0	2.1	0.89	2.8	1.9	0.83	1.4	0.94	0.40	1.5	1.2	0.38
5×10^6	1.4	0.99	0.45	1.3	0.88	0.47	4.7	5.9	2.5	6.1	5.2	2.4	1.9	2.2	1.1	4.7	2.1	1.1
	$2_{20-2_{11}}$																	
4×10^5	1.1	0.19	8.6(-2)	0.31	0.21	8.1(-2)	1.8	1.3	0.75	2.1	1.1	0.4	0.58	0.54	0.24	1.0	0.47	0.18
1×10^6	0.30	0.32	0.13	0.34	0.32	0.13	2.5	2.1	0.96	1.9	1.8	0.81	0.93	0.78	0.33	1.1	1.0	0.31
5×10^6	0.50	0.50	0.25	0.26	0.43	0.26	1.2	4.1	1.9	1.8	3.5	1.9	0.18	1.3	0.75	2.6	1.2	0.74
	$3_{31-4_{04}}$																	
4×10^5	8.4(-3)	5.5(-3)	5.0(-3)	5.8(-3)	2.6(-3)	2.3(-3)	0.46	0.45	0.42	5.7(-2)	4.0(-2)	3.8(-2)	7.9(-2)	7.1(-2)	7.0(-2)	2.2(-2)	1.3(-2)	1.2(-2)
1×10^6	-1.8(-3)	-3.7(-3)	-3.9(-3)	1.6(-3)	1.1(-5)	-1.6(-4)	0.16	0.13	0.13	6.4(-2)	3.9(-2)	3.6(-2)	1.6(-3)	-6.7(-3)	-7.3(-3)	1.3(-2)	4.5(-3)	3.5(-3)
5×10^6	-2.5(-4)	-3.2(-5)	-1.1(-5)	-2.9(-4)	-2.5(-5)	-2.6(-6)	-1.7(-2)	-3.0(-2)	-3.1(-2)	8.6(-3)	-2.3(-3)	-3.3(-3)	-1.5(-3)	-1.2(-3)	-1.2(-3)	2.4(-4)	-1.9(-4)	-1.7(-4)
	$4_{22-3_{31}}$																	
4×10^5	3.7(-2)	2.2(-2)	2.0(-2)	2.9(-2)	1.5(-2)	1.3(-2)	0.44	0.40	0.43	0.26	0.20	0.19	0.12	9.3(-2)	9.2(-2)	9.1(-2)	5.7(-2)	5.4(-2)
1×10^6	2.7(-2)	1.0(-2)	7.2(-3)	2.5(-2)	9.1(-3)	6.0(-3)	0.41	0.31	0.29	0.30	0.20	0.19	0.11	5.9(-2)	5.2(-2)	9.2(-2)	4.6(-2)	3.8(-2)
5×10^6	5.7(-3)	3.0(-4)	-8.6(-4)	6.0(-3)	7.3(-4)	-3.9(-4)	0.24	5.2(-2)	1.9(-2)	0.25	6.0(-2)	2.8(-2)	3.3(-2)	2.3(-3)	-5.5(-3)	3.8(-2)	6.1(-3)	-1.5(-3)
	$4_{22-4_{13}}$																	
4×10^5	0.14	6.8(-2)	2.8(-2)	0.13	6.3(-2)	2.4(-2)	1.4	0.61	0.42	1.4	0.60	0.49	0.40	0.22	0.12	0.40	0.21	0.11
1×10^6	0.10	4.7(-2)	1.2(-2)	0.10	4.7(-2)	1.2(-2)	1.8	0.74	0.35	1.7	0.69	0.34	0.42	0.19	7.0(-2)	0.43	0.19	6.4(-2)
5×10^6	4.2(-2)	8.5(-3)	1.1(-3)	4.16(-2)	8.6(-3)	1.2(-3)	1.5	0.55	7.1(-2)	1.4	0.56	8.6(-2)	0.32	8.0(-2)	7.8(-3)	0.31	8.3(-2)	1.0(-2)
	$5_{24-4_{31}}$																	
4×10^5	3.1(-2)	2.6(-2)	2.6(-2)	2.0(-2)	1.5(-2)	1.4(-2)	0.50	0.49	0.51	0.19	0.17	0.16	0.13	0.12	0.12	6.7(-2)	5.5(-2)	5.4(-2)
1×10^6	1.5(-2)	8.3(-3)	7.6(-3)	1.3(-2)	7.0(-3)	6.2(-3)	0.40	0.34	0.35	0.23	0.19	0.19	8.2(-2)	6.5(-2)	6.2(-2)	6.3(-2)	4.3(-2)	4.1(-2)
5×10^6	-9.9(-5)	-9.4(-4)	-1.1(-3)	3.3(-4)	-3.7(-4)	-4.9(-4)	6.0(-2)	1.3(-2)	7.5(-3)	7.7(-2)	3.0(-2)	2.4(-2)	2.3(-3)	-6.9(-3)	-8.7(-3)	7.8(-3)	-1.0(-3)	-2.6(-3)

^a The abundance combinations are as follows: **1:** $X_0 = 10^{-4}$, **2:** $X_0 = 10^{-6}$ and **a:** $X_d = 10^{-6}$, **b:** $X_d = 10^{-7}$, **c:** $X_d = 10^{-8}$

Note: $A(B)$ denotes $A \times 10^B$

Chapter 8

Searching for gas-rich disks around T Tauri stars in Lupus

Abstract In this chapter, we characterize the molecular environment of classical T Tauri stars in Lupus observed with the Spitzer Space Telescope in our search for gas-rich disks toward these sources. Submillimeter observations of ^{12}CO , ^{13}CO , and C^{18}O in the $J=3-2$ and $2-1$ lines were obtained with the James Clerk Maxwell Telescope toward a sample of 21 T Tauri stars with disks in the Lupus molecular clouds. Pointings at the sources and at selected off-positions are presented in order to disentangle material associated with disks from ambient cloud material. One source, IM Lup (Sz 82), was found with the double-peaked ^{12}CO and ^{13}CO profiles characteristic of a large rotating gas disk. The inclination of the disk is found to be $\sim 20^\circ$, with an outer radius of 400-700 AU. For most other sources, including GQ Lup with its substellar companion, the single-dish ^{12}CO lines are dominated by extended cloud emission with a complex velocity structure. No evidence of molecular outflows is found. Due to dense circumstellar material, compact C^{18}O emission was detected toward only two sources. Future searches for gas-rich disks in Lupus should either use interferometers or perform very deep single-dish integrations in dense gas tracers to separate the cloud and disk emission.

T. A. van Kempen, E. F. van Dishoeck, C. Brinch and M. R. Hogerheijde, 2007, *A&A*, 461, 983

8.1 Introduction

A general characteristic of pre-main sequence (PMS) stars is the presence of circumstellar disks, which have been observed for a wide range of evolutionary stages associated with low-mass star formation (e.g., Lada 1987; André et al. 1993; Greaves 2005). These disks contain all the necessary ingredients for forming complex planetary systems similar to our own solar system, now also seen around other stars (e.g., Ruden 1999; Marcy & Butler 1995). The gas-rich phase of disks is crucial in the evolution, since gas is needed to build Jovian-type planets. Also, the presence of gas affects the dynamics and evolution of the dust in the system and the migration of any planets embedded in the disk (e.g., Gorti & Hollenbach 2004). With time, the disk will lose its gas through processes such as photoevaporation, stellar winds, formation of gas-rich planets, and accretion onto the star (e.g., Hollenbach et al. 2000; Alexander et al. 2005). However, the timescale for gas dissipation in disks is still poorly constrained observationally, and it is even unclear whether gas and dust are lost simultaneously from disks when they evolve from the massive optically-thick to the tenuous optically-thin ‘debris’ phase.

To constrain these timescales, surveys of gas in disks in a variety of environments are needed with sensitivities that are sufficient for detecting a Jupiter mass of gas ($\sim 10^{-3} M_{\odot}$). Surveys to date have focussed on CO millimeter observations, mostly of disks in the Taurus molecular cloud (e.g. Thi et al. 2001). Although CO is known to be a poor tracer of the gas mass due to the combined effects of photodissociation in the upper layers and freeze-out in the midplane (e.g., van Zadelhoff et al. 2003), it is much simpler to observe with current instrumentation than other tracers, including H_2 (Thi et al. 2001) or atomic fine-structure lines (Kamp et al. 2003). Interferometer surveys have detected gas-rich disks around a large fraction ($>60\%$) of classical T Tauri stars in Taurus-Auriga with ages up to a few Myr and gas masses of at least a few times $10^{-4} M_{\odot}$, depending on assumptions about the CO abundance (Koerner & Sargent 1995; Dutrey et al. 1996, 2003). In contrast, the detection rate is only 10% for the more evolved weak-line T Tauri stars (Duvert et al. 2000). Similar statistics are found in a single-dish submillimeter survey of CO in a spatially more distributed sample of Herbig Ae and Vega excess stars (Dent et al. 2005) and in CO infrared surveys (Najita et al. 2003; Blake & Boogert 2004).

Surprisingly little is known about the presence of gas-rich disks around T Tauri stars in other nearby star-forming regions such as Lupus, Chamaeleon and Corona Australis. This is largely due to the absence of interferometers in the Southern sky, and even Ophiuchus has been poorly sampled with current facilities. We present here an initial search for gas-rich disks in the Lupus molecular clouds, using a single-dish telescope.

The Lupus clouds, located at around galactic coordinates $335^{\circ} \leq l \leq 341^{\circ}$ and $7^{\circ} \leq b \leq 17^{\circ}$ (Hughes et al. 1994), are among the closest star-forming regions to the Sun at ~ 150 pc (see reviews by Krautter & Reipurth 1991; Comerón 2006). Mid M-type stars dominate the stellar population of Lupus, which contains no confirmed O or B-type stars. In total 69 pre-main sequence (PMS) objects were found by Schwartz (1977), distributed over four clouds now known as Lupus 1–4 (see also Hughes et al. 1994). In addition, some 130 new weak-line T Tauri stars were detected in ROSAT images

(Krautter et al. 1994, 1997). The most massive stars in the complex are two A-type stars, HR 5999 and HR 6000, present in the sub-group that is richest in stars and complexity, Lupus 3. A good overview of the clouds is given by the extinction map made by Cambr esy (1999), based on star counts. Recently a higher resolution ($\sim 30''$) map was published by Teixeira et al. (2005). The Lupus clouds have been studied at millimeter wavelengths both in molecular emission lines and in the continuum. ^{12}CO (Tachihara et al. 2001), ^{13}CO (Tachihara et al. 1996) and C^{18}O (Hara et al. 1999) $J=1-0$ large-scale maps were made at $2.6'$ resolution with the NANTEN telescope. Higher resolution observations were done with the Swedish-ESO Submillimeter Telescope (SEST) over more limited regions with $\sim 45''$ resolution by Gahm et al. (1993) (mostly ^{12}CO 1-0 in Lupus 2), Rizzo et al. (1998) (^{12}CO 1-0 in Lupus 1 and 4 filaments) and Vilas-Boas et al. (2000) (^{13}CO and C^{18}O 1-0 in localized dark cores in Lupus 1-4). N urnberger et al. (1997) performed a continuum survey of 32 T Tauri stars in Lupus at 1.3 mm with the SEST, probing the cold circumstellar dust.

The Lupus star-forming region appears to differ in several aspects from other low-mass star-forming clouds. In contrast to Ophiuchus and Taurus, which contain a significant fraction of deeply embedded Class 0 and Class I objects, Lupus has at most a few embedded objects (Krautter & Reipurth 1991; Tachihara et al. 1996; Comer on 2006). This could be an indication that Lupus is more evolved than other star-forming regions. The peak in the age distribution is 3×10^6 yr for stars in Lupus 3 and 4, calculated from the PMS evolutionary tracks of D'Antona & Mazzitelli (1994) for a distance of 150 pc (Hughes et al. 1994). Under the same assumptions, Lupus 1 and 2 PMS stars are younger with a peak of 1×10^6 yr. These age estimates are comparable to those for other star-forming regions such as Chamaeleon (Hartigan 1993), but are about double that of the Taurus cloud (Simon et al. 1993). Thus, a study of disks in Lupus is interesting because this is precisely the age range in which significant evolution of the gas disk is expected.

A second characteristic of the Lupus clouds is the distribution of spectral types. Compared to the Taurus cloud, Lupus is dominated by lower-mass stars. The peak of the distribution in spectral type is M0, with very few stars having spectral types higher than K7. In contrast, the peak of the spectral type distribution in Taurus is at K7.

In this chapter, single-dish submillimeter observations of CO toward a sample of 21 classical T Tauri stars with disks are presented. They were obtained with a beam of $15''$, much smaller than that of previous data. The sources are a subset of the PMS stars found by Schwartz (1977), Krautter & Reipurth (1991), and Hughes et al. (1994), and they have been observed with the *Spitzer Space Telescope* in the context of the 'From Molecular Cores to Planet Forming Disks' (c2d) Legacy survey (Evans et al. 2003). The aim of the CO observations is to characterize the molecular environment of the T Tauri stars at high angular resolution and to search for gas-rich disks suitable for future follow-up interferometer observations.

8.2 Observations

The submillimeter CO observations were carried out in two runs in April and July 2005 at the James Clerk Maxwell Telescope (JCMT)¹. The ^{12}CO $J=3-2$ and C^{18}O $J=3-2$ and $2-1$ transitions (depending on weather conditions) were observed with the dual-polarization B3 and single-polarization A3 receivers. The beam sizes are $15''$ and $20''$, respectively. The Digital Autocorrelator Spectrometer was used as the back-end with a bandwidth of 125 MHz, giving a spectral resolution of 98 kHz for the A-receiver corresponding to 0.10 km s^{-1} at 230 GHz, and 196 kHz for the dual-polarization B-receiver corresponding to 0.22 km s^{-1} at 345 GHz. The integration times were such that the RMS is around 70–100 mK in a 0.2 km s^{-1} velocity bin for the B-receiver and 50 mK for the A-receiver, depending on source and observing conditions, on a T_{mb} scale. Pointing was checked regularly for these southern sources and found to vary within $2''$. Beam efficiencies were taken to be 0.65 for RxA3 and 0.63 for RxB3².

Frequency switching with a switch of 16.4 MHz was adopted for ^{12}CO because no emission-free position could readily be found for many of the sources in our sample. If a signal was detected on source, additional observations were carried out at $30''$ offsets to the east and south of the source to characterize its environment and constrain the on-source contribution. If indications were found of a gas-rich disk, additional follow-up observations were done on-source in ^{13}CO $3-2$ using a beam switch of $180''$ in AzEl. C^{18}O $3-2$ or $2-1$ observations were performed for nearly all sources, also using a beam switch of $180''$. Table 1 summarizes the observed lines per source. The data were reduced with the SPECX and CLASS reduction packages.

Our observing strategy is similar to that for the single-dish observations of gas-rich disks in Taurus by Thi et al. (2001). Because the surface layers of disks are warm, the ^{12}CO $3-2$ line is well-suited to observing these regions. Also, the smaller beam size at higher frequencies is more favorable to observing disks, which have typical sizes of a few hundred AU corresponding to a few arcsec at the distance of Lupus. Typical ^{12}CO $3-2$ antenna temperatures of disks in Taurus are 0.5–1 K, so that an RMS of <0.1 K needs to be reached. To distinguish gas associated with disks from that of surrounding clouds, observations on-source and at nearby off-source positions need to be taken. Gas-rich disks should show a characteristic double-peaked line profile and a stronger signal on-source than at the off-source positions, while cloud emission should produce a comparable signal at all positions. Finally, disks in Taurus have not been detected in C^{18}O with single-dish telescopes. On the other hand, such beam-switched C^{18}O observations have been found to be a good probe of any dense circumstellar gas or remnant envelope associated with the source. For example, Class I sources show typical C^{18}O intensities of 0.5–2 K (Hogerheijde et al. 1998; Jørgensen et al. 2002).

Our sample of classical T Tauri stars in Lupus was selected from targets belonging to the InfraRed Spectrometer (IRS) sample of the c2d Legacy program on *Spitzer* (See Table 1). They are a subset of the T Tauri stars studied by Schwartz (1977), Krautter &

¹The JCMT is operated at the summit of Mauna Kea, Hawaii by the Joint Astronomy Center on behalf of the United Kingdom Particle Physics and Astronomy Research Council, the Netherlands Organization for Scientific Research, and the National Research Council of Canada

²Observed by the JCMT staff over many observations; see the JCMT website <http://www.jach.hawaii.edu/JCMT/>

Reipurth (1991) and Hughes et al. (1994), selected to be brighter than 200 mJy at 12 μm and excluding sources contained in the *Spitzer-IRS* guaranteed time programs. Infrared photometry and spectroscopy was performed on all sources giving estimates of their spectral types (see Table 1). In total 21 PMS stars were observed, most of them located in Lupus 3. All sources show a clear 10 μm emission feature due to warm silicates, confirming the presence of a circumstellar disk (Kessler-Silacci et al. 2006). Some of the selected stars are known binaries. Where available, results of the 1.3 mm continuum emission are reported (Nürnberg et al. 1997). This emission is presumably dominated by the cold dust in the disk.

The distances to individual Lupus clouds have considerable uncertainty. Hughes et al. (1993) found 140 ± 20 pc from the spectroscopic parallax of field stars around the clouds. However, observations of reddening and interstellar absorption lines toward individual stars by, e.g., Knude & Høg (1998) and Crawford (2000) find distances ranging from 100 to 200 pc. A good discussion can be found in Comerón (2006). The depth of the Lupus clouds may be non-negligible and can be as large as 50 pc. Also, it has been suggested that not all clouds of Lupus are related; in particular Lupus 2 could be located as far away as 360 pc (Knude & Nielsen 2001). However, this seems unlikely, given the narrow ranges in mean velocity of the clouds (see e.g., Tachihara et al. 1996, Vilas-Boas et al. 2000 and this chapter § 8.3). The distance used here for all sources is that most commonly adopted, 150 pc.

8.3 Results

The observed ^{12}CO 3–2 line intensities are presented in Table 2, together with the peak intensities. Typical examples of spectra that illustrate the range of observed profiles, both on-source as well as at off-source positions, are shown in Fig. 8.1. The remainder of the spectra can be found in the on-line material.

Only a single source is found in our sample with a clear signal of gas associated with the source itself, namely IM Lup. A classic double-peaked disk profile is found toward the source position, which is largely absent at the 30'' east and south positions offset from the source (see Fig. 8.1). The profile, with a maximum peak of 2.5 K, is significantly broader than the one associated with quiescent gas. This source is discussed further in § 8.4.1.

None of the other sources show indications of gas-rich disks surrounding the central T Tauri star. Three sources, RY Lup, EX Lup and Sz 111, appear to be located outside any cloud material and have no detectable disk emission at our sensitivity limit. Using the formula in Thi et al. (2001) with the observed limits on ^{12}CO emission, upper limits of the gas masses of $1 \times 10^{-6} M_{\odot}$ are obtained for these disks with a CO/H₂ ratio of 10^{-4} . For a more realistic overall CO/H₂ disk abundance of 10^{-6} , the limits would increase to $1 \times 10^{-4} M_{\odot}$ (see also § 8.4).

Most sources have a strong ^{12}CO line on source, but these signals are also detected at the off-positions with comparable strengths (see Fig. 8.1). These lines must originate in the large-scale molecular cloud material in the line of sight of the source. The complex profiles seen for many sources indicate a complex structure of different molecular clouds moving at different velocities, either in the fore- or background. For example,

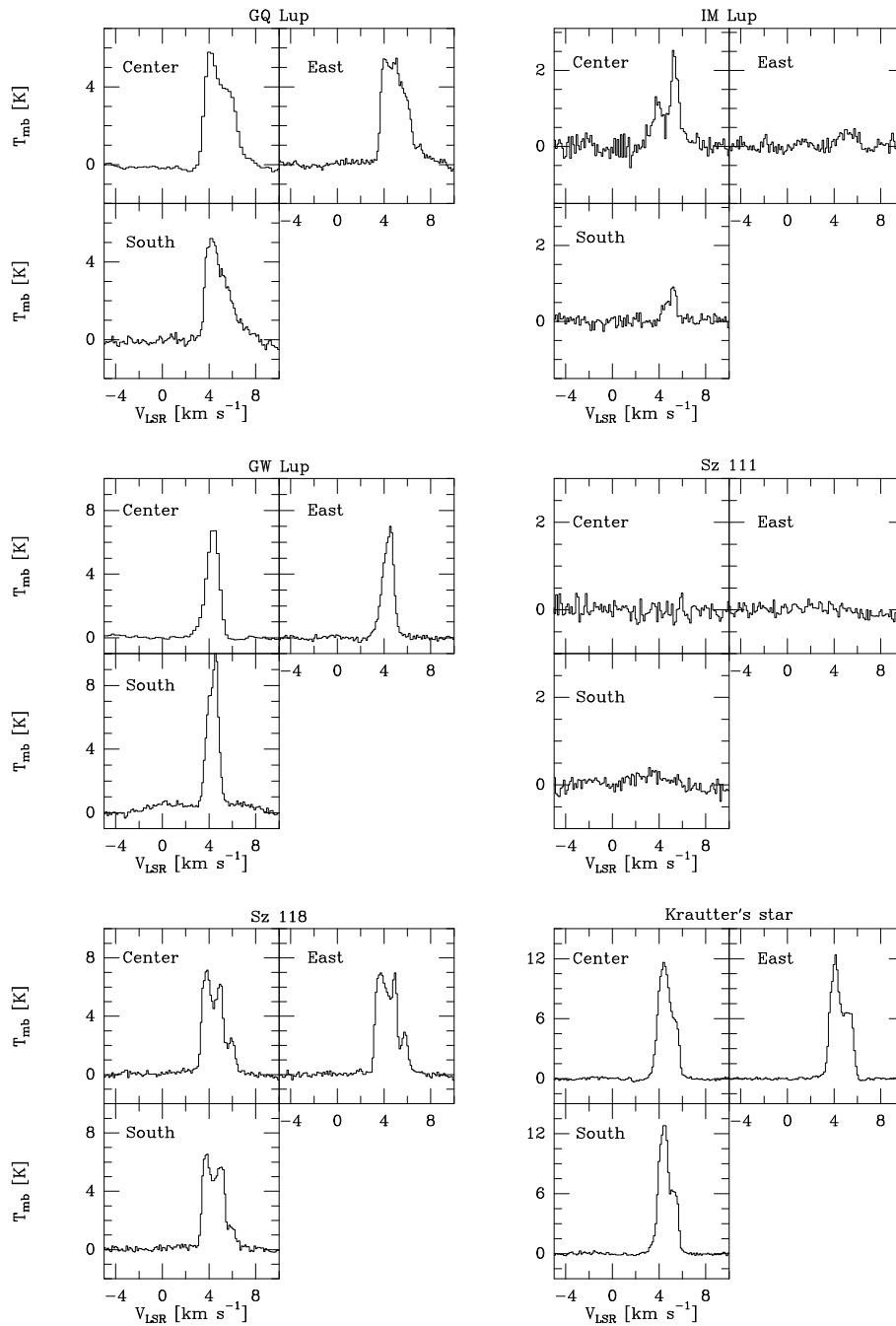


Figure 8.1 — ^{12}CO 3–2 lines of selected sources in Lupus, with off-positions $30''$ south and east of source. Other sources can be found in the appendix of this chapter in Fig. A.1.

the spectra toward Sz 118 (see Fig. 8.1) show three peaks with different intensities at all positions with widths of ~ 0.8 km s⁻¹ and velocities that differ by 1–1.5 km s⁻¹. The C^{18}O molecule is not detected at all for this source. Comparison with the large scale maps shows that observations of ^{12}CO 3–2 with peak temperatures of 2–20 Kelvin are consistent with the lower-resolution ^{12}CO surveys (Gahm et al. 1993; Tachihara et al. 1996).

Table 8.1 — Summary of the properties of T Tauri stars and observed lines in Lupus

Source	RA (J2000)	Dec (J2000)	Sp. ^a	Cloud	$F_{1.3\text{mm}}^b$	^{12}CO	Off.	C^{18}O
HT Lup ^c	15 45 12.87	−34 17 30.6	K2	Lup. 1	135	3–2	E S	3–2/2–1
GW Lup	15 46 44.68	−34 30 35.4	M2-M4	Lup. 1	106	3–2	E S	3–2/2–1
HM Lup	15 47 50.63	−35 28 35.4	M3	Lup. 1	<45	3–2	E S	3–2/2–1
Sz 73	15 47 56.98	−35 14 35.1	M0	Lup. 1	26	3–2	E S	2–1
GQ Lup ^e	15 49 12.12	−35 39 05.0	K7-M0	Lup. 1	38	3–2	E S	2–1
IM Lup ^e	15 56 09.17	−37 56 06.4	M0	Lup. 2	260	3–2	E S	2–1
RU Lup	15 56 42.31	−37 49 15.5	K7-M0	Lup. 2	197	3–2	E S	3–2
Sz 84	15 58 02.52	−37 36 02.8	M5.5	Lup. 2	<36	3–2	E S	2–1
RY Lup	15 59 28.39	−40 21 51.2	K4	Lup. 3	-	3–2	-	3–2
EX Lup	16 03 05.52	−40 18 24.9	M0	Lup. 3	-	3–2	-	3–2
HO Lup ^c	16 07 00.61	−39 02 19.4	M1	Lup. 3	<24	3–2	E S	3–2
Sz 96	16 08 12.64	−39 08 33.3	M1.5	Lup. 3	<45	3–2	E S	3–2
Krautter ^d	16 08 29.70	−39 03 11.2	K0	Lup. 3	<30	3–2	E S	3–2
Sz 107	16 08 41.78	−39 01 36.4	M5.5	Lup. 3	-	3–2	E S	-
Sz 109	16 08 48.17	−39 04 19.0	M5.5	Lup. 3	-	3–2	E S	3–2
Sz 110	16 08 51.56	−39 03 17.5	M2	Lup. 3	-	3–2	E S	3–2
Sz 111	16 08 54.74	−39 37 17.5	M1.5	Lup. 3	-	-	-	3–2
V908 Sco	16 09 01.84	−39 05 12.1	M4	Lup. 3	-	3–2	E S	3–2
Sz 117	16 09 44.34	−39 13 30.4	M2	Lup. 3	-	3–2	E S	3–2
Sz 118	16 09 48.68	−39 11 17.2	K6	Lup. 3	-	3–2	E S	3–2
Sz 123	16 10 51.58	−38 53 13.7	M1	Lup. 3	-	3–2	E S	3–2

^a Spectral type, from Hughes et al. (1994).

^b in mJy, from Nürnberger et al. (1997), where available.

^c Known binaries (Nürnberger et al. 1997).

^d Krautter’s star.

^e Additional ^{13}CO 3–2 observations taken.

The ^{12}CO line widths of $\sim 0.8 \text{ km s}^{-1}$ are comparable to those found in Vilas-Boas et al. (2000) and Tachihara et al. (2001), taking multiple clouds at different velocities into account. No evidence of line wings at $\geq 2 \text{ km s}^{-1}$ from line center is found at the level $T_{\text{MB}} < 0.15 \text{ K}$ (2σ), providing limits on any small-scale molecular outflows associated with these T Tauri stars. For RU Lup, this is consistent with Gahm et al. (1993), who reported no outflows from CO 1–0 data in a larger beam.

Although no direct correlation can be inferred due to the confusion of cloud emission around most sources, it is interesting to note that the largest 1.3 mm flux found by Nürnberger et al. (1997) is associated with IM Lup. Thus it also contains the most surrounding dust, in addition to being the only source with CO disk emission.

The results for the C^{18}O and ^{13}CO line intensities are included in Table 2. The ^{13}CO 3–2 molecule was observed for only two objects: IM Lup and GQ Lup. A more detailed description for these two objects can be found in § 8.4. Figure 2 shows some examples of observed C^{18}O lines.

Only two sources in our sample show a C^{18}O line above the noise level, HT Lup

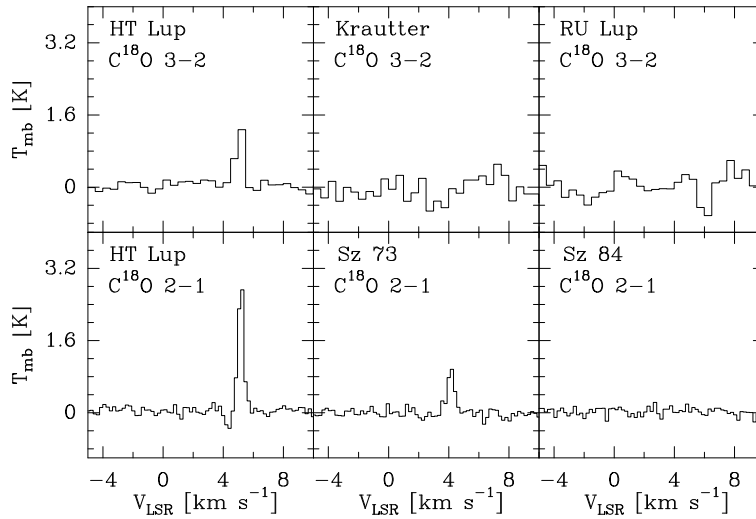


Figure 8.2 — C¹⁸O lines toward selected sources in Lupus.

and Sz 73, and HT Lup is the only source toward which both C¹⁸O 2-1 and 3-2 lines have been detected in our survey. Because the data were taken in 180'' beam-switched mode, the bulk of the emission is likely to be directly associated with the source. This could point towards a small circumstellar envelope. The 2-1/3-2 line ratio of > 1 indicates either very cold gas (< 15 K) or densities less than 10^5 cm⁻³ for $T \approx 20$ K. The inferred C¹⁸O column density for these conditions is $\sim 10^{15}$ cm⁻², corresponding to a CO column density of 5×10^{17} cm⁻² for $^{16}\text{O}/^{18}\text{O}=540$ (Wilson & Rood 1994) and an H₂ column density of 6×10^{21} cm⁻² for a dark cloud C¹⁸O abundance of 1.7×10^{-7} (Frerking et al. 1982). Thus, the extinction directly associated with the source is $A_V \approx 6$ mag using $N_{\text{H}}/A_V = 1.8 \times 10^{21}$ cm⁻² mag⁻¹

As mentioned before, our observations are not sensitive to extended C¹⁸O emission because of beam-switching by 3'. The lack of any features at the 2σ level of < 0.1 K in C¹⁸O 2-1 and < 0.3 K in 3-2 implies that either any large scale cloud emission must be very smooth on a 3' scale or that there is no C¹⁸O at this limit. Vilas-Boas et al. (2000) and Hara et al. (1999) find C¹⁸O 1-0 antenna temperatures of 0.2 to 1.5 K for the densest cores. For typical dark cloud conditions, the 2-1 line should be comparable in strength, whereas the 3-2 line should be factors of 2-4 weaker, so that these lines would have been detectable at the positions of strongest 1-0 emission. However, most of our sources are located at the edge or outside the C¹⁸O contours of Hara et al. (1999), suggesting that C¹⁸O is indeed largely absent. The lack of C¹⁸O 2-1 emission at the level of 0.08 K (2σ) indicates a C¹⁸O column density of less than 5×10^{13} cm⁻², or H₂ less than 3×10^{20} cm⁻² using the dark cloud abundance. In this diffuse cloud regime, however, the C¹⁸O abundance may be significantly lower than the standard dark cloud value (van Dishoeck & Black 1988), increasing the H₂ column density.

8.4 Individual objects

Several objects showed interesting enough spectra to probe deeper. IMLup and GQLup are presented here with a more indepth analysis.

Table 8.2 — Observed line intensities toward T Tauri stars in Lupus

Source	$\int T_{\text{MB}} dV$		Peak T_{MB}			
	$^{12}\text{CO } 3-2$ [K km s $^{-1}$]	$^{13}\text{CO } 3-2$ [K km s $^{-1}$]	^{12}CO [K]	$\text{C}^{18}\text{O } 3-2^a$ [K]	$\text{C}^{18}\text{O } 2-1^a$ [K]	$^{13}\text{CO } 3-2$ [K]
HT Lup	26.5		15	1.9	3.5	
GW Lup	9.1		6.7	< 0.16	< 0.08	
HM Lup	6.4		5.2	< 0.15	< 0.08	
Sz 73	15.8		9.0		1.0	
GQ Lup	13.4	< 0.14 ^c	5.8		< 0.05	< 0.25 ^c
IM Lup	4.7	0.52	2.4		< 0.09	0.35
RU Lup	-		-	< 0.27		
Sz 84	0.6		0.8		< 0.09	
RY Lup	^b		< 0.25	< 0.31		
EX Lup	^b		< 0.16	< 0.40		
HO Lup	1.3		0.8	< 0.17		
Sz 96	25.1		12	< 0.16		
Krautter's star	17.5		11.7	< 0.25		
Sz 107	18.3		12			
Sz 109	34.8		26	< 0.15		
Sz 110	26.1		21	< 0.25		
Sz 111	^b		< 0.2	< 0.30		
V908 Sco	22.6		13.7	< 0.26		
Sz 117	11.4		5.5	< 0.22		
Sz 118	14.3		7.2	< 0.27		
Sz 123	2.4		1.6	< 0.20		

^a If no line was detected, a $2\sigma_{\text{rms}}$ (see § 8.2.1) limit in $\delta v = 0.25 \text{ km s}^{-1}$ is given.^b No detection. See peak value for RMS^c see § 8.4.2

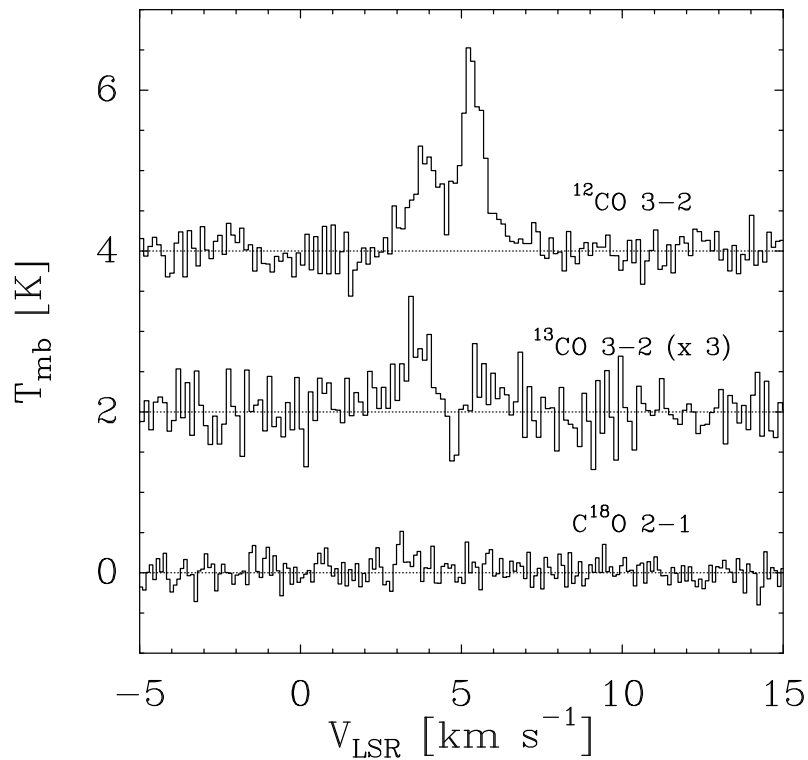


Figure 8.3 — ^{12}CO 3–2, ^{13}CO 3–2, and C^{18}O 2–1 spectra observed toward IM Lup (Sz 82) shifted by +4, +2, and 0 K, respectively.

IM Lup is the only T Tauri star in our sample with a clear detection of ^{12}CO emission associated with the source. A double-peaked profile with peak separations of about 2 km s^{-1} is seen in both ^{12}CO and ^{13}CO , consistent with a rotating gas disk (see Fig. 3). In addition, the lack of C^{18}O emission over 0.09 K in a 0.25 km s^{-1} bin implies the absence of a significant contribution of a dense circumstellar envelope. The existence of a large disk around IM Lup has recently been shown in scattered light images at visible and near-infrared wavelengths with the *Hubble Space Telescope* (Padgett et al, priv. comm. Schneider et al, priv. comm.).

The ^{12}CO peak intensity for IM Lup is comparable to that of the brighter sources with gas-rich disks in Taurus observed by Thi et al. (2001). The much weaker ambient cloud material seen at the south off-position (see Fig. 1) modestly affects the disk profile, however, especially the red peak at $V_{\text{LSR}} = 5 \text{ km s}^{-1}$. The blue peak at $V_{\text{LSR}} = 3 \text{ km s}^{-1}$ is not contaminated so is taken as the actual disk signal for both peaks. The ^{13}CO peaks of 0.2 K are comparable to those for Taurus disks and do not seem to be affected by ambient cloud material.

The observed $^{12}\text{CO}/^{13}\text{CO}$ integrated intensity ratio of 6.0 ± 1.5 indicates ^{12}CO and ^{13}CO optical depths of 2.3 and 0.15, respectively, assuming that the excitation temperatures are both the same for both isotopes and constant throughout the disk. The uncertainties are dominated by calibration errors. If the peak temperatures of the blue wing are used (1.5 for ^{12}CO and 0.4 K for ^{13}CO , respectively), optical depths of 3 and 0.3 are found.

Thi et al. (2001) give several methods for deriving disk masses from different observations. Assuming that most of the ^{13}CO 3–2 emission is optically thin and originates in the cold gas of the outer disk with a single excitation temperature, the total gas mass is given by

$$M_{\text{gas}} = 3 \times 10^{-6} \left(\frac{[^{12}\text{CO}]/[^{13}\text{CO}]}{60} \right) \left(\frac{\text{H}_2/^{12}\text{CO}}{10^4} \right) \left(\frac{T_{\text{ex}} + 0.89}{e^{-16.02/T_{\text{ex}}}} \right) \left(\frac{\tau}{1 - e^{-\tau}} \right) \left(\frac{d}{100 \text{ pc}} \right)^2 \int T_{\text{mb}} dV \quad M_{\odot}. \quad (8.1)$$

The H_2/CO and $^{12}\text{CO}/^{13}\text{CO}$ ratios have been set to 10^4 and 60, following standard conversion factors. This results in a derived gas mass of $2 \times 10^{-4} M_{\odot}$ for IM Lup at $d = 150$ pc, using $T_{\text{ex}} \simeq 30$ K. For comparison, the disk mass found from the 1.3 mm continuum flux (Nürnberger et al. 1997) is $6 \times 10^{-2} M_{\odot}$, assuming a gas/dust ratio of 100, $T_{\text{dust}} = 30$ K and a dust opacity coefficient κ of $0.01 \text{ cm}^2 \text{ g}^{-1}$. The factor of 300 between these two numbers is comparable to that found for other disks (e.g., Dutrey et al. 1996; Mannings & Sargent 2000; Thi et al. 2001) and is commonly explained by the fact that CO is not a good tracer of the gas mass due to the combined effects of photodissociation by stellar and interstellar UV radiation and of the freeze-out of CO onto the grains in cold regions of the disk (van Zadelhoff et al. 2001; Aikawa et al. 2002).

The ^{12}CO profile can be used to obtain estimates of two other important disk parameters, the disk size and inclination. Assuming optically thick ^{12}CO 3–2 emission and following the method described in Dutrey et al. (1997):

$$\int T_{\text{mb}} d\nu = T_{\text{ex}}(\rho\delta v) \left(\frac{\pi(R_{\text{out}}^2 - R_{\text{in}}^2)}{d^2} \cos i \right) \Omega_a^{-1} \quad (8.2)$$

where R_{in} and R_{out} are the inner and outer radii, δv the turbulent velocity, and ρ a geometrical factor. Also, Ω_a^{-1} is the telescope beam on the sky and i the inclination, with 0 degrees being face-on with respect to the line of sight. For IM Lup, $R_{\text{in}} = 0$ AU, a mean disk excitation temperature T_{ex} of 25, 40, and 50 K and $(\rho\delta v)$ of 0.3 km s^{-1} are chosen.

The disk sizes calculated from Eq. (2) are given in $R_{\text{out}}\sqrt{\cos(i)}$. Scattered light images indicate that the inclination is on the order of 10° to 30° , so that $\cos(i) \approx 1$ is a reasonable approximation. The disk sizes found with $T_{\text{ex}} = 25$ and $T_{\text{ex}} = 40$ K are 730 and 580 AU, respectively. Such numbers are comparable to the observed radius of the dust disk in scattered light, about $4.3''$ or 600 AU (Padgett et al., priv. comm., Schneider et al., priv. comm.)

To better understand the observed line profile of ^{12}CO , a simple disk model has been used, together with a ray-tracing program (Hogerheijde & van der Tak 2000) to compute the line profile. Such models are better-suited to constraining parameters using an χ^2 method with the observed spectrum. The populations of the ^{12}CO rotational levels are assumed to be in LTE throughout the entire disk. The surface density of the

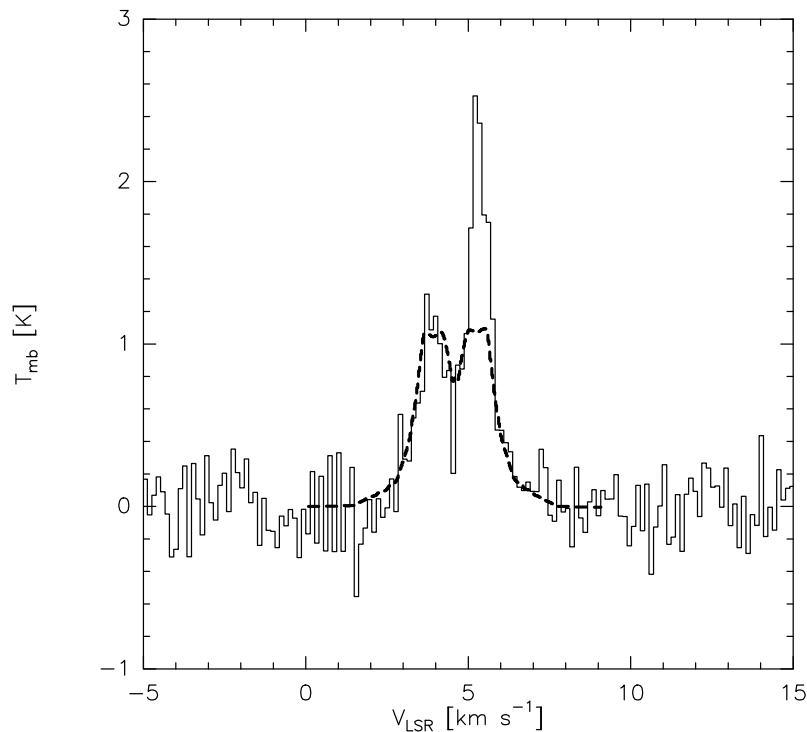


Figure 8.4 — Comparison of the observed ^{12}CO $J=3-2$ line toward IM Lup with the best-model fit with a disk of $i=20^\circ$, $R=600$ AU.

disk is defined as $\Sigma(r) = \Sigma_0(r/1 \text{ AU})^{-1.5}$ with a typical value of $4.57 \times 10^{26} \text{ cm}^{-2}$ at 1 AU. The disk is assumed to be isothermal in the vertical direction. The abundance of CO is set to be 5×10^{-5} with respect to H_2 , except in areas with temperatures below 30 K where CO is frozen out onto the grains. There, abundances are taken to be 5×10^{-10} . It is assumed that the gas is in Keplerian orbits around a $0.5 M_\odot$ star. The inner radius is set at 0.1 AU. The radial temperature profile is only constrained by a radial exponent of -0.5 and the luminosity. The turbulent velocity is taken to be 0.1 km s^{-1} , following Thi et al. (2001) and Qi et al. (2004).

The parameters to be fitted are the inclination, the outer radius of the disk, and the temperature at the inner radius. The best-fit is presented in Fig 4. It has a best fit outer radius between 400 and 700 AU, consistent with the result of 600 AU found above. The line profile is not very sensitive to the outer radius or the CO abundance in the outer areas because temperatures are too low to have a significant impact on the 3–2 emission. The observed line is quite sensitive to the inclination of the disk, which is constrained to $20^\circ \pm 5^\circ$. The temperature at the inner radius is taken to be 1200 K, but model results are not sensitive to the precise choice of temperature.

The classical T Tauri star GQ Lup has recently attracted attention because adaptive optics imaging has revealed a substellar companion, perhaps a massive Jupiter-like planet, with a separation of ~ 100 AU (Neuhäuser et al. 2005). As for all objects in our sample, the GQ Lup spectrum shows an infrared excess and a silicate emission feature at $10 \mu\text{m}$, indicating the presence of a dust disk. This object is potentially interesting for our understanding of the influence of a companion on the disk structure and evolution.

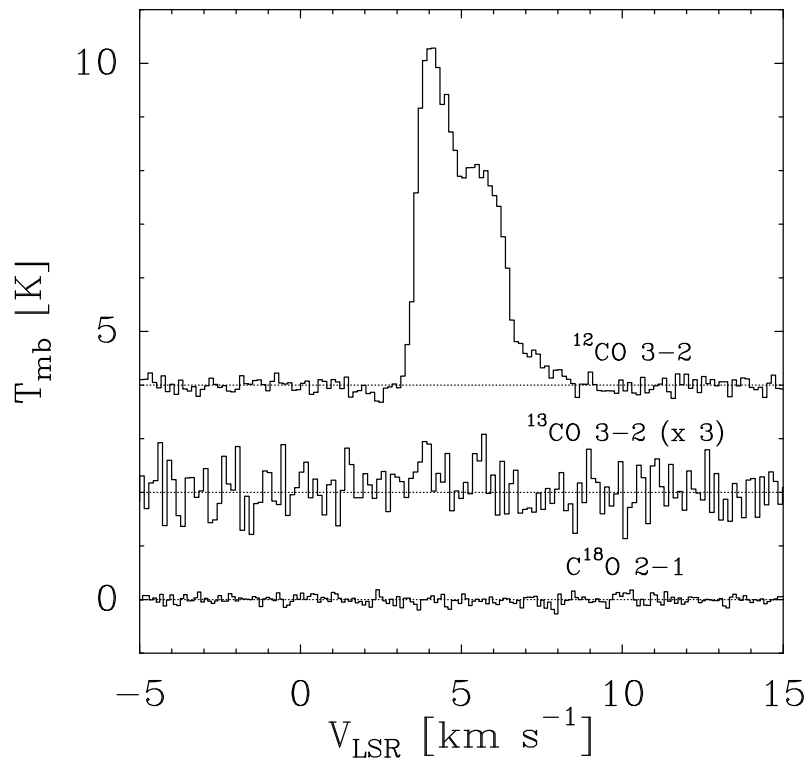


Figure 8.5 — ^{12}CO 3–2, ^{13}CO 3–2, and C^{18}O 2–1 lines toward GQ Lup, shifted by +4, +2, and 0 K, respectively.

High signal-to-noise observations were taken toward this object (Fig. 8.5), but, like most other sources in our sample, only diffuse interstellar cloud material is detected in ^{12}CO , as proven in the observations at off-positions. The ^{13}CO spectrum shows a hint of two peaks centered around $V_{\text{LSR}}=5 \text{ km s}^{-1}$ of equal height at $T_{\text{mb}}=0.25 \text{ K}$, but deeper integrations are needed to confirm this. Also, C^{18}O 2–1 was not detected at all down to 5 mK (2σ) in a 0.25 km s^{-1} bin. This constrains the maximum column density of C^{18}O directly associated with the source to $\sim 2 \times 10^{12} \text{ cm}^{-2}$. An unresolved disk would then be limited to a gas mass of $< 2.3 \times 10^{-5} M_{\odot}$ for $\text{C}^{18}\text{O}/\text{H}_2 = 1.67 \times 10^{-7}$ or $< 2.3 \times 10^{-3} M_{\odot}$ for a lower ratio of $\text{C}^{18}\text{O}/\text{H}_2 = 1.67 \times 10^{-9}$. The mass derived from the 1.3 mm flux of 38 mJy is 2.1×10^{-3} , assuming a gas/dust ratio of 100, $T_{\text{dust}} = 30 \text{ K}$ and a dust opacity κ of $0.01 \text{ cm}^2 \text{ g}^{-1}$ (Nürnberg et al. 1997).

8.5 Concluding remarks

The main conclusions of this chapter are as follows:

- A ^{12}CO $J=3-2$ survey of 21 classical T Tauri stars with dust disks in Lupus taken in frequency-switched mode has revealed mostly extended diffuse cloud material with a few magnitudes of extinction and a complex velocity structure.
- A C^{18}O $J=3-2$ and 2–1 survey of the same 21 sources taken in beam-switched mode shows dense compact circumstellar material associated with only 2 sources, HT Lup and Sz 73.

- Only a single source, IM Lup (Sz 82), has been found with clear evidence of a gas-rich disk. Modeling of the line intensity and line profile indicates a large disk with radius ~ 600 AU and inclination 20° . This source will be a prime target for future interferometer observations in the southern sky, especially with the *Atacama Large Millimeter Array*.

That we do not detect gas disks in Lupus in the current survey does not imply that the gas has been dissipated from these disks; rather, it shows the limitations of single-dish CO line observations for revealing them. Future searches need to either **(i)** focus on high density single-dish tracers, such as HCO^+ $J=4-3$ or HCN $J=4-3$ to distinguish the warm, dense gas in the disk from the cold, diffuse cloud material, or **(ii)** use newly commissioned interferometers, such as the SubMillimeter Array (SMA). From comparison with other disks in Taurus (Thi et al. 2004; Greaves 2004), these lines are expected to have peak intensities of at most 0.1 K in a single-dish $15''$ beam, and it will be very difficult to detect. Increased sensitivity to compact emission is only possible with interferometer studies. Interferometric surveys will therefore be essential in determining the fraction of gas-rich disks in Lupus and thus the timescale for gas dissipation in this star-forming region compared with other regions such as Taurus.

Acknowledgements

The authors are grateful to Remo Tilanus for carrying out part of the observations and to Karl Stapelfeldt, Debbie Padgett, Glenn Schneider, and Jean-Charles Augereau for communicating information about the HST images of IM Lup before publication. TvK and astrochemistry at Leiden Observatory are supported by a Spinoza grant and by grant 614.041.004 from the Netherlands Organization for Scientific Research (NWO).

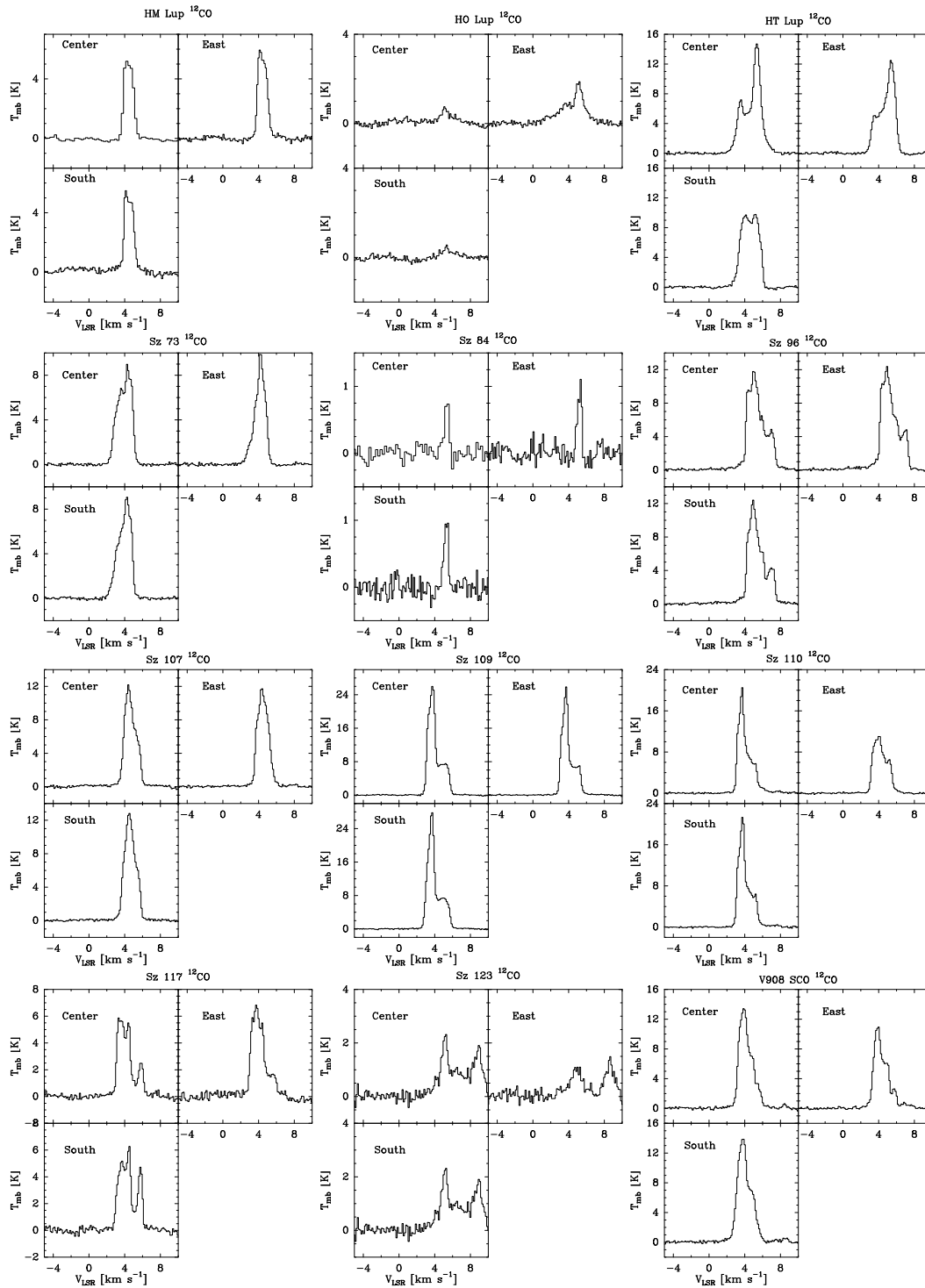


Figure A.1 — ^{12}CO 3–2 lines of selected sources in Lupus, with off-positions 30'' south and east of source.

Bibliography

- Adams, F. C., Lada, C. J., & Shu, F. H. 1987, *ApJ*, 312, 788
- Aikawa, Y., van Zadelhoff, G. J., van Dishoeck, E. F., & Herbst, E. 2002, *A&A*, 386, 622
- Alexander, R. D., Casali, M. M., André, P., Persi, P., & Eiroa, C. 2003, *A&A*, 401, 613
- Alexander, R. D., Clarke, C. J., & Pringle, J. E. 2005, *MNRAS*, 358, 283
- André, P. & Montmerle, T. 1994, *ApJ*, 420, 837
- André, P., Ward-Thompson, D., & Barsony, M. 1993, *ApJ*, 406, 122
- André, P., Ward-Thompson, D., & Barsony, M. 2000, *Protostars and Planets IV*, 59
- Andrews, S. M. & Williams, J. P. 2007, *ApJ*, 671, 1800
- Arce, H. G. & Goodman, A. A. 2002, *ApJ*, 575, 928
- Arce, H. G. & Sargent, A. I. 2005, *ApJ*, 624, 232
- Arce, H. G., Shepherd, D., Gueth, F., et al. 2007, in *Protostars and Planets V*, ed. B. Reipurth, D. Jewitt, & K. Keil, 245–260
- Ashby, M. L. N., Bergin, E. A., Plume, R., et al. 2000, *ApJ*, 539, L119
- Bachiller, R., Pérez Gutiérrez, M., Kumar, M. S. N., & Tafalla, M. 2001, *A&A*, 372, 899
- Bachiller, R. & Tafalla, M. 1999, in *The Origin of Stars and Planetary Systems*, ed. C. J. Lada, , & N. D. Kylafis (Kluwer, Dordrecht), 227
- Bachiller, R., Tafalla, M., & Cernicharo, J. 1994, *ApJ*, 425, L93
- Barsony, M., Kenyon, S. J., Lada, E. A., & Teuben, P. J. 1997, *ApJ*, 112, 109
- Barsony, M., Ressler, M. E., & Marsh, K. A. 2005, *ApJ*, 630, 381
- Bergin, E. A., Kaufman, M. J., Melnick, G. J., Snell, R. L., & Howe, J. E. 2003, *ApJ*, 582, 830
- Bergin, E. A. & Melnick, G. J. 2005, in *IAU Symposium, Vol. 231, Astrochemistry: Recent Successes and Current Challenges*, ed. D. C. Lis, G. A. Blake, & E. Herbst, 309–318
- Bergin, E. A. & Snell, R. L. 2002, *ApJ*, 581, L105

- Bisschop, S. E., Jørgensen, J. K., van Dishoeck, E. F., & de Wachter, E. B. M. 2007, *A&A*, 465, 913
- Blake, G. A. & Boogert, A. C. A. 2004, *ApJ*, 606, L73
- Blake, G. A., Sandell, G., van Dishoeck, E. F., et al. 1995, *ApJ*, 441, 689
- Blake, G. A., van Dishoeck, E. F., Jansen, D. J., Groesbeck, T. D., & Mundy, L. G. 1994, *ApJ*, 428, 680
- Bontemps, S., André, P., Kaas, A. A., et al. 2001, *A&A*, 372, 173
- Bontemps, S., André, P., Terebey, S., & Cabrit, S. 1996, *A&A*, 311, 858
- Boogert, A., Pontoppidan, K., Knez, C., et al. 2008, *ArXiv e-prints*, 801
- Boogert, A. C. A., Hogerheijde, M. R., Ceccarelli, C., et al. 2002, *ApJ*, 570, 708
- Boogert, A. C. A., Tielens, A. G. G. M., Ceccarelli, C., et al. 2000, *A&A*, 360, 683
- Boonman, A. M. S., Doty, S. D., van Dishoeck, E. F., et al. 2003, *A&A*, 406, 937
- Bottinelli, S., Ceccarelli, C., Lefloch, B., et al. 2004, *ApJ*, 615, 354
- Bottinelli, S., Ceccarelli, C., Williams, J. P., & Lefloch, B. 2007, *A&A*, 463, 601
- Bourke, T. L. 2001, *ApJ*, 554, L91
- Bourke, T. L., Garay, G., Lehtinen, K. K., et al. 1997, *ApJ*, 476, 781
- Bourke, T. L., Hyland, A. R., & Robinson, G. 1995, *MNRAS*, 276, 1052
- Brandner, W., Sheppard, S., Zinnecker, H., et al. 2000, *A&A*, 364, L13
- Brinch, C., Crapsi, A., Jørgensen, J. K., Hogerheijde, M. R., & Hill, T. 2007, *A&A*, 475, 915
- Brown, A. 1987, *ApJ*, 322, L31
- Brown, J. M., Blake, G. A., Dullemond, C. P., et al. 2007, *ApJ*, 664, L107
- Butner, H. M., Charnley, S. B., Ceccarelli, C., et al. 2007, *ApJ*, 659, L137
- Butner, H. M., Evans, II, N. J., Lester, D. F., Levreault, R. M., & Strom, S. E. 1991, *ApJ*, 376, 636
- Cabrit, S. & Bertout, C. 1990, *ApJ*, 348, 530
- Cabrit, S. & Bertout, C. 1992, *A&A*, 261, 274
- Cambrésy, L. 1999, *A&A*, 345, 965

- Ceccarelli, C., Baudry, A., Caux, E., et al. 2001, in *ESA Special Publication, Vol. 460, The Promise of the Herschel Space Observatory*, ed. G. L. Pilbratt, J. Cernicharo, A. M. Heras, T. Prusti, & R. Harris, 219–+
- Ceccarelli, C., Boogert, A. C. A., Tielens, A. G. G. M., et al. 2002, *A&A*, 395, 863
- Ceccarelli, C., Castets, A., Caux, E., et al. 2000, *A&A*, 355, 1129
- Ceccarelli, C., Caux, E., Loinard, L., et al. 1999, *A&A*, 342, L21
- Ceccarelli, C., Caux, E., White, G. J., et al. 1998, *A&A*, 331, 372
- Ceccarelli, C., Hollenbach, D. J., & Tielens, A. G. G. M. 1996, *ApJ*, 471, 400
- Cernicharo, J., Bachiller, R., & Gonzalez-Alfonso, E. 1996, *A&A*, 305, L5
- Cernicharo, J. & Crovisier, J. 2005, *Space Science Reviews*, 119, 29
- Cernicharo, J., Thum, C., Hein, H., et al. 1990, *A&A*, 231, L15
- Chandler, C. J. & Richer, J. S. 2000, *ApJ*, 530, 851
- Chapman, N., Mundy, L., Lai, S.-P., & Evans, N. 2008, *ApJ*, in press
- Charnley, S. B., Rodgers, S. D., & Ehrenfreund, P. 2001, *A&A*, 378, 1024
- Charnley, S. B., Tielens, A. G. G. M., & Millar, T. J. 1992, *ApJ*, 399, L71
- Chernin, L. M. & Masson, C. R. 1991, *ApJ*, 382, L93
- Chini, R., Kämpgen, K., Reipurth, B., et al. 2003, *A&A*, 409, 235
- Comerón, F. 2006, in *Handbook of southern starforming regions*, ed. B. Reipurth (ESO press), in press
- Comeron, F., Rieke, G. H., Burrows, A., & Rieke, M. J. 1993, *ApJ*, 416, 185
- Crapsi, A., van Dishoeck, E. F., Hogerheijde, M. R., Pontoppidan, K. M., & Dullemond, C. P. 2008, *ArXiv e-prints*, 801
- Crawford, I. A. 2000, *MNRAS*, 317, 996
- Damjanov, I., Jayawardhana, R., Scholz, A., et al. 2007, *ApJ*, 670, 1337
- D'Antona, F. & Mazzitelli, I. 1994, *ApJ*, 90, 467
- de Graauw, T., Caux, E., Guesten, R., et al. 2005, in *Bulletin of the American Astronomical Society*, 1219
- de Graauw, T. & Helmich, F. P. 2001, in *ESA Special Publication, Vol. 460, The Promise of the Herschel Space Observatory*, ed. G. L. Pilbratt, J. Cernicharo, A. M. Heras, T. Prusti, & R. Harris, 45–+

- Dent, W. R. F., Greaves, J. S., & Coulson, I. M. 2005, *MNRAS*, 359, 663
- Di Francesco, J., Johnstone, D., Kirk, H., MacKenzie, T., & Ledwosinska, E. 2008, *ApJ*, 175, 277
- Dickman, R. L. & Herbst, W. 1990, *ApJ*, 357, 531
- Dopita, M. A., Evans, I., & Schwartz, R. D. 1982, *ApJ*, 263, L73
- Doty, S. D. 2000, *ApJ*, 535, 907
- Doty, S. D. & Leung, C. M. 1994, *ApJ*, 424, 729
- Doty, S. D. & Neufeld, D. A. 1997, *ApJ*, 489, 122
- Dowell, C. D., Allen, C. A., Babu, R. S., et al. 2003, Presented at the Society of Photo-Optical Instrumentation Engineers (SPIE) Conference, 4855, 73
- Draine, B. T. 2003, *ApJ*, 598, 1017
- Draine, B. T. & Roberge, W. G. 1984, *ApJ*, 282, 491
- Dubernet, M.-L., Daniel, F., Grosjean, A., et al. 2006, *A&A*, 460, 323
- Dubernet, M.-L. & Grosjean, A. 2002, *A&A*, 390, 793
- Dunham, M. M., Crapsi, A., Evans, II, N. J., et al. 2008, *ArXiv e-prints*, 806
- Dutrey, A., Guilloteau, S., Duvert, G., et al. 1996, *A&A*, 309, 493
- Dutrey, A., Guilloteau, S., & Guelin, M. 1997, *A&A*, 317, L55
- Dutrey, A., Guilloteau, S., & Simon, M. 2003, *A&A*, 402, 1003
- Duvert, G., Guilloteau, S., Ménard, F., Simon, M., & Dutrey, A. 2000, *A&A*, 355, 165
- Elias, J. H. 1978, *ApJ*, 224, 453
- Elitzur, M., Hollenbach, D. J., & McKee, C. F. 1989, *ApJ*, 346, 983
- Enoch, M. L., Evans, N. J., Sargent, A. I., & Glenn, J. 2008, *ApJ*, submitted
- Enoch, M. L., Young, K. E., Glenn, J., et al. 2006, *ApJ*, 638, 293
- Evans, N. J. 1999, *ARA&A*, 37, 311
- Evans, N. J., Allen, L. E., Blake, G. A., et al. 2003, *PASP*, 115, 965
- Evans, N. J., Harvey, P. M., Dunham, M. M., et al. 2007, c2d delivery document
- Evans, II, N. J., Lee, J.-E., Rawlings, J. M. C., & Choi, M. 2005, *ApJ*, 626, 919
- Faure, A., Crimier, N., Ceccarelli, C., et al. 2007, *A&A*, 472, 1029

- Felli, M., Brand, J., Cesaroni, R., et al. 2007, *A&A*, 476, 373
- Fernandes, A. J. L. 2000, *MNRAS*, 315, 657
- Flower, D. R. 2001, *Journal of Phys. B Atom. Molec. Phys.*, 34, 2731
- Flower, D. R., Le Bourlot, J., Pineau Des Forets, G., & Roueff, E. 1994, *A&A*, 282, 225
- Fraser, H. J., Collings, M. P., McCoustra, M. R. S., & Williams, D. A. 2001, *MNRAS*, 327, 1165
- Frerking, M. A., Langer, W. D., & Wilson, R. W. 1982, *ApJ*, 262, 590
- Fridlund, C. V. M., Sandqvist, A., Nordh, H. L., & Olofsson, G. 1989, *A&A*, 213, 310
- Froebrich, D. 2005, *ApJ*, 156, 169
- Furlan, E., McClure, M., Calvet, N., et al. 2008, *ApJ*, 176, 184
- Furuya, R. S., Kitamura, Y., Wootten, A., Claussen, M. J., & Kawabe, R. 2003, *ApJ*, 144, 71
- Gahm, G. F., Johansson, L. E. B., & Liseau, R. 1993, *A&A*, 274, 415
- Gensheimer, P. D., Mauersberger, R., & Wilson, T. L. 1996, *A&A*, 314, 281
- Giannini, T., Lorenzetti, D., Tommasi, E., et al. 1999, *A&A*, 346, 617
- Giannini, T., Nisini, B., & Lorenzetti, D. 2001, *ApJ*, 555, 40
- Goldsmith, P. F. & Langer, W. D. 1978, *ApJ*, 222, 881
- Gorti, U. & Hollenbach, D. 2004, *ApJ*, 613, 424
- Greaves, J. S. 2004, *MNRAS*, 351, L99
- Greaves, J. S. 2005, *Science*, 307, 68
- Green, S., Maluendes, S., & McLean, A. D. 1993, *ApJ*, 85, 181
- Greene, T. P. & Meyer, M. R. 1995, *ApJ*, 450, 233
- Greene, T. P., Wilking, B. A., Andre, P., Young, E. T., & Lada, C. J. 1994, *ApJ*, 434, 614
- Groppi, C. E., Hunter, T. R., Blundell, R., & Sandell, G. 2007, *ApJ*, 670, 489
- Grosjean, A., Dubernet, M.-L., & Ceccarelli, C. 2003, *A&A*, 408, 1197
- Güsten, R., Baryshev, A., Bell, A., & Belloche, A. 2008, (*SPIE*), 7020
- Güsten, R., Nyman, L. Å., Schilke, P., et al. 2006, *A&A*, 454, L13
- Gutermuth, R. A., Myers, P. C., Megeath, S. T., et al. 2008, *ApJ*, 674, 336

- Haikala, L. K., Juvela, M., Harju, J., et al. 2006, *A&A*, 454, L71
- Hara, A., Tachihara, K., Mizuno, A., et al. 1999, *PASJ*, 51, 895
- Harju, J., Haikala, L. K., Mattila, K., et al. 1993, *A&A*, 278, 569
- Hartigan, P. 1993, *AJ*, 105, 1511
- Hartmann, L., Megeath, S. T., Allen, L., et al. 2005, *ApJ*, 629, 881
- Harwit, M., Neufeld, D. A., Melnick, G. J., & Kaufman, M. J. 1998, *ApJ*, 497, L105
- Hatchell, J., Fuller, G. A., & Ladd, E. F. 1999, *A&A*, 344, 687
- Hatchell, J., Fuller, G. A., & Richer, J. S. 2007a, *A&A*, 472, 187
- Hatchell, J., Fuller, G. A., Richer, J. S., Harries, T. J., & Ladd, E. F. 2007b, *A&A*, 468, 1009
- Heathcote, S., Morse, J. A., Hartigan, P., et al. 1996, *AJ*, 112, 1141
- Helmich, F. P., van Dishoeck, E. F., Black, J. H., et al. 1996, *A&A*, 315, L173
- Henning, T., Burkert, A., Launhardt, R., Leinert, C., & Stecklum, B. 1998, *A&A*, 336, 565
- Henning, T. & Launhardt, R. 1998, *A&A*, 338, 223
- Henning, T., Pfau, W., Zinnecker, H., & Prusti, T. 1993, *A&A*, 276, 129
- Heyminck, S., Kasemann, C., Güsten, R., de Lange, G., & Graf, U. U. 2006, *A&A*, 454, L21
- Hiramatsu, M., Hayakawa, T., Tatematsu, K., et al. 2007, *ApJ*, 664, 964
- Hirano, N. & Taniguchi, Y. 2001, *ApJ*, 550, L219
- Hogerheijde, M. R. & van der Tak, F. F. S. 2000, *A&A*, 362, 697
- Hogerheijde, M. R., van Dishoeck, E. F., Blake, G. A., & van Langevelde, H. J. 1997, *ApJ*, 489, 293
- Hogerheijde, M. R., van Dishoeck, E. F., Blake, G. A., & van Langevelde, H. J. 1998, *ApJ*, 502, 315
- Hogerheijde, M. R., van Dishoeck, E. F., Salverda, J. M., & Blake, G. A. 1999, *ApJ*, 513, 350
- Hollenbach, D. J., Yorke, H. W., & Johnstone, D. 2000, *Protostars and Planets IV*, 401
- Hughes, J., Hartigan, P., & Clampitt, L. 1993, *AJ*, 105, 571
- Hughes, J., Hartigan, P., Krautter, J., & Kelemen, J. 1994, *AJ*, 108, 1071

- Ivezić, Z. & Elitzur, M. 1997, *MNRAS*, 287, 799
- Jacq, T., Henkel, C., Walmsley, C. M., Jewell, P. R., & Baudry, A. 1988, *A&A*, 199, L5
- Jacq, T., Walmsley, C. M., Henkel, C., et al. 1990, *A&A*, 228, 447
- Jansen, D. J., van Dishoeck, E. F., & Black, J. H. 1994, *A&A*, 282, 605
- Jansen, D. J., van Dishoeck, E. F., Keene, J., Boreiko, R. T., & Betz, A. L. 1996, *A&A*, 309, 899
- Jayawardhana, R., Hartmann, L., & Calvet, N. 2001, *ApJ*, 548, 310
- Jensen, E. L. N., Mathieu, R. D., & Fuller, G. A. 1996, *ApJ*, 458, 312
- Johnstone, D., Fich, M., Mitchell, G. F., & Moriarty-Schieven, G. 2001, *ApJ*, 559, 307
- Johnstone, D., Wilson, C. D., Moriarty-Schieven, G., et al. 2000, *ApJ*, 545, 327
- Jørgensen, J. K. 2004, *A&A*, 424, 589
- Jørgensen, J. K., Bourke, T. L., Myers, P. C., et al. 2007, *ApJ*, 659, 479
- Jørgensen, J. K., Johnstone, D., Kirk, H., et al. 2008, *ApJ*, in press
- Jørgensen, J. K., Johnstone, D., van Dishoeck, E. F., & Doty, S. D. 2006, *A&A*, 449, 609
- Jørgensen, J. K., Schöier, F. L., & van Dishoeck, E. F. 2002, *A&A*, 389, 908
- Jørgensen, J. K., Schöier, F. L., & van Dishoeck, E. F. 2004, *A&A*, 416, 603
- Jørgensen, J. K., Schöier, F. L., & van Dishoeck, E. F. 2005a, *A&A*, 437, 501
- Jørgensen, J. K., Schöier, F. L., & van Dishoeck, E. F. 2005b, *A&A*, 435, 177
- Kamp, I., van Zadelhoff, G.-J., van Dishoeck, E. F., & Stark, R. 2003, *A&A*, 397, 1129
- Kasemann, C., Güsten, R., Heyminck, S., et al. 2006, Presented at the Society of Photo-Optical Instrumentation Engineers (SPIE) Conference, 6275
- Kaufman, M. J. & Neufeld, D. A. 1996, *ApJ*, 456, 611
- Kaufman, M. J., Wolfire, M. G., Hollenbach, D. J., & Luhman, M. L. 1999, *ApJ*, 527, 795
- Kenyon, S. J., Gomez, M., Marzke, R. O., & Hartmann, L. 1994, *AJ*, 108, 251
- Kessler-Silacci, J., Augereau, J.-C., Dullemond, C. P., et al. 2006, *ApJ*, 639, 275
- Kirk, H., Johnstone, D., & Di Francesco, J. 2006, *ApJ*, 646, 1009
- Klein, B., Philipp, S. D., Krämer, I., et al. 2006, *A&A*, 454, L29
- Knee, L. B. G. 1992, *A&A*, 259, 283

- Knee, L. B. G. & Sandell, G. 2000, *A&A*, 361, 671
- Knude, J. & Høg, E. 1998, *A&A*, 338, 897
- Knude, J. & Nielsen, A. S. 2001, *A&A*, 373, 714
- Koerner, D. W. & Sargent, A. I. 1995, *AJ*, 109, 2138
- Krautter, J., Alcalá, J. M., Wichmann, R., Neuhauser, R., & Schmitt, J. H. M. M. 1994, *Revista Mexicana de Astronomía y Astrofísica*, vol. 29, 29, 41
- Krautter, J. & Reipurth, B. 1991, in *ESO Scientific Reports*, Vol. 11 (ESO press), 127
- Krautter, J., Wichmann, R., Schmitt, J. H. M. M., et al. 1997, *A&AS*, 123, 329
- Kreysa, E., Bertoldi, F., Gemuend, H.-P., et al. 2003, Presented at the Society of Photo-Optical Instrumentation Engineers (SPIE) Conference, 4855, 41
- Lada, C. J. 1987, in *IAU Symp. 115: Star Forming Regions*, ed. M. Peimbert, J. Jugaku, & P. W. J. L. Brand (Reidel, Dordrecht), 1
- Lada, C. J. & Kylafis, N. D., eds. 1999, *The Origin of Stars and Planetary Systems*
- Lada, C. J. & Wilking, B. A. 1984, *ApJ*, 287, 610
- Lahuis, F., van Dishoeck, E. F., Boogert, A. C. A., et al. 2006, *ApJ*, 636, L145
- Lee, C.-F., Mundy, L. G., Stone, J. M., & Ostriker, E. C. 2002, *ApJ*, 576, 294
- Lee, J.-E., Di Francesco, J., Bourke, T. L., Evans, II, N. J., & Wu, J. 2007, *ApJ*, 671, 1748
- Lehtinen, K., Haikala, L. K., Mattila, K., & Lemke, D. 2001, *A&A*, 367, 311
- Lehtinen, K., Harju, J., Kontinen, S., & Higdon, J. L. 2003, *A&A*, 401, 1017
- Liseau, R., Ceccarelli, C., Larsson, B., et al. 1996, *A&A*, 315, L181
- Liseau, R., White, G. J., Larsson, B., et al. 1999, *A&A*, 344, 342
- Liu, M. C., Graham, J. R., Ghez, A. M., et al. 1996, *ApJ*, 461, 334
- Lizano, S. & Giovanardi, C. 1995, *ApJ*, 447, 742
- Loinard, L., Torres, R. M., Mioduszewski, A. J., & Rodríguez, L. F. 2008, *ApJ*, 675, L29
- Lommen, D., Jørgensen, J. K., van Dishoeck, E. F., & Crapsi, A. 2008, *A&A*, 481, 141
- Looney, L. W., Mundy, L. G., & Welch, W. J. 2000, *ApJ*, 529, 477
- Loren, R. B. 1979, *ApJ*, 227, 832
- Loren, R. B. 1989, *ApJ*, 338, 902

- Loren, R. B., Wootten, A., & Wilking, B. A. 1990, *ApJ*, 365, 269
- Lorenzetti, D., Tommasi, E., Giannini, T., et al. 1999, *A&A*, 346, 604
- Luhman, K. L., Allen, L. E., Allen, P. R., et al. 2008, *ApJ*, 675, 1375
- Luhman, K. L. & Rieke, G. H. 1999, *ApJ*, 525, 440
- Mannings, V. & Sargent, A. I. 2000, *ApJ*, 529, 391
- Marcy, G. W. & Butler, R. P. 1995, *Bulletin of the American Astronomical Society*, 27, 1379
- Maret, S., Ceccarelli, C., Caux, E., Tielens, A. G. G. M., & Castets, A. 2002, *A&A*, 395, 573
- Maret, S., Ceccarelli, C., Caux, E., et al. 2004, *A&A*, 416, 577
- Maret, S., Ceccarelli, C., Tielens, A. G. G. M., et al. 2005, *A&A*, 442, 527
- Mezger, P. G., Sievers, A., Zylka, R., et al. 1992, *A&A*, 265, 743
- Micono, M., Davis, C. J., Ray, T. P., Eisloffel, J., & Shetrone, M. D. 1998, *ApJ*, 494, L227+
- Moriarty-Schieven, G. H. & Snell, R. L. 1988, *ApJ*, 332, 364
- Motte, F. & André, P. 2001, *A&A*, 365, 440
- Motte, F., André, P., & Neri, R. 1998, *A&A*, 336, 150
- Mueller, K. E., Shirley, Y. L., Evans, N. J., & Jacobson, H. R. 2002, *ApJ*, 143, 469
- Myers, P. C., Evans, II, N. J., & Ohashi, N. 2000, *Protostars and Planets IV*, 217
- Myers, P. C. & Ladd, E. F. 1993, *ApJ*, 413, L47
- Najita, J., Carr, J. S., & Mathieu, R. D. 2003, *ApJ*, 589, 931
- Neufeld, D. A. & Dalgarno, A. 1989, *ApJ*, 340, 869
- Neufeld, D. A. & Kaufman, M. J. 1993, *ApJ*, 418, 263
- Neufeld, D. A., Snell, R. L., Ashby, M. L. N., et al. 2000, *ApJ*, 539, L107
- Neuhäuser, R., Guenther, E. W., Wuchterl, G., et al. 2005, *A&A*, 435, L13
- Nisini, B., Antonucci, S., Giannini, T., & Lorenzetti, D. 2005, *A&A*, 429, 543
- Nisini, B., Benedettini, M., Giannini, T., et al. 1999, *A&A*, 350, 529
- Nisini, B., Giannini, T., & Lorenzetti, D. 2002, *ApJ*, 574, 246
- Noriega-Crespo, A., Morris, P., Marleau, F. R., et al. 2004, *ApJ*, 154, 352

- Nuernberger, D., Brandner, W., Yorke, H. W., & Zinnecker, H. 1998, *A&A*, 330, 549
- Nürnberg, D., Chini, R., & Zinnecker, H. 1997, *A&A*, 324, 1036
- Nutter, D., Kirk, J. M., Stamatellos, D., & Ward-Thompson, D. 2008, *MNRAS*, 384, 755
- Nutter, D. J., Ward-Thompson, D., & André, P. 2005, *MNRAS*, 357, 975
- Olberg, M., Reipurth, B., & Booth, R. S. 1992, *A&A*, 259, 252
- Olofsson, G., Hultgren, M., Kaas, A. A., et al. 1999, *A&A*, 350, 883
- Osorio, M., D'Alessio, P., Muzerolle, J., Calvet, N., & Hartmann, L. 2003, *ApJ*, 586, 1148
- Ossenkopf, V. & Henning, T. 1994, *A&A*, 291, 943
- Padgett, D. L., Rebull, L. M., Stapelfeldt, K. R., et al. 2008, *ApJ*, 672, 1013
- Parise, B., Belloche, A., Leurini, S., et al. 2006, *A&A*, 454, L79
- Parise, B., Caux, E., Castets, A., et al. 2005, *A&A*, 431, 547
- Park, G. & Choi, M. 2007, *ApJ*, 664, L99
- Persi, P., Marenzi, A. R., Gómez, M., & Olofsson, G. 2001, *A&A*, 376, 907
- Persi, P., Marenzi, A. R., Kaas, A. A., et al. 1999, *AJ*, 117, 439
- Persi, P., Marenzi, A. R., Olofsson, G., et al. 2000, *A&A*, 357, 219
- Phillips, T. R., Maluendes, S., & Green, S. 1996, *ApJ*, 107, 467
- Poelman, D. R. & Spaans, M. 2005, *A&A*, 440, 559
- Poelman, D. R. & van der Tak, F. F. S. 2007, *A&A*, 475, 949
- Poglitsch, A., Waelkens, C., & Geis, N. 2001, in *ESA Special Publication, Vol. 460, The Promise of the Herschel Space Observatory*, ed. G. L. Pilbratt, J. Cernicharo, A. M. Heras, T. Prusti, & R. Harris, 29–+
- Pontoppidan, K. M., Dullemond, C. P., van Dishoeck, E. F., et al. 2005, *ApJ*, 622, 463
- Pontoppidan, K. M., Fraser, H. J., Dartois, E., et al. 2003, *A&A*, 408, 981
- Pontoppidan, K. M., van Dishoeck, E. F., & Dartois, E. 2004, *A&A*, 426, 925
- Qi, C., Ho, P. T. P., Wilner, D. J., et al. 2004, *ApJ*, 616, L11
- Rachford, B. L., Snow, T. P., Tumlinson, J., et al. 2002, *ApJ*, 577, 221
- Raga, A. C., de Colle, F., Kajdič, P., Esquivel, A., & Cantó, J. 2007, *A&A*, 465, 879
- Raymond, J. C., Morse, J. A., Hartigan, P., Curiel, S., & Heathcote, S. 1994, *ApJ*, 434, 232

- Reipurth, B., Chini, R., Krugel, E., Kreysa, E., & Sievers, A. 1993, *A&A*, 273, 221
- Reipurth, B. & Heathcote, S. 1991, *A&A*, 246, 511
- Reipurth, B., Jewitt, D., & Keil, K., eds. 2007, *Protostars and Planets V*
- Reipurth, B. & Raga, A. C. 1999, in *NATO ASIC Proc. 540: The Origin of Stars and Planetary Systems*, ed. C. J. Lada & N. D. Kylafis, 267–+
- Reipurth, B., Rodríguez, L. F., Anglada, G., & Bally, J. 2002, *AJ*, 124, 1045
- Ridge, N. A., Di Francesco, J., Kirk, H., et al. 2006, *AJ*, 131, 2921
- Risacher, C., Vassilev, V., Monje, R., et al. 2006, *A&A*, 454, L17
- Ristorcelli, I., Falgarone, E., Schöier, F., et al. 2005, in *IAU Symposium*, ed. D. C. Lis, G. A. Blake, & E. Herbst, 184
- Rizzo, J. R., Morras, R., & Arnal, E. M. 1998, *MNRAS*, 300, 497
- Robitaille, T. P., Whitney, B. A., Indebetouw, R., & Wood, K. 2007, *ApJ*, 169, 328
- Robitaille, T. P., Whitney, B. A., Indebetouw, R., Wood, K., & Denzmore, P. 2006, *ApJ*, 167, 256
- Ruden, S. P. 1999, in *NATO ASIC Proc. 540: The Origin of Stars and Planetary Systems*, 643
- Sandell, G. & Knee, L. B. G. 2001, *ApJ*, 546, L49
- Santos, N. C., Yun, J. L., Santos, C. A., & Marreiros, R. G. 1998, *AJ*, 116, 1376
- Schöier, F. L., Jørgensen, J. K., Pontoppidan, K. M., & Lundgren, A. A. 2006, *A&A*, 454, L67
- Schöier, F. L., Jørgensen, J. K., van Dishoeck, E. F., & Blake, G. A. 2002, *A&A*, 390, 1001
- Schöier, F. L., Jørgensen, J. K., van Dishoeck, E. F., & Blake, G. A. 2004, *A&A*, 418, 185
- Schöier, F. L., van der Tak, F. F. S., van Dishoeck, E. F., & Black, J. H. 2005, *A&A*, 432, 369
- Schuster, K. F., Harris, A. I., Anderson, N., & Russell, A. P. G. 1993, *ApJ*, 412, L67
- Schuster, K.-F., Russell, A. P. G., & Harris, A. I. 1995, *A&Space Sciences*, 224, 117
- Schwartz, R. D. 1977, *ApJ*, 35, 161
- Schwartz, R. D. & Greene, T. P. 2003, *AJ*, 126, 339
- Shirley, Y. L., Evans, N. J., Rawlings, J. M. C., & Gregersen, E. M. 2000, *ApJ*, 131, 249

- Shirley, Y. L., Evans, II, N. J., & Rawlings, J. M. C. 2002, *ApJ*, 575, 337
- Shu, F. H. 1977, *ApJ*, 214, 488
- Simon, M., Ghez, A. M., & Leinert, C. 1993, *ApJ*, 408, L33
- Siringo, G., Kreysa, E., & Kovacs, A. 2008, (*SPIE*), 7020
- Smith, H., Hills, R. E., Withington, S., et al. 2003, Presented at the Society of Photo-Optical Instrumentation Engineers (*SPIE*) Conference, 4855, 338
- Smith, R. G., Sellgren, K., & Tokunaga, A. T. 1989, *ApJ*, 344, 413
- Snell, R. L., Dickman, R. L., & Huang, Y.-L. 1990, *ApJ*, 352, 139
- Snell, R. L., Howe, J. E., Ashby, M. L. N., et al. 2000, *ApJ*, 539, L101
- Spaans, M., Hogerheijde, M. R., Mundy, L. G., & van Dishoeck, E. F. 1995, *ApJ*, 455, L167+
- Stanke, T., McCaughrean, M. J., & Zinnecker, H. 1999, *A&A*, 350, L43
- Stanke, T., Smith, M. D., Gredel, R., & Khanzadyan, T. 2006, *A&A*, 447, 609
- Stark, R., Sandell, G., Beck, S. C., et al. 2004, *ApJ*, 608, 341
- Stäuber, P., Doty, S. D., van Dishoeck, E. F., Jørgensen, J. K., & Benz, A. O. 2004, *A&A*, 425, 577
- Tachihara, K., Dobashi, K., Mizuno, A., Ogawa, H., & Fukui, Y. 1996, *PASJ*, 48, 489
- Tachihara, K., Toyoda, S., Onishi, T., et al. 2001, *PASJ*, 53, 1081
- Taylor, K. N. R. & Storey, J. W. V. 1984, *MNRAS*, 209, 5P
- Teixeira, P. S., Lada, C. J., & Alves, J. F. 2005, *ApJ*, 629, 276
- Terebey, S., Chandler, C. J., & Andre, P. 1993, *ApJ*, 414, 759
- Thi, W. F., van Dishoeck, E. F., Blake, G. A., et al. 2001, *ApJ*, 561, 1074
- Thi, W.-F., van Zadelhoff, G.-J., & van Dishoeck, E. F. 2004, *A&A*, 425, 955
- Turner, B. E., Fourikis, N., Morris, M., Palmer, P., & Zuckerman, B. 1975, *ApJ*, 198, L125
- van der Tak, F., Neufeld, D., Yates, J., et al. 2005, in *ESA Special Publication*, Vol. 577, *ESA Special Publication*, ed. A. Wilson, 431–432
- van der Tak, F. F. S., Black, J. H., Schöier, F. L., Jansen, D. J., & van Dishoeck, E. F. 2007, *A&A*, 468, 627
- van der Tak, F. F. S., van Dishoeck, E. F., Evans, N. J., & Blake, G. A. 2000, *ApJ*, 537, 283

- van der Tak, F. F. S., Walmsley, C. M., Herpin, F., & Ceccarelli, C. 2006, *A&A*, 447, 1011
- van Dishoeck, E. F. 2003, in *SFCHEM 2002: Chemistry as a Diagnostic of Star Formation*, proceedings of a conference held August 21-23, 2002 at University of Waterloo, Waterloo, Ontario, Canada N2L 3G1. Edited by Charles L. Curry and Michel Fich. NRC Press, Ottawa, Canada, 2003, p. 201., ed. C. L. Curry & M. Fich, 201
- van Dishoeck, E. F. & Black, J. H. 1988, *ApJ*, 334, 771
- van Dishoeck, E. F. & Blake, G. A. 1998, *ARA&A*, 36, 317
- van Dishoeck, E. F., Blake, G. A., Draine, B. T., & Lunine, J. I. 1993, in *Protostars and Planets III*, ed. E. H. Levy & J. I. Lunine, 163–241
- van Dishoeck, E. F., Blake, G. A., Jansen, D. J., & Groesbeck, T. D. 1995, *ApJ*, 447, 760
- van Kempen, T. A., Hogerheijde, M. R., van Dishoeck, E. F., et al. 2006, *A&A*, 454, L75
- van Kempen, T. A., van Dishoeck, E. F., Salter, D. M., et al. 2008, *A&A*
- van Zadelhoff, G.-J., Aikawa, Y., Hogerheijde, M. R., & van Dishoeck, E. F. 2003, *A&A*, 397, 789
- van Zadelhoff, G.-J., Dullemond, C. P., van der Tak, F. F. S., et al. 2002, *A&A*, 395, 373
- van Zadelhoff, G.-J., van Dishoeck, E. F., Thi, W.-F., & Blake, G. A. 2001, *A&A*, 377, 566
- Velusamy, T., Langer, W. D., & Marsh, K. A. 2007, *ApJ*, 668, L159
- Vilas-Boas, J. W. S., Myers, P. C., & Fuller, G. A. 2000, *ApJ*, 532, 1038
- Walawender, J., Bally, J., Kirk, H., & Johnstone, D. 2005, *AJ*, 130, 1795
- Walker, C. K., Narayanan, G., Buettgenbach, T. H., et al. 1993, *ApJ*, 415, 672
- Ward-Thompson, D. & Buckley, H. D. 2001, *MNRAS*, 327, 955
- Watson, D. M., Bohac, C. J., Hull, C., et al. 2007, *Nature*, 448, 1026
- White, G. J., Liseau, R., Men'shchikov, A. B., et al. 2000, *A&A*, 364, 741
- Whitney, B. A., Wood, K., Bjorkman, J. E., & Cohen, M. 2003a, *ApJ*, 598, 1079
- Whitney, B. A., Wood, K., Bjorkman, J. E., & Wolff, M. J. 2003b, *ApJ*, 591, 1049
- Whittet, D. C. B., Bode, M. F., Baines, D. W. T., Longmore, A. J., & Evans, A. 1983, *Nature*, 303, 218
- Wiling, B. A. & Lada, C. J. 1983, *ApJ*, 274, 698
- Wiling, B. A., Lada, C. J., & Young, E. T. 1989, *ApJ*, 340, 823

- Wilking, B. A., McCaughrean, M. J., Burton, M. G., et al. 1997, *AJ*, 114, 2029
- Wilking, B. A., Taylor, K. N. R., & Storey, J. W. V. 1986, *AJ*, 92, 103
- Wilson, T. L. & Rood, R. 1994, *ARA&A*, 32, 191
- Wootten, A. 1989, *ApJ*, 337, 858
- Young, C. H. & Evans, II, N. J. 2005, *ApJ*, 627, 293
- Young, C. H., Jørgensen, J. K., Shirley, Y. L., et al. 2004, *ApJ*, 154, 396
- Young, C. H., Shirley, Y. L., Evans, II, N. J., & Rawlings, J. M. C. 2003, *ApJ*, 145, 111
- Young, K. E., Enoch, M. L., Evans, II, N. J., et al. 2006, *ApJ*, 644, 326

Nederlandse samenvatting

Protosterren

Onze Zon is een ster in de Melkweg met een relatief lage massa (1 Zonsmassa = 2×10^{30} kg). De meeste sterren zijn ongeveer even zwaar als onze Zon. Veel zwaardere sterren (>5 Zonsmassa's), ook al stralen zij vele tientallen malen zoveel het licht uit als onze Zon, zijn veel zeldzamer. Zowel hoge als lage-massa sterren worden gevormd in donkere moleculaire wolken. Deze wolken zijn overal te vinden in ons Melkwegstelsel en kunnen meerdere lichtjaren groot zijn. Het meest bekende voorbeeld is de Orion wolk. Toch valt de grootte van zo'n wolk in het niet met die van ons hele Melkwegstelsel (100,000 lichtjaar in diameter). Lage-massa sterren komen in bijna alle wolken voor, maar alleen in de grootste moleculaire wolken (GMC's) worden naast lage massa sterren ook massieve sterren gevormd. Normaal bestaat er in de moleculaire wolk een balans tussen zijn eigen zwaartekracht en de inwendige thermische druk. Maar op sommige plaatsen verzamelt er zich genoeg materiaal zodat lokaal de zwaartekracht hoger wordt dan de druk en vormt zich een ster door het ineenstorten van dat deel van de wolk. Toch zijn veel details over hoe sterren worden geboren nog onbekend. Sterren vormen zich over een relatief korte tijd van ongeveer 1 tot 2 miljoen jaar en worden ook wel protosterren genoemd, voordat kernfusie in het inwendige van de ster ontbrandt. Vooral over de tijd totdat de ster de 'hoofdreeks' bereikt en zich nog bevindt in de moleculaire wolk, is weinig bekend. De hoofdreeks is het evolutie-model dat een ster correct beschrijft over het grootste deel van zijn leven.

Moleculaire wolken zijn koud ($T = 10 - 20$ Kelvin¹) en bestaan hoofdzakelijk uit moleculair waterstof, H_2 , en het edel-gas helium, He. Een kleine hoeveelheid stof en andere moleculen zoals water (H_2O), koolstofmonoxide (CO), formyl-ionen (HCO^+), methanol (CH_3OH) of formaldehyde (H_2CO) complementeren de samenstelling van de wolken. Ook al is de hoeveelheid van dit stof en deze moleculen klein (ongeveer 1 % in massa), toch spelen deze een cruciale rol tijdens de vorming van sterren.

Het ineenstorten van een deel van de wolk in een protoster is beter bekend als de *inside-out collapse*, aangezien de binnenste delen als eerste instorten. Deze *collapse* genereert veel warmte, die de interne druk verhoogt, maar emissie in spectraal lijnen van de kleine hoeveelheid moleculen zorgt ervoor dat de energie wordt weggestraald, zodat de druk niet tot grote hoogtes stijgt. In het binnenste vormt zich de centrale ster, met daaromheen verscheidende componenten. Het geheel noemen we een *protostellair object*. In het centrum bevindt zich de protoster zelf. Daaromheen, in het draaiingsvlak van de ster, bevindt zich de circumstellaire schijf, waaruit planeten uiteindelijk zullen worden gevormd. Hieromheen bevindt zich een protostellair omhulsel van gas en

¹Graden Kelvin worden geteld ten opzichte van het absolute nulpunt, -273 graden Celsius staat gelijk aan 0 graden Kelvin

stof. Het gehele systeem bevindt zich ook nog eens diep in de binnenste delen van de moleculaire wolk. Het stof in zowel het omhulsel als de moleculaire wolk absorbeert al het ultra-violet en zichtbare licht. Daardoor zijn protosterren moeilijk waar te nemen met conventionele methoden in het zichtbare deel van het licht-spectrum.

Componenten van een protoster.

Een protoster bestaat uit vier componenten met daaromheen de moleculaire wolk waarin de protoster zich bevindt. Aangezien de moleculaire wolk ook invloed heeft op de protoster wordt de wolk hieronder als vijfde component beschreven, ook al vormt deze geen fysisch onderdeel van het protostellaire object. Niet alle componenten zijn aanwezig in alle fasen van stervorming.

In de huidige theorie van stervorming worden sterren gevormd over vier fasen.

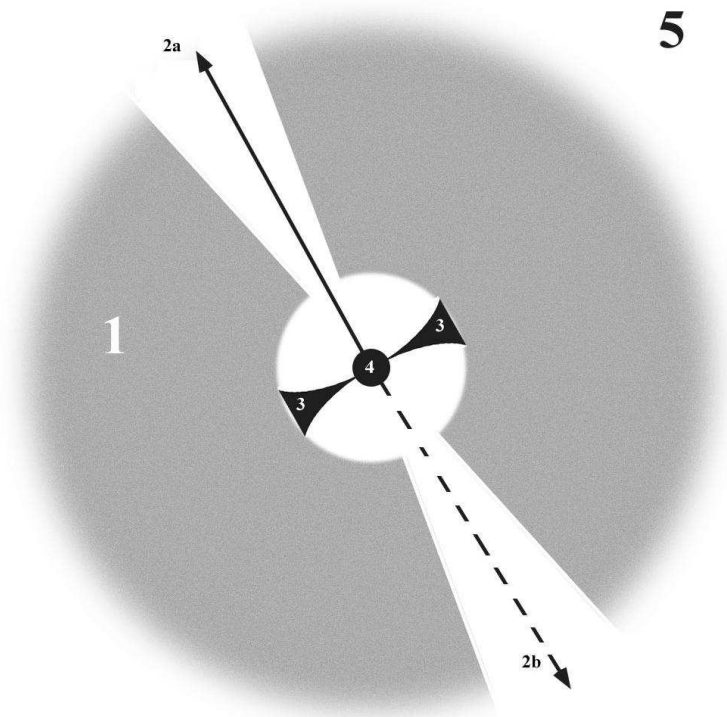
- Fase 0, waarin het grootste deel van de massa nog in het omhulsel zit. Schijven worden net gevormd rondom de nieuwe protoster.
- Fase 1, waarin de protoster is gegroeid en al een groot percentage (>90%) van zijn uiteindelijke massa heeft gekregen. De schijf en het omhulsel hebben nu vergelijkbare massa's.
- Fase 2, waarin het omhulsel is verdwenen. De schijf bevat nog zowel gas en stof. Deze fase staat beter bekend als de pre-hoofdreeks of T Tauri fase.
- Fase 3, waarin de schijf nog maar een kleine hoeveelheid materiaal bevat, voornamelijk stof.

Om stervorming in de twee vroege fasen goed te begrijpen, is het eerst essentieel om de componenten van een protoster te beschrijven. De componenten van een protoster zijn schematisch te zien in Figuur. 9.1.

Centrale ster : In het centrum bevindt zich de centrale ster. Alhoewel fusie van deuterium al gaande is, heeft de protoster nog niet zijn uiteindelijke massa bereikt. Pas aan het einde van Fase 1 zal de centrale ster zijn uiteindelijke massa hebben. De accretie van materiaal tijdens de eerdere fasen produceert een significant deel van de totale hoeveelheid licht.

Circumstellaire schijf: In het draaiingsvlak van de protoster vormt zich, door de wet van behoud van impuls, een protostellaire schijf. Deze schijf is in het begin vooral aanwezig als een tussenstation voor de materie die van het protostellaire omhulsel op de centrale ster valt. Deze schijf kan ongeveer 500 AU (AU = Astronomische Eenheid, de gemiddelde afstand tussen de Zon en de Aarde van ongeveer 150 miljoen kilometer) groot zijn en vele tientallen AU dik. In latere fasen van stervorming is de circumstellaire schijf de locatie waar planeten, zowel Aarde-achtige als gas-reuzen zoals Jupiter, zich vormen.

Protostellaire omhulsel: Het materiaal dat zich als een bol rondom de centrale ster bevindt wordt het protostellaire omhulsel genoemd. Dit omhulsel, dat de massa-reserves die nog op de protoster moeten vallen bevat, verhult de centrale ster en schijf en absorbeert al het zichtbare en kortgolvlige licht zoals UV en röntgen-straling. Het gas en stof is voor het overgrote deel koud (< 30 K) en straalt in het verre infra-rood en het (sub)millimeter-gebied.



Figuur 9.1 — Een model van de structuur van een protoster. De vijf componenten hierin zijn: 1: het protostellair omhulsel, 2: de straalstroom, 3: de circumstellaire schijf, 4: de centrale ster en 5: de omgeving.

Straalstroom: Bij een groot aantal protosterren zijn straalstromen gedetecteerd en het is aanneemlijk dat alle protosterren straalstromen hebben ergens in de vroege fases van stervorming. Straalstromen bestaan uit een hoge energetische 'jet', die materiaal uit het omhulsel en wolk kan opvegen en meeslepen. Zulke 'jets' zijn nodig om het overschot aan impuls weg te halen uit de binnenste delen, zodat materiaal op de centrale ster kan vallen. Een kleine hoeveelheid massa wordt met grote snelheid de interstellaire ruimte ingeschoten, waarbij het eveneens een wisselwerking heeft met zowel het omhulsel als met de omringende wolk. Straalstromen kunnen direct worden waargenomen, maar in het submillimeter gebied worden waarnemingen gedomineerd door de opgeveegde massa van de moleculaire wolk en omhulsel.

Omgeving: De omgeving waarin de protoster zich bevindt kan een belangrijke invloed hebben op hoe protostellaire objecten zich voor een waarnemer manifesteren. Een voorgrond van koud materiaal kan bijvoorbeeld het infra-rood licht van de circumstellaire schijf verhullen. Een groot deel van de omgeving zal uiteindelijk door de straalstroom worden verspreid of gebruikt worden om andere sterren te vormen.

Waarnemingen

Het doen van waarnemingen van protosterren is beperkt tot langere golflengtes. In het visueel absorbeert het materiaal in het omhulsel en omringende wolk al het zichtbare, UV en röntgen licht. Ook in het nabije infra-rood wordt een groot deel van het licht



Figuur 9.2 — Het Chajnantor Plateau op ~ 5200 meter in noord-Chili met rechts de APEX telescoop. Deze foto is genomen tijdens mijn waarnemingreis naar deze telescoop door Sven Thorwirth.

geabsorbeerd en gebruikt om de wolk te verwarmen. Door de lage temperaturen in de omhulsels zijn de beste golflengtes om waar te nemen het verre infra-rood gebied en het (sub)-millimeter gebied. Het breedbandige licht op deze golflengtes bestaat uit straling van het koude stof. Het gas straalt in een grote hoeveelheid nauwe spectraallijnen van de moleculen. Deze spectraallijnen bevatten veel informatie over de fysische en chemische structuur van het gas, de temperaturen in het protostellair omhulsel en de turbulentie of het snelheidsveld dat in protostellaire objecten aanwezig is. Vooral de emissie van het CO molecuul wordt vaak gebruikt om deze parameters te bepalen. Lage frequentie lijnen van CO traceren vooral het koude gas en de totale kolom aan materiaal. De temperatuur van het gas kan worden bepaald door de hoge frequentie lijnen van CO. Alleen voor materiaal met hogere dichtheid moet een ander molecuul gebruikt. Lijnen van het HCO^+ molecuul zijn hiervoor goed geschikt.

Voorbeelden van submillimeter telescopen zijn de *James Clerk Maxwell Telescoop* (JCMT) en de *Atacama Pathfinder EXperiment* (APEX). Deze staan respectievelijk op de Mauna Kea vulkaan in Hawaii en op het Chajnantor plateau in Chili. Een foto van het Chajnantor plateau is te zien in Fig. 9.2.

Omdat de ruimtelijke resolutie van zulke telescopen nog niet vergelijkbaar is met dat van optische telescopen, wordt de straling geheel gedomineerd door emissie van het protostellair omhulsel. Alleen van protosterren die bijna hun hele omhulsel al zijn kwijtgeraakt kan de schijf en ster direct worden waargenomen. Schijven in deze vroege fases van stervorming kunnen veel beter worden waargenomen met submillimeter interferometers², die door de komst van de *Submillimeter Array* (SMA) in de laatste jaren ook het submillimeter gebied kunnen waarnemen.

Dit Proefschrift

Het onderzoek in dit proefschrift, gedaan met waarnemingen van de JCMT en APEX telescopen, heeft zich vooral toegespitst op de eerste fases van ster-vorming en de fysische structuur van het protostellair omhulsel, straalstroom en de directe omgeving van protosterren, en hun wisselwerkingen. Er is intensief gebruik gemaakt van moleculaire lijnen en vooral het gebruik van spectrale lijnkaarten.

²Een interferometer of “synthese telescoop” bestaat uit een verzameling van telescopen die door de samenwerking een resolutie tienmaal hoger dan een normale submillimeter telescoop kan halen. Dit gaat alleen ten koste van de gevoeligheid voor emissie op grotere schalen. Interferometers zijn daardoor minder geschikt om het volledige protostellair omhulsel waar te nemen.

Spectraallijn kaarten

In bijna elk hoofdstuk worden spectrale lijnkaarten gebruikt als de basis voor onze analyse. Zulke kaarten geven een duidelijker beeld van protosterren en hun interactie met de omgeving dan individuele spectra op de centrale positie van het protostellaire object. Zulke kaarten spelen in hoofdstukken 2, 4, 5 en 6 een centrale rol. Ook al worden zulke kaarten al sinds de jaren 70 gemaakt en intensief gebruikt bij lagere frequenties, de komst van nieuwe instrumenten met meerdere pixels bij submillimeter golflengtes, zoals CHAMP⁺ (14 pixels, 350 μm en 450 μm) en HARP-B (16 pixels, 850 μm), heeft ervoor gezorgd dat zulke kaarten met vele malen hogere snelheid en gevoeligheid kunnen worden gemaakt, in het bijzonder van warme en dichte gebieden.

Warm gas

Protosterren bevatten warm gas in de binnenste regionen van het omhulsel. Dit gas is direct waargenomen met het CHAMP⁺ instrument, het enige instrument ter wereld met meerdere pixels dat de hoogste submillimeter frequenties (600-800 GHz) kan waarnemen. In hoofdstukken 5 en 6 worden deze data besproken. In hoofdstuk 5 wordt de HH 46 bron gepresenteerd, waarvoor wij met alle CO lijnen tussen 200 en 850 GHz zowel het warme als koude gas kunnen traceren. Het warme gas blijkt daar op vier verschillende plaatsen voor te komen. Ten eerste wordt gas passief verwarmd door het absorberen van het sterlicht aan de binnenkant van omhulsel. Dit is een relatief klein gebied van slechts enkele tientallen tot een honderd AU. Ten tweede komt warm gas voor in het opgeveegde gas, dat door de passerende schok wordt verwarmd tot temperaturen van ~ 100 K. Deze twee scenario's zijn al sinds de jaren tachtig bekend, ook al waren veel kwantitatieve details onbekend. Verrassender is dat er ook warm gas wordt gevonden in het grensgebied van het omhulsel met de straalstroom. Dit wordt verwarmt door UV straling dat door de vorm van het schoongeveegde straalstroom kanaal vrij baan krijgt om deze wanden op de veel grotere afstanden van 3,000-5,000 AU te bereiken. Dit soort warm gas wordt ook gezien bij de wanden van de straalstroom met de omringende wolk op afstanden tot wel 60,000 AU. De benodigde UV straling wordt geproduceerd door schokken van de 'jet'. Hoofdstuk 6, waarin we acht protostellaire objecten hebben waargenomen, laat zien dat dit mechanisme van de verwarming van de straalstroom-wanden niet alleen bij HH 46 voorkomt, maar ook bij een groot aantal andere protosterren.

Gas met een hoge dichtheid

Naast het warme gas is er ook gas met een hoge dichtheid (tot 10^8 deeltjes per cm^3) te vinden in de binnenste delen van het protostellaire object. In hoofdstuk 2 laten we zien dat deze component goed getraceerd kan worden met emissie van het HCO⁺ molecuul. Dit molecuul speelt een sleutelrol in het classificeren en karakteriseren van protosterren. In de laatste jaren was al waargenomen dat een aantal T Tauri sterren, d.w.z. sterren die geen omhulsel meer hebben, waren geclassificeerd als protosterren door de hoek waaronder we ze waarnemen. Spatiële variatie van de emissie van het HCO⁺ molecuul blijkt uniek centraal geconcentreerd te zijn bij echte protosterren, terwijl zowel schijven als achtergrondbronnen óf een veel egalere variatie met positie laten zien

óf niet gedetecteerd worden.

In de Ophiuchus wolk, één van de dichtsbijzijnde moleculaire wolken waarin sterren worden gevormd (zie Fig. 1.1), hebben wij meer dan 40 jonge sterren, inclusief alle protosterren en een aantal schijven als controle, waargenomen. Van deze groep blijken maar 17 objecten echte protostellaire objecten te zijn. Een significant deel van deze groep zijn T Tauri sterren. Ook in hoofdstuk 4 wordt deze methode gebruikt om van een aantal zuidelijke bronnen te bepalen of het protosterren zijn. Ook hier laten wij zien dat niet alle objecten die op dit moment bekend staan als protosterren dat ook zijn.

Straalstromen

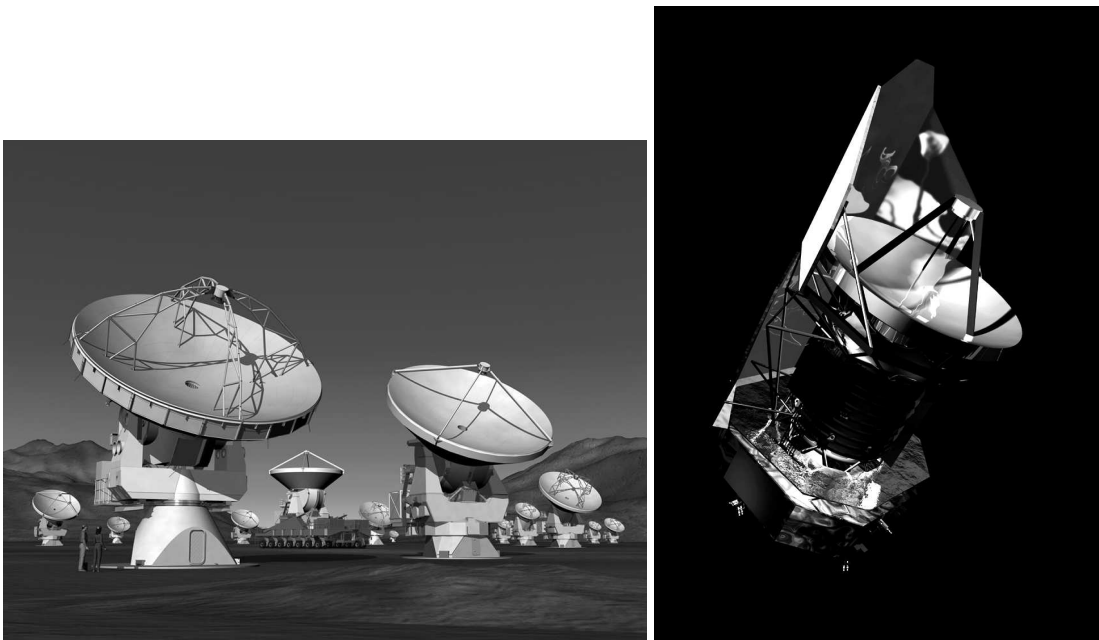
Bi-polaire straalstromen zijn een karakteristiek onderdeel van protosterren. Zulke stromen zijn niet altijd te zien, maar theoretische modellen voorspellen dat alle protosterren ze moeten produceren. In hoofdstuk 3 t/m 6 bespreken we een aantal straalstromen met behulp van emissie van het CO molecuul. In hoofdstuk 3 en 4 gebruiken we CO lijnen met lagere frequenties en in hoofdstuk 6 met hogere frequenties. Voor HH 46 in hoofdstuk 5 gebruiken we alle overgangen die waargenomen kunnen worden in het submillimeter. In alle gevallen bepalen we de temperatuur, opgeveegde massa en andere eigenschappen van de outflows. De belangrijkste conclusie is dat we voor het eerst temperaturen van rond de 100 Kelvin afleiden voor het opgeveegde gas, en dat deze temperaturen constant zijn langs de as van de straalstroom. Zulke temperaturen en temperatuurvariaties worden al sinds de jaren 90 voorspeld voor dit gas met het meest gangbare model voor outflows, het 'jet-driven' model, waarin gas van de moleculaire wolk wordt opgeveegd. Waarnemingen hebben deze temperaturen slechts zelden kunnen bevestigen.

Water-emissie van protosterren

Naast CO en H₂ is water, H₂O, één van de meest voorkomende moleculen in moleculaire wolken en in protostellaire objecten. Door de atmosfeer van de Aarde zijn water-lijnen moeilijk vanaf de grond waar te nemen. Met de lancering van Herschel zal water emissie voor het eerst waargenomen kunnen worden met ruimtelijke resoluties vergelijkbaar met submillimeter telescopen op aarde. In hoofdstuk 7 presenteren wij een grote hoeveelheid modellen die de sterkte van de wateremissie uit protostellaire omhulsels quantificeren. Deze modellen laten zien dat de emissie van water sterk afhankelijk is van de fysische structuur in het omhulsel.

Invloed van de omgeving

In hoofdstukken 2, 4 en 8 wordt duidelijk dat de omgeving van protosterren een grote invloed kan uitoefenen op zowel de fysische structuur, als op waarnemingen van protostellaire objecten. In hoofdstuk 2 laten we zien dat infra-rood licht jonge objecten met alleen schijven verkeerd kan identificeren als protosterren. Dit komt door de voorgrond extinctie van de moleculaire wolk. Doordat deze extinctie sterker is voor korte golflengtes, lijken deze bronnen veel jonger dan ze werkelijk zijn. Waarnemingen van



Figuur 9.3 — Toekomstige telescopen: ALMA (*links*, <http://www.eso.org>) en Herschel (*rechts*, <http://www.esa.int>).

gas door middel van moleculair lijn-emissie kan het verschil tussen echte protosterren en schijven duidelijk maken. Het gebruik van spectraallijn kaarten is hierin essentieel.

Een gas-rijke circumstellaire schijf in Lupus

In hoofdstuk 8 hebben we een groot aantal sterren met circumstellaire schijven waargenomen op zoek naar gas in dit soort schijven. In één schijf (IM Lup) hebben we ook inderdaad gas gevonden met onze waarnemingen. Verder onderzoek naar zulk soort schijven vertelt veel over de initiële condities van planeetvorming. Daarnaast vonden wij dat emissie van gas in dit soort schijven veelal wordt verhuld door emissie van de moleculaire wolk waarin dit soort sterren zich bevinden.

Toekomst

Onderzoek naar stervorming zal in de komende jaren nog veel intensiever worden gedaan door de komst van twee nieuwe telescopen. Allereerst is er de *Herschel Space Observatory*, die zal gaan waarnemen op golflengtes van 60 tot 600 micron. Dit golflengtegebied kan niet of nauwelijks worden waargenomen met telescopen van de aarde en staat bekend als één van de laatste 'onontdekte' golflengte-gebieden in de sterrenkunde. Protostellare objecten zenden veel straling uit op deze golflengtes. Ook naar veel nog niet waargenomen moleculen kan worden gezocht

Met de komst van de *Atacama Large Millimeter/Submillimeter Array*, een interferometer van maar liefst 50 12-meter telescopen, zal een gigantische stap voorwaarts worden gemaakt in ruimtelijke resolutie, gevoeligheid en waarneemsnelheid. De locatie, naast de APEX telescoop op het Chajnantor Plateau in Chili, zal ook voor de eerste maal

interferometrische waarnemingen van hoge kwaliteit toelaten bij de allerhoogste submillimeter frequenties, die vanaf de aarde kunnen worden gedaan.

Stervorming zal een hoofdrol spelen in de programma's die gepland staan voor deze twee faciliteiten. Een goed voorbeeld hiervan is het WISH (*Water In Star-forming regions with Herschel*) programma, dat vele lijnen van het water-molecuul zal waarnemen in een grote hoeveelheid protosterren. Fig. 9.3 laat computer-modellen zien van deze twee telescopen. Herschel zal in het begin van 2009 worden gelanceerd, terwijl ALMA, waar de bouw al van aan de gang is, haar eerste waarnemingen rond 2011 zal doen.

Curriculum vitae

Op 5 september 1980 ben ik geboren te Utrecht. Mijn basisschool doorliep ik aan de Oranje Nassauschool in Zandvoort, vooral het eerste deel wonende boven de apotheek van mijn vader. Interesse in de wetenschap, met name natuurkunde en paleontologie, had ik al vanaf deze jaren. Tijdens de overgang naar de middelbare school, verhuisden we naar Heemstede, waar ik op het Stedelijk Gymnasium Haarlem terechtkwam. Al snel werd duidelijk dat mijn talenten lagen in de exacte vakken, ondanks de bijbehorende practica. De interesse in sterrenkunde kwam eigenlijk pas in de vijfde klas, als een perfecte mix tussen wiskunde, natuurkunde en later ook scheikunde. Het volgen van een zomerschool te Dwingeloo, geleid door Prof. Icke en Dr. Jaffe in de zomer van 1997, nam mijn twijfels weg of ik de studie wel aankon.

In september 1998 begon ik aan mijn studie sterrenkunde in Leiden. Tijdens mijn studie heb ik onderzoek gedaan naar continuüm straling van lage massa protosterren onder begeleiding van Drs. Jørgensen en Prof. van Dishoeck. Mijn afstudeerproject ging over de golflengte-afhankelijkheid in de stralingstransport van de SIMPLEX code, onder begeleiding van Prof. Icke en Drs. Ritzerveld. Juni 2004 studeerde ik af met de beslissing om door te gaan in de sterrenkunde.

In september 2004 begon ik bij Prof. van Dishoeck aan mijn promotie-onderzoek op het gebied van lage-massa sterren. Het onderzoek zou vooral gebruik maken van hogere excitatie lijnen, om de structuur in de meer naar binnen gelegen delen van de protoster te bepalen. Het gebruik van stralingstransport kwam uitgebreid aan bod onder begeleiding van co-promotor Dr. Hogerheijde. Ook eventuele waarnemingen met Herschel zouden aan bod komen, binnen het WISH (*Water In Starforming regions with Herschel*) programma, waarvoor ik drie jaar lang de website heb onderhouden en ook het logo heb ontworpen.

Mijn promotie heeft me de kansen gegeven de wereld te zien. Ik nam deel aan conferenties in Parijs, Leiden, Monterey, Kona (Hawaii), Aarhus, Flagstaff, Madrid en Austin. De waarneemreizen die ik heb gemaakt naar Mauna Kea (Hawaii, drie maal) en Chajnantor (Chili, twee maal) hebben mooie data en ervaringen opgeleverd. Vooral het waarnemen op grote hoogte met APEX heeft diepe indrukken achtergelaten. Ik heb deelgenomen aan de IRAM Herfstschool in Granada. In December 2007 bracht ik een werkbezoek aan Garching. Tijdens mijn promotie heb ik Demerese Salter en Bas Nefs begeleid tijdens hun onderzoek, heb ik geassisteerd bij het vak Sterrenkundig Practicum 1 en was ik algemeen begeleider van het Bachelor Onderzoek. Ook was ik gedurende mijn promotie lid van de sociale commissie en de publiekscontacten commissie. In Januari 2008 heb ik mijn werk voorgedragen in Garching (Duitsland), Austin, Ann Arbor, Cambridge, Pasadena (allen VS) en Victoria (Canada).

Na mijn promotie zal ik als postdoc mijn onderzoek naar de structuur en evolutie van protosterren voortzetten aan de andere kant van de oceaan, in Boston, VS, als SMA-postdoc in de groep van Dr. David Wilner en Prof. Phil Myers.

Nawoord

De laatste pagina in een proefschrift is traditioneel de plaats waar je de laatste 4 jaar kan overzien. Toen ik 4 jaar geleden begon met dit proefschrift heb ik niet beseft wat voor ervaring dit zou worden en wat voor mogelijkheden er zouden komen. Maar deze 4 jaar heb ik lang niet al het werk alleen gedaan en vele mensen verdienen veel respect voor de steun die ze mij hebben gegeven.

Ten eerste David, Tycho, Aart, Erik, Kirsten, Liesbeth, Jeanne, Christine en Anita. Jullie fantastisch ondersteunend werk op alle gebieden maakt het doen van een promotie een stuk soepeler. Mijn kamergenoten, Herma, Sandrine (I still haven't tasted the tea), Bruno (teaching Americans what barbequeing really is about), Guido en Christian: het was me een genoegen, ook alle gesprekken over de jaren, in de kamer of de Grand Canyon. De grote astro-chem groep heeft me ook altijd in de gelegenheid gesteld om over van alles en nogwat tijdens lunches te praten : Jordy, Karin, Suzanne, Vincent, Kalle (great to have sailed with you), Sergio, Isa, Jeannette, Dave, Lars, Ruud, Antonio, Olja en Demerese. De vele mensen die ik heb leren kennen over de jaren zijn teveel om op te noemen, maar het sociale aspect van de sterrewacht zal moeilijk te overtreffen zijn.

The people who supported me at the JCMT (Remo, Jan, Jim and Ben) and APEX (Andreas, Per and Claudio) deserve an incredible amount of respect. I would also like the opportunity to express my appreciation to the people who made conferences and observing trips a lot of fun. There are many, but in particular Peter, Sven (Radiohead is playing, the picture is in the thesis!), Berengere and the Peruvian chef at APEX who kept calling me Kimpin , but who cooked the best meat I tasted in all of South America. Steve, you have my gratitude for all that I have learned from you about modelling and the great cooperation on the water chapter.

Ik denk met veel plezier terug aan de tijd die ik met Forza heb gevoetbald. Pedro, Anthony, Richard, Ivo en Davor, ik hoop dat we ooit nog een keer mooi gaan voetballen op Hawaii. De Floraboys en girls, Tijmen, Lara, Victor, Marije, Merlijn, 1, Kirrie, Mitch, Lexi, Pit, Rig, Jazzy, de Tante, Oli4, Cootje, Tube en Ca, ik denk met veel plezier terug aan de mooie tijden in Spa, Zeeland of gewoon in de mooiste stad van Nederland. Jullie zijn altijd welkom! Pa, ma, Ivo en Ben, jullie steun is altijd fantastisch.

De laatste woorden in dit proefschrift zijn maar voor een enkele persoon. Jij hebt me altijd bijgestaan en gesteund, ook al was ik soms ver weg of in een moeilijke tijd. De dingen die we samen hebben gezien en gedaan zullen voor altijd bij me blijven. We gaan nu op een nog groter avontuur in de komende jaren en ik zou niet weten met wie ik dat meer wil delen.

